



**HAL**  
open science

# Study and modelling of impacts on hybrid epoxy foam - aramid ply composite structures

Lara Boutros

► **To cite this version:**

Lara Boutros. Study and modelling of impacts on hybrid epoxy foam - aramid ply composite structures. Materials. Université Paul Sabatier - Toulouse III; Université de Balamand (Tripoli, Liban), 2022. English. NNT: 2022TOU30278 . tel-04251365

**HAL Id: tel-04251365**

**<https://theses.hal.science/tel-04251365>**

Submitted on 20 Oct 2023

**HAL** is a multi-disciplinary open access archive for the deposit and dissemination of scientific research documents, whether they are published or not. The documents may come from teaching and research institutions in France or abroad, or from public or private research centers.

L'archive ouverte pluridisciplinaire **HAL**, est destinée au dépôt et à la diffusion de documents scientifiques de niveau recherche, publiés ou non, émanant des établissements d'enseignement et de recherche français ou étrangers, des laboratoires publics ou privés.



# THÈSE

**En vue de l'obtention du  
DOCTORAT DE L'UNIVERSITÉ DE TOULOUSE  
Délivré par l'Université Toulouse 3 - Paul Sabatier**

**Cotutelle internationale: University of Balamand**

---

**Présentée et soutenue par  
Lara BOUTROS**

Le 17 novembre 2022

**Etude et modélisation d'impacts sur structures composites  
hybrides mousse époxy / plis d'aramide**

---

Ecole doctorale : **MEGEP - Mécanique, Energétique, Génie civil, Procédés**

Spécialité : **Génie mécanique, mécanique des matériaux**

Unité de recherche :  
**ICA - Institut Clément Ader**

Thèse dirigée par  
**Jean-François FERRERO et Issam TAWK**

Jury

**M. Patrick ROZYCKI, Rapporteur**  
**M. Olivier POLIT, Rapporteur**  
**M. Pablo NAVARRO, Examineur**  
**Mme Valentina LOPRESTO, Examinatrice**  
**M. Jean-François FERRERO, Directeur de thèse**  
**M. Issam TAWK, Co-directeur de thèse**







## Acknowledgements

First and foremost, I am highly honored that Prof. Lopresto, Prof. Polit, and Prof. Rozycki were part of my jury, their presence added so much value to my work. Thank you to my supervisors, Prof. Ferrero, Dr. Navarro, and Dr. Tawk for their invaluable advice, continuous support, and patience during my Ph.D. study.

Thomas M. you have been a great help, and your contribution to this work is undeniable, I wish you all the best in your future adventures.

Thank you to the ICA staff, and technicians for always showing support and being a great help, especially Louison. You have been wonderful support on the professional and personal levels. I have won a friend.

Thank you to my colleagues and friends, the current Ph.D. students, and the ICA Alumni. Thank you for making our coffee breaks so fun and interesting. Alexy and Arthur, thank you for being such awesome friends, particularly in the last few months when the stress level was too high. Adrien, thank you for always showing a smile and for spreading positive vibes. Julien S. thank you for making our baby foot sessions so fun since you are a very bad loser. Thibaut and Marion, thank you for all the brunches and dinners, being over at your house felt like home. Adama and Jennifer, thank you for being a great support. Jeny you are an amazing friend and I am lucky to have you in my life. Angelique, Léa, and Julien L. thank you for always showing support and for saying encouraging words.

Moving to the best office of the ICA, as Ldjoudi once said, the bureau AR2020. Ldjoudi thank you for always sharing your experience and wisdom with me. Marta your presence added an amazing flavor to our office when we needed Spanish vibes. Hassan thank you for listening, thank you for your amazing dishes, cakes, and funniest stories. Louis, no words can describe how much I appreciate your friendship, I consider you as part of my family now...deal with it.

The CT team, thank you for supporting me in the last few months of this journey. Thank you for your encouragement, you really are the " Les fleurons de l'industrie française ". Ange, you were at the very beginning of this journey, and at the very end, and your presence always made a very big difference.

Patrick Azar, you are the best neighbor I have ever wished for. Thank you for your support and your help, daily. You being by my side made everything easier.

Moving to the Lebanese side, I would like to thank my cousins for always being by my side. My brother Elie and his wife Sandra, thank you for being my backbone. Mom and Dad, thank you for all your sacrifice, I hope that I made you proud.

Finally, I would like to thank my greatest support, my partner Fadi, I am lucky to have you.





---

# Table of content

---

<b>Table of content</b> .....	<b>i</b>
<b>Chapter I. Introduction and Literature Review</b> .....	<b>1</b>
Résumé en français .....	1
I.1 Introduction .....	3
I.1.1 Context .....	3
I.1.2 Problematic and manuscript organization .....	4
I.2 Literature Review .....	7
I.2.1 Overview of impact and standard solutions for protection .....	7
I.2.2 Composite materials for protection applications.....	16
I.2.3 Polymer foams.....	38
I.2.4 Conclusion.....	47
References .....	49
<b>Chapter II. Experimental Study of Low-Velocity Impact Behavior of Hybrid Structures</b> .....	<b>59</b>
Résumé en français.....	59
Dynamic response of epoxy foam structures reinforced by aramid plies subjected to low velocity impact .....	61
Abstract:.....	61
II.1 Introduction .....	61
II.2 Experimental procedure.....	65
II.2.1 Manufacturing of the structures .....	65
II.2.2 Drop weight impact test .....	67
II.3 Results and discussion .....	68
II.3.1 Impact response of neat epoxy foams .....	68
II.3.2 Influence of the number of Aramid plies located in the middle.....	69
II.3.3 Influence of aramid plies location .....	72
II.3.4 Influence of foam density variation .....	78

II.4	Summary.....	84
II.5	Conclusion.....	85
	References .....	87
<b>Chapter III. Experimental Study of High-Velocity Impact Behavior of Hybrid Structures .....</b>		<b>91</b>
	Résumé en français.....	91
	Abstract:.....	94
III.1	Introduction .....	94
III.2	Experimental procedure.....	97
III.2.1	Base materials .....	97
III.2.2	Structure preparation.....	98
III.2.3	Backing material .....	100
III.2.4	High-velocity impact test .....	101
III.3	Results and discussion .....	102
III.3.1	Morphology of damage .....	102
III.3.2	Back Face Signature and indentation.....	110
III.4	Conclusion.....	117
	References .....	119
<b>Chapter IV. Numerical Modeling of Epoxy Foam/Aramid Fabric Hybrid Structures .....</b>		<b>123</b>
	Résumé en français.....	123
	Abstract.....	126
IV.1	Introduction .....	126
IV.2	Aramid plies modeling strategy.....	130
IV.2.1	Developed semi-continuous model.....	130
IV.2.2	Parameter identification .....	134
IV.3	Epoxy foam modeling strategy.....	134
IV.3.1	Formulation .....	134
IV.3.2	Damage.....	135

IV.3.3	Parameters identification.....	135
IV.4	Numerical results and discussion .....	136
IV.4.1	Drop weight impact test .....	136
IV.4.2	Gas gun impact test .....	142
IV.5	Conclusion.....	149
	Acknowledgment.....	150
	Reference.....	151
<b>Chapter V.</b>	<b>General Conclusion and Perspectives.....</b>	<b>155</b>
	Résumé en français.....	155
V.1	Conclusion .....	158
V.2	Perspectives .....	161
V.2.1	Structures design .....	161
V.2.2	Semi-continuous numerical model.....	163
V.2.3	Epoxy foam model .....	163
	References .....	165
<b>Appendix A.</b>	<b>Hybrid Structures fabrication.....</b>	<b>167</b>
<b>Appendix B.</b>	<b>Clay witness validation and modeling .....</b>	<b>177</b>
<b>Appendix C.</b>	<b>Aramid epoxy semi-continuous model development and parameters identification.....</b>	<b>185</b>
<b>Appendix D.</b>	<b>Epoxy foam characterization and parameters identification .....</b>	<b>219</b>
<b>Appendix E.</b>	<b>Experimental and Numerical Results for Low-Velocity Impact.....</b>	<b>233</b>



---

# Chapter I. Introduction and Literature Review

---

## Résumé en français

### INTRODUCTION ET ETUDE BIBLIOGRAPHIQUE

La première partie du chapitre est consacrée à la présentation de la problématique principale de ce travail et à l'organisation du manuscrit.

La protection contre l'impact est un facteur essentiel dans le domaine du transport tout comme dans la protection individuelle (civile et militaire). Les systèmes de protection sont des produits qui combinent à la fois une résistance élevée aux impacts et une faible masse. Il est donc essentiel de trouver des matériaux de protection innovants et légers pour faire face aux menaces possibles rencontrées. Cette recherche vise à étudier la capacité d'absorption d'énergie et de protection d'un nouveau matériau hybride, combinant des fibres d'aramide et des mousses époxy, lorsqu'il est soumis à un impact. De multiples paramètres sont étudiés à travers des essais d'impact à basse et haute vitesses.

Cette thèse est constituée de cinq chapitres principaux. Le chapitre 1 présente le contexte du travail et la bibliographie. Les chapitres 2, 3 et 4 constituent le cœur de ce travail, et sont présentés sous forme d'articles. Ces chapitres sont soutenus par des annexes qui servent à développer certaines idées et méthodologies de modélisation qui ne peuvent pas être incluses dans les articles. Le chapitre 5 présente la conclusion et les perspectives. Chaque chapitre débute par une introduction en français.

Le premier chapitre est consacré à la problématique et à la bibliographie. Le deuxième chapitre est dédié à l'étude du comportement d'un matériau hybride lors d'un impact à basse vitesse. Le troisième chapitre présente le comportement de ce même matériau hybride soumis à un impact haute vitesse. Le quatrième chapitre présente la stratégie numérique utilisée pour modéliser ces structures hybrides. Cette stratégie est basée sur le scénario d'endommagement



## *Introduction and literature review*

observé pour les impacts à basse et haute vitesses. Enfin, le cinquième chapitre résume les objectifs atteints durant cette thèse ainsi que les perspectives.

La première partie de la bibliographie présente une synthèse des types d'impacts existants et de leur classification, des tests expérimentaux utilisés dans la littérature pour réaliser ces impacts et des matériaux de protection actuels. Les matériaux métalliques, céramiques, cellulaires et textiles à haute performance sont les matériaux les plus utilisés pour les applications de protection. Le choix d'un matériau de protection approprié est basé sur l'énergie d'impact définie par la vitesse et la masse du projectile.

La deuxième partie de la bibliographie se concentre sur l'application des matériaux composites dans le domaine de la protection et sur leur comportement face à l'impact. Au cours de leur vie, les matériaux composites sont soumis à des impacts basse et haute vitesses. Les principaux modes d'endommagement résultant d'un impact à faible vitesse sont la rupture des fibres, le délaminage et la fissuration matricielle. Quant à l'impact à haute vitesse, en plus des précédents, les matériaux composites subissent une création d'un bouchon sous l'impacteur, appelé "shear plug", et une déformation des fibres primaires et secondaires. La réponse des matériaux composites à l'impact est influencée par plusieurs facteurs : le type de fibre, le type de résine, la géométrie de l'impacteur. Cette partie décrit également les stratégies numériques utilisées pour modéliser les matériaux composites.

La troisième et dernière partie de la bibliographie est axée sur les mousses polymères appliquées aux systèmes de protection (transport, emballage, accessoires de sport). Leur comportement lors d'impact y est décrit. Enfin, un aperçu des stratégies numériques utilisées pour modéliser les mousses est présenté.

## **I.1 Introduction**

### **I.1.1 Context**

Safety is among the most critical factors in the transportation industry, i.e., aircraft, automobiles, and personal protection, i.e., civilians and military. Protection systems are life-saving products that combine high-impact resistance and lightweight properties simultaneously.

Protection systems can be subjected to numerous impacts, a cyclist's helmet impacts the ground, a tool drop during maintenance, a racecar hitting the roadside barrier, a bird striking an aircraft during takeoff, and a high-speed bullet striking a body armor. The hazards against protection systems are many and differ according to the shape of the impactor, its speed, and its kinetic energy.

Finding innovative, lightweight protection material is essential to stand against possible threats. Recent research highlighted the importance of the lightweight feature in protective materials. In the transportation industry, composite materials substitute traditional protective materials like metal, offering the same level of protection, less weight, and less fuel consumption. Composite materials are among the most used materials in protection applications against impacts. High-performance fibers are used in most aircraft protection systems against tool drop impact, fragments, bird strikes, and ballistic impacts.

On the other hand, cellular materials gained extensive focus recently due to their capacity to absorb energy due to their microstructure. Polymer foams are used in modern automobiles as shock absorbents to protect the driver and passengers in case of impact. Sports protective accessories contain polymer foams to protect the players from injuries resulting from impacts, i.e., helmets and ankle protection. Lightweight criteria are crucial in such applications to ensure flexibility and comfort for personals.

Regardless of the effectiveness of the recent protective materials, continuous effort is put into improving their effectiveness to weight ratio, using numerous techniques, such as hybridization and reinforcement by fillers. Hybridization techniques combine several materials resulting in a final one with improved properties.

## *Introduction and literature review*

In the presented work, the capacity of protection of a novel hybrid material is studied when subjected to impact. The hybrid material combines aramid fibers and polymer epoxy foam. The potential of this novel material is assessed based on its behavior and modes of failure.

### **I.1.2 Problematic and manuscript organization**

This research aims to study the energy absorption and protection capacity of a novel hybrid material that combines aramid fibers and epoxy foams when subjected to impact. Multiple parameters are studied through low and high-speed impact tests.

The challenges that this study encountered are the following:

- Studying the behavior of a new hybrid material against low and high-velocity impact and deducing the damage modes in such materials.
- Studying the energy absorption capacity that this material can provide and the level of protection on the protected material's back face, therefore deducing optimized configurations.
- Finding a numerical model that can represent the scenario of damage seen physically during impact can be used for optimization purposes in future work.

This thesis is divided into five main chapters. Chapter 1 presents the context of the work and a literature review. The core of the work, chapters 2, 3, and 4, are shown in the form of articles. Chapter 5 concludes the work presented in this manuscript and proposes perspectives for future work. Appendixes are used to expand specific ideas and modeling methodology that cannot be included in the articles. An introduction in French complements each chapter.

The dissertation structure is presented in Figure I-1.

## Introduction and literature review

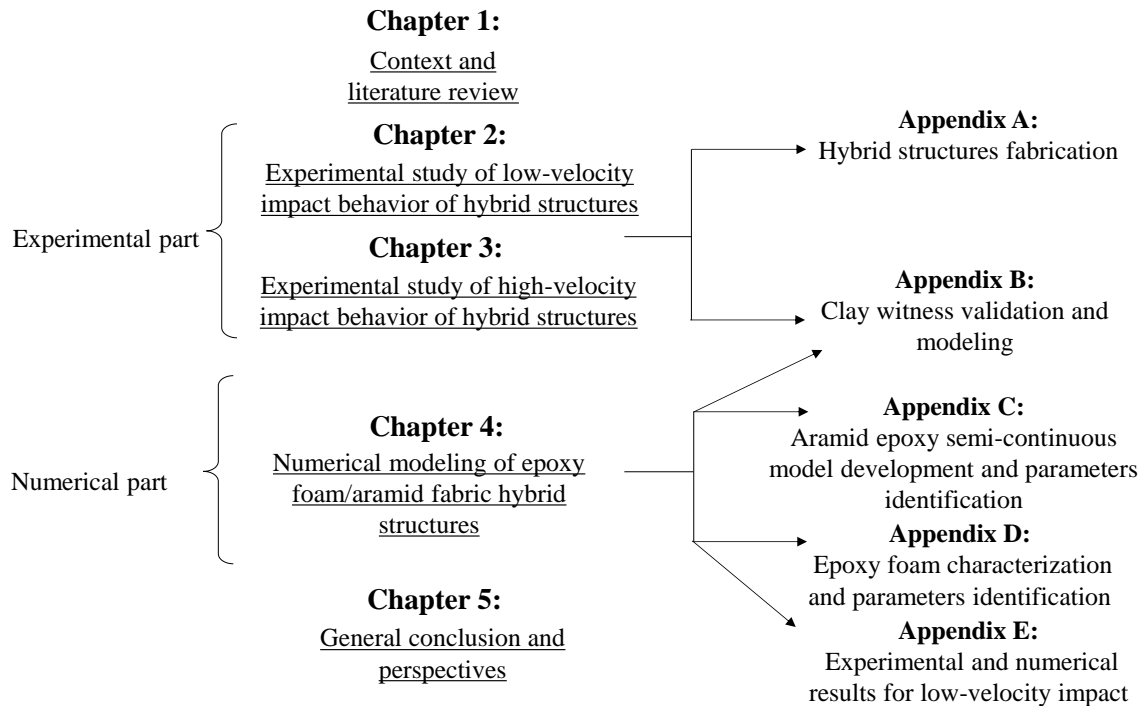


Figure I-1: Manuscript structure

The first chapter deals with the context, the problematic, and the literature review. This work aims to study the impact behavior of a hybrid material subject to low to high-velocity impact. The literature review focuses on the recent solutions used in protection systems, emphasizing woven composite materials and polymer foams. Numerical strategies are presented to model these materials; the semi-continuous approach is privileged to model the aramid composites based on physical observations.

The second chapter sets out the behavior of the hybrid structure when subjected to low-velocity impact. The structures are designed by varying numerous parameters, such as foam density, the number of aramid fabric plies, and their location. The designed structures are tested and examined based on load versus displacement curves, permanent indentation, capacity to protect the back face, and damage morphology.

The third chapter presents the behavior of the hybrid materials when subject to high-velocity impact. Several configurations are tested by varying the aramid fiber location and the epoxy foam density. A technique used to test body armor is adopted in this chapter to study the capacity to protect the back face of the structures.

## *Introduction and literature review*

The fourth chapter presents the numerical modeling strategy used to model these hybrid structures. It is based on the scenario of damage observed for the low and high-velocity impacts. A model based on a semi-continuous strategy is used to represent the aramid plies. The epoxy foam is modeled with an existing material law in the FE software RADIOSS.

The fifth chapter summarizes the objectives and perspectives achieved in this work. These hybrid structures are potential structures for protection systems. Several design improvements are proposed to improve the effectiveness-to-weight ratio of the hybrid structures. Moreover, perspectives concerning the numerical model are presented.

## **I.2 Literature Review**

Various protection systems exist in the market, and their selection relies on the hazard type and the intended application. This section presents an overview of the type of impacts that exist and their classification, the experimental tests used in the literature to simulate those impacts, and the current protection material. An overview of the application of composite material in the protective domain is presented, along with the behavior of composite material under impact. Then, an outline of the behavior of polymer foam under impact is presented. The numerical tools are presented to simulate the damage inside the studied materials. Finally, a conclusion summarizing the literature findings and redirecting the field of focus of this work is established.

### **I.2.1 Overview of impact and standard solutions for protection**

#### **I.2.1.1 Impact problematic**

An impact is a collision between two bodies in a short period that causes a velocity change in those bodies [1]. The impact can occur between fluid-fluid, fluid-solid, and solid-solid. The fluid-fluid impact can include reservoir filling with liquid. Fluid-solid impact consists of slamming and sloshing impacts. Hydrodynamic impacts can lead to critical damage. Slamming impact can be characterized by a wave impact on the surface of a ship or the impact of an aircraft emergency landing in the sea [2]. Sloshing is the motion of a liquid confined in a container or reservoir. The excitation of this liquid causes damage to the wall of the structures, which is contained in it [3]. Another fluid-solid impact is the bird strikes (Figure I-2), the contact between a moving vehicle and an airborne avian creature [4]. A bird strike is one of the major causes of fatal failures in aeronautical fields; almost 90% of the damage resulting from the impact of a foreign object is caused by bird strikes [5].

## Introduction and literature review



Figure I-2: Typical bird strike scenario [4]

The solid-solid impacts (Figure I-3) can include the impact of the helmet of a cyclist on the ground, a tool drop during maintenance on a vehicle or aircraft floor, a tennis bat on a ball, or even a bullet on a tank or body armor.



(a)



(b)

Figure I-3: (a) Vertical impact test on cyclist helmet [6], (b) bullets impacts on a body armor [7]

### **I.2.1.2 Impact classification**

All types of impact mentioned above can be classified according to the velocity of the impact or its kinetic energy. The energy transfer between the impactor and the structure and the damage propagation depends on the impact velocity and kinetic energy. Three types of impact velocities can be listed:

a) *Low-velocity impact*: an extended contact between the impactor and the structure. In this case, the structure will absorb more energy in proportion to the impact energy. The low-velocity impactor has a speed between 1 and 10 m/s [8]. This impact can occur by a tool drop during maintenance on an aircraft or vehicle floor [9].

b) *High-velocity impact*: less contact time than the low-velocity impact, dominated by stress waves. The damage is localized, and the impactor's speed is generally between 100 and 1000 m/s. This type of impact can be represented by a bird strike on aircraft or bullets impacts on body armors [8].

c) *Hyper-velocity impact*: the damage is localized, and the impactor's velocity exceeds 1000m/s [8].

This study will focus on the low-velocity, 6 m/s, and high-velocity impacts that reach up to 180m/s.

### **I.2.1.3 Impact tests apparatus**

Different experimental apparatus exists to simulate the actual impact structures undergo during their service life. The drop weight test and the pendulum test are the most frequently used to simulate low-velocity impacts, as for intermediate and high-velocity impacts, it is the gas gun test [8].

#### **Drop weight apparatus**

The drop weight apparatus usually simulates a low-velocity impact of a large mass. The velocity range of such a device can be from 1 to 10 m/s [8]. A weight is dropped from a predefined height using a release system to reach the desired kinetic energy [10]. During the



## Introduction and literature review

test, a sensor records the load with the time history. A sensor or a high-speed camera can capture the velocity of the impactor before and during the impact, Figure I-4.

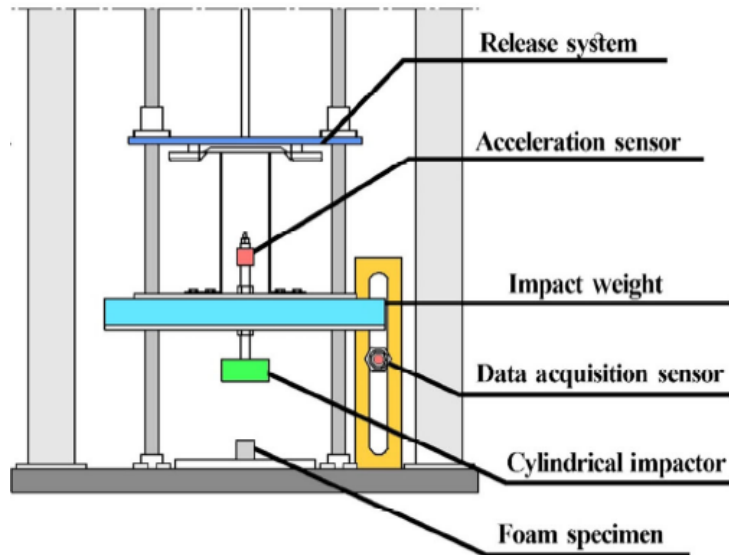


Figure I-4: Schematic of a drop-weight impact apparatus [11]

### Pendulum impact

The Charpy test is one of the pendulum impact tests. This test aims to simulate a low-velocity impact to identify the resistance of the impacted material [12]. Figure I-5 shows the apparatus of the Charpy test.

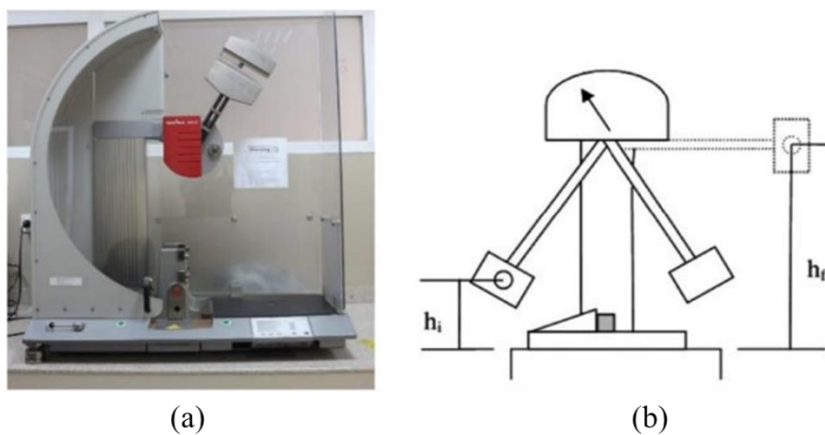


Figure I-5: (a) Apparatus and (b) schematic of the Charpy test machine [13]

## Introduction and literature review

The specimens are placed horizontally on the apparatus. The impact is achieved when the pendulum-like hammer is released from its system and strikes the specimens. The total energy dissipated is calculated by multiplying the mass, the gravity, and the difference between  $h_f$  and  $h_i$  [12].

### Gas gun apparatus

The gas gun test is the most used to simulate high-velocity impact. The apparatus can represent the impact of a bird strike on an aircraft or a bullet impact on a body armor material [8,10]. Figure I-6 shows a high-velocity impact apparatus. The projectile is launched at the desired velocity through the compressed gas pressure contained inside the pressure vessel. A high-speed camera is usually used to capture the velocity of the impactor before striking the target. Another high-speed camera can be added at the other extremity of the structure to record the residual velocity after impact in case of perforation.

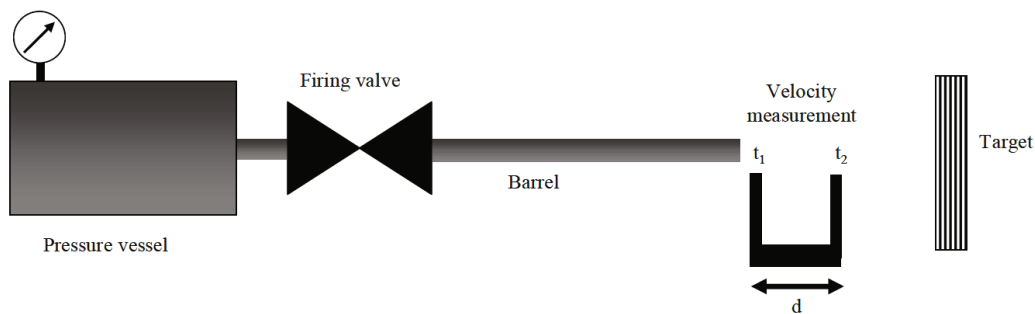


Figure I-6: schematic of a high-velocity impact apparatus [14]

The high-velocity impact test helps compare the tested structures based on the area of damage, the mode of damage, residual velocity, if the projectile is stopped or not, and permanent indentation.

However, a high-velocity impact test can identify another critical parameter: the back face signature (BFS). The BFS is the trauma left by the impacted target on a backing material. The backing material is usually soft clay, also known as a clay witness [15]. The objective of the clay witness is to represent the consistency of the human body. This technique is used to assess

## Introduction and literature review

the performance of body armor materials. The clay is heated before each impact at 40°C for three hours to ensure a similar consistency between the clay witness and the human body [16]. Figure I-7.a shows the apparatus of a high-velocity impact with a backing material. The target is placed on the clay witness and fixed with elastic bands; the clay is confined within a wooden box. After the impact, the BFS is measured underneath the impact area, Figure I-7.b.

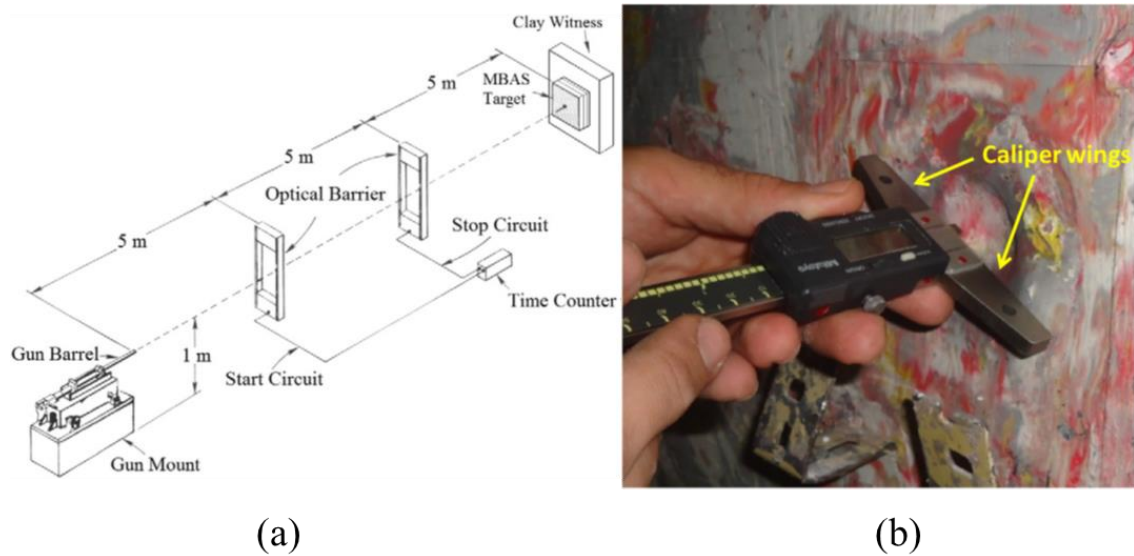


Figure I-7: (a) High-velocity apparatus with backing material, (b) BFS measurement on the backing material [15]

### I.2.1.4 Recent solutions for protection

The need to protect, save and guard is increasing with the threat advancement. Protective materials are needed in day-to-day applications. Metallic materials, ceramics, cellular materials, and high-performance textiles are the most used materials for protection applications. The choice of a suitable protective material is based on the type of impact, the velocity, and the mass of the projectile.

*Metallic materials* are one of the most primitive materials used for protection. Steel armor is widely used in vehicle shielding [17]. Metallic armors have several benefits: their low price, ability to be easily manufactured, and capacity to endure multi-impacts. Aluminum alloy is also

## *Introduction and literature review*

introduced as a protective material for vehicle shielding (Figure I-8); due to its relatively low density compared to steel; thicker sections can be used to provide optimum protection [18]



Figure I-8: Rear of a military vehicle made from an aluminum alloy plate [18].

In addition, metal is introduced in sandwich structures as a metallic foam core. Metallic foam cores are characterized by a lightweight, high energy absorption and energy dissipation [19]. In aerospace, aluminum honeycomb is used extensively due to its shock absorption capacity and efficiency-to-weight ratio. For instance, the landing gear in Apollo 11 lunar module was made from a crushable aluminum honeycomb[20].

*Ceramic material* is known for its high hardness and brittleness [18]. Ceramics are usually used against ballistic impact, especially in body armor protection. Ceramics plates are vital in a multilayered armor system (MAS) (Figure I-9), where they are placed as impact face and backed with less rigid material, Figure I-9. The purpose of the ceramic tiles in a MAS is to deform the head of the bullet and fragment it, then collect the shattered pieces.

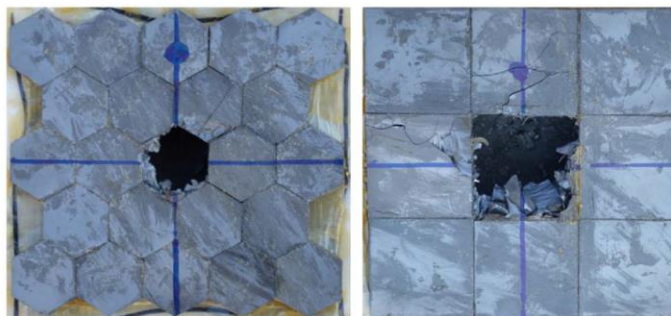


Figure I-9: Ceramic plates with different geometry as impact face in a MAS [21]

## Introduction and literature review

In recent years, *cellular material* gained extreme interest as a potential replacement for heavy and bulky protective materials. The microstructure of cellular materials, honeycombs, and foams give them the advantage of high energy absorption. In addition to aluminum foams applications in car bumpers for shock absorption [22], polymer foams also show good impact resistance properties. Polymer foams are used in transport, packaging, and protection fields. Polymer foams are a part of the protection system of military helmets (Figure I-10), cyclist helmets, and soccer players' protection accessories, i.e., shin and ankle protection [23].

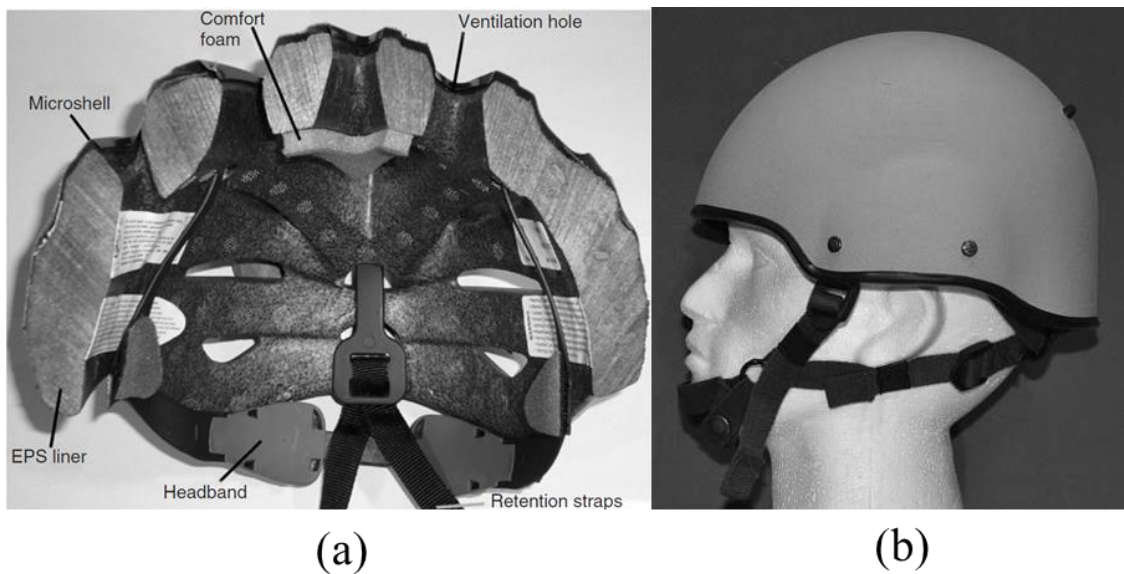


Figure I-10: (a) Cyclist helmet with EPS, expanded polystyrene foam [23], and (b) military helmet with composite shell and high-density polymer foam liner [17]

*High-performance textiles* are an excellent candidate for obtaining lightweight and efficient protective material. Composite materials are lightweight materials used in various protection fields, namely, personal protection, automotive, aeronautical, and naval. The most used fibers in protection applications are aramid, UHMWPE (ultra-high molecular weight polyethylene), carbon, and glass [17]. In the automotive field, composite materials are progressively replacing traditional metallic parts, which help reduce weight and fuel consumption while providing good impact resistance [24], Figure I-11.

## Introduction and literature review

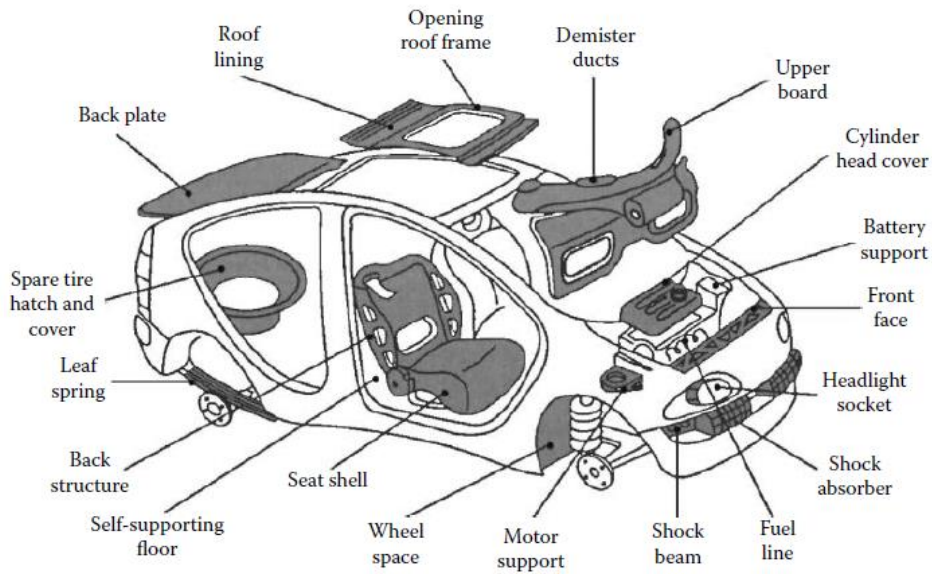


Figure I-11: Composite parts in an automobile [24]

In aviation, composite materials offer structural strength comparable to traditional metals while decreasing the weight [4]. Figure I-12 shows that around 50% of the Boeing 787 materials are composites.

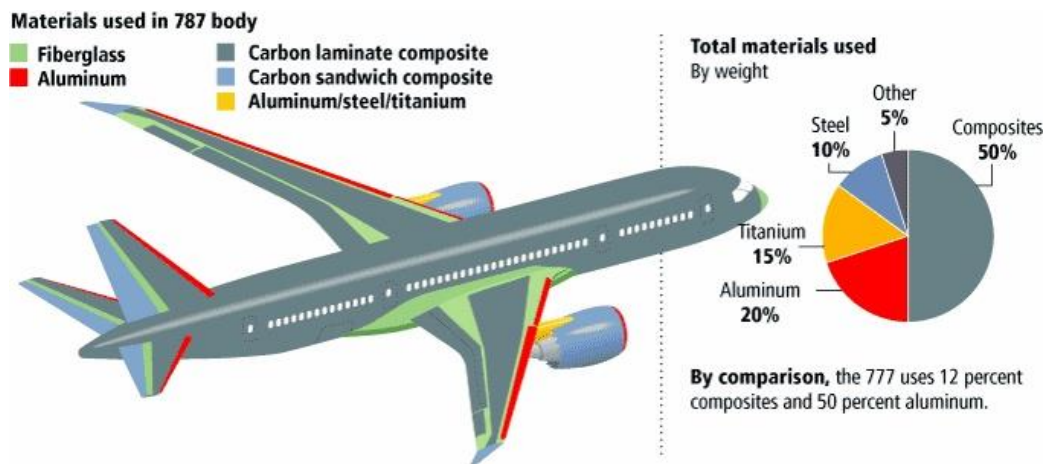


Figure I-12: Usage of various materials in the Boeing 787 Dreamliner [25]



## *Introduction and literature review*

Composite fabrics play an essential role in body armor, where most soft body armor that aims to protect against stabbing and gunshots is made of composite textiles [17]. The most popular fibers used in body armor are aramid and UHMWPE.

In the present study, the focus will be on composite materials and polymer foams as protective materials.

### **I.2.2 Composite materials for protection applications**

Composite materials offer a superior strength-to-weight ratio. These materials are widely used in various applications, such as the transportation field, construction field, and military applications, i.e., body armor and aircraft shielding.

Impact loading affects composite materials during their service life. The impact loading might vary from a low-velocity impact to a high-velocity impact. The high-velocity impact can be flying fragments striking aircraft during landing and takeoff, whereas low-velocity impact can be a tool drop during maintenance. Hence, substantial efforts are made to improve the impact resistance of composite materials.

Recent solutions are used to improve composites protection capacities, such as reinforcing composites with nanoparticles, using different fiber architecture, and hybridization techniques. The efforts also include inventing new ballistic fibers.

The design of an optimal safe structure comes from understanding its damage tolerance and mode of failure. The damage modes depend on the loading type and its direction towards the target, the velocity, and the kinetic energy of the threat. They include matrix cracks, delamination, and fiber breakage. Numerical tools come in handy when designing composite structures, especially protection applications. Finite element models proved to be an effective way to predict the scenario of damage inside composite material while saving time and cost.

#### **I.2.2.1 Overview of composite materials**

Composite materials have two phases: the continuous phase and the reinforcement phase. The *reinforcement phase*, the fiber, is embedded inside the continuous phase called the matrix. The reinforcement can be woven, unidirectional, or nonwoven felt [17]. The most used

## Introduction and literature review

protection applications are unidirectional and woven. In unidirectional laminates, fibers in a single layer are parallel to each other, resulting in high load-carrying capacity in the direction of the fibers. As for woven fabrics, two different types exist, the 2D and the 3D woven fabric. 2D woven fabric is characterized by interlacing two types of yarns, where yarns that run along the fabric are called the warp, and the ones that float over and beneath the warp yarns are called weft [26]. Figure I-13 shows three different weaving patterns of a 2D woven fabric. 3D woven fabric exists in three structures: the 3D braid, the orthogonal, and the multi-axial (Figure I-14). Different fabric structures are blended in some applications to optimize their impact resistance.

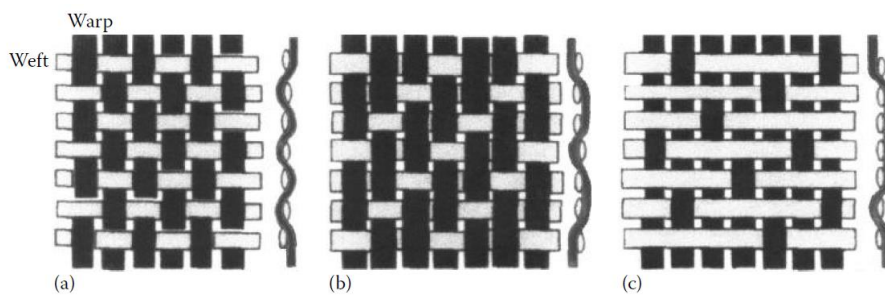


Figure I-13: 2D woven fabric, (a) plain weave, (b) twill weave, and (c) satin weave [24]

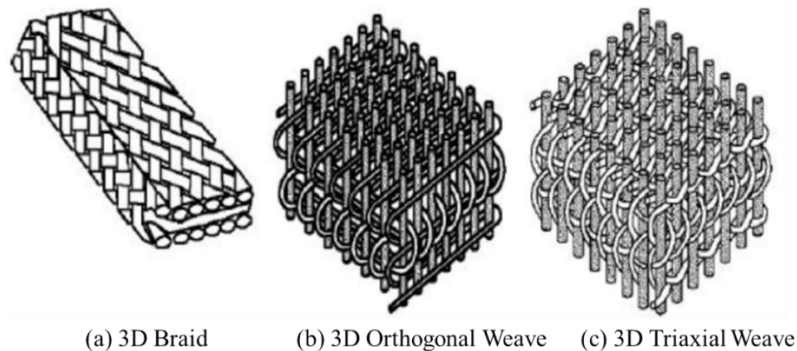


Figure I-14:3D fabric structure [26]

The role of the resin, *the continuous phase*, is to bind the fibers together and ensure load transfer from one fiber to another. Two main types of the continuous phase, or matrix, exist thermoset and thermoplastic.



## *Introduction and literature review*

Thermoset resins include epoxy, polyester, and vinyl ester. Thermoset resins are most common in structural, automotive, and aeronautical applications [27]; they are characterized by low initial viscosity, rapid cure, and low curing shrinkage for dimensional control [28]. Thermoplastic resins include polypropylene, nylon, and Polyetheretherketone. Thermoplastics are temperature-dependent, softening when heated and stiffening when cooled [29]. The dependency on temperature limits the application of thermoplastic resins. However, thermoplastic resins have high flexibility and efficient shock absorption

### **I.2.2.2 The behavior of composite material subjected to impact**

The understanding of the mode of damage inside composite materials is vital. Composite materials are subjected to low and high-velocity impacts, and knowing the damaging effect is essential to designing improved structures. This section presents the damage modes in composite materials that result from low and high-velocity impacts.

#### **Low-velocity impact behavior**

During their service life, composite materials are subjected to low-velocity impacts. Abrate [14] indicates that the low-velocity impact results in fiber breakage, delamination, and matrix failure. Delamination and matrix crack strongly depend on the matrix type, whereas fiber failure depends on the fiber type. Figure I-15 shows the different damage types according to the extent of the impact [30]. Liu et al. [31] showed that the *matrix cracks* happen before the delamination, resulting from property mismatch between fibers and matrix.

As for *delamination*, it results from a bending stiffness mismatch between two adjacent layers. Delamination can be characterized by cracks between plies of different fiber orientations [31]. Many studies tried to link delamination with matrix cracking. Ouyang et al. [32] study revealed that delamination is more likely to occur when two inter-laminar cracks meet.

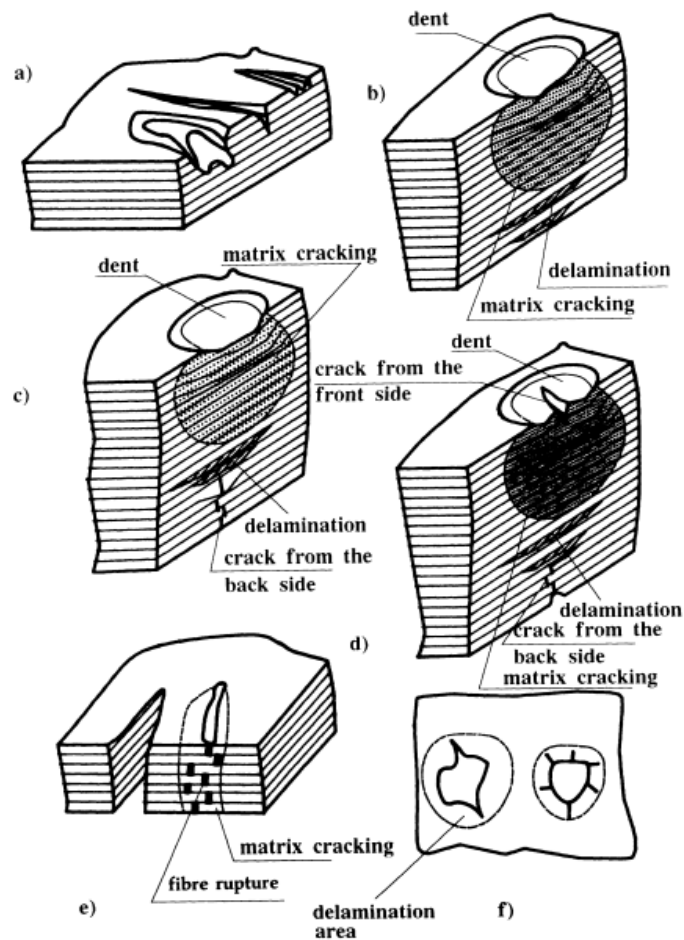


Figure I-15: Damage types of composite material [30]

*Fiber failure* happens at a later stage in the impact chronology. Fiber failure requires higher impact energy than matrix crack to appear. Fiber rupture is due to exceeding the elastic limit. The failure in the fibers underneath the impactor is due to high-localized stress, whereas on the opposite side of the impact, fibers fail due to high bending stresses [14]. Fiber failure leads to the final failure of the material due to a significant reduction in residual properties.

### High-velocity impact behavior

Unlike low-velocity impact, high-velocity impact does not give the impacted structure enough time to respond. Naik et al. studied the high-velocity impact damage mechanisms of glass/epoxy and carbon/epoxy [33]. It is shown that the modes of damage are cone formation, matrix cracking, delamination, shear plugging, and deformation of the primary and secondary yarns.

## *Introduction and literature review*

As the impactor strikes the target, this latter is subjected to compressive stress waves. Due to compressive and transverse shear waves, the primary yarn and secondary yarns are subjected to deformation.

*Cone formation* happens when the impactor strikes the target; the undamaged layers deform in a conical shape on the back face of the structure. The cone is formed due to the shear waves that propagate along with the thickness of the structures [26].

*Primary yarns tensile failure:* primary yarns are the most prone to failure since they are located directly under the impactor. They face the higher strain and resist the most against projectile penetration. They fail when the induced tensile strain exceeds the primary yarn ultimate strain.

*Secondary yarns deformation:* all yarns other than the primary are called secondary yarns; they also take a share in energy absorption.

Figure I-16 shows the cone formation on the back face of the target and indicates the location of the primary and secondary yarns.

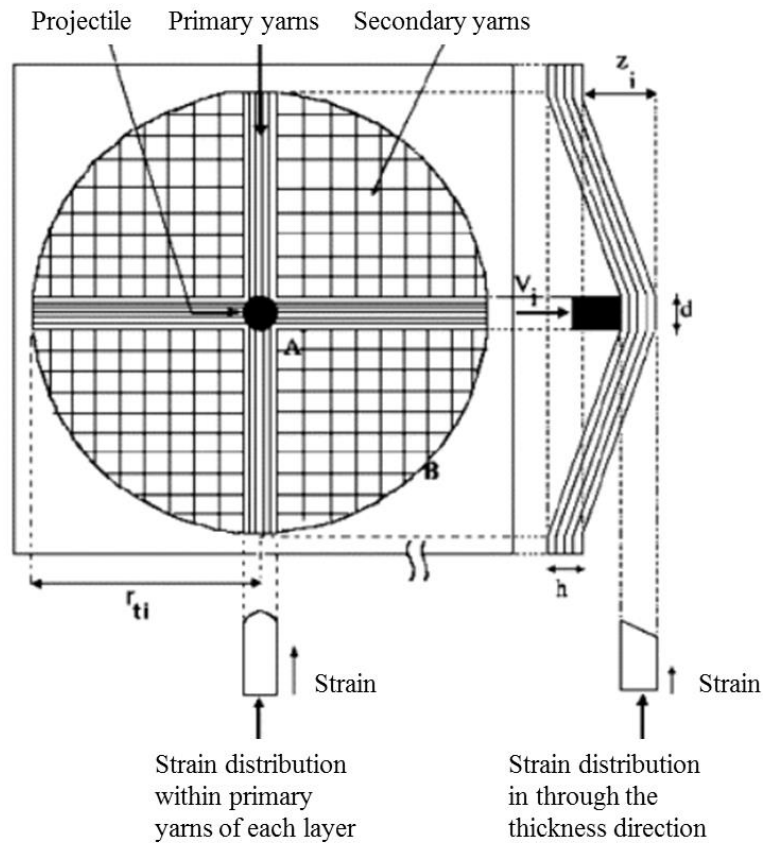


Figure I-16: Cone formation and yarns deformation [33]

*Shear plugging* is one of the effective energy absorption mechanisms in woven composites. The shear plug is created due to the plugging stress around the impactor edges when it enters the target [26]. Figure I-17 shows a scenario of damage according to the impact velocity. When the impact velocity exceeds the ballistic limit of the material, a cutout zone (plug) travels away from the target (Figure I-17.c). If the induced shear plugging stress exceeds the strength, a failure in the material occurs.

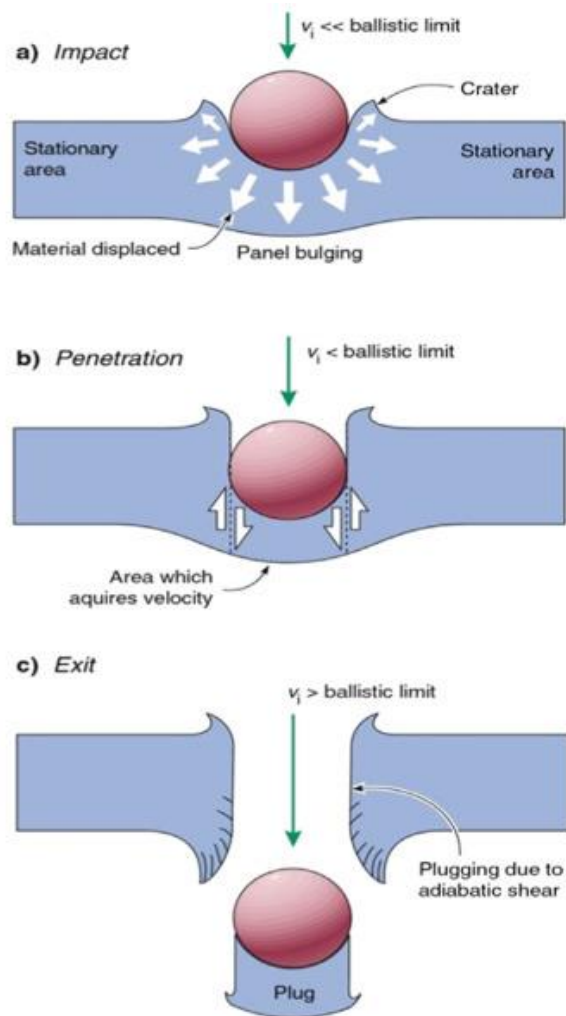


Figure I-17: Shear plug formation [34]

*Friction* is another aspect involved in decreasing the impactor's kinetic energy. Friction energy between the yarns and the impactor also contributes to energy absorption. Chu et al. studied the effect of coating aramid fiber with particles deposited on the surface of the fibers to increase inter-yarn friction [35]. The study deduces that the friction coefficient increases, enhancing the impact resistance in woven composites.

### **I.2.2.3 Parameters influencing the dynamic behavior**

Composite materials over the past decades proved to be good candidates for protection applications. Nevertheless, the impact behavior of composite material can be influenced by numerous factors. Efforts have been implemented to identify the factors that can influence the

behavior of composite materials. Among those factors are the fiber architecture and weaving pattern, fiber and matrix materials, the bonding type between the plies, the projective geometry, hybridization, and friction [26].

### **Influence of fiber architecture**

Fiber architecture plays an essential role in the response of composite material when subjected to impact. Aramid fiber with different weaving patterns, twill, basket, and satin, was tested when subjected to high-impact velocity. Samples of 1/1 plain weave, twill weave, 2x2 basket, and satin weaving construction are tested by high-velocity rifles [36]. The investigation showed that high-speed 2×2 Basket fabric had the highest ballistic resistance performance than the plain weave construction (Figure I-18).

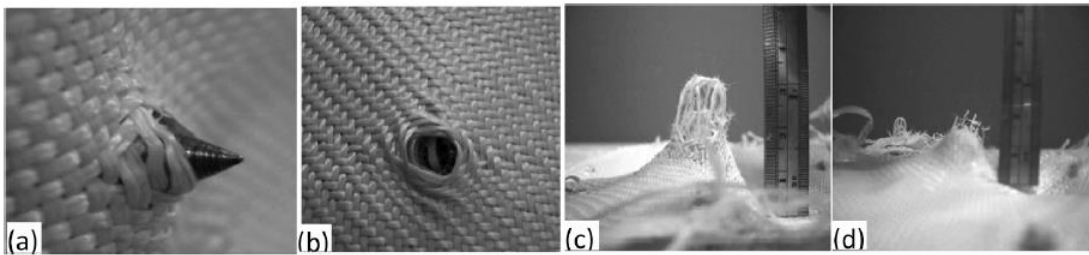


Figure I-18: Fabrics after impact: (a) Steel-cored bullet test of 2×2 Basket weave fabrics, (b) Twill fabrics with a steel-cored bullet removed, (c) General view of Satin weave fabric damaged with fibers drawn out, and (d) General view of Plain weave fabric damaged with torn fibers [36]

Zhou et al. showed the influence of the weaving pattern of UHMWPE fibers on the impact of its impact behavior numerically. The numerical investigation included five models of woven fabrics: plain, 2/1 twill, 3/1 twill, 5-end satin, and 7-end satin. The study showed that plain weave absorbs higher energy (Figure I-19). The study revealed that this increase in energy absorption might result from more intercalating points in the plain weave pattern, where stress can be transmitted into a larger area of the fabric [37].

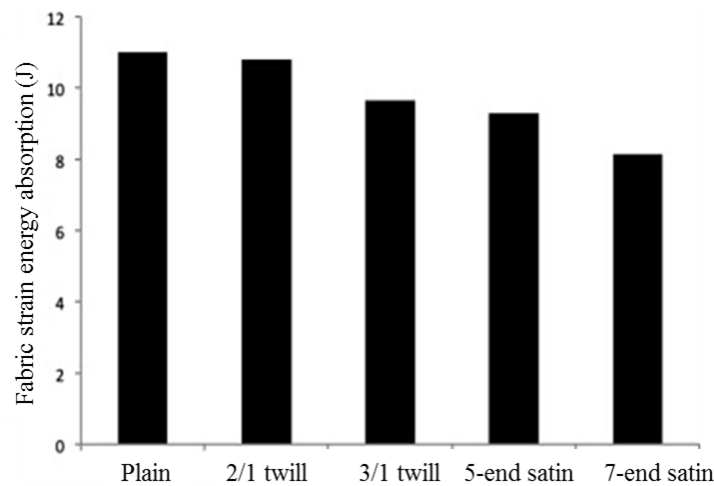


Figure I-19: Energy absorption of a single ply of UHMWPE [37]

### **Influence of matrix type**

Many studies focus on the influence of the resin on the behavior of the composite laminates behavior. Lee et al. [38] studied the effect of impregnation on the penetration failure of a woven fabric of Spectra (UHMWPE). The comparison is between samples with one ply of Spectra non-impregnated and one ply impregnated with vinyl ester resin. The results show that the impregnated sample absorbs higher energy than the non-impregnated. In addition, the impregnated ply attains a higher peak load since a higher load is needed to break the yarns of the fabric.

Vieille et al. [39] investigate the low-velocity impact response of carbon fiber with thermoplastic (TP) and thermoset resin (TS). The thermoplastic resins used are PEEK and PPS, and the thermoset resin is Epoxy. Figure I-20 presents the load versus displacement curves of carbon fibers impregnated with three different resins. Results show that carbon/PEEK, and carbon/PPS composite absorb higher energy than carbon/epoxy. The study shows that carbon/epoxy composite shows a higher delamination area than carbon/TP.

## Introduction and literature review

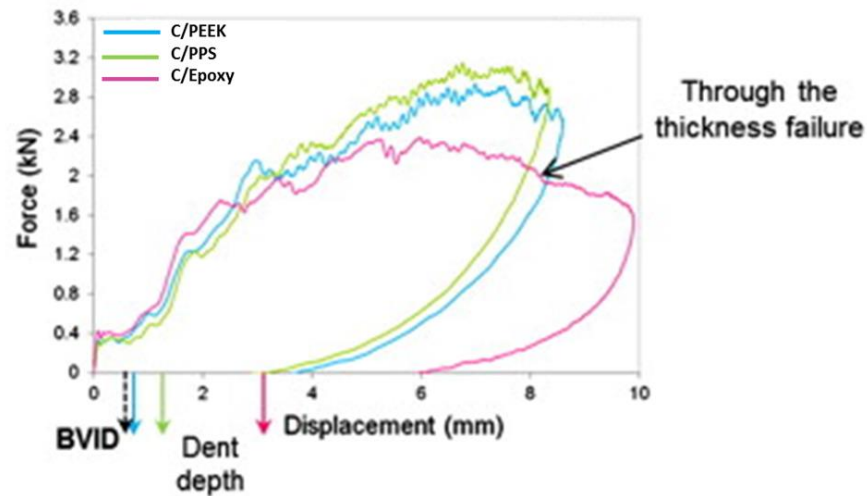


Figure I-20: Comparison of load-displacement curves for three different materials at an impact of 17 J [39]

Polymer resins can be reinforced by adding various toughening agents. Presently one of the most popular fillers is carbon nanotubes. Carbon nanotubes are an effective way to improve the mechanical properties of composites. Carbon nanotubes can be single-walled (SWCNT) or multi-walled (MWCNT) [40].

Liu et al. studied the influence of adding 1wt.% of MWNT on glassy and rubbery epoxy resin. They suggest that nanotube-based composite increase the fracture toughness and the stiffness of the composite [41]. Davis et al. investigate the mechanical properties of a carbon/epoxy composite reinforced by carbon nanotubes [42]. The properties studied are tensile strength, stiffness, and resistance to damage and failure due to cyclic loadings. Compared to un-reinforced composite, carbon nanotube-reinforced composite show improvement in the mechanical properties without significant weight addition. It is proved that the carbon nanotubes hinder the crack propagation inside the epoxy matrix, which was more critical in the case of neat composite.

Studies show that carbon nanotubes are effective fillers for composite materials. CNT tends to aggregate during fabrication resulting in a non-uniform composite. Adding the right amount and ensuring a homogenous dispersion inside the resin is challenging and can affect the expected mechanical properties.



**Influence of fiber type**

One of the most important factors that influence the dynamic behavior of composite materials is the properties of the fibers. Table I-1 shows some of the mechanical properties of several fiber types that affect the energy absorption capacity and failure mechanisms in composite materials.

Table I-1: Mechanical properties of some fibers used in protection applications [43]

Fibre	Density (kg/m <sup>3</sup> )	Tensile Strength (MPa)	Specific Strength (m <sup>2</sup> /s <sup>2</sup> )	Elastic Modulus (GPa)	Specific Stiffness (m <sup>2</sup> /s <sup>2</sup> )	Failure Strain (%)
Aramid (low modulus)	1440	2900	2.01 × 10 <sup>6</sup>	60	4.17 × 10 <sup>7</sup>	3.6
Aramid (high modulus)	1450	2900	2.00 × 10 <sup>6</sup>	120	8.28 × 10 <sup>7</sup>	1.9
Polyethylene (low modulus)	970	2700	2.78 × 10 <sup>6</sup>	89	9.18 × 10 <sup>7</sup>	3.5
Polyethylene (high modulus)	970	3200	3.30 × 10 <sup>6</sup>	99	1.02 × 10 <sup>8</sup>	3.7
E-glass	2600	3500	1.35 × 10 <sup>6</sup>	72	2.77 × 10 <sup>7</sup>	4.8
S-glass	2500	4600	1.84 × 10 <sup>6</sup>	86	3.44 × 10 <sup>7</sup>	5.2
Carbon (high strength)	1780	3400	1.91 × 10 <sup>6</sup>	240	1.35 × 10 <sup>8</sup>	1.4
Carbon (high modulus)	1850	2300	1.24 × 10 <sup>6</sup>	390	2.11 × 10 <sup>8</sup>	0.5

Glass fibers are one of the most traditional fibers used in protection applications. Many advantages make glass fibers popular even in the most recent application: high chemical resistance, high tensile strength, and impact resistance [17]. Numerous glass fiber grades exist; the most used nowadays are E-glass and S-glass. However, S-glass shows higher strength and elongation at break than E-glass [43]. Okhawilai et al. [44] studied the impact response of S-glass and E-glass as impact face of a protective system backed with aramid plies. The results showed that S-glass as an impact face exhibit significantly less damage area and indentation depth than E-glass. The authors justified this by the fact that S-glass possesses higher tensile strength than E-glass, which leads to a higher capacity to withstand tensile force before failure.

## Introduction and literature review

Regardless of the effective impact performance of glass fibers, several studies focus on the potential of replacing glass fibers with cheaper fibers. Basalt fibers recently received significant interest as a potential replacement for glass fibers [31]. Basalt fibers are organic, present low-cost, and eco-friendly. Lopresto et al. [45] investigate the mechanical behavior of basalt fibers and compare them to glass fibers. Results of standard tensile, bending, and compressive tests proved that basalt fiber properties are superior to glass fiber and can be a potential replacement (Figure I-21). Manikandan et al. [46] studied the impact performance of acid-treated basalt compared to treated glass. The pendulum impact test showed that the impact properties of treated basalt are 90% higher than those of glass.

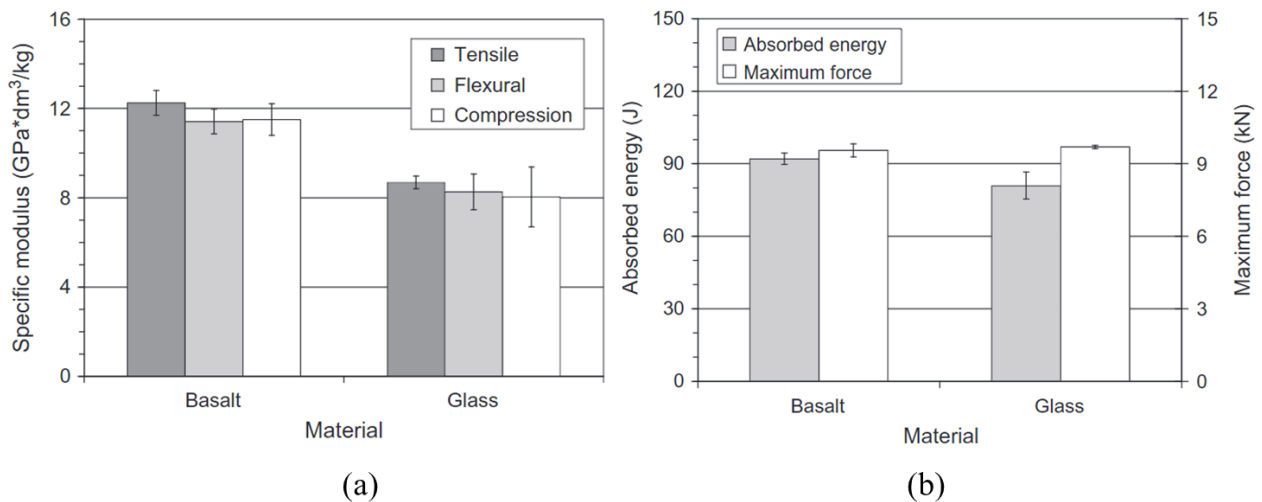


Figure I-21: (a) Mechanical properties and (b) impact properties of Basalt and Glass fibers [45]

Carbon fibers are most used in the aeronautical, transportation, and protection fields. These fibers possess excellent tensile strength and efficiency-to-weight ratio. Cartie et al.[47] studied the low-velocity impact of two types of carbon fibers, Toray HTA and IMS. Results of the drop weight test showed that. IMS fibers are 25% stiffer and 60% stronger than HTA fibers.

Aramid fiber is one of the most common fibers in protective applications due to its exceptional impact properties. Aramid fibers exist under two main trade names, Kevlar® and Tawron®. Abtew et al. [26] showed that aramid fibers (density 1.44 g/cc) have 43% less weight compared to glass fibers (density 2.55 g/cc); they are two times stronger than E-glass and have the same high strength as carbon fibers on a specific tensile strength basis. Aramid fibers are

## *Introduction and literature review*

an essential component in multilayered armor systems, where they serve as backing material for ceramic plates. Several studies focused on the potential of replacing Kevlar fibers with natural and eco-friendly ones, such as Ramie and Curaua [15,48]. Both studies showed that the primary role of Kevlar is to capture the fragments of the projectile, and hence natural fibers can replace it with the characteristics of the same yarn.

Ultra-high-molecular-weight-polyethylene (UHMWPE) is also among the high-performance fibers and is progressively used in protection applications [17]. The mechanical and impact performance properties of the UHMWPE fibers make them a real competitive of aramid fibers. UHMWPE exists under Dyneema<sup>TM</sup> and Spectra<sup>TM</sup>. According to the manufacturer data sheets, it has a 40% higher strength-to-weight ratio than aramid fibers [26,49].

The impact performance of Kevlar® aramid, Spectra® polyethylene, and Zylon® PBO was investigated and compared to an aluminum alloy plate as a part of the FAA research program [50]. Results showed that Kevlar and UHMWPE absorbed 6 to 7 times as much as the aluminum alloy plate (on an equal areal density basis), yet PBO absorbed 13 times as much energy.

The mentioned fibers above have excellent impact behavior; nevertheless, recent studies focused on the potential of improving the behavior of the fibers by adding reinforcement. Shear thickening fluid (STF) is one of the additions that can improve the performance of fibers. STF is a non-Newtonian fluid that increases in viscosity when subjected to impact.

Lee et al. [51] studied the influence of the addition of STF on the ballistic performance of Kevlar fibers. The comparative study investigates the behavior of Kevlar fabric impregnated with STF and Kevlar fabric non-impregnated. The samples are tested with a gas gun at a velocity of 244 m/s. Results show that the impregnated samples with STF dissipate higher energy Figure I-22. The authors justified this increase in energy dissipation by increasing inter the yarn pull-out force upon the transition of the STF to its rigid state.

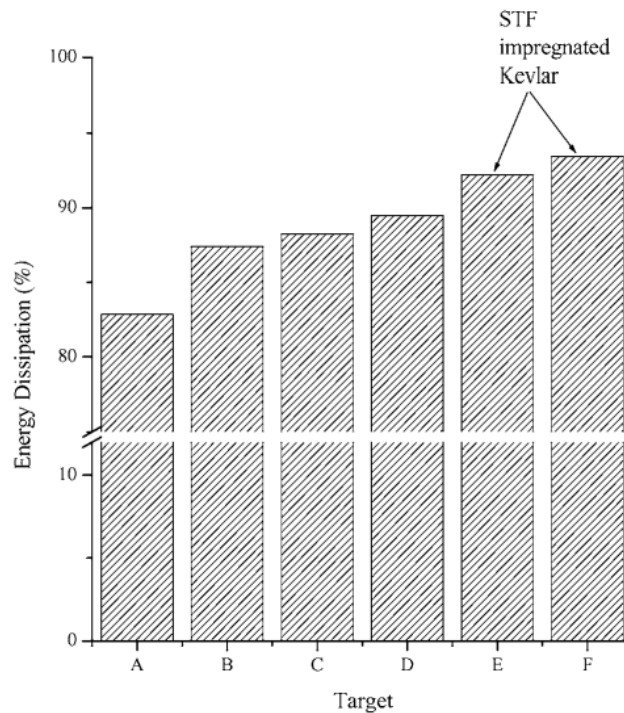


Figure I-22: Energy dissipation of targets not impregnated with STF (A, B, C, and D) versus targets with impregnated aramid with STF (E and F) [51]

### **Influence of hybridization and layering sequence**

High-performance fibers offer an excellent strength-to-weight ratio in many application areas. However, recent researchers focus on mixing different types of fibers, aiming to get an improved material. This technique is called hybridization. Hybridization in composite materials is a technique where two or more materials are bound together in a common matrix. Hybridizing several fibers can produce higher performance than composite material with single fibers.

Tirillò et al. [52] investigated the behavior of hybrid carbon-basalt/ epoxy composite subjected to high impact velocity. Carbon fibers have high tensile strength but low toughness and poor impact resistance. The role of Basalt fiber is to improve the resistance of carbon since it is a ductile fiber. Configurations with different layering sequences are presented, having sandwiches layering, BCBS and CBCS, or intercalating layering, BCBI, and CBCI, where B is Basalt, C is Carbon, and S and I denote sandwich and intercalating, respectively. A gas gun tests the laminates at a velocity of 474 m/s. Results show that hybrid laminates have a higher energy absorption than carbon laminates, especially those with a higher number of basalt layers,

## Introduction and literature review

Figure I-23. The flexural strength of the hybrid laminates has slightly decreased, but it is compensated by a better energy absorption mechanism, higher ballistic limit, and lower cost.

The authors also showed the influence of the layering sequence of Basalt and Carbon fibers in the hybrid laminates. Results showed that intercalating structures attain a higher ballistic limit, especially those with higher basalt content; this might be due to the high number of interfaces that lead to better impact performance.

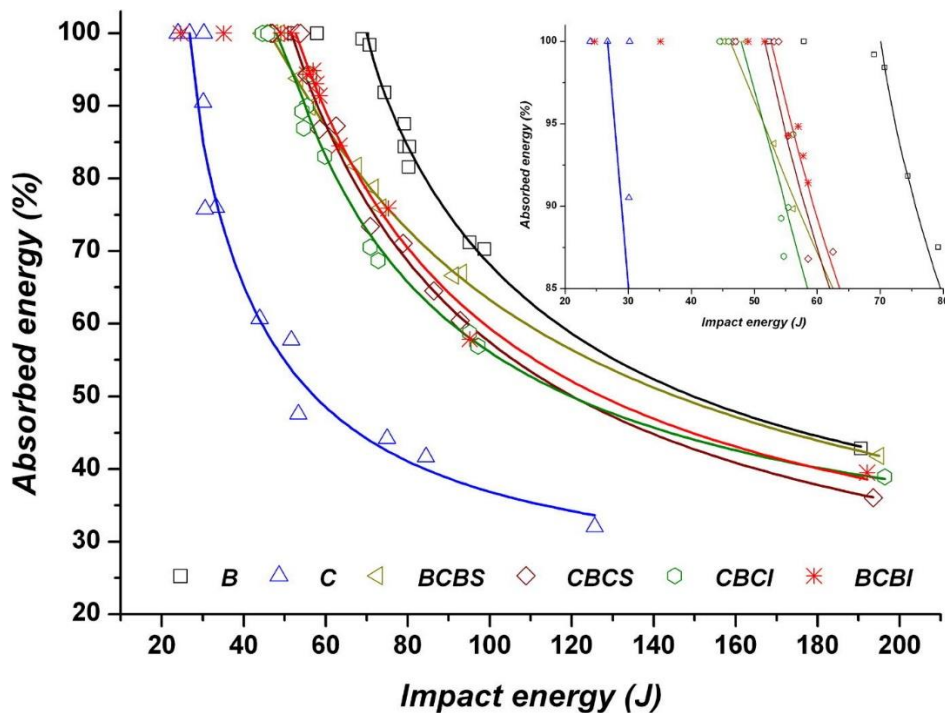


Figure I-23: Absorbed Energy vs. Impact Energy for all configurations [52]

Chen et al. [53] compared the low-velocity impact behavior of conventional carbon, glass, and basalt laminates with hybrid laminates with a sandwich-like layering sequence. Results showed that carbon fibers attain the lowest peak load among the entire configuration and display a progressive failure after reaching the peak Figure I-24. Hybrid configuration, conventional glass, and basalt laminates show a sudden drop in load after reaching their peak load. It was shown that hybrid laminates have an improved impact performance over carbon fibers regardless of the configuration. According to the authors, ductile fiber dominates the major mechanical performance regardless of stacking sequence and fiber types used.

## Introduction and literature review

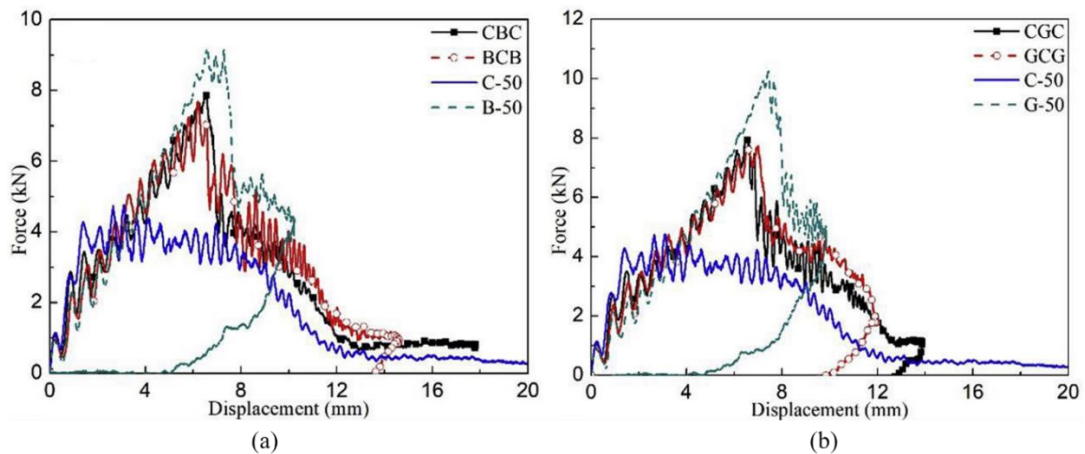


Figure I-24: Impact force-displacement curves for (a) CFRP laminates hybrid with basalt fiber layer, (b) CFRP laminates hybrid with glass fiber layer [53]

Bandaru et al. [54] studied the ballistic performance of hybrid Kevlar-basalt/PP composite. Two configurations are tested non-symmetric (H-1) stacking and symmetric (H-2) stacking (Figure I-25). The impact test is through a gas gun at 395 m/s. The results show the importance of stacking sequences in hybrid laminates. The structure with 3D woven aramid as impact face (K3D) attains higher ballistic limit and lower back face damaged area.

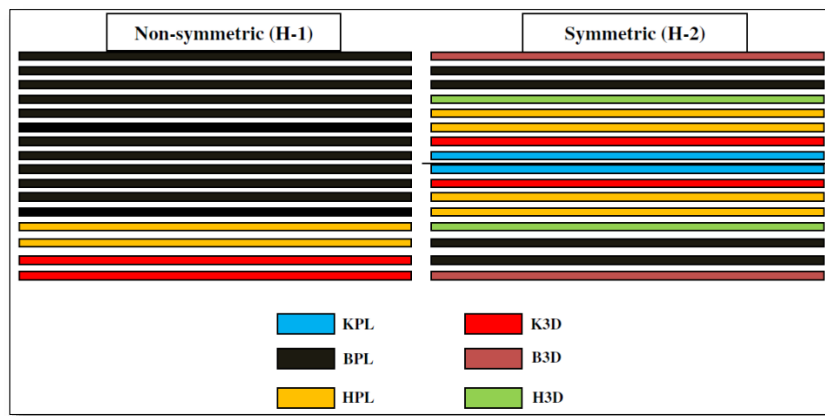


Figure I-25: Stacking sequence of hybrid structures [54]

Studies that deal with hybridization agree that the fiber type, the number of layers, and the stacking sequence play an essential role in the impact response of the hybrid structures.

### Influence of impactor geometry

Besides the factors that depend on the composite laminates, layering, fiber type, and matrix type, the impact test conditions greatly influence the behavior of the composite laminates. The geometry of the projectile can significantly influence the response of the impacted structures. Ulven et al. [55] studied the influence of the shape of the projectile on carbon/epoxy laminates when subjected to high-velocity impact. The impacted laminates are tested with conical, flat, hemispherical, and fragment-simulating projectiles. The tests were conducted on a 6.5- and 3.2-mm thickness. The conical shape projectile resulted in the highest energy absorption at the ballistic limit, then the flat, hemispherical, and fragment-simulating projectile (Figure I-26). The authors also described the dominant mode of failure resulting from all the impact, characterized by plugging and separation of fibers.

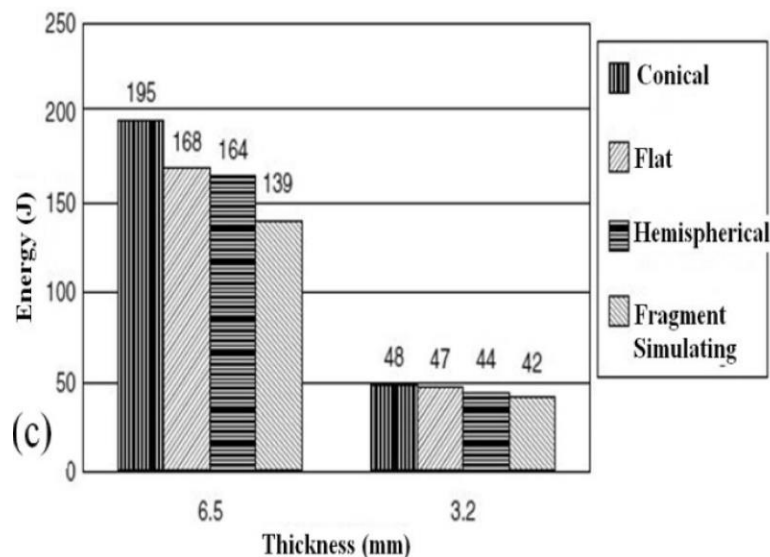


Figure I-26: Energy absorption of carbon/epoxy laminate when impacted with different projectiles geometry [54]

A single aramid (Tawron<sup>®</sup>) plain woven ply is tested with a high-velocity impact with numerous projectile geometries, hemispherical, flat, ogive, and conical. The impact resulted in different modes of failure associated with each impactor geometry. Yarn pull-outs were more significant in hemispherical projectiles than ogive and conical shape projectiles due to their capacity to slip through the fabric [26,61]. The end of the yarns impacted by the flat projectile seemed to be even and in order (Figure I-27).

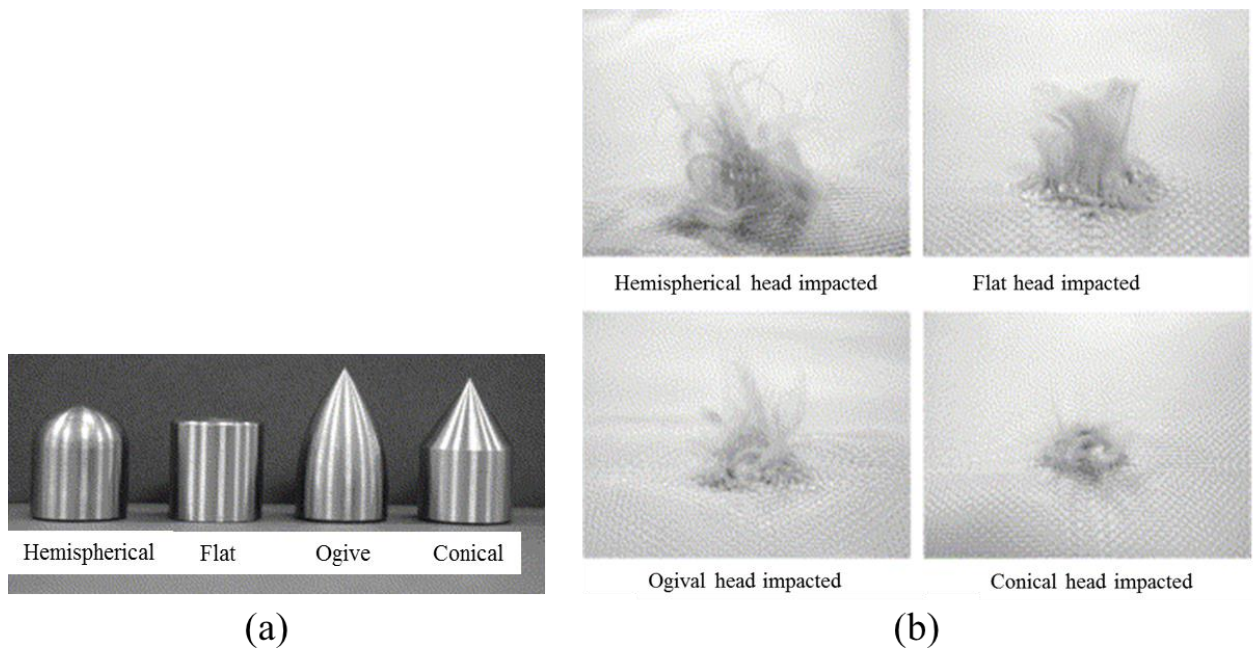


Figure I-27: (a) The geometry of the projectiles, and (b) Yarn failure of 1ply of Tawron<sup>®</sup> when subject to different projectile geometries impact [56]

#### **I.2.2.4 Modeling of failure mechanism in woven composites**

Energy absorption mechanisms in woven composites are numerous. They can be affected by several parameters, namely, the fibers properties, the resin properties, the thickness of the structure, the stacking sequence, and the mass and shape of the impactor [8]. Hence, numerical models are essential to predict woven composite behavior while saving time and cost.

##### **Modeling scales**

A numerical model that can study the impact behavior of woven composite is a model that can represent the damage mechanism seen physically during impact. Modeling composite materials can be challenging, especially if there is an interest in representing the actual damage mechanisms. Several scales exist for modeling composite plies: the microscale, the macroscale, the mesoscale, and the multiscale, Figure I-28.



## Introduction and literature review

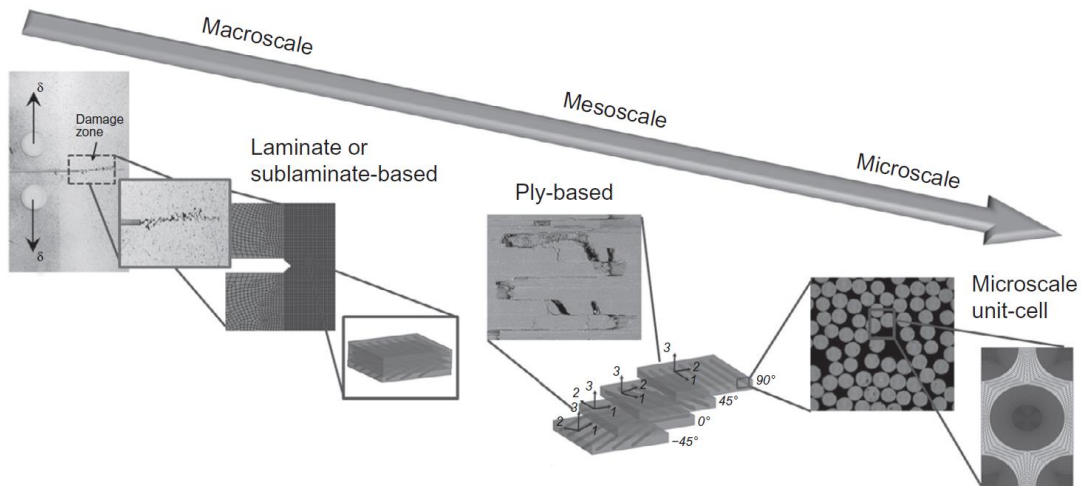


Figure I-28: A schematic representation of the various scales involved in modeling the damage the behavior of composites [57]

The *macroscopic scale* modeling is based on the level of the laminate or sub-laminate. It is usually used for modeling significant scale structures. The rule of mixture based on the laminate plate theory can define the properties of the lamina in this modeling scale. This model aims to predict the global response of the laminate, the global stiffness, load-carrying capacity, stability, and post-peak behavior of the laminates rather than predicting the detailed damage events [57]. The damage criteria in such models can be based on Tsai-Wu or Tsai-Hill criteria [58].

The *microscopic scale* is based on the fiber level. The primary purpose of this modeling scale is to understand the physical behavior of the composite. This modeling scale is not used for design engineering problems. The modeling is based on a representative unit cell with a detailed geometry. Several studies focused on microscale modeling to investigate the progressive failure, fiber-matrix debonding, and friction [59–61]. This modeling scale is unsuitable for large structures due to the high computational time.

The *mesoscale*, ply-based model is intermediate between macro and micro-level modeling. Homogenous layers represent the laminates or sub-laminates throughout the thickness [62], and the interface can be added between the layers to model the delamination [57]. This modeling scale can predict the essential mode of failure in composite laminates: delamination, fiber

failure, and matrix crack. Mesoscale modeling can represent the fabric architecture and the yarn-to-yarn interaction, making it suitable for modeling impact problems [63].

The *multiscale model* is a recent modeling strategy that represents the behavior of the material/structure at different scales [57]. Two types of multiscale exist, the hierarchical and the concurrent multiscale models. Hierarchical is one of the popular approaches, where the property of the material is transferred from microscale modeling to macroscale modeling, using homogenization theories [57], [64]. As for the concurrent multiscale modeling, both scales can exist simultaneously in the model. The macroscopic scale represents the undamaged areas, whereas the microscopic scale models the damaged area.

### **Modeling approaches**

Modeling the damage evolution and fracture in the composite material can be achieved by several modeling approaches. The continuum and discrete are the most used.

#### a) Continuum damage model

The continuum damage model is typically used to model intralaminar damage. The continuum damage mechanics (CDM) aims to predict the influence of microscale damage on the macroscale level. This prediction is made through mathematical relations linking the damage to the macroscale properties of the material [57,65]. Those relations can be based on stress, strain, or energy equivalence [65]. The damage prediction of composite material can be complex. Thus, several damage variables can be introduced into the stiffness matrix. A challenging aspect of the CDM is the damage variable evolution.

#### b) Discrete damage model:

This approach aims to model the intralaminar damage and the interlaminar one. This approach uses interface elements to model the interlaminar damage. The differentiation between those two modes of damage introduces a discontinuity, making the approach discrete. Several studies used this modeling approach to simulate the interlaminar damage (delamination) in composite materials since it is the principal failure mode. Lammerant et al. [66] were the first to introduce the discrete modeling approach, where they searched to

## Introduction and literature review

understand the coupling between matrix cracks and delamination. Shi et al. [67] also used cohesive elements between the plies to predict the delamination in composite laminates when subjected to low-velocity impact. The study showed that the numerical model could predict a similar delamination area compared to experimental results.

Bouvet et al. [68] proposed a modeling approach called Discrete Ply Modeling Method; the model introduces cohesive elements representing the interlaminar and intralaminar damage Figure I-29. The coupling between intra- and inter-laminar damage is considered. Refined mesh size is a must in this model to represent the ply's orthotropic behavior. Four different mesh types are developed at  $0^\circ$ ,  $90^\circ$ ,  $45^\circ$ , and  $-45^\circ$ . The proposed model could represent the impact response on UD carbon/epoxy fibers taking into account the relationship between matrix cracking and delamination.

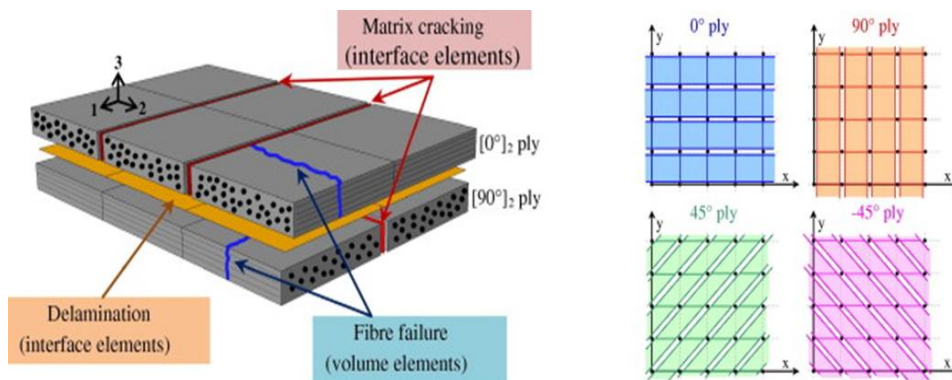


Figure I-29: Discrete ply model approach [68]

### c) The semi-continuous approach:

The semi-continuous approach is a modeling strategy based on the mesh level of the woven plies. The semi-continuous modeling strategy was found by Navarro et al. and further developed by Pascal et al. [74, 75]. The main principle of this strategy is to differentiate between matrix and fiber failure. Navarro et al. [69] first introduced the semi-continuous approach. It can represent the continuous behavior of the undamaged composite plies and the discrete behavior where the fibers are left non-stabilized when the matrix is fully damaged. The model was further developed by Pascal et al. [70] to respect the weaving patterns of composite laminates; a graphical representation of this model is shown in Figure I-30. In the presented model, shell

elements represent the matrix, and rod elements represent the fibers, which exist in five different configurations to represent the fibers' weaving pattern. Virtual nodes are used to place the fibers, and they are distanced of  $h/4$  from the neutral axis of the shell element ( $h$  is the ply thickness). The connection between the shell elements and the virtual nodes happens through rigid links. This approach has many advantages; it can model the non-stabilized fibers even when the matrix is damaged and is based on physical observation. It can represent the architecture of the fabric.

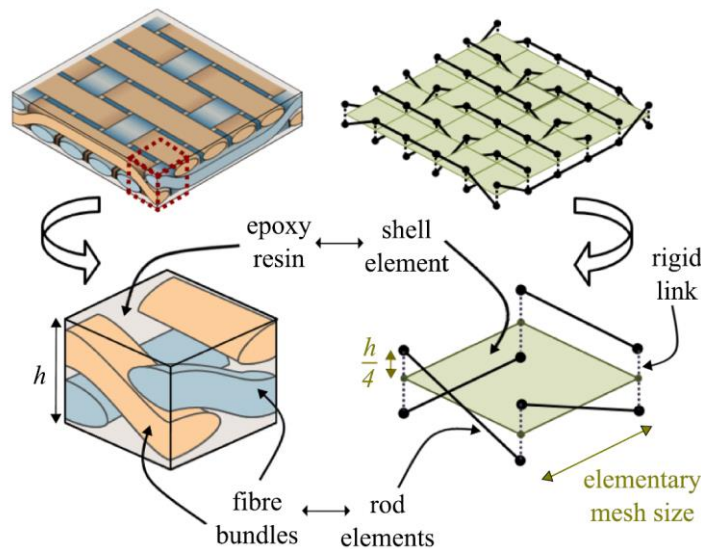


Figure I-30: Modeling strategy of 5-harness satin woven ply [71]

### **Numerical modeling of impact damage**

Modeling the impact damages (matrix cracks, fiber failure, delamination) that are generated from impact loading can be classified into four categories: a failure criteria approach (which can be based on the equivalent stress or strain); a fracture mechanics approach (based on energy release rates); a plasticity or yield surface approach, and a damage mechanics approach [72].

Starting with the failure criteria approach, it includes the Chang-Chang [73] and the Tsai-Wu [58] failure criteria. These types of criteria can be complemented by any type of fracture mechanics approaches. Hou et al.[74] added a Brewer-Lagace criterion to model delamination

## *Introduction and literature review*

in addition to Chang-Chang failure criteria to model fiber failure and matrix crack. Failure criteria are often mixed fracture mechanics, and damage mechanics approach.

The damage mechanics approach is usually applied to matrix cracking. This approach can apply to intralaminar damage if a proper link to fracture mechanics is defined [72].

Plasticity is used to model particular behavior characterized by permanent deformation seen in some composite materials.

All the approaches discussed are usually combined to result in realistic modeling. In their developed numerical model, Shi et al. [67] used Hashin criterion and Puck Schurmann criterion to simulate the damage initiation in the fibers and the matrix. However, the damage evolution was simulated by an energy-based variable that can be defined for each failure mode.

### **I.2.3 Polymer foams**

This section describes the areas where foams are used for protection applications, the different types of polymer foams, the energy absorption mechanism, and the numerical models used to simulate the impact on foams.

#### **I.2.3.1 Overview on foams**

Cellular materials are among the most popular materials for their energy absorption capacities. Foams and honeycombs have gained significant interest in automotive, aeronautical, packaging, and personal protection. Foams can be created from widespread base materials, metal, ceramic, and polymers.

#### **Areas of Application**

Foams can be found in many sectors for protection, transportation, construction, packaging, personal protection, and many more.

It is essential to provide high performance against impact and crash while maintaining lightweight in the *automotive industry*. Metallic foams, especially aluminum foams, are widely used due to their high stiffness and gas permeability [22]. In recent years, polymer foams proved

## *Introduction and literature review*

to be an efficient material when high-energy absorption is required. Polymer foams are applied in energy-absorbing structures, such as head impact safety components in cars [75]. Rigid polymer foams are also a lightweight and low-cost reinforcement for side impacts in modern cars. Another application for foams in the automotive sector is in the bumper. The bumper is subjected to impact, and its role is to offer high-energy absorption levels to prevent the transfer of the shock waves from the car to the driver and passengers. Polymer foams such as PU are the most used bumper materials since they can provide high toughness yet high shock absorption [76].

Polymer foams are a good candidate for the *packaging industry*. Modern packaging relies on cost-effectiveness and high-energy absorption materials. Polymer foams are the most used for these applications since it is lightweight and can provide protection against impacts during transportation. Heavy electronics and devices are protected by polymer foam to provide safety while adding low additional weight [77]. Polymer foams are preferable for stacking, among other materials, due to their high compression resistance. In particular, polymer foams are also used for military packaging applications, i.e., weapons and missiles.

Polymer foams are essential materials used for *personal protection*. Head injuries can be life-threatening. Hence, foams are widely used in helmets for civilians and the military. Bicycle helmets are made from Expanded Polystyrene or PU foams [23]. Military helmets are designed with high-density polymeric foams to protect against non-ballistic impacts and fragments [23]. Foams are used in numerous sports to protect players from impacts, such as football and rugby [23]. The application areas include shin guards, ankle protection, and goal padding. Polymeric foams are advantageous for personal protection applications due to their high-energy absorption, wearability, and lightweight.

In the following sections, the focus will be on polymer foams.

### **Fabrication of polymer foams**

Foam materials are built from various base materials like polymers, metals, ceramics, and glasses [78]. The fabrication process of polymer foams is mainly divided into mixing and molding [79]. In the mixing phase, bubble nucleation or foaming happens. The foaming process can be achieved through mechanical, physical, or chemical [80].

## *Introduction and literature review*

*In mechanical foaming*, the polymer is mixed mechanically or frothed for the air to get inside the liquid polymer and form the foam system. The advantage of this technique is that no additional foaming agent is needed.

As for *physical foaming*, a low boiling point agent is added to the polymer before frothing. The liquid mix is heated to change into foam.

Two chemical solutions (polymers) are combined and frothed mechanically in *chemical foaming*. A chemical reaction produces gases; afterward, the polymer is foamed by pressuring and heating [80].

Polymer foams can be categorized according to their raw material: thermoplastic, thermoset, and elastomers [78]. Thermoplastic foams include Polystyrene (PS), Polyethylene (PE), and Polyvinyl chloride (PVC); thermoset foams include, Polyurethane (PU), Phenolic resin, and Epoxy resin [79].

### **Foams microstructure**

The mechanical behavior of polymer foams depends on their fabrication process, cell microstructure, and density. Two types of cell microstructures exist closed-cell and open-cell foam.

A closed-cell foam consists of a wall surrounding all the cells, separating them from one another. Open-cell walls are open to each other, making it impossible to entrap gas or liquid inside. As a result of the cell microstructure, closed cells tend to be stiffer where the cell geometry resists air leakage and shows more strength than open cells, where the foam tends to be softer [79,81,82].

The mechanical properties of polymer foams are proportional to their densities. The mechanical strength of a polymer foam decreases when the porosity increases. Feng et al. and Gibson [78,80] both show the influence of the density on the mechanical properties of polymer foams.

### I.2.3.2 The behavior of polymer foam subjected to impact

The response of polymer foams, when subjected to impact, is extensively studied. Understanding their behavior when impacted is crucial to designing improved protective systems.

Under *compressive loading*, all-foam stress-strain curves show three regions: linear-elastic or Hookian region, plateau region, and densification region [77]. Figure I-31 shows the stress versus strain of an elastic-plastic foam under compression loading. The linear elastic region is governed by the bending of the cell walls, where Young's modulus is the slope of this linear behavior. The collapse of the cells characterizes the plateau region; elastic buckling for elastomeric foams and brittle crushing for brittle foams such as ceramic or epoxides. When all the cells are crushed or compacted, a rapid increase in stress describes the densification region [77,78]. The energy absorption happens in the plateau region, where the cells collapse.

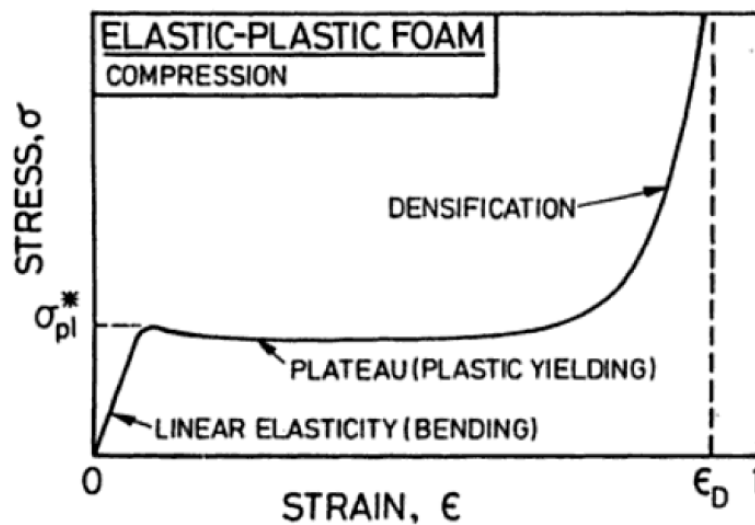


Figure I-31: Stress-strain curve of an elastic-plastic foam under compressive loading [78]

Ouellet et al. [83] studied the influence of strain rate on the behavior of polymeric foam. The polymeric foam samples were compressed using a drop weight tower at a strain range of 101 to 102/s. Results showed that the polymeric foam response strongly depends on the strain rate. When the strain rate increased, the elastic modulus of the material and plateau increased, and the densification strain decreased (Figure I-32). The authors supposed this behavior is more



significant with closed-cell foams, where the air entrapped is compressed locally within the cell, increasing strain rate sensitivity.

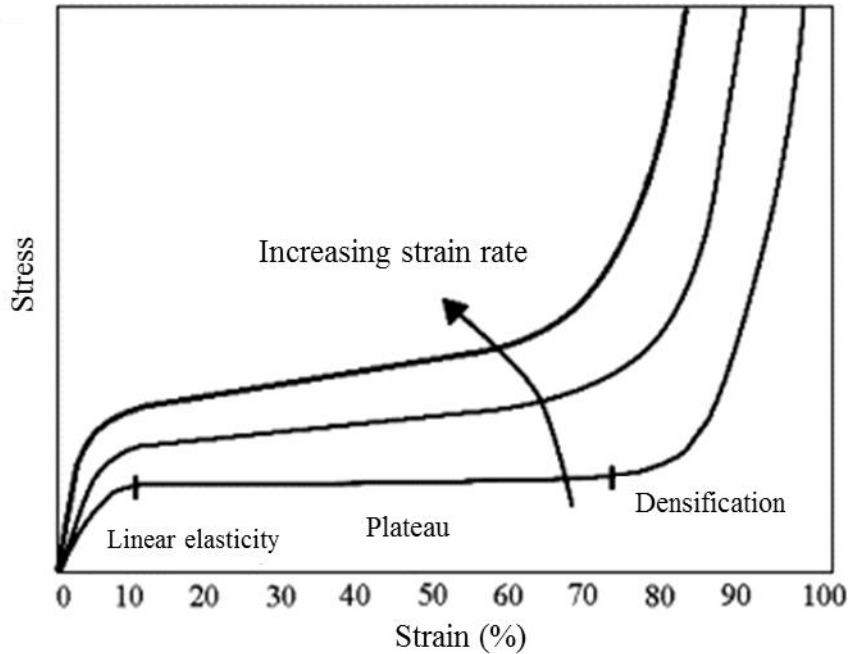


Figure I-32: Strain rate dependency under compressive loading [83]

Yan et al. [84] also studied the influence of the strain rate on the behavior of polymer foams under compressive loading. The study similarly revealed that when the strain rate increases, the plateau stress increases, and the densification happens sooner. The behavior of the polymer foams is monitored by the speed at which the air escapes the foam cells.

The foam density also greatly influences its behavior under compressive loading. As the density of the foam increases, the material elastic modulus and plateau stress increase as well [85].

The density of the foam as well influences its *tensile response*. Kabir et al. [86] showed that the tensile modulus increases as the density increases Figure I-33.

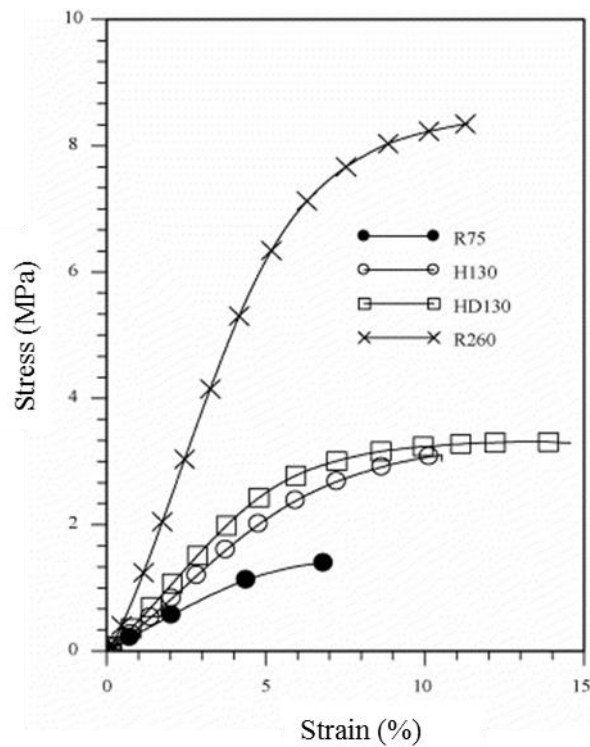


Figure I-33: Tensile behavior of different foam densities [86]

The foam response to tensile stress is first linear elastic controlled by bending and stretching the cell walls. Elastomeric foams show a linear behavior. In contrast, plastic foams attain a yield point and an augmentation in stress until failure. However, brittle foams show a significant brittle failure after the elastic region, where cracks propagate rapidly throughout the structure [77].

The behavior of polymer foams under *impact* can be analyzed through a force-displacement curve and a visual inspection of the sample. The impact of behavior is extensively studied in the literature. The impact starts with localization, localized deformation underneath the indenter. The cells' shape deforms and leads to local strain rates. A second phase, the micro-inertia, follows the local deformation, characterized by buckling of the cells. Finally, the densification, where the stress increases rapidly when the cell walls are in contact [77]. The energy absorption mainly happens in the second feature when the cell walls collapse, and particularly for brittle foam, energy absorption occurs by cell fracture and crushing.

Zhang et al. [87] studied the dynamic impact response of three different foam densities, EPS 9, 13, and 18 ( $\text{kg/m}^3$ ). The force versus time curve shows that the foam with higher density, EPS18, attains the higher force, followed by EPS13 and then EPS9 (Figure I-34). The impact time also decreases when the foam density increases.

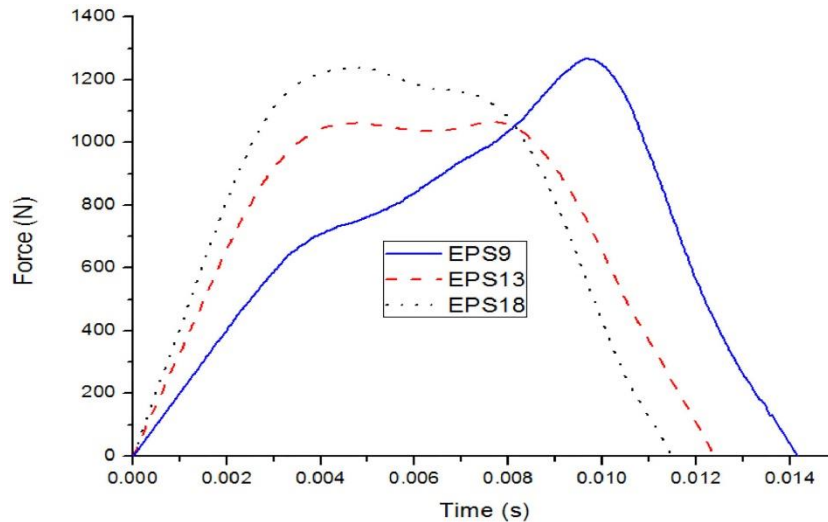


Figure I-34: Force versus time of different foam densities subjected to impact [87]

### **I.2.3.3 Polymer foam reinforcement**

Regardless of the advantageous properties of polymer foam, recent studies make a great effort to improve its mechanical properties to increase its potential in future applications. Reinforcement of polymer foams can be achieved by integrating fillers and reinforcing particles in fabrication. Those reinforcements aim to obtain mechanical properties superior to those obtained in ordinary or foam without reinforcement. Those properties include increased modulus, strength, and energy absorption; modulation of electrical properties; and tailoring thermal properties such as thermal expansion, thermal conductivity, and glass transition temperature ( $T_g$ ) [88]. Fillers are tiny solid particles that are typically used in small quantities to enhance the value of the foam, and they include fibrous fillers (glass fiber, aramid fiber, and carbon fiber), Nanofillers (nanoclays, graphite nanotubes), and rubber particles [89].

Fibrous fillers can be in the form of chopped strands of fiber filament. They act to reinforce the foam by switching the stress from the low stiffness foam to the fibers [90]. Yang et al. [91] studied the behavior of Polypropylene (PP) thermoplastic foam reinforced by short glass fibers

## *Introduction and literature review*

(diameter of about 13  $\mu\text{m}$ ). The study proves that adding around a 20% wt ratio of GF to the PP foam improves the tensile strength and modulus, the specific bending stress, and modulus by 59.45%, 54.81%, 94.75%, and 82.42%, respectively, compared to neat PP foam. As for short carbon fibers, Wenzhe et al. [92] show that adding short carbon fibers (SCF) to epoxy foam improves fracture toughness up to 113% compared to neat epoxy foam. Organic fiber can also be a successful additive to polymer foams; studies dealing with Kenaf fiber [93] and bamboo fiber [94] as a reinforcement show that their addition improves the mechanical and thermal properties of the foam compared to ordinary foam.

Carbon Nanotubes, Nanofibers, and rubber particles as reinforcement are also very popular since they have low density due to their hollow core [88]. Awad et al. and Kumar et al. [95,96] both study the addition of MWCNT to polymers foams. Both studies prove that adding nanoparticles improves mechanical properties (tensile strength and modulus) and thermal stability.

While adding reinforcement into the epoxy foams might increase the fracture toughness, introducing those fillers significantly decreases compressive strength compared to neat unreinforced foam [92].

### **I.2.3.4 Modeling of foams**

#### **Modeling scales**

Cellular materials and foam, in particular, show a mechanical behavior dependent on the foam base material, density, foaming process, and microstructure [78]. This diversity in mechanical behavior makes its numerical modeling complex and challenging.

Several studies drew significant attention to modeling the behavior of polymer foams. The modeling scales are microscale, mesoscale, and macroscale [97] (Figure I-35).

## *Introduction and literature review*

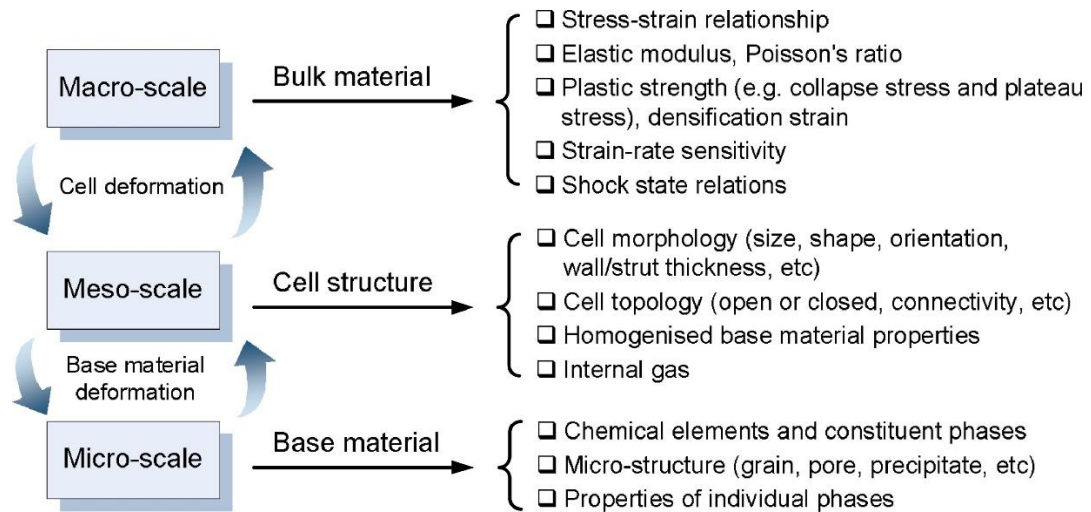


Figure I-35: Characteristic and material properties associated with each modeling scale [97]

The micro modeling scale can describe the heterogeneity of the base material itself. In this type of modeling, the covering scale is between  $10^{-6}$  and  $10^{-4}$  m [97]. As for mesoscale modeling, it can represent the cell morphology while considering homogenous base material properties. Several studies focused on the influence of microstructure heterogeneity (cell wall imperfection, precipitation) on the behavior of foams. The cell microstructure can be replicated and constructed with mathematical or experimental approaches. Li et al. [98] studied the effect of the foam cell size on its dynamic behavior. The microstructure of the cell was constructed based on a 3D model. The study showed that the cell size could influence Young's modulus of the material.

Finally, the foam is considered homogenous and treated as a continuum material at the macroscopic level. This modeling scale is the most suitable for design and engineering applications; it can represent the average response of the structure as a meso or micro-scale collection.

After mentioning the influence of the microstructure on the behavior of cellular material, and the advantages that micro and meso scale modeling can offer, it induces a great computational time. An optimized modeling strategy will be based on multiscale modeling, where the bulk material behavior is linked to the cell structure or base material. Aubry et al. [99] proposed a numerical model based on the microstructure behavior while improving the computational time.

The authors studied the behavior of a Rohacell polymeric foam with a repetitive unit cell model. The modeling strategy possesses a change in scale approach to link the micro and macro scale.

### **Constitutive material models for foam**

Foam material models can be differentiated into *non-linear elastic* and *elastic-plastic*. For the non-linear elastic, the response is calculated from a strain energy function [23]. The non-linear elastic foam behavior, usually presented by high compressible low-density foams, is modeled based on the hyper-elastic and viscoelastic theories. A non-linear stress-strain relationship characterizes these models; hence, shape functions are used to find stress-strain curves by fitting methods [23]. Ogden [100] proposed a strain energy function to derive the stress-strain relationship for isotropic foams. Then, Jemiolo et al. [101] extended this model to cover the anisotropy under finite deformation.

On the other hand, the elastic-plastic constitutive models include the most classic one developed by Deshpande and Fleck [102], which is also known in the commercial FE package Abaqus under "crushable foam" [103]. Deshpande and Fleck's model is based on defining a yield surface, and the evolution of this surface has been studied for uniaxial and hydrostatic stress paths. The developed model applied to the metallic foam showed good agreement between experimental and theoretical results. While this model defined the hydrostatic strength, getting this type of data was challenging. However, Carranza et al. [104] propose a characterizing procedure for crushable foam applied to polymeric foam by defining the yield surface by more straightforward uniaxial tests. As for foam failure, a user subroutine is added to account for failure in tension and shear. The study showed good agreement between numerical and experimental results.

### **1.2.4 Conclusion**

This bibliographical study allows examining the present knowledge on protection systems against low and high-speed impacts in numerous fields.

A specific interest is given to composite materials. Over the past decades, composite material proved to be a good candidate for protection applications and was able to replace conventional protective methods. Recent research highlighted the importance of hybridization and twinning

## *Introduction and literature review*

between two or more materials to produce a hybrid material with superior properties to the originals. That being the case, another high-energy absorbent material is studied: polymer foams. The bibliographical study showed the diversity of application of polymer foams in protection applications. Based on this knowledge, this work will present a hybridization between aramid plies and polymer foam and a study of the protection capacity of this material when subjected to impact. This protection capacity is studied for low-velocity impact simulated by a drop weight test and a high-velocity impact simulated by a gas gun test.

The choice of aramid plies is based on its excellent strength-to-weight ratio and its popularity in impact application. As for the polymer foam, three different densities are chosen to investigate its influence on the mechanical behavior when combined with aramid plies.

A predictive numerical model is proposed to simulate the impact on the hybrid structures. Presently, several numerical models can replicate the behavior of the studied materials. Each modeling strategy encounters its complexity, time consumption, and accuracy. The numerical approach used to model the aramid plies is based on the semi-continuous approach. The semi-continuous approach is adopted since it can represent the damage to the composite material when subjected to impact while characterizing the actual waving pattern of the fabric. The polymer foam will be modeled on a macroscale with a classical material law in the FE software RADIOSS since it can represent the mechanical behavior of the epoxy foam tested.

## **References**

- [1] Sandor BI. Engineering mechanics: statics and dynamics. [Textbook]. 1983 [cited 2022 Jun 9]; Available from: <https://www.osti.gov/biblio/6651937>.
- [2] Wen X, Qu Q, Liu P, et al. Theoretical study on slamming and transition stages of normal impacts of symmetrical bodies on calm and wavy water surfaces. *Appl Ocean Res.* 2022;119:102986.
- [3] Korkmaz FC. Damping of sloshing impact on bottom-layer fluid by adding a viscous top-layer fluid. *Ocean Eng.* 2022;254:111357.
- [4] Bird Strike: An Experimental, Theoretical and Numerical Investigation - Reza Hedayati, Mojtaba Sadighi - Google Books [Internet]. [cited 2022 Jun 9]. Available from: <https://books.google.fr/books?>
- [5] Meguid SA, Mao RH, Ng TY. FE analysis of geometry effects of an artificial bird striking an aeroengine fan blade. *Int J Impact Eng.* 2008;35:487–498.
- [6] Bliven E, Rouhier A, Tsai S, et al. Evaluation of a novel bicycle helmet concept in oblique impact testing. *Accid Anal Prev.* 2019;124:58–65.
- [7] Medvedovski E. Ballistic performance of armour ceramics: Influence of design and structure. Part 2. *Ceram Int.* 2010;36:2117–2127.
- [8] Abrate S. Impact on Composite Structures [Internet]. [cited 2022 Jun 9]. Available from: <https://www.cambridge.org/core/books/impact-on-composite-structures/F77D6F3382519F7CC0E32492602DDA81>.
- [9] Shin KB, Lee JY, Cho SH. An experimental study of low-velocity impact responses of sandwich panels for Korean low floor bus. *Compos Struct.* 2008;84:228–240.
- [10] A review of impact testing on marine composite materials: Part I – Marine impacts on marine composites - ScienceDirect [Internet]. [cited 2022 Jun 9]. Available from: <https://www.sciencedirect.com/science/article/pii/S0263822317338710>.
- [11] Numerical and experimental analysis of the closed-cell aluminium foam under low velocity impact using computerized tomography technique | SpringerLink [Internet]. [cited 2022 Jun 9]. Available from: <https://link.springer.com/article/10.1007/s10409-018-0795-7>.
- [12] Ashter SA. Thermoforming of Single and Multilayer Laminates: Plastic Films Technologies, Testing, and Applications. William Andrew; 2013.
- [13] Development of composites, reinforced by novel 3D woven orthogonal fabrics with enhanced auxeticity - Muhammad I Khan, Jehanzeb Akram, Muhammad Umair, Syed TA Hamdani, Khubab Shaker, Yasir Nawab, Muhammad Zeeshan, 2019 [Internet].



## *Introduction and literature review*

- [cited 2022 Jun 9]. Available from: [https://journals.sagepub.com/doi/full/10.1177/1528083718795912?casa\\_token=ynwyntxvwCEAAAAA%3AP21nAwNvntC5dNZztYigJUUbGcQ1EVrtNp9toC\\_abWlrVjJlS4qL6vYSFvjyv\\_5sGhm\\_gtctFhteZQ](https://journals.sagepub.com/doi/full/10.1177/1528083718795912?casa_token=ynwyntxvwCEAAAAA%3AP21nAwNvntC5dNZztYigJUUbGcQ1EVrtNp9toC_abWlrVjJlS4qL6vYSFvjyv_5sGhm_gtctFhteZQ).
- [14] Abrate S. *Impact Engineering of Composite Structures*. Springer Science & Business Media; 2011.
- [15] Monteiro SN, Milanezi TL, Louro LHL, et al. Novel ballistic ramie fabric composite competing with Kevlar™ fabric in multilayered armor. *Mater Des*. 2016;96:263–269.
- [16] NIJ Standard 0101.06 Ballistic Resistance of Body Armor - [PDF Document] [Internet]. [fddocuments.nl](https://fddocuments.nl). [cited 2022 Jun 9]. Available from: <https://fddocuments.nl/document/nij-standard-010106-ballistic-resistance-of-body-armor.html>.
- [17] *Lightweight Ballistic Composites* | ScienceDirect [Internet]. [cited 2022 Jun 9]. Available from: <https://www.sciencedirect.com/book/9780081004067/lightweight-ballistic-composites>.
- [18] Hazell P. *Armour: Materials, Theory, and Design*. ARMOUR Mater. Theory Des. 2015.
- [19] Zaid N, Rejab R, Mohamed N. Sandwich Structure Based On Corrugated-Core: A Review. *MATEC Web Conf*. 2016;74:00029.
- [20] Ashab AA, Ruan D, Lu G, et al. Experimental investigation of the mechanical behavior of aluminum honeycombs under quasi-static and dynamic indentation. 2015;
- [21] Hu D, Zhang Y, Shen Z, et al. Investigation on the ballistic behavior of mosaic SiC/UHMWPE composite armor systems. *Ceram Int*. 2017;13:10368–10376.
- [22] Sunder Sharma S, Yadav S, Joshi A, et al. Application of metallic foam in vehicle structure: A review. *Mater Today Proc* [Internet]. 2022 [cited 2022 Jun 9]; Available from: <https://www.sciencedirect.com/science/article/pii/S2214785322015383>.
- [23] Mills NJ. *Polymer foams handbook: engineering and biomechanics applications and design guide*. 1. ed. Amsterdam Heidelberg: Elsevier; 2007.
- [24] Gay D, Hoa SV, Tsai SW. *Composite Materials: Design and Applications*. CRC Press; 2002.
- [25] *Composites in the Aircraft Industry* [Internet]. [cited 2022 Jun 9]. Available from: [https://www.appropedia.org/Composites\\_in\\_the\\_Aircraft\\_Industry](https://www.appropedia.org/Composites_in_the_Aircraft_Industry).
- [26] Abte MA, Boussu F, Bruniaux P, et al. Ballistic impact mechanisms – A review on textiles and fibre-reinforced composites impact responses. *Compos Struct*. 2019;223:110966.

## *Introduction and literature review*

- [27] Spasowka E. AUTOMOTIVE PLASTICS AND COMPOSITES: MATERIALS AND PROCESSING. *Polimery*. 2021;66:153–154.
- [28] Mallick PK. Chapter 6 - Thermoset matrix composites for lightweight automotive structures. In: Mallick PK, editor. *Mater Des Manuf Lightweight Veh Second Ed* [Internet]. Woodhead Publishing; 2021 [cited 2022 Jun 9]. p. 229–263. Available from: <https://www.sciencedirect.com/science/article/pii/B9780128187128000069>.
- [29] Carey JP. *Handbook of Advances in Braided Composite Materials: Theory, Production, Testing and Applications*. Woodhead Publishing; 2016.
- [30] Zagainov GI, Lozino-Lozinski GE. *Composite Materials in Aerospace Design*. Springer Science & Business Media; 1996.
- [31] Liu D, Malvern LE. Matrix Cracking in Impacted Glass/Epoxy Plates. *J Compos Mater*. 1987;21:594–609.
- [32] Ouyang T, Sun W, Bao R, et al. Effects of matrix cracks on delamination of composite laminates subjected to low-velocity impact. *Compos Struct*. 2021;262:113354.
- [33] Naik NK, Shrirao P. Composite structures under ballistic impact. *Compos Struct*. 2004;66:579–590.
- [34] Pandian A, Sultan MTH, Marimuthu U, et al. Low Velocity Impact Studies on Fibre-Reinforced Polymer Composites and Their Hybrids – Review. In: Hashmi S, Choudhury IA, editors. *Encycl Renew Sustain Mater* [Internet]. Oxford: Elsevier; 2020 [cited 2022 Jun 9]. p. 119–130. Available from: <https://www.sciencedirect.com/science/article/pii/B9780128035818112895>.
- [35] Chu Y, Chen X, Sheel DW, et al. Surface modification of aramid fibers by atmospheric pressure plasma-enhanced vapor deposition. *Text Res J*. 2014;84:1288–1297.
- [36] Chu C-K, Chen Y-L. Ballistic-proof Effects of Various Woven Constructions. *Fibres Text East Eur* [Internet]. 2010 [cited 2022 Jun 9];Nr 6 (83). Available from: <http://yadda.icm.edu.pl/baztech/element/bwmeta1.element.baztech-17108ac0-1592-47db-a457-94ed21eb2aa8>.
- [37] Zhou Y, Chen X. A numerical investigation into the influence of fabric construction on ballistic performance. *Compos Part B Eng*. 2015;76:209–217.
- [38] Lee BL, Walsh TF, Won ST, et al. Penetration Failure Mechanisms of Armor-Grade Fiber Composites under Impact. *J Compos Mater*. 2001;35:1605–1633.
- [39] Vieille B, Casado VM, Bouvet C. About the impact behavior of woven-ply carbon fiber-reinforced thermoplastic- and thermosetting-composites: A comparative study. *Compos Struct*. 2013;101:9–21.

## *Introduction and literature review*

- [40] Kharitonov AP, Simbirtseva GV, Tkachev AG, et al. Reinforcement of epoxy resin composites with fluorinated carbon nanotubes. *Compos Sci Technol.* 2015;107:162–168.
- [41] Liu L, Wagner HD. Rubbery and glassy epoxy resins reinforced with carbon nanotubes. *Compos Sci Technol.* 2005;65:1861–1868.
- [42] Davis DC, Wilkerson JW, Zhu J, et al. Improvements in mechanical properties of a carbon fiber epoxy composite using nanotube science and technology. *Compos Struct.* 2010;92:2653–2662.
- [43] Edwards MR. Materials for military helicopters. *Proc Inst Mech Eng Part G J Aerosp Eng.* 2002;216:77–88.
- [44] Okhawilai M, Hiziroglu S, Rimdusit S. Measurement of ballistic impact performance of fiber reinforced polybenzoxazine/polyurethane composites. *Measurement.* 2018;130:198–210.
- [45] Lopresto V, Leone C, De Iorio I. Mechanical characterisation of basalt fibre reinforced plastic. *Compos Part B Eng.* 2011;42:717–723.
- [46] Manikandan V, Winowlin Jappes JT, Suresh Kumar SM, et al. Investigation of the effect of surface modifications on the mechanical properties of basalt fibre reinforced polymer composites. *Compos Part B Eng.* 2012;43:812–818.
- [47] Cartié DDR, Irving PE. Effect of resin and fibre properties on impact and compression after impact performance of CFRP. *Compos Part Appl Sci Manuf.* 2002;33:483–493.
- [48] Braga F de O, Bolzan LT, Lima Jr. ÉP, et al. Performance of natural curaua fiber-reinforced polyester composites under 7.62mm bullet impact as a stand-alone ballistic armor. *J Mater Res Technol.* 2017;6:323–328.
- [49] Dyneema® Fiber [Internet]. @dyneema. [cited 2022 Jun 9]. Available from: [https://www.dsm.com/dyneema/en\\_GB/our-products/dyneema-fiber.html](https://www.dsm.com/dyneema/en_GB/our-products/dyneema-fiber.html).
- [50] Shockey DA, Erlich DC, Simons JW. Full-Scale Tests of Lightweight Fragment Barriers on Commercial Aircraft [Internet]. SRI INTERNATIONAL MENLO PARK CA; 1999 [cited 2022 Jun 9]. Available from: <https://apps.dtic.mil/sti/citations/ADA372648>.
- [51] Lee YS, Wetzel ED, Wagner NJ. The ballistic impact characteristics of Kevlar® woven fabrics impregnated with a colloidal shear thickening fluid. *J Mater Sci.* 2003;38:2825–2833.
- [52] Tirillò J, Ferrante L, Sarasini F, et al. High velocity impact behaviour of hybrid basalt-carbon/epoxy composites. *Compos Struct.* 2017;168:305–312.

## *Introduction and literature review*

- [53] Chen D, Luo Q, Meng M, et al. Low velocity impact behavior of interlayer hybrid composite laminates with carbon/glass/basalt fibres. *Compos Part B Eng.* 2019;176:107191.
- [54] Bandaru AK, Ahmad S, Bhatnagar N. Ballistic performance of hybrid thermoplastic composite armors reinforced with Kevlar and basalt fabrics. *Compos Part Appl Sci Manuf.* 2017;97:151–165.
- [55] Ulven C, Vaidya UK, Hosur MV. Effect of projectile shape during ballistic perforation of VARTM carbon/epoxy composite panels. *Compos Struct.* 2003;61:143–150.
- [56] Tan VBC, Lim CT, Cheong CH. Perforation of high-strength fabric by projectiles of different geometry. *Int J Impact Eng.* 2003;28:207–222.
- [57] Camanho P, Hallett S. *Numerical Modelling of Failure in Advanced Composite Materials.* Woodhead Publishing; 2015.
- [58] Tsai SW, Wu EM. A General Theory of Strength for Anisotropic Materials. *J Compos Mater.* 1971;5:58–80.
- [59] Tabiei A, Ivanov I. Materially and geometrically non-linear woven composite micro-mechanical model with failure for finite element simulations. *Int J Non-Linear Mech.* 2004;39:175–188.
- [60] Caporale A, Luciano R, Sacco E. Micromechanical analysis of interfacial debonding in unidirectional fiber-reinforced composites. *Comput Struct.* 2006;84:2200–2211.
- [61] Rao GVG, Mahajan P, Bhatnagar N. Micro-mechanical modeling of machining of FRP composites – Cutting force analysis. *Compos Sci Technol.* 2007;67:579–593.
- [62] Boubaker BB, Haussy B, Ganghoffer J-F. Consideration of the yarn–yarn interactions in meso/macro discrete model of fabric: Part II: Woven fabric under uniaxial and biaxial extension. *Mech Res Commun.* 2007;34:371–378.
- [63] Liu L, Cai M, Luo G, et al. Macroscopic numerical simulation method of multi-phase STF-impregnated Kevlar fabrics. Part 2: Material model and numerical simulation. *Compos Struct.* 2021;262:113662.
- [64] Wu L, Noels L, Adam L, et al. A multiscale mean-field homogenization method for fiber-reinforced composites with gradient-enhanced damage models. *Comput Methods Appl Mech Eng.* 2012;233–236:164–179.
- [65] Williams KV, Vaziri R, Poursartip A. A physically based continuum damage mechanics model for thin laminated composite structures. *Int J Solids Struct.* 2003;40:2267–2300.
- [66] Lammerant L, Verpoest I. Modelling of the interaction between matrix cracks and delaminations during impact of composite plates. *Compos Sci Technol.* 1996;56:1171–1178.

## *Introduction and literature review*

- [67] Shi Y, Swait T, Soutis C. Modelling damage evolution in composite laminates subjected to low velocity impact. *Compos Struct.* 2012;94:2902–2913.
- [68] Bouvet C, Castanié B, Bizeul M, et al. Low velocity impact modelling in laminate composite panels with discrete interface elements. *Int J Solids Struct.* 2009;46:2809–2821.
- [69] Navarro P, Aubry J, Marguet S, et al. Semi-continuous approach for the modeling of thin woven composite panels applied to oblique impacts on helicopter blades. *Compos Part Appl Sci Manuf.* 2012;43:871–879.
- [70] Pascal F, Navarro P, Marguet S, et al. On the modelling of low to medium velocity impact onto woven composite materials with a 2D semi-continuous approach. *Compos Struct.* 2015;134:302–310.
- [71] Rogani A, Navarro P, Marguet S, et al. Tensile post-impact behaviour of thin carbon/epoxy and glass/epoxy hybrid woven laminates – Part I: Experimental study. *Compos Struct.* 2019;230:111508.
- [72] Iannucci L, Willows ML. An energy based damage mechanics approach to modelling impact onto woven composite materials—Part I: Numerical models. *Compos Part Appl Sci Manuf.* 2006;37:2041–2056.
- [73] A Progressive Damage Model for Laminated Composites Containing Stress Concentrations - Fu-Kuo Chang, Kuo-Yen Chang, 1987 [Internet]. [cited 2022 Jun 9]. Available from: <https://journals.sagepub.com/doi/abs/10.1177/002199838702100904>.
- [74] Hou JP, Petrinic N, Ruiz C, et al. Prediction of impact damage in composite plates. *Compos Sci Technol.* 2000;60:273–281.
- [75] Obi B. *Polymeric Foams Structure-Property-Performance: A Design Guide.* William Andrew; 2017.
- [76] de Souza FM, Choi J, Ingsel T, et al. Chapter 6 - High-performance polyurethanes foams for automobile industry. In: Song H, Nguyen TA, Yasin G, et al., editors. *Nanotechnol Automot Ind* [Internet]. Elsevier; 2022 [cited 2022 Jun 9]. p. 105–129. Available from: <https://www.sciencedirect.com/science/article/pii/B9780323905244000062>.
- [77] Eaves D, editor. *Handbook of polymer foams.* Shawbury, Shrewsbury, Shropshire: Rapra Technology Limited; 2004.
- [78] Gibson LJ. Cellular Solids. *MRS Bull.* 2003;28:270–274.
- [79] Liu P, Chen G-F. *Porous materials: processing and applications.* Amsterdam Boston Paris: Elsevier Butterworth-Heinemann; 2014.

## *Introduction and literature review*

- [80] Feng D, Aymerich F. Effect of core density on the low-velocity impact response of foam-based sandwich composites. *Compos Struct.* 2020;239:112040.
- [81] Jin F-L, Zhao M, Park M, et al. Recent Trends of Foaming in Polymer Processing: A Review. *Polymers.* 2019;11:953.
- [82] Kaewunruen S, Ngamkhanong C, Papaalias M, et al. Wet/dry influence on behaviors of closed-cell polymeric cross-linked foams under static, dynamic and impact loads. *Constr Build Mater.* 2018;187:1092–1102.
- [83] Ouellet S, Cronin D, Worswick M. Compressive response of polymeric foams under quasi-static, medium and high strain rate conditions. *Polym Test.* 2006;25:731–743.
- [84] Yang LM, Shim VPW. A visco-hyperelastic constitutive description of elastomeric foam. *Int J Impact Eng.* 2004;30:1099–1110.
- [85] Drobny JG. *Handbook of Thermoplastic Elastomers.* :464.
- [86] Kabir MdE, Saha MC, Jeelani S. Tensile and fracture behavior of polymer foams. *Mater Sci Eng A.* 2006;429:225–235.
- [87] Zhang B, Zhang X, Wu S, et al. Indentation of expanded polystyrene foams with a ball. *Int J Mech Sci.* 2019;161–162:105030.
- [88] Gupta N, Pinisetty D, Shunmugasamy VC. *Reinforced Polymer Matrix Syntactic Foams: Effect of Nano and Micro-Scale Reinforcement.* Springer Science & Business Media; 2013.
- [89] Dong Y, Umer R, Lau AKT. *Fillers and Reinforcements for Advanced Nanocomposites.* Woodhead Publishing; 2015.
- [90] Murphy J. *Additives for Plastics Handbook.* Elsevier; 2001.
- [91] Yang C, Wang G, Zhao J, et al. Lightweight and strong glass fiber reinforced polypropylene composite foams achieved by mold-opening microcellular injection molding. *J Mater Res Technol.* 2021;14:2920–2931.
- [92] Song W, Konstantellos G, Li D, et al. Short carbon fibre-reinforced epoxy foams with isotropic cellular structure and anisotropic mechanical response produced from liquid foam templates. *Compos Sci Technol.* 2019;184:107871.
- [93] Abu Hassan NA, Ahmad S, Chen RS, et al. Synergistically enhanced mechanical, combustion and acoustic properties of biopolymer composite foams reinforcement by kenaf fibre. *Compos Part Appl Sci Manuf.* 2022;155:106826.
- [94] Tang Q, Fang L, Guo W. Effects of Bamboo Fiber Length and Loading on Mechanical, Thermal and Pulverization Properties of Phenolic Foam Composites. *J Bioresour Bioprod.* 2019;4:51–59.

## *Introduction and literature review*

- [95] Awad SA, Fellows CM, Mahini SS. Effects of accelerated weathering on the chemical, mechanical, thermal and morphological properties of an epoxy/multi-walled carbon nanotube composite. *Polym Test*. 2018;66:70–77.
- [96] Vinoth Kumar S, Subramanian J, Giridharan A, et al. Processing and characterization of organic PU foam reinforced with nano particles. *Mater Today Proc*. 2021;46:1077–1084.
- [97] Sun Y, Li QM. Dynamic compressive behaviour of cellular materials: A review of phenomenon, mechanism and modelling. *Int J Impact Eng*. 2018;112:74–115.
- [98] Li L, Xue P, Chen Y, et al. Insight into cell size effects on quasi-static and dynamic compressive properties of 3D foams. *Mater Sci Eng A*. 2015;636:60–69.
- [99] Aubry J, Navarro P, Marguet S, et al. Change of scale strategy for the microstructural modelling of polymeric rohacell foams. *CMC-Comput Mater Contin*. 2014;21–47.
- [100] Ogden RW. *Non-linear Elastic Deformations*. Courier Corporation; 1997.
- [101] Jemioło S, Telega JJ. Transversely isotropic materials undergoing large deformations and application to modelling of soft tissues. *Mech Res Commun*. 2001;28:397–404.
- [102] Deshpande VS, Fleck NA. Isotropic constitutive models for metallic foams. *J Mech Phys Solids*. 2000;48:1253–1283.
- [103] Abaqus Theory Manual. :1172.
- [104] Carranza I, Crocombe AD, Mohagheghian I, et al. Characterising and modelling the mechanical behaviour of polymeric foams under complex loading. *J Mater Sci*. 2019;54:11328–11344.







---

## **Chapter II. Experimental Study of Low-Velocity Impact Behavior of Hybrid Structures**

---

### **Résumé en français**

ÉTUDE EXPERIMENTALE DU COMPORTEMENT DES STRUCTURES HYBRIDES FACE AUX IMPACTS A BASSE VITESSE.

#### Introduction :

Cette étude porte sur le comportement des structures en mousse époxy renforcées par des tissus d'aramide soumis à l'impact poids tombant. Le nombre de couches d'aramide, leurs emplacements dans la structure, et l'influence de la densité de la mousse sont étudiés. Des essais d'impact poids tombant à basse vitesse sont effectués. Les courbes effort-déplacement, la morphologie du dommage et l'indentation permanente sont analysées.

#### Principaux travaux et résultats :

Les structures hybrides sont fabriquées avec trois densités différentes de mousse époxy (PB170, PB250 et PB400 kg/m<sup>3</sup>). De nombreuses configurations sont testées en faisant varier le nombre de plis d'aramide et leur emplacement.

Les structures sont impactées avec une énergie de 40 J en utilisant une tour de chute. Lors de l'impact, l'indentation que les structures provoquent sur le matériau support en plastiline est mesurée. La capacité de protection des différentes configurations testées est ensuite comparée.

L'analyse des résultats expérimentaux et le dépouillement des essais d'impact à basse vitesse ont permis de déduire les points suivants :

- Lorsque la densité de la mousse augmente, sa capacité à résister à l'impact augmente également.
- Un ou trois plis d'aramide au milieu de la mousse époxy améliorent le comportement en diminuant la propagation des fissures et en atteignant un effort maximal plus élevé par rapport à la mousse sans fibre.

### *Experimental study of low-velocity impact behavior of hybrid structures*

- L'emplacement des plis d'aramide peut grandement influencer la morphologie des dommages de la structure. Lorsque le pli d'aramide est placé comme face d'impact, la raideur de la structure augmente. Lorsque le pli d'aramide est placé comme face arrière, il empêche la propagation des fissures.

- Dans les structures bi-mousse, lorsque la face d'impact est de densité plus élevée, la réponse à l'impact des structures est améliorée : l'effort maximal est plus élevé et l'indentation permanente est plus faible.

#### Conclusion :

Cette étude montre qu'une combinaison réfléchie entre les plis d'aramide et la mousse époxy peut empêcher la rupture de la mousse fragile et augmenter sa raideur initiale. Les essais d'impact à faible vitesse ont permis de comprendre le scénario de dommage des structures hybrides. En se basant sur ces essais, des conclusions ont été tirées dans l'objectif d'optimiser l'architecture de ces structures hybrides. Ainsi, une densité plus élevée sur la face d'impact entraîne une meilleure réponse à l'impact. De plus, les plis d'aramide peuvent augmenter la rigidité des structures lorsqu'ils sont placés sur la face d'impact et empêcher la propagation des fissures lorsqu'ils sont mis en œuvre sur la face opposée à l'impact.

Les essais réalisés ont également été utilisés comme référence pour la validation du modèle numérique présenté dans le chapitre IV.

## **Dynamic response of epoxy foam structures reinforced by aramid plies subjected to low velocity impact**

L. Boutros, P. Navarro, S. Marguet, I. Tawk, J.F.Ferrero

### **Abstract:**

*This study investigates the impact response of epoxy foam structures reinforced by aramid woven fabrics through drop weight tests. The number of aramid plies and their location are varied, and the influence of foam density is studied. Low-velocity drop weight tests are conducted. Load-displacement curves, the morphology of damage, and indentation are analyzed. Results reveal that increasing the number of aramid layers in the middle of the structure improves crack propagation and increases the peak load. In addition, adding one aramid layer to the structure's back face hinders crack propagation. A parameter called back face signature (BFS) is measured to study the protection capacity that the hybrid structures possess. The back face signature indicates the level of trauma left by the impacted structure on the backing material, usually called clay witness. Finally, in bi-foam structures, having a higher density as an impact face leads to an improved protection capacity.*

### **II.1 Introduction**

Cellular materials are essential lightweight materials used progressively in several engineering areas for thermal insulation, electromagnetic interference shielding of an electric component, and core material for sandwich-type composite materials. In this study, the behavior of epoxy foam reinforced by aramid fibers under low-velocity impact will be investigated experimentally.

Foam materials are built from various base materials like polymers, metals, ceramics, and glasses [1]. The fabrication process of polymer foams is mainly divided into mixing and molding [2]. The foaming process can be achieved through mechanical, physical, or chemical [3]. Mechanical foaming is where the polymer is mixed mechanically or frothed for the air to get inside the liquid polymer and form the foam system. As for physical foaming, a low boiling point agent should be added to the polymer before the frothing to create the foam system.

On the other hand, chemical foaming is when two chemical solutions (polymers) are added together and frothed mechanically. At this point, a chemical reaction occurs and produces gases. Afterward, the polymer is foamed by pressuring and heating [3]. Polymer foams can be categorized according to their raw material: thermoplastic, thermoset, and elastomers [1]. Thermoplastic foams can include, Polystyrene (PS), Polyethylene (PE), and Polyvinyl chloride (PVC); thermoset foams include, Polyurethane (PU), Phenolic resin, and Epoxy resin [2].

The mechanical behavior of polymer foams strongly depends on the fabrication process, base material, morphology of their microstructure, and density. Under compressive loading, all-polymer foam stress-strain curves show three different regions: linear-elastic or Hookian region, plateau region, and densification region [4, 1]. The linear elastic region is governed by the bending of the cell walls, where Young's modulus of the foam is the slope of this linear behavior. The collapse of the cells characterizes the plateau region; elastic buckling for elastomeric foams and brittle crushing for brittle foams such as ceramic or epoxides. When all the cells are crushed or compacted, an increase in stress describes the densification region [4, 1]. The tensile response of polymer foams is also connected to the foam density and raw material. The foam response to tensile stress is first linear elastic controlled by bending and stretching the cell walls. Elastomeric foams show a linear behavior, whereas plastic foams attain a yield point and an augmentation in stress until failure. However, brittle foams show a significant brittle failure after the elastic region, where cracks propagate rapidly throughout the structure [1].

As for the cell microstructures, two types exist closed cell and open cell foam [5]. A closed-cell foam consists of a wall surrounding all the cells, separating them from one another. Open-cell walls are open to each other, making it impossible to entrap gas or liquid inside. As a result of the cell microstructure, closed cells tend to be stiffer, where the cell geometry resists air leakage and shows more strength than open cells, where the foam tends to be softer [6, 7]. Usually, the density governs the mechanical properties of polymer foam: as the density of the foam increases, the mechanical properties increase [5, 8].

Foam behavior under dynamic loading is sensitive to the strain rate of the impact. Yan et al. studied the influence of the strain rate on the behavior of polymer foams under compressive loading [9]. It was shown that when the strain rate increases, the plateau stress increases, and

the densification happens sooner. The behavior of the polymer foams is monitored by the speed at which the air escapes the foam cells.

Polymer foams are extensively used due to their ability to absorb energy under impact. The behavior of polymer foams under impact can be analyzed through a force-displacement curve and a visual inspection of the sample. Impact starts with a localized deformation underneath the indenter, followed by a buckling of the cells and collapse. Finally, the densification, where the stress increases rapidly when the cell walls are in contact. The energy absorption mainly happens in the second feature when the cell walls collapse, and particularly for brittle foam, energy absorption occurs by cell fracture and crushing [4, 10].

Regardless of the advantageous properties of polymer foam, recent studies make a great effort to improve its mechanical properties to increase its potential in future applications. Reinforcement of polymer foams can be achieved by integrating fillers and reinforcing particles in fabrication. Those reinforcements aim to obtain mechanical properties superior to those obtained in ordinary or foam without reinforcement. Those properties include increased modulus, strength, and energy absorption; modulation of electrical properties; and tailoring thermal properties such as thermal expansion, thermal conductivity, and glass transition temperature ( $T_g$ ) [11]. Fillers are tiny solid particles that are typically used in small quantities to enhance the value of the foam, and they include fibrous fillers (glass fiber, aramid fiber, and carbon fiber), Nanofillers (nanoclays, graphite nanotubes), and rubber particles [12].

Fibrous fillers can be in the form of chopped strands of fiber filament. They act to reinforce the foam by switching the stress from the low stiffness foam to the fibers [13]. Yang et al. studied the behavior of Polypropylene (PP) thermoplastic foam reinforced by short glass fibers (diameter of about 13  $\mu\text{m}$ ). The study proves that adding around a 20% wt ratio of GF to the PP foam improves the tensile strength and modulus, the specific bending stress, and modulus by 59.45%, 54.81%, 94.75%, and 82.42%, respectively, compared to neat PP foam [14]. As for short carbon fibers, Wenzhe et al. show that adding short carbon fibers (SCF) to epoxy foam improves fracture toughness by up to 113% compared to neat epoxy foam [15]. Organic fiber can also be a successful additive to polymer foams; studies dealing with Kenaf fiber [16] and bamboo fiber [17] as a reinforcement show that their addition improves the mechanical and thermal properties of the foam compared to ordinary foam.

Carbon Nanotubes, Nanofibers, and rubber particles as reinforcement are also very popular since they have low density due to their hollow core [11]. Awad et al. and Kumar et al. both study the addition of MWCNT to polymers foams. Both studies prove that adding nanoparticles improves mechanical properties (tensile strength and modulus) and thermal stability [18, 19].

While adding reinforcement into the epoxy foams might increase the fracture toughness, the introduction of those fillers leads to a significant decrease in the compressive strength compared to neat unreinforced foam [15]. In addition, adding silica particles to polyurethane foam in a high concentration shows a decrease in tensile strength compared to neat foam [20]. Javni et al. show that the reinforcement of polyurethane foam with Nano-silica improves the hardness and compression strength but decreases the rebound resilience [21]. On the other hand, adding filler during the preparation of polymer foam faces several challenges on the fabrication level, especially in maintaining a uniform dispersion inside the foam media and the orientation of the nanoparticles [10].

Many attempts are undertaken to improve the strength of polymer foam, especially the one having a brittle behavior. However, substantial efforts focus on ameliorating polymer foams on the microstructural level. A reinforcement method is applied in the current study without modifying the foam's microstructure. The reinforcement is realized by adding woven composite fabric within epoxy foam layers, eliminating the need for sophisticated mixing techniques. The fabric is selected based on its impact behavior. Hence, aramid plies are used in the current study as a reinforcement of a closed-cell epoxy foam. The aramid plies are added in different configurations and locations to study their ability to hinder crack propagation. The study focuses on assessing the capacity of energy absorption and the morphology of damage to those structures under low-velocity impact. It is shown that adding one aramid ply as the structure's bottom layer prevents crack propagation. Structures with a higher number of aramid plies in the middle attain a higher peak load. Impact face foam density influences the stiffness and impact performance of the structure.

## **II.2 Experimental procedure**

This experimental study aims to observe and analyze the influence of the following parameters: number of aramid plies, location of aramid plies, and the epoxy foam density. The tested configurations include structures made of neat foam (unreinforced by aramid plies), structures having one or three aramid plies in the middle or distributed in different locations in the thickness of the specimen, and finally, structures having two foam densities separated in the middle by one or three aramid plies. The structures are assessed based on their capacity to absorb energy. A technique usually used for high impact velocity is applied in this study. Clay witness material is placed underneath the structure during impact [22]. After impact, the indentation left on the clay, also called back face signature (BFS), indicates the level of protection that the structures can achieve.

### **II.2.1 Manufacturing of the structures**




In the current study, three densities of epoxy foam are studied, 170, 250, and 400 kg/m<sup>3</sup>. The epoxy foam used is provided by Sicomin [23]. The epoxy foams used are closed-cell foams with different expansion rates. The PB epoxy foam has two components: epoxy resin (PB) and a hardener (DM03). When the two components are mixed, they expand due to chemical foaming. For the epoxy foam preparation, a specific amount of liquid epoxy and hardener is added to a container and then mechanically frothed for 4 minutes.

The aramid fibers used in this study are a four-harness satin woven fabric with an areal density of 175 g/m<sup>2</sup> and thickness of 0.26 mm. The matrix is an Araldite® LY 5052 (resin)/Aradur® 5052 (hardener) epoxy with a fiber volume fraction of 37%.

The configurations fabricated are based on studying the influence of several parameters mentioned above. The influence of the number of aramid plies is studied by fabricating structures with mono-foam having one or three plies of aramid in the middle (Table II-1). Each configuration is fabricated with three different foam densities (170, 250, and 400 kg/m<sup>3</sup>). Blocks of neat foam are also manufactured, [PB170-neat], [PB250-neat], and [PB400-neat], to help better understand the influence of each parameter. (For more fabrication details refer to Appendix A).








Table II-1: Mono-foam density structure with aramid plies in the middle and neat foam

configuration	[PB-1ply-PB]	[PB-3plies-PB]	[PB-neat]
representation			

The influence of aramid plies location is studied through structures having mono-foam density with (Table II-2):

- One ply of aramid in three different locations; on the top, middle, and bottom.
- Three plies of aramid: one ply on the top and two in the middle, two in the middle and one on the top, and finally one on the top, one in the middle, and one on the bottom.

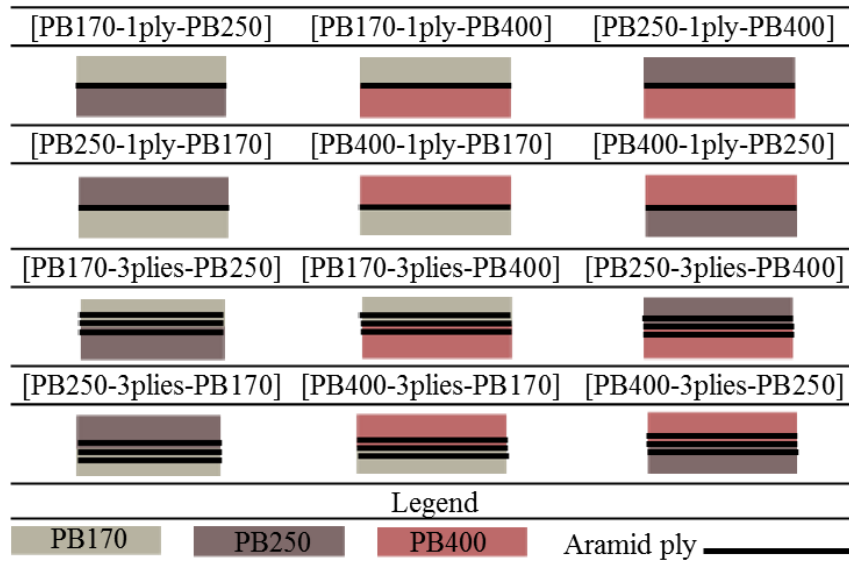
Table II-2: Mono-foam density structure with aramid plies distributed in different locations

configuration	[1ply-PB]	[PB-1ply]	[1ply-PB-2plies-PB]	[PB-2plies-PB-1ply]	[1ply-PB-1ply-PB-1ply]
representation					

Finally, foam density is studied with structures having one or three plies in the middle but with bi-foam density (Table II-3). In this case, the upper foam part of the structure has a different density than the bottom part. Several combinations are fabricated, combining PB250 and PB170, PB400 and PB170, and finally, PB400 and PB250.

Table II-3: Bi-foam density structure with aramid plies in the middle

*Experimental study of low-velocity impact behavior of hybrid structures*



The fabrication process of the global structures starts with impregnating the aramid plies, then preparing the epoxy foam mix. The structures are fabricated inside a closed mold. The impregnated aramid plies are fixed on the edges of the mold in case they are in the middle. Alternatively, they are placed on the bottom or top to create the configurations needed. Afterward, the mold is placed in a hot air oven at 40°C for 12 hours. Samples are cut using a water jet-cutting machine into square structures of 100mm×100mm, having a thickness of about 30 mm.

## II.2.2 Drop weight impact test

The capacity of energy absorption is assessed through a low-velocity impact test. A hemispherical-end steelhead with a mass of 2 kg and a diameter of 16 mm impact the structures. The velocity of the impact is 6.3 m/s, equivalent to an impact energy of 40 J. The structures are simply placed on a soft clay material to help measure the dent trauma left after the impact, also known as back face signature (BFS) (Appendix B). The clay material is confined inside a wooden box. The clay is heated before the test to reach a temperature of around 38°C [24]. Test setup and mounting are shown in Figure II-1. While performing the test, the load and displacement are recorded. The outputs of the drop weight test are the following: visual inspection of the structures, load-displacement curves, permanent indentation, and back face signature (BFS).

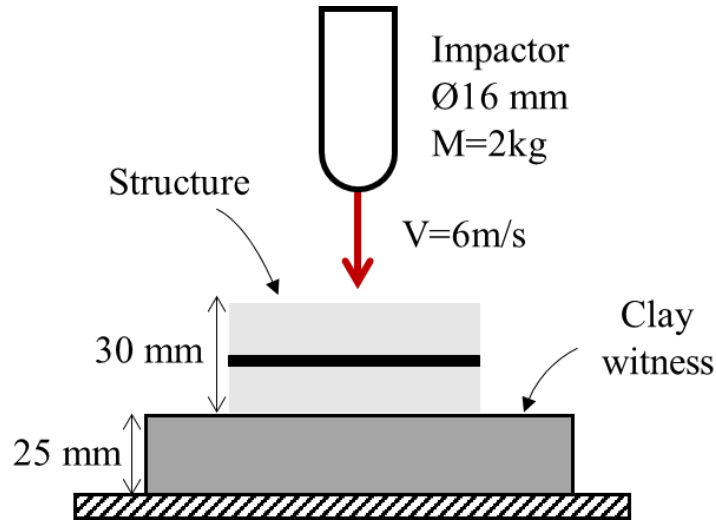


Figure II-1: Experimental setup of drop weight impact test

### **II.3 Results and discussion**

In this section, the low-velocity impact test results are described. Morphology of damage, as well as measurements of the indentation, are compared. Further, load-displacement curves are presented as a function of the number of aramid plies, their position, and their epoxy foam density variation.

#### **II.3.1 Impact response of neat epoxy foams**

The curves of the impact force versus the indenter displacement are given in Figure II-2. The linear phase of the load-displacement curve indicates the elastic response of the epoxy foam. The increased load observed afterward describes the bending and crushing of the foam cells, where most of the impact energy is dissipated. A significant load drop occurs hereafter, indicating the epoxy foam's brittle failure. In addition, foam density plays an essential role in response to impact. As the density increases, the peak load and the stiffness in the linear phase also increase.

Figure II-2.b, shows how the indenter perforates the structure. The impact leads to brittle failure, which tears the epoxy foam into pieces. The severity of the crack is due to the high cross-linked density in all epoxides materials [25]. All three structures with different densities show the exact morphology of damage.

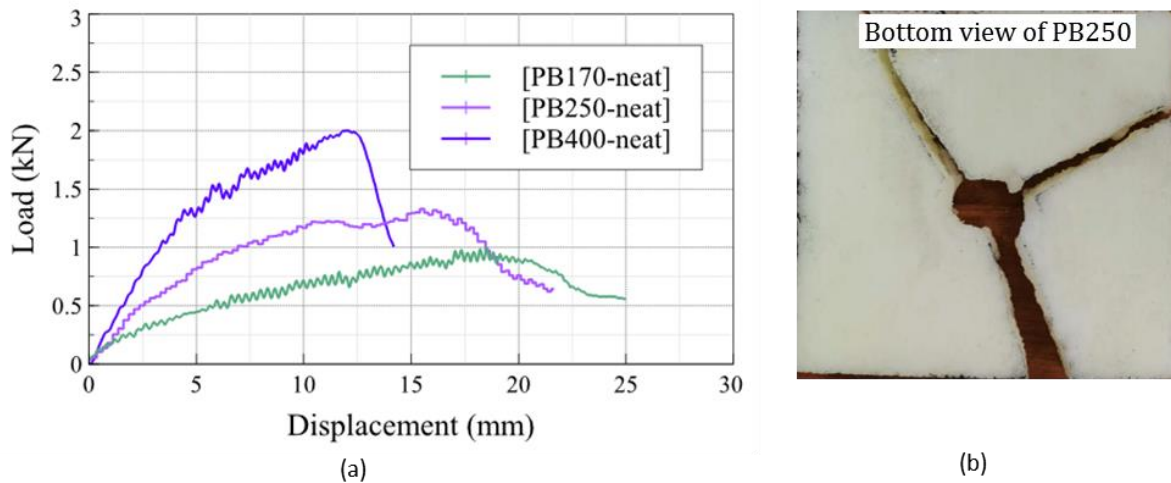


Figure II-2: a) Load-displacement curves of neat epoxy foam, b) morphology of damage of [PB250-neat]

### II.3.2 Influence of the number of Aramid plies located in the middle

This section demonstrates the effect of the number of aramid layers in the middle of mono-foam structures. The representative load-displacement curves of the PB170, PB250, and PB400 with one and three aramid plies in the middle are plotted in Figure II-3.

For PB170 structures (Figure II-3.a), the first region from zero to 10 mm in displacement, the curves show a linear behavior, with a slight change in slope at 5 mm displacement. This might be due to the material densification underneath the impactor. An increase in load happens and reaches 2.2 kN in the case of three aramid plies in the middle. Three plies of aramid in the middle increase the peak load reached by 120% and 10% compared to a structure with one aramid ply and neat epoxy foam structure, respectively. The increase in load indicates that the impactor attained the aramid plies. Then a load drop occurs, which means that the aramid plies are perforated. A further drop in load indicates the failure of the bottom face of the epoxy foam.

Adding one or three aramid plies in the middle delays the full rupture of the structures and increases the peak load.

Structure with PB250 (Figure II-3.b) with one aramid ply in the middle shows a drop in load after attaining a maximum of 2.6 kN; this means a failure at the level of the aramid plies. Thus, the structure with PB250 and three aramid plies do not exhibit fiber perforation; the three

*Experimental study of low-velocity impact behavior of hybrid structures*

aramid plies were able to stop the impact at this level. Unlike the structure reinforced by aramid plies, [PB250-neat] fails at a displacement of 10 mm, after attaining a maximum effort of 1.2 kN.

Finally, structure with PB400 with aramid plies (Figure II-3.c); a linear response is observed from early stages until a displacement of around 10mm. An increase in load occurs when the impactor attains the aramid plies and rebounds before the aramid plies are perforated. This behavior is similar for both structures, whether with one or three aramid plies. However, a structure with only PB400, [PB400-neat], shows an 82% decrease in stiffness compared to the other structures with PB400.

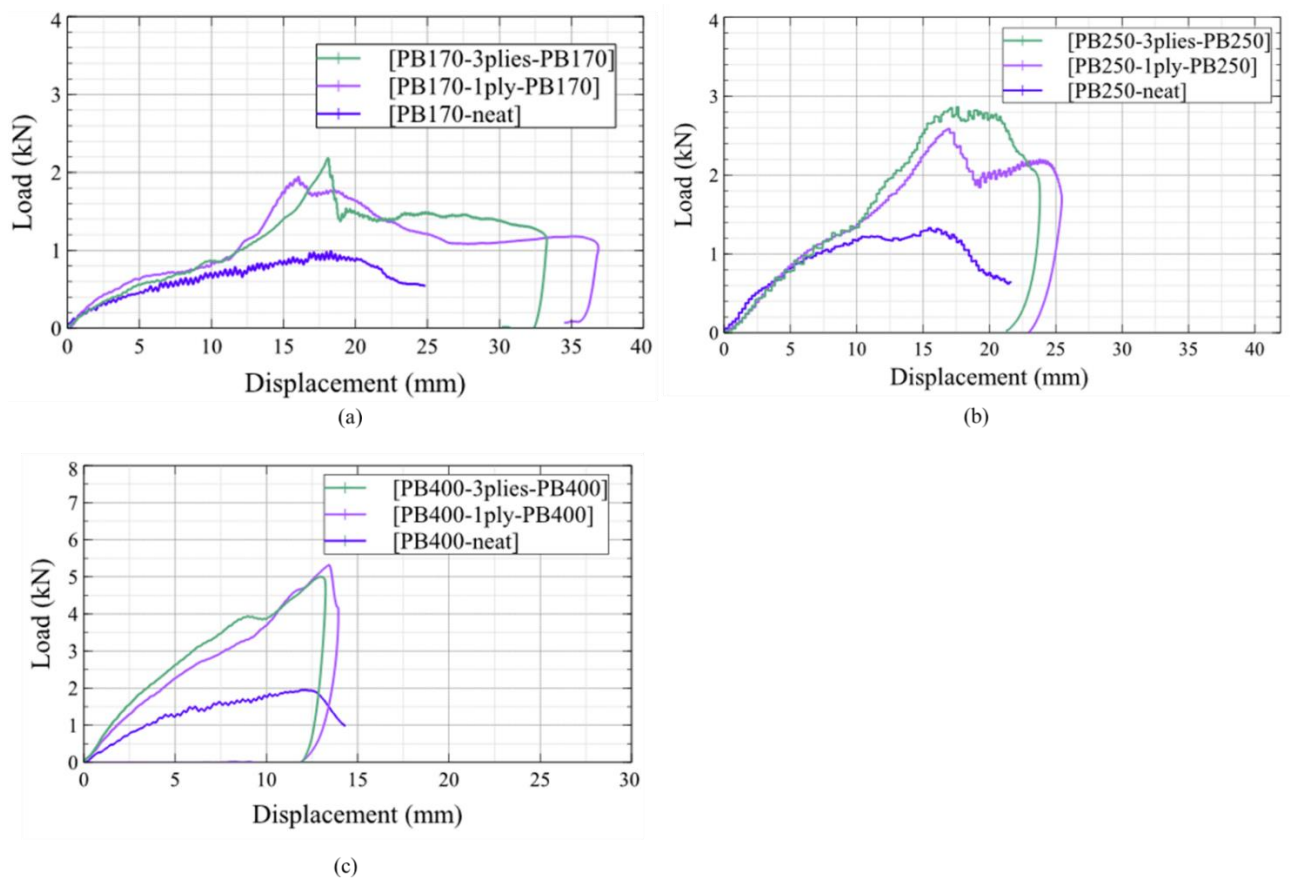


Figure II-3: Load-displacement curves for mono foam structures with aramid plies in the middle

Figure II-4 compares the morphology of the damage of each structure having PB170 with aramid plies in different locations. It is shown that all structures with PB170 are fully perforated. A clear hole is formed on the impact and bottom face with a diameter of around 16

*Experimental study of low-velocity impact behavior of hybrid structures*

mm. Having the lowest density, PB170 epoxy foam possesses higher porosity levels and lower cell wall thickness, which leads to a lower load-carrying capacity.

Yet, for structures having PB250, a clear hole is observed on the upper layer. Fiber breakage and matrix cracking are shown in a structure having 1ply of aramid in the middle leading to a perforation of the aramid. Further, the deformation of the aramid fiber in a conical shape (Figure II-4, third column) led to the brittle foam failure. It is represented by cracks on the bottom face and delamination between the aramid ply and the bottom layer of epoxy foam. As for the structure having three aramid plies in the middle shows that the foam under the indenter is compacted, and a plug of this densified foam is created (Figure II-4, fourth column) at the level of upper foam/ aramid plies. As the applied load increases, the compacted material is further pushed, causing the aramid plies to deform. Aramid plies are not perforated; rather, they are deformed, leading to crack propagation and delamination between the aramid plies and the bottom foam layer.

As for the PB400, only the one having one aramid ply in the middle shows cracks on the surface of the bottom face, whereas the one having three aramid plies only shows the damage caused by the indenter on the impact face. The PB400 governs the behavior of these structures since the indenter rebounded before perforating the aramid plies.

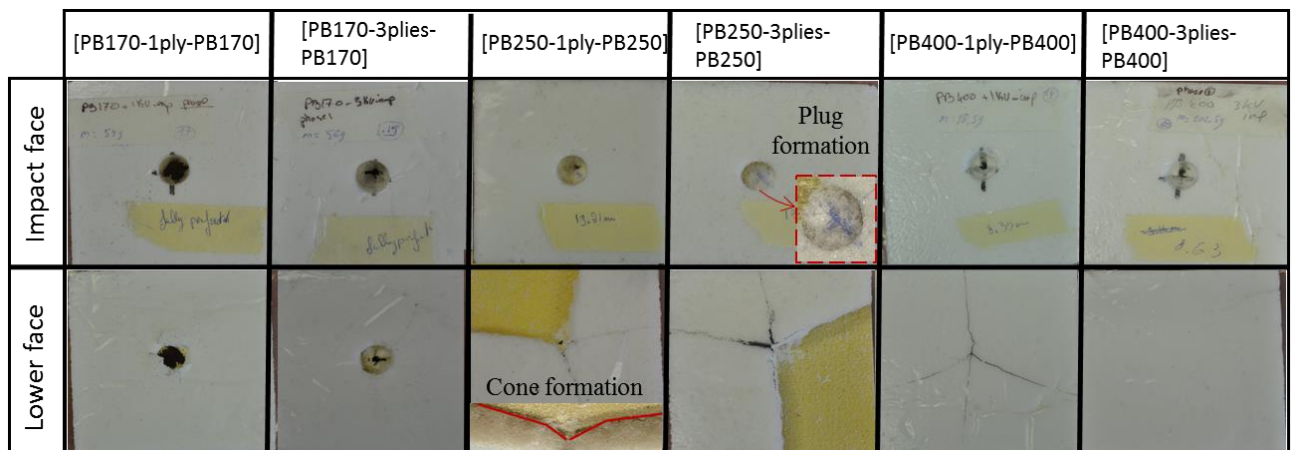


Figure II-4: Morphology of the damage to the structures having one or three aramid plies in the middle

The measurements of the back face signature show the ability of the structure to provide protection for the back face and stop the indenter, Figure II-5. Structures with PB170 are fully perforated; therefore, the BFS cannot give any significance. As for structures with PB250, the three aramid plies have a lower BFS of 21% compared to the structure with only one aramid

ply. As for PB400, since the indenter is stopped at the first layer of epoxy foam, there is no visible deformation on the back face. The back face signature measured represents only the deformation that the four edges of the structures leave when it sinks inside the soft clay during impact.

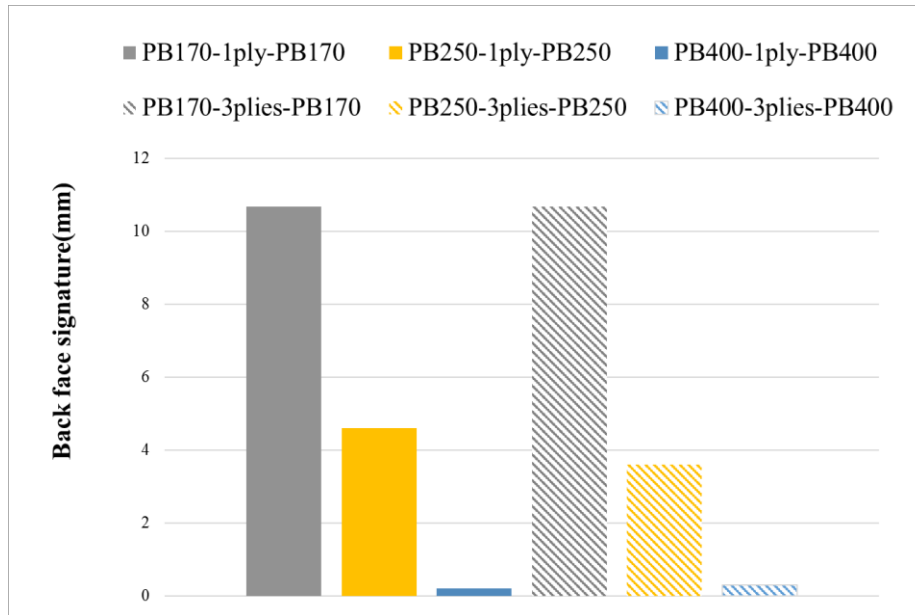


Figure II-5: Back face signature of mono-foam structures with aramid plies in the middle

Increasing the number of aramid plies in the middle decreased the crack propagation and increased the peak load reached in the case of PB250 and PB400. The increase of aramid plies in the middle with PB170 showed no enhancement.

### **II.3.3 Influence of aramid plies location**

The influence of the location of aramid plies is shown in Figure II-6. The load-displacement curves of the PB170 epoxy foam with one or three plies in different locations are presented.

Structure with only one ply on top, [1ply-PB170], shows increased stiffness by 22 % compared to the structures with PB170. After reaching a maximum load of 1.2 kN (Figure II-6.a), the structure fails with significant brittleness. On the other hand, adding aramid fiber on the bottom, [PB170-1ply], shows a progressive increase in load, meaning that the foam crushes and densifies until an increase in load happens at a displacement of 30 mm where the indenter reaches the aramid ply. The aramid ply on the bottom decreases the displacement by 11%



compared to when it is located in the middle. The structure having one aramid as the bottom layer stops the indenter faster.

Figure II-6.b also analyses the influence of modifying the location of the three-aramid plies. Equally, to the analysis above, adding one aramid ply on top of the structure increased the stiffness. However, structures having one ply on the bottom, [1ply-PB170-1ply-PB170-1ply] and [PB170-2plies-PB170-1ply] increase load to reach a peak of around 2 kN when the indenter reaches the middle and the bottom aramid plies, and rebound without perforation. Structure with three aramid plies in the middle, [PB170-3plies-PB170] attains the higher peak load (this is due to three aramid plies stacked together in the middle). Nevertheless, a structure without aramid ply on the bottom shows a drop in load after the perforation of the aramid fibers in the middle, leading to a full perforation of the structure.

The delay in attaining the peak load for the structure with the three aramid plies, observed in Figure II-6.b, is due to fabrication. Indeed, the location of the aramid plies might vary during the expansion phase of the foam inside the mold, which changes its position slightly.

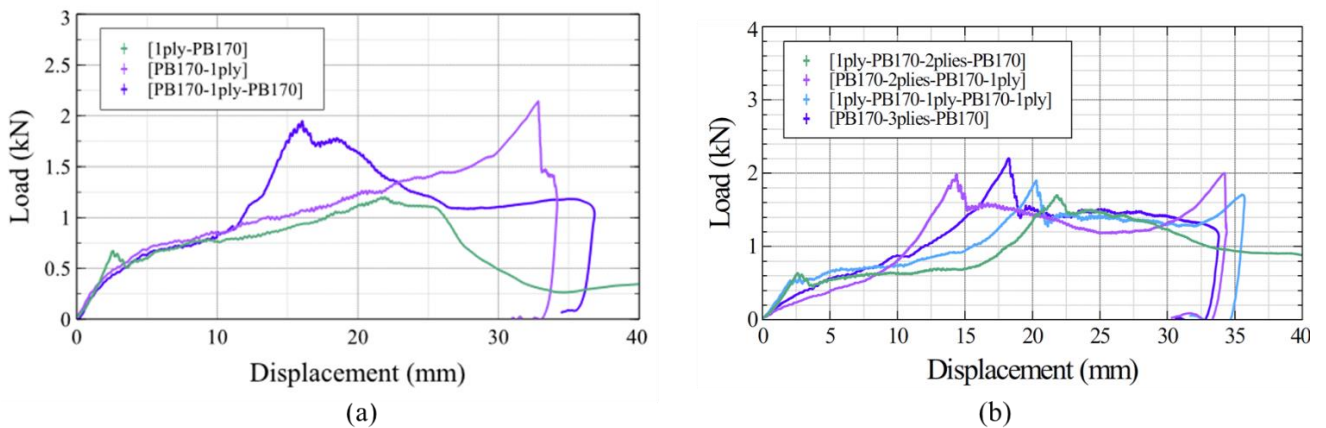


Figure II-6: Load-displacement curves for mono foam PB170 structures with a) 1ply either on top or bottom and b) 3plies distributed differently in the structure

The morphology of the damage for five specimens is presented in Figure II-7. Structure [1ply-PB170] shows clear propagation of the cracks on the lower face, whereas structure with one aramid ply on the bottom shows no sign of failure. Yet, [1ply-PB170-2plies-PB170] is fully perforated similarly to [PB170-3plies-PB170]. [PB170-2plies-PB170-1ply] and [1ply-PB170-1ply-PB170-1ply] only show a slight deformation on the bottom face.



*Experimental study of low-velocity impact behavior of hybrid structures*

The presence of a ply of aramid on the structure's top face improves the structure's initial stiffness. Whereas the presence of a ply on the bottom face improves the impact response; by hindering the crack propagation on the bottom face of the structures.

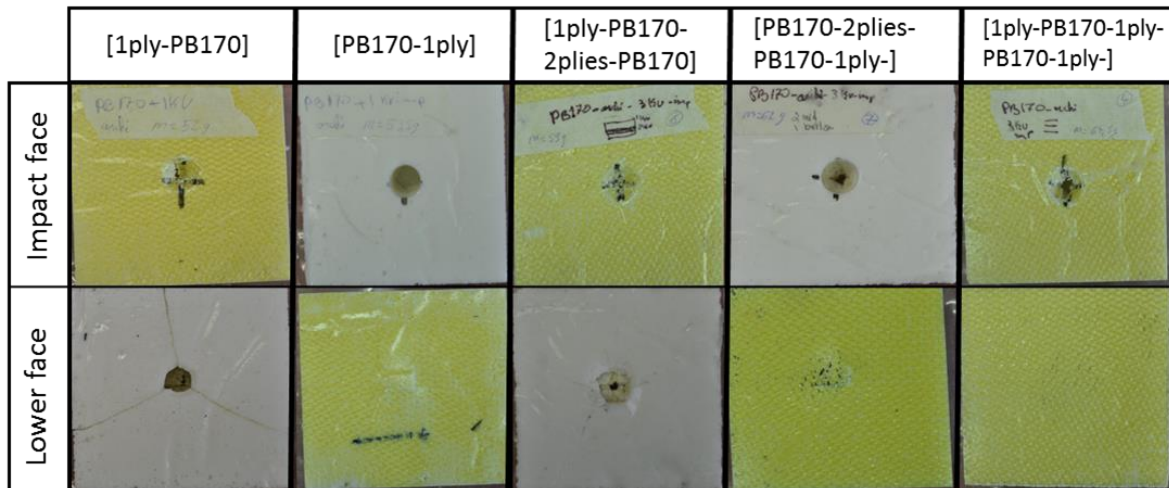


Figure II-7: Morphology of the damage for mono-foam PB170 structure with aramid plies in different locations

The amount of deformation that the structures left on the soft clay are illustrated in Figure II-8. The representation of the BFS for PB170 structures can illustrate the capacity of protection those structures possess.

Structures that do not have aramid fiber on the bottom face are fully perforated, and therefore they have the higher back face signature since the indenter sinks inside the clay witness. The structure protected by an aramid ply at the bottom shows a lower back face signature. In particular, structures with three aramid plies distributed in the top, middle, and bottom present the lowest back face signature.

The addition of aramid ply on the bottom does not only eliminate the cracks but also. As a result, it decreases the back face signature. In addition, the increase of the initial stiffness due to adding one ply on top also improves the back face signature.

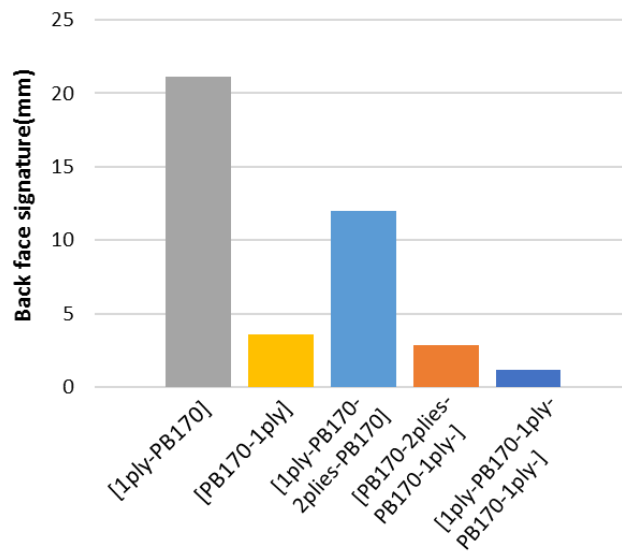


Figure II-8: Back face signature of mono-foam PB170 structures with aramid plies in different locations

Figure II-9 shows the load-displacement curves of structures with PB250 reinforced with one or three aramid plies in different locations. Figure II-9.a, similarly to the previous analysis made for Figure II-6.a, the densification is clear from the early stages for both structures. Then a brittle fracture occurs for the structure having one aramid ply on top. The one having one ply on the bottom reaches a peak load of around 2.5 kN, and the indenter rebounds before reaching the aramid ply, which is located at 30 mm. For a structure with aramid ply in the middle, the peak load reach is 2.6 kN at a displacement of 15 mm, then after the aramid failure. The indenter rebounds after attaining a maximum displacement of 22 mm. Figure II-9.b proves that all three structures could stop the indenter at a displacement of around 20 mm.

Structures having aramid ply on top possess higher stiffness. Structure [PB250-3plies-PB250] show similar behavior as [PB250-2plies-PB250-1ply]. Increasing the number of aramid in the middle does not improve the peak load.

*Experimental study of low-velocity impact behavior of hybrid structures*

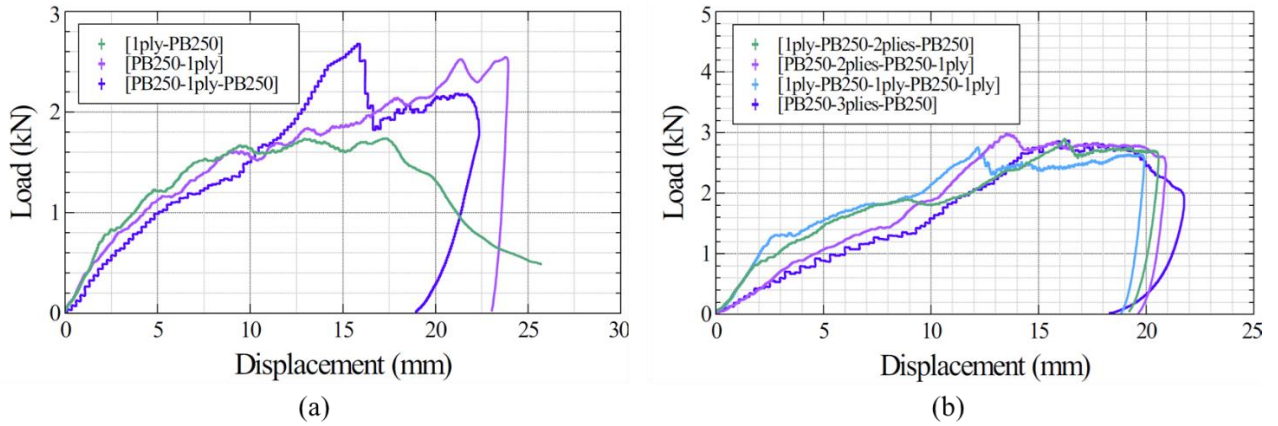


Figure II-9: Load-displacement curves for mono foam PB250 structures with aramid plies in different locations

The morphology of damage to those structures is coherent with the one found in Figure II-7, which reveals that when adding aramid ply on the bottom, the epoxy foam is reinforced and does not display cracks or brittle failure.

Figure II-10 presents the back face signature of the structures having PB250 foam with aramid plies in multiple locations. The structure having one aramid ply on the impact face fails similarly to the structure of [PB250-neat]; therefore, it has a higher BFS since it is fully perforated. The structure with one aramid ply on the bottom significantly improves behavior where the perforation is prevented, and the BFS is improved. While [1ply-PB250-2plies-PB250] does not possess a ply at the bottom, it still has better BFS than [PB250-1ply] by 31%. This is due to the aramid plies on top and in the middle, which increase the stiffness and peak load of the structure. However, [PB250-2plies-PB250-1ply] and [1ply-PB250-1ply-PB250-1ply] only show a slight BFS located on the four edges of the structure due to its sinking inside the clay. Therefore, it does not imply damage in the location of the load applied.

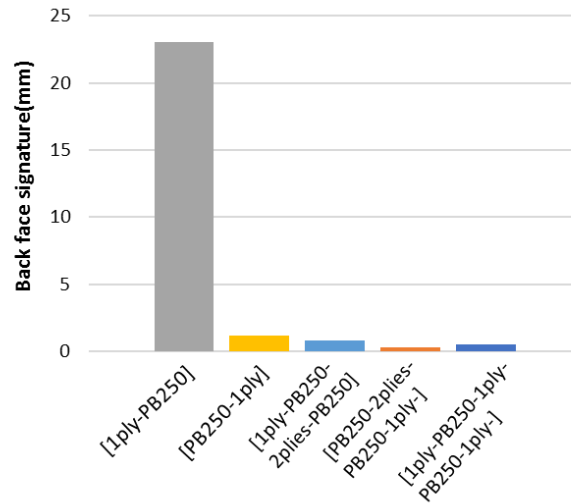


Figure II-10: Back face signature of mono-foam PB250 structures with aramid plies in different locations

For the structures with PB400, the influence of aramid location is not illustrated clearly, Figure II-11. PB400 has the highest density; it can stop the impact without the interference of the aramid plies reinforcement, leaving no back face signature other than the edges of the structure. Only structure [1ply-PB400] results in full perforation towards the impact.

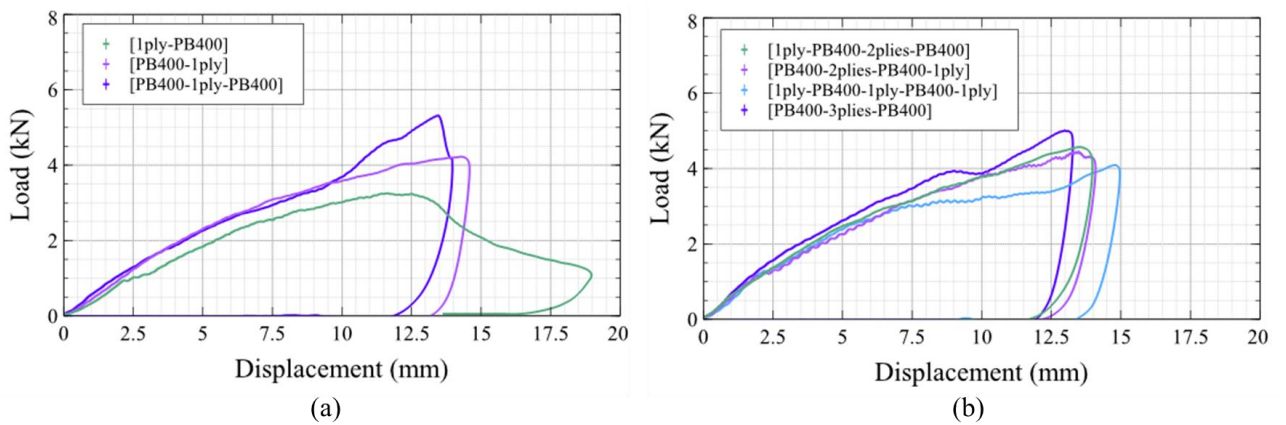


Figure II-11: Load-displacement curves for mono foam PB400 structures with aramid plies in different

These results underline the importance of the location of aramid plies inside the structure. An improvement in crack propagation was observed when a ply of aramid was added on the bottom face of the structure, where it reinforces the epoxy foam by hindering crack propagation and eliminating the de-bonding at the interface foam/aramid. Additionally, it was established that one ply of aramid could increase the initial stiffness of the structure. Those improvements also manifest in the back face signature, which decreases when the brittle failure of the epoxy foam

is avoided. However, the foam density also plays a significant role in improving the back face signature. The structure having PB250 with aramid one ply on the bottom shows a lower back face signature by 68% compared to the same configuration structure but with PB170.

Besides, the permanent indentation inside the structure can be significant in assessing the capacity of protection of the structure. Figure II-12 shows the permanent indentation of the configuration [1ply-PB-1ply-PB-1ply] with the three different densities. These results confirm that the BFS improves when the density of foam increases and the permanent indentation left inside the structure after the impact is significantly improved by up to 47%. However, the total density of the structure is increased by 70%. Consequently, the influence of density variation inside a single structure is studied in the next section to investigate the potential of decreasing the density of a structure while keeping the same performance towards impact.

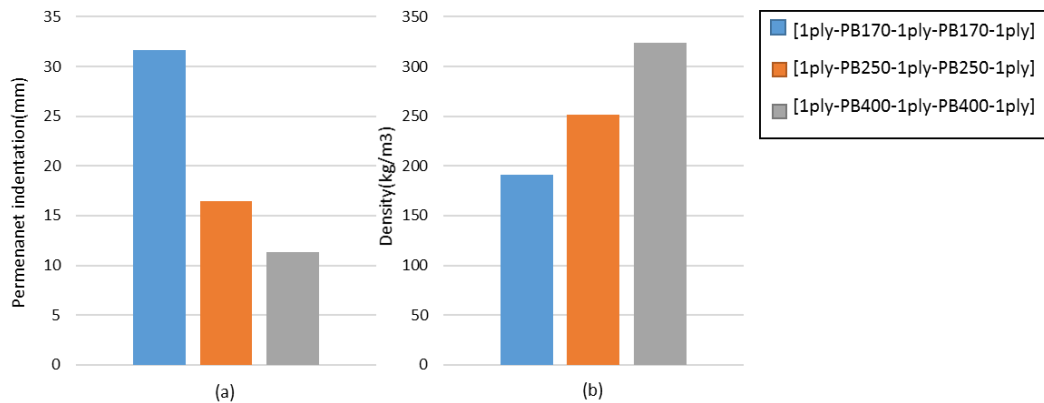


Figure II-12: a) Permanent indentation and b) density of mono-foam structure of configuration [1ply-PB-1ply-PB-1ply]

### II.3.4 Influence of foam density variation

The following section compares mono-foam and bi-foam structures with three aramid plies in the middle. This comparison aims to evaluate the influence of the epoxy foam density inside a single structure. This section outlines three combinations, PB170/PB250, PB170/PB400, and PB250/PB400.

Figure II-13 compares structures having bi-foam, PB170, and PB250 in a single structure. It presents configurations where PB170 is the top layer and PB250 is the back one, [PB170-3plies-PB250], and the other configuration is the reverse, [PB250-3plies-PB170]. An additional presentation of mono-foam is for comparison purposes.

*Experimental study of low-velocity impact behavior of hybrid structures*

The load-displacement curves show that the structure having PB250 as the top layer has improved stiffness and peak load by 120% and 17%, respectively, compared to the other structures. On the other hand, the permanent indentation of [PB250-3plies-PB170] and the BFS compared to [PB170-3plies-PB250] is decreased by 30% and 74%, respectively. While the curves yielded that the behavior of [PB250-3plies-PB170] and [PB250-3plies-PB250] is very similar, this later shows a higher BFS of 200%. This is due to the rigidity of the PB250, which results in crack propagation, leaving a higher BFS as pieces of foam sink inside the clay. Whereas PB170, as the bottom layer, fails due to high shearing around the edges on the indenter. This can also be justified since [PB250-3plies-PB170] has higher permanent indentation than [PB250-3plies-PB250].

While [PB170-3plies-PB250] and [PB250-3plies-PB170] have the same density, the behavior of the structure having the highest density as impact face improved the impact response of the structure.

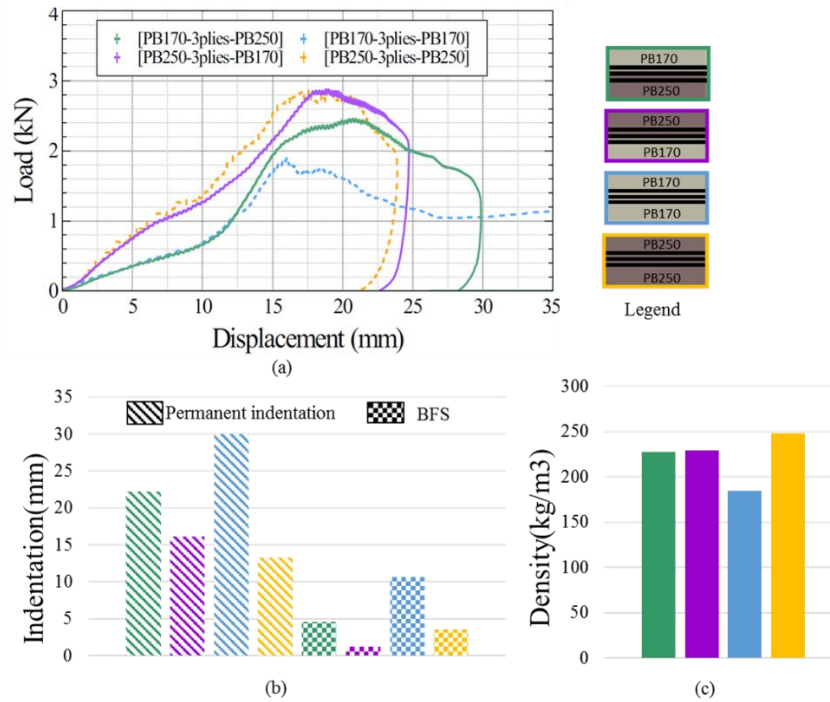
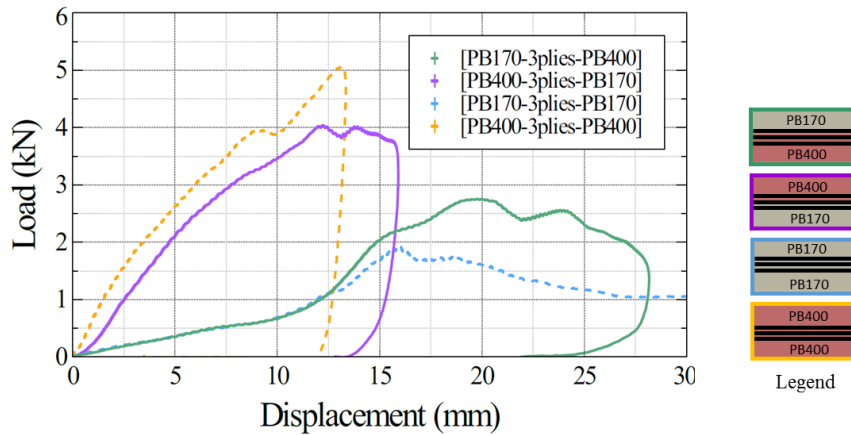


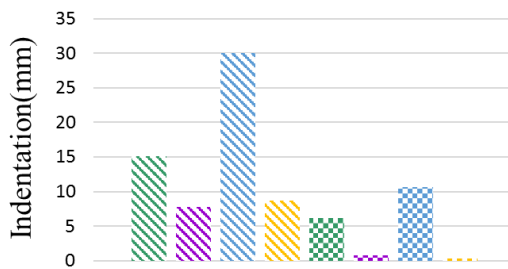
Figure II-13: (a) load-displacement curves, (b) Indentation and back face signature, and (c) density of PB170/PB250 with three aramid plies

From the data shown in Figure II-14, the perforation of [PB170-3plies-PB170] can be prevented by replacing the bottom layer with a layer of PB400. However, replacing the upper layer with PB400 instead of PB170 prevents perforation and increases the stiffness by 480%. The structure configuration [PB400-3plies-PB170] also shows an improved permanent indentation and BFS compared to [PB170-3plies-PB400] by about 48% and 87%, respectively. On the other hand, comparing the structure having the mono-foam, [PB400-3plies-PB400], with [PB400-3plies-PB170], both have very similar behavior and indentation; however, the structure having PB170 as the bottom layer shows a reduced density by around 9%.

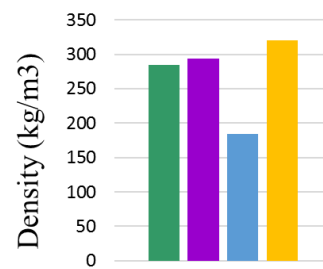
*Experimental study of low-velocity impact behavior of hybrid structures*



(a)



(b)



(c)

Figure II-14: (a) load-displacement curves, (b) Indentation and back face signature, and (c) density of PB170/PB400 with three Aramid plies

Figure II-15, presents structures having a combination of PB400 and PB250 with three aramid plies in the middle. It can be shown on the load-displacement curve that the structure [PB250-3plies-PB250] has a similar behavior as [PB250-3plies-PB400], but comparing it with [PB400-3plies-PB250], an increase in the stiffness occurs by 178%. In the case of the structures having PB400 as the top layer, the aramid plies in the middle do not play a very important role since the impactor does not even reach them.



Experimental study of low-velocity impact behavior of hybrid structures

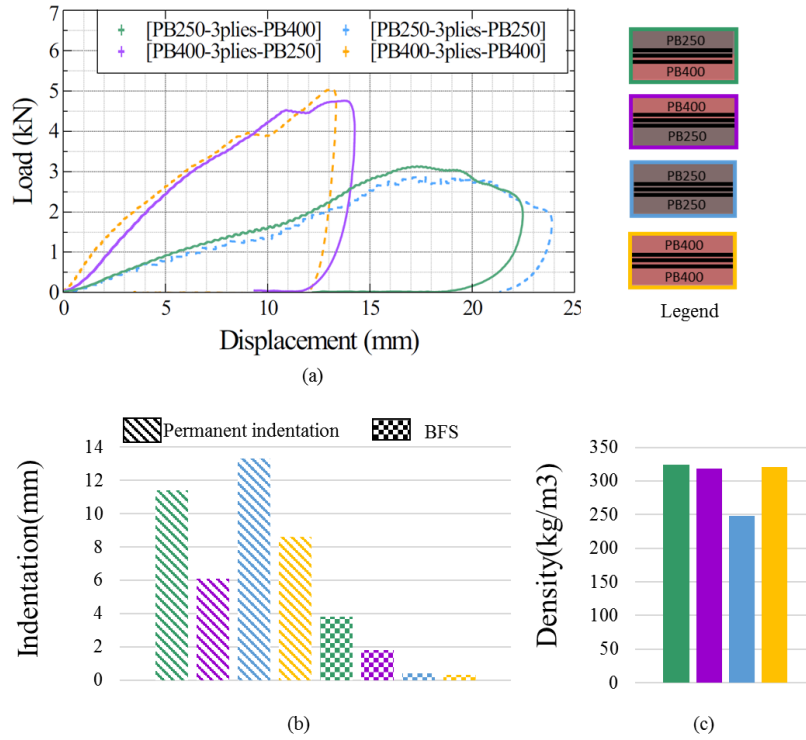


Figure II-15: (a) load-displacement curves, (b) Indentation and back face signature, and (c) density of PB250/PB400 with three Aramid plies

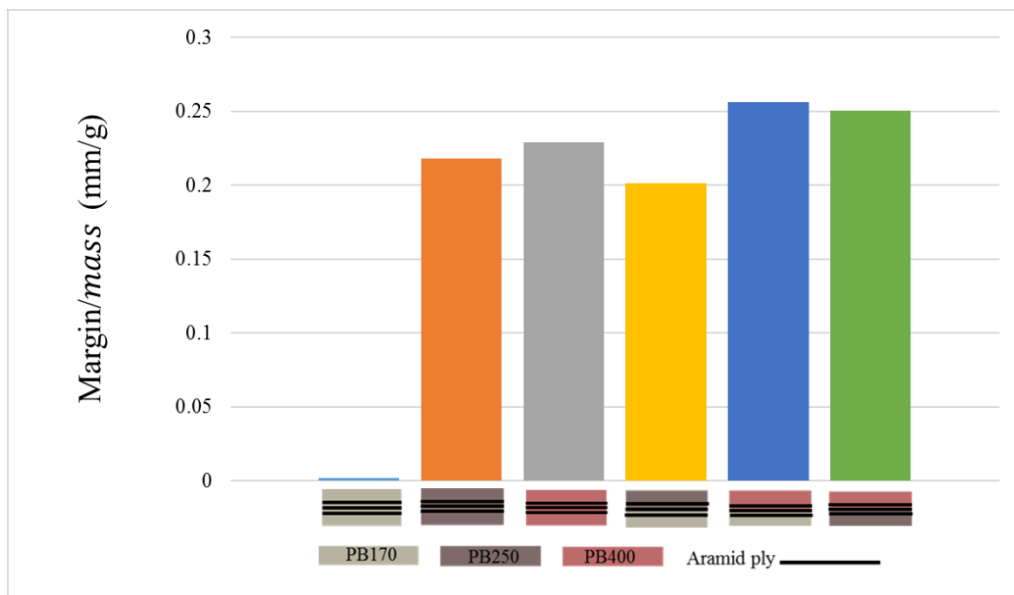


Figure II-16: Margin over mass ratio for mono and bi-foam structures

The influence of the epoxy foam density is also studied by calculating the ratio *margin/mass* (mm/g). The margin is the *plate thickness - indentation depth* left by the indenter inside the structures. This ratio aims to compare the structures with different global

densities. This ratio helps study the ability of the structures to stop the indenter while taking into account their mass. The higher the ratio, the more effective the structure is against the impact. The results of the ratio *margin/mass* are presented in Figure II-16.

[PB170-3plies-PB170], having the lowest weight, exhibits the lowest ratio, showing its poor capacity to stop the impact, especially when the structure is fully perforated. Replacing the impact face by PB250 increases the ratio by 100%. However, structure [PB250-3plies-PB250] has an increased ratio by 9% compared to [PB250-3plies-PB170]. This is due to the presence of PB170 on the back face, which leads to higher permanent indentation.

Structure with PB400 as impact face, whether mono or bi-foams structures, the ratio is higher than the rest of the structures. However, structures with PB400 as the impact face with PB170 or PB250 as the back face show an increased ratio of 12% and 8%, respectively, compared to [PB400-3plies-PB400]. This means that bi-foam structures with PB400 show a better capacity to stop the indenter per unit mass than mono-foam structures with PB400. The structure that maximizes this ratio the most is [PB400-3plies-PB170].

The findings presented in this section show that a structure with a higher foam density as an impact face showed higher initial stiffness and yielded better permanent indentation and BFS while having the same global density as the structure. Having the lowest foam density as impact face, i.e., [PB170-3plies-PB400], led to full penetration of the upper foam, then damage of aramid plies, which led to a cone formation on the bottom face, ending with cracks propagation on the bottom face of the PB400. Figure II-17 clearly illustrated the damage morphology inside both structures combining PB170 and PB400. The failure of the aramid plies in the middle is represented by a cone formation on the lower face, leading to a brittle failure of the bottom layer of epoxy foam.

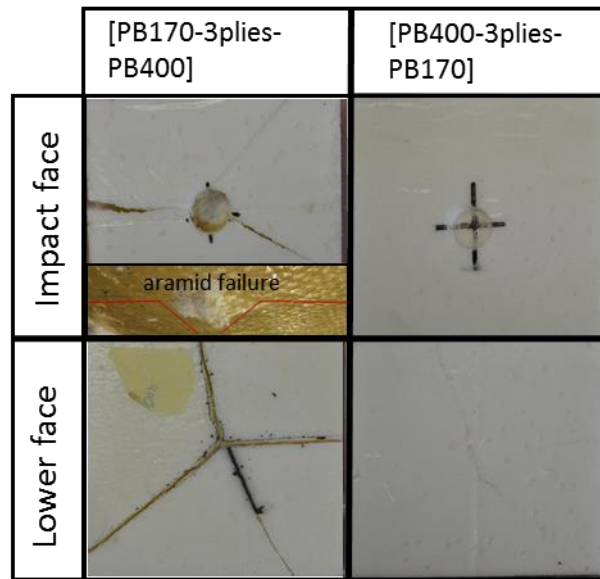


Figure II-17: Morphology of the damage to bi-foam PB170/PB400 structure with three aramid plies in the middle

However, even when adding a higher foam as the top face, which monitors mainly the behavior of the structure, it could not obstruct the crack propagation due to the brittleness of the structures.

That being the case, the structures that could stop the indenter before perforating the aramid plies or not even reaching it (PB250 and PB400) show an improved morphology of damage, leading to a better back-face signature.

## II.4 Summary

The analysis of the experimental results and observation of the low-velocity impact tests done on the structures deduced the following points:

- As the foam density increases, its capacity to carry load increases. One or three aramid plies in the middle of the epoxy foam improve the behavior by decreasing the crack propagation and attaining a higher peak load.
- Aramid plies location can significantly influence the morphology of damage inside the structure by controlling its stiffness when added to the top face and then protecting the bottom face from crack propagation.
- Structures with bi-foam with three plies of aramid in the middle are monitored by the top layer foam density behavior. The highest density as the top face backed with three aramid

plies proved enough to stop the indenter with minimum damage left of the clay (BFS) compared to the structures with low-density foam as the top face.

- The ratio margin/mass shows that replacing the impact face density of mono-foam structures with a higher density improves the ability to stop the indenter per unit mass. However, in the case of PB400 as an impact face, replacing the bottom foam layer with lower foam density improves the protection level per unit mass.

## **II.5 Conclusion**

The behavior of epoxy foam reinforced by aramid layers is investigated experimentally through low-velocity impact tests. Several configurations are tested to study the influence of the location and number of aramid plies and the foam density variation inside a single structure. The comparison and analysis are based on load-displacement curves, damage morphology, and indentation (BFS and permanent). This paper investigation attributes the following outcomes:

1. Foam density indicates the capacity of load carrying. PB400 shows a higher stiffness since it has a higher density. Therefore, higher wall thickness leads to higher mechanical properties. However, no matter how stiff they are, neat epoxy foam fails with significant brittleness due to crack propagation.
2. Adding one or three aramid plies to the PB170 does not prevent complete perforation but induces a different damage mode. However, for PB250 and PB400 adding the plies in the middle prevent perforation. Increasing the aramid plies in the middle shows higher peak load and less crack propagation on the bottom.
3. Crack propagation is only prevented for all foam densities when one ply of aramid is added to the bottom face of the structure. [1ply-PB] shows a similar behavior as [PB-neat]. Hence, adding one ply of aramid on top does not prevent perforation. However, [PB-1ply] eliminates the epoxy foam's brittle response, which leads to a lower back face signature. This ply plays a significant role in reinforcing the brittle nature of epoxy foam by hindering crack propagation.
4. The damage propagation scenario inside the structures starts when the indenter crushes the upper layer of foam. When the impactor reaches the aramid plies, it causes a failure represented by matrix cracks, fiber breakage, and cone formation on the lower face of the aramid plies. This damage induces the failure of the lower layer of epoxy foam.

*Experimental study of low-velocity impact behavior of hybrid structures*

5. Foam density influences and monitors the behavior of the structures, especially when the highest density is the impact face. Structures with the configuration [PB250-3plies-PB170], [PB400-3plies-PB250], and [PB400-3plies-PB170] show better impact behavior and can stop the indenter before perforating the three aramid plies. Substituting the bottom layer of the mono-foam PB400 with PB250 or PB170 can guarantee the same stiffness and approximately comparable indentation levels while saving weight.
6. The ratio margin/mass is calculated to compare the ability of the structure to stop the indenter per unit mass. Structures with PB400 as impact face exhibit the highest ratio, meaning the best protection level per unit mass. Replacing the bottom layer of [PB400-3plies-PB400] with PB170 or PB250 keeps the same level of protection while decreasing the mass by 24%.
7. This study demonstrates that aramid plies can reinforce epoxy foam. Modifying the number of aramid plies and the location of those plies while varying the epoxy foam density can significantly improve the impact response of the structures. Hence, those structures can be used in the future as promising candidates for protection applications.

## **References**

- [1] Gibson, L. J. (2003). Cellular solids. *Mrs Bulletin*, 28(4), 270-274.188
- [2] Liu, P. S., & Chen, G. F. (2014). *Porous materials: processing and applications*. Elsevier.
- [3] Jin, F. L., Zhao, M., Park, M., & Park, S. J. (2019). Recent trends of foaming in polymer processing: A review. *Polymers*, 11(6), 953.
- [4] Eaves, D. (Ed.). (2004). *Handbook of polymer foams*. iSmithers Rapra Publishing.
- [5] Drobny, J. G. (2014). *Handbook of thermoplastic elastomers*. Elsevier.
- [6] Kaewunruen, S., Ngamkhanong, C., Papaalias, M., & Roberts, C. (2018). Wet/dry influence on behaviors of closed-cell polymeric cross-linked foams under static, dynamic and impact loads. *Construction and Building Materials*, 187, 1092-1102.
- [7] Mills, N. (2007). *Polymer foams handbook: engineering and biomechanics applications and design guide*. Elsevier.
- [8] Feng, D., & Aymerich, F. (2020). Effect of core density on the low-velocity impact response of foam-based sandwich composites. *Composite Structures*, 239, 112040
- [9] Yang, L. M., & Shim, V. P. W. (2004). A visco-hyperelastic constitutive description of elastomeric foam. *International journal of impact engineering*, 30(8-9), 1099-1110.
- [10] Michler, G. H., & Balta-Calleja, F. J. (2016). *Mechanical properties of polymers based on nanostructure and morphology*. CRC Press.
- [11] Gupta, N., Pinisetty, D., & Shunmugasamy, V. C. (2013). *Reinforced polymer matrix syntactic foams: effect of nano and micro-scale reinforcement*. Springer Science & Business Media.
- [12] Dong, Y., Umer, R., & Lau, A. K. T. (Eds.). (2015). *Fillers and reinforcements for advanced nanocomposites*. Woodhead Publishing.
- [13] Murphy, J. (Ed.). (2001). *Additives for plastics handbook*. Elsevier.

[14] Yang, C., Wang, G., Zhao, J., Zhao, G., & Zhang, A. (2021). Lightweight and strong glass fiber reinforced polypropylene composite foams achieved by mold-opening microcellular injection molding. *Journal of Materials Research and Technology*, 14, 2920-2931.

[15] Song, W., Konstantellos, G., Li, D., & Lee, K. Y. (2019). Short carbon fibre-reinforced epoxy foams with isotropic cellular structure and anisotropic mechanical response produced from liquid foam templates. *Composites Science and Technology*, 184, 107871.

[16] Hassan, N. A. A., Ahmad, S., Chen, R. S., & Natarajan, V. D. (2022). Synergistically Enhanced Mechanical, Combustion and Acoustic Properties of Biopolymer Composite Foams Reinforcement by Kenaf Fibre. *Composites Part A: Applied Science and Manufacturing*, 106826.

[17] Tang, Q., Fang, L., & Guo, W. (2019). Effects of bamboo fiber length and loading on mechanical, thermal and pulverization properties of phenolic foam composites. *J Bioresour Bioprod* 4 (1): 51–59.

[18] Awad, S. A., Fellows, C. M., & Mahini, S. S. (2018). Effects of accelerated weathering on the chemical, mechanical, thermal and morphological properties of an epoxy/multi-walled carbon nanotube composite. *Polymer Testing*, 66, 70-77

[19] Kumar, S. V., Subramanian, J., Giridharan, A., Gupta, M., Adhikari, A., & Gayen, M. (2021). Processing and characterization of organic PU foam reinforced with nano particles. *Materials Today: Proceedings*, 46, 1077-1084.

[20] Nunes, R. C. R., Fonseca, J. L. C., & Pereira, M. R. (2000). Polymer–filler interactions and mechanical properties of a polyurethane elastomer. *Polymer testing*, 19(1), 93-103.

[21] Javni, I., Zhang, W., Karajkov, V., Petrovic, Z. S., & Divjakovic, V. (2002). Effect of nano-and micro-silica fillers on polyurethane foam properties. *Journal of cellular plastics*, 38(3), 229-239.

[22] Armor, P. B. (2008). Ballistic Resistance of Personal Body Armor NIJ Standard–0101.04.

[23] Sicomin. (2014). Systèmes époxydes pour production de mousses alvéolaires. <http://sicomin.com/produits/systemes-epoxy/moussage-structurel>

[24] <https://www.plastiline.fr/>

[25] Bagheri, R., Marouf, B. T., & Pearson, R. A. (2009). Rubber-toughened epoxies: a critical review. *Journal of Macromolecular Science®*, Part C: Polymer Reviews, 49(3), 201-225.





## **Chapter III. Experimental Study of High-Velocity Impact Behavior of Hybrid Structures**

---

### **Résumé en français**

#### ÉTUDE EXPERIMENTALE DU COMPORTEMENT DES STRUCTURES HYBRIDES FACE AUX IMPACTS A HAUTE VITESSE

##### Introduction :

Le comportement à l'impact à haute vitesse de structures hybrides mousse époxy/fibres d'aramide est étudié dans ces travaux. Les performances de ces structures sont examinées en étudiant la profondeur de l'empreinte formée sur un matériau de support en plastiline lors de l'impact. Cette empreinte est appelée "Back Face Signature (BFS)". Les structures sont impactées par un dispositif de canon à gaz projetant une bille à une vitesse de 180 m/s. Les résultats montrent que plusieurs paramètres influencent la réponse à l'impact pour un nombre fixe de plis d'aramide, tels que la densité de la mousse époxy, l'emplacement des couches d'aramide et leur niveau d'imprégnation de résine époxy. L'étude montre que l'ajout d'une couche de mousse époxy sur la face inférieure des couches d'aramide améliore la BFS par rapport aux stratifiés composites conventionnels.

##### Principaux travaux et résultats :

Quatorze configurations sont fabriquées avec des fibres d'aramide sèches, et imprégnées de résine époxy. Les configurations sont fabriquées avec deux densités de mousse PB250 et PB400 ( $\text{kg/m}^3$ ). L'influence de la position des plis d'aramide, du niveau d'imprégnation et de la densité de la mousse époxy sont testés. Deux stratifiés composites non hybrides (25 plis d'aramide secs et 25 plis imprégnés) sont fabriqués comme structures de référence.

Les structures sont testées avec une bille sphérique ( $m = 11 \text{ g}$ , diamètre = 14 mm) à une vitesse de 180 m/s. Après l'impact, la morphologie des dommages, la BFS et l'indentation permanente sont évaluées.

Les stratifiés composites conventionnels présentent respectivement une BFS de 8 mm et 34 mm dans le cas de plis d'aramide imprégnés et secs, Il est démontré que la réponse à l'impact des fibres d'aramide secs est étendue. L'impact est caractérisé par la déformation des fibres primaires et secondaires.

En revanche, les plis imprégnés montrent une réponse très localisée se traduisant par des fissures matricielles sur les bords de la région d'impact de la face impactée. Une rupture de fibres en forme de croix sur la face arrière est observée.

L'influence de la position des plis d'aramide est étudiée, et montre que le fait de placer les 25 plis d'aramide comme face d'impact avec une épaisseur de mousse époxy élimine la BFS par rapport aux stratifiés conventionnels, tout en augmentant la masse de 50%. La structure avec de la mousse époxy comme face d'impact, quelle que soit la densité de mousse utilisée (PB250 ou PB400), présente une perforation complète. L'impacteur n'est arrêté qu'au niveau des plis d'aramide. Diminuer le nombre de plis d'aramide sur la face d'impact à 20 s'avère insuffisant pour arrêter l'impacteur sans pénétration dans la couche de mousse époxy.

Le niveau d'imprégnation des plis d'aramide est analysé. Les plis d'aramide imprégnés, lorsqu'ils sont placés à l'arrière, laissent une BFS inférieure de 61% pour la PB250 et de 91% pour la PB400 par rapport aux plis secs. La résine époxy contient les fibres et empêche leur déformation, ce qui entraîne un BFS et une indentation permanente plus faible.

La densité de la mousse époxy joue un rôle important sur la réponse des structures hybrides. Les résultats montrent que la PB400 peut arrêter l'impacteur plus rapidement que la PB250. Les structures avec de la PB400 comme face d'impact et avec 25 plis d'aramide imprégnés à l'arrière montrent une BFS inférieure de 80% comparées à la PB250. Un dommage peu visible est observé sur les plis d'aramide dans le cas de la PB400 tandis qu'un endommagement des fibres en forme de croix est observé dans le cas de la PB250 (longueur du dommage 29 mm).

Les structures hybrides ont des masses différentes car elles ont des densités de mousse et des niveaux d'imprégnation différents. Un paramètre appelé marge/masse est étudié pour mieux évaluer leur capacité de protection. La marge est l'épaisseur non endommagée laissée dans l'éprouvette après l'impact. Ce rapport montre que les structures avec 25 plis d'aramide comme faces d'impact ont la plus grande capacité de protection spécifique.

### *Experimental study of high-velocity impact behavior of hybrid structures*

Ces structures peuvent éliminer la BFS observée dans les stratifiés composites conventionnels, tout en augmentant la masse de 50 %. Comme les 25 plis d'aramide ne sont pas perforés, l'épaisseur de la couche de mousse époxy peut être réduite, ce qui entraîne une diminution de la masse. Sur la base des résultats présentés ci-dessus, il existe des possibilités d'optimisation de la masse de ces structures hybrides.

#### Conclusion :

Le comportement à l'impact des structures hybrides mousse époxy/fibres d'aramide est étudié lorsqu'elles sont soumises à un impact à haute vitesse. Ce travail étudie la capacité de ce matériau hybride à préserver l'intégrité de la structure à protéger. La capacité de protection est examinée pour plusieurs configurations en comparant les BFS, l'indentation permanente et l'inspection visuelle post-impact des structures. Sur la base des recherches effectuées dans cette étude, les nouvelles structures hybrides avec des plis d'aramide imprégnés comme faces d'impact s'avèrent être un matériau de protection potentiel. Le matériau proposé peut être utilisé dans des applications de protection où l'épaisseur n'est pas une contrainte. Plusieurs facteurs d'amélioration peuvent être soulignés, tels que la diminution de l'épaisseur de la couche d'époxy, la répartition des plis d'aramide au cœur des structures, et l'utilisation de plusieurs densités de mousse dans une seule structure pour améliorer le rapport efficacité/masse.

## **Epoxy foam/aramid fibers hybrid structures for high velocity impact protection**

L. Boutros, P. Navarro, S. Marguet, I. Tawk, J.F.Ferrero

### **Abstract:**

*The behavior of epoxy foam/ aramid fibers hybrid structures under high velocity impact is studied in the present work. Closed-cell epoxy foam is combined with layers of aramid fibers fabrics and impacted with a gas gun device at a velocity of 180 m/s. The performance of these structures is examined by studying the damage and Back Face Signature (BFS), which is the indentation left on a reference material placed behind the structures during impact. Results show that several parameters influence the impact response for a fixed number of aramid plies, such as the epoxy foam density, location of aramid plies through the thickness, and the level of impregnation with epoxy resin. The study reveals that adding an epoxy foam layer on the lower face of aramid plies enhances the BFS compared to conventional composite laminates.*

### **III.1 Introduction**

Nowadays, the need to find adequate protection material rises with the rise of threats and impact risks. Several studies focus on the improvement of conventional protection materials. Protection systems are used in numerous fields, such as transportation, packaging, and buildings. The purpose of protective materials can be to save lives or guarantee the integrity of the protected structure. Various protection systems exist, and their selection relies on the hazard type and the intended application.

Metal, ceramics, high-performance textiles, and cellular materials are used for protection. Composite materials are among the most used materials in protection applications. Aramid and ultra-high molecular weight polyethylene (UHMWP) fibers are the most employed for protection against high-velocity impact. Aramid fibers marked under Kevlar<sup>®</sup> and Twaron<sup>®</sup> show superior impact properties since they have a high strength-to-weight ratio, high modulus, and good tenacity [1,2]. Lee et al. [3] studied the performance of Kevlar<sup>®</sup> as a personal protection material. This study showed that a 1.4 mm thickness of Kevlar<sup>®</sup> can stop a projectile

of 1.1 grams with 250 m/s velocity leaving 21 mm of penetration depth inside a backing material. The backing material is usually used in personal protection testing to simulate the consistency of the human body. The indentation left on the backing material is called the Back Face Signature (BFS). The less the BFS is, the more the target can stop the projectile and provide protection [3].

The impact response of aramid fibers is influenced by several parameters, such as fabric architecture, matrix type, and friction between the yarns [2]. Aramid fibers with different architectures are intriguing in many protection applications. Bandaru et al. [4] studied the high-velocity impact on aramid composite laminates with 2D plain woven, 3D orthogonal, and 3D angle interlock fabrics. The results showed that 3D fabrics have superior performance and ballistic limits, yet they have increased areal density by 53%. Being part of composite material, the effect of the matrix type also showed an influence on the impact behavior. Khodadadi et al. [5] studied the influence of the matrix type of a 2D plain-woven aramid, including thermoset, low-density rubber, and high-density rubber. The study concluded that improved impact resistance is shown for aramid fibers impregnated with high-density rubber where the plies experience maximum stretch with no detachment.

Regardless of the superior impact resistance properties that aramid and UHMWP possess, many studies dealt with reinforcing these fibers by shear thickening fluids (STF) impregnation. The purpose of this impregnation is to decrease the delamination between the plies, increase the friction between the yarns, and enhance the impact resistance of fibrous materials. STF is a combination of metal oxide particles suspended in a liquid polymer. Once subjected to an impact, the viscosity increases, and the material shows solid like-behavior [6]. It was shown that STF impregnation leads to higher friction between the yarns and layers of Kevlar®, which can reduce the number of Kevlar® plies needed against ballistic impact by 50 %. Similarly, Mishra et al. [7] studied the influence of STF impregnation on unidirectional UD-UHMWP fibers through a ballistic impact test. They observed that UHMWP impregnated with STF had enhanced impact resistance compared to neat UHMWP.

Polymer foams are also an interesting material for protection purposes. Polymer foams gained extensive focus due to their capacity to absorb energy due to their microstructure. These materials are used in numerous protection systems, such as shock absorbers in modern automobiles, military helmets, and racecar road barriers [8]. Polymer foams are applied in

energy-absorbing structures, such as head impact safety components in cars. In addition to low-cost reinforcement for side impacts in modern automobiles [9]. Bicycle helmets are made essentially from Expanded Polystyrene or PU foams [8]. Military helmets are designed with high-density polymeric foams to protect against non-ballistic impacts and fragments [2]. Polymeric foams are advantageous for protection applications due to their high-energy absorption and lightweight.

Many studies show the potential of combining different materials to create hybrid structures. Hybridization techniques can be applied by combining different fibers to deliver a superior response compared to mono-material. Hazell et al. [10] studied the high-velocity impact response of hybrid composite reinforced with aramid plies. Plies of neat aramid are added to CFRP-based composites and showed the best weight-efficient energy absorption improvement compared to conventional composites. Grujicic et al. [11] examined numerically the influence of adding Kevlar<sup>®</sup> fiber-reinforced epoxy with carbon fiber-reinforced epoxy in different stacking sequences. They concluded that hybrid structures show higher ballistic performance than conventional materials and that the stacking sequence inside the hybrid structures strongly influences them. Bandaru et al. [12] investigated the impact behavior of hybrid composite structures combining aramid and basalt fibers. They observed that structures with intercalation between basalt and aramid show improved ballistic limits. The stacking sequence played a vital role in preventing delamination. Hybridization proved one of the most effective techniques to enhance energy absorption and increase weight efficacy.

Based on the literature, it is shown that aramid fibers are classical fibers used against impact due to their superior impact resistance, and polymer foams proved efficient in protection applications due to their high capacity to absorb energy. Hence, twining the advantages of polymer foams with aramid fibers can be a promising protective hybrid material. This work presents a hybridization between epoxy foams and aramid plies.

This study investigates the impact behavior of hybrid epoxy foam/aramid fiber structures by a high-velocity impact test. Several configurations for a fixed number of aramid plies (25 plies) are tested to study the influence of aramid plies location, level of impregnation, and epoxy foam

density on the protection capacity. The analysis of the results is based on the Back Face Signature (BFS).

## **III.2 Experimental procedure**

In the present study, structures combining aramid plies (neat or impregnated with epoxy resin) and epoxy foam are fabricated and impacted by a gas gun device at 180 m/s. A backing material (clay witness) is put behind the structures to measure the Back Face Signature after the impact. The BFS allows the measurement of the protective performance of the structures.

### **III.2.1 Base materials**

The aramid fibers fabrics used in this study have a four-harness satin architecture, an areal density of  $175 \text{ g/m}^2$ , and a thickness of 0.26 mm. The resin used to fabricate the impregnated plies is an Araldite<sup>®</sup> LY 5052 (resin)/Aradur<sup>®</sup> 5052 (hardener) epoxy. The fiber volume fraction is 37%.

The epoxy foams used are closed-cell foams with different expansion rates. Two different densities, 250 and  $400 \text{ kg/m}^3$ , are used. The epoxy foam has two components: epoxy resin (PB) and a hardener (DM03). The fabrication procedure of the epoxy foam is based on the recommendations of the supplier [13]. When the two components are mixed, they expand due to chemical foaming. To prepare the epoxy foam, a specific amount of liquid epoxy and hardener are added into a container and then mechanically frothed for 4 minutes. The liquid foam is poured inside a mold and set inside a hot air oven for 12 hours at  $40 \text{ }^\circ\text{C}$ . The properties of epoxy foams and aramid fabric, presented in Table III-1, are obtained with classic tensile and compression tests. Epoxy resin properties are obtained from the supplier data sheet [14].

Table III-1: Mechanical properties of the materials used in the fabrication of the hybrid structures

	Aramid	Epoxy resin	PB250	PB400
Density ( $\text{kg/m}^3$ )	-	1.17	250	400
Areal density ( $\text{g/m}^2$ )	175	-	-	-
Tensile modulus (MPa)	45000	3500	180	200
Tensile strength (MPa)	1700	49	2.81	5.2
Compression modulus (MPa)	-	-	72	150
Compressive yield strength (MPa)	-	-	2.9	8.2



### **III.2.2 Structure preparation**

The hybrid structure configurations aim to study the influence of the epoxy foam density, the location of aramid plies, and the impregnation of the aramid. The number of aramid plies is fixed to 25 to respect the range used in previous studies [2,6]. The aramid plies can be neat or impregnated with an epoxy resin.

Fourteen configurations, presented in Figure III-1, are studied. Structures A and B are made of neat and impregnated aramid plies, respectively; both are made without epoxy foam. Those structures serve as a reference. Structures C, E, G, and I are fabricated with 25 neat aramid plies and (PB250 or PB400 epoxy foam). The neat aramid plies are placed on either the impact face (C, & G) or the bottom face (E, & I). Structures with 25 impregnated aramid fibers (structures D, F, H, and J) and with (20/5) aramid plies distribution (structures K, L, M, and N) are also fabricated. In all cases, aramid plies are placed on the impact or bottom face. Similarly, those structures are fabricated with PB250 or PB400 as Epoxy foam.

Structures with neat aramid plies are fabricated simply by bonding 25 plies of aramid between each other and on blocks of foam using double-sided adhesive applied on the edges. A one-shot procedure is used to fabricate the structures with impregnated aramid plies. The aramid plies are impregnated by hand layup and put inside a mold. Then the liquid foam is poured on top. Afterward, the mold is closed and placed inside a hot air oven at 40°C for 12 hours. (For more fabrication details refer to Appendix A).

The mass and thickness of each structure are presented in Table III-2. On average, the foam thickness for the hybrid structures is between 44 and 49 mm. All structures have a dimension of 200 x 200 mm.

*Experimental study of high-velocity impact behavior of hybrid structures*

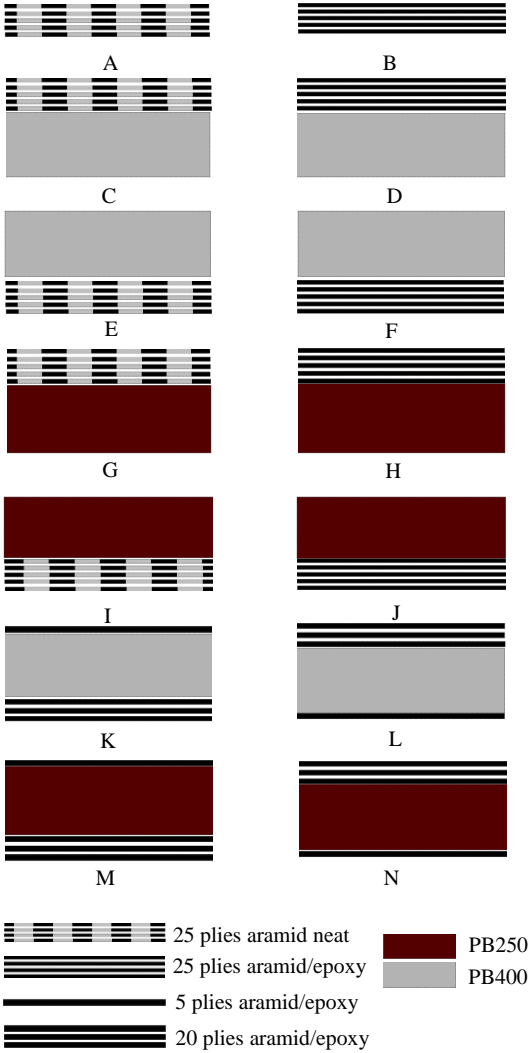


Figure III-1: Hybrid structures configuration with neat and impregnated aramid plies

Table III-2: Configurations of the fabricated hybrid structures

Structures	Description	Mass (g)	Thickness (mm)
A	25 aramid plies neat	200	11.5
B	25 aramid plies imp	378	7.6
C	25 plies neat -PB400	821	57
D	25 plies imp -PB400	888	49
E	PB400-25 plies neat	800	57
F	PB400-25 plies imp	900	52
G	25 plies neat -PB250	669	57
H	25 plies imp -PB250	789	50
I	PB250-25 plies neat	700	58
J	PB250-25 plies imp	801	50
K	5 imp plies-PB400-25 imp plies	902	48
L	20 imp plies-PB400-5 imp plies	885	48
M	5 imp plies-PB250-20 imp plies	762	49
N	20 imp plies-PB250-5 imp plies	770	49

imp: impregnated with epoxy resin

### III.2.3 Backing material

A backing material, also known as clay witness, is placed behind the structures during the high-velocity impact test to measure the Back Face Signature after each impact test. This technique is usually implemented when testing body armor materials [15]. The present work adopts the same approach to measure the protection capacity of the hybrid material by analyzing the indentation left on the back face.

The clay witness (plastiline) used has a soft firmness level, and the density is  $1525 \text{ kg/m}^3$  [16].

The consistency of the clay must be validated first based on the NIJ Standard 0101.06 through a drop weight test [15] (Appendix B). The boundary conditions and temperature are the same for this validation test and the impact test presented in section 2.4.

The clay material is confined inside a wooden box having a dimension of  $300 \times 300 \times 60 \text{ mm}^3$ . The clay is heated at  $40^\circ\text{C}$  for three hours to reach an approximately homogenous temperature

### *Experimental study of high-velocity impact behavior of hybrid structures*

between 38 and 40°C, measured in different locations. A drop weight test is performed. A spherical shape impactor of 61 mm diameter with a weight of 1 kg is dropped from a height of 2 m (Figure III-2.a). A high-speed camera is placed to measure the velocity of the impactor just before the impact occurs. The maximum indentation inside the clay is measured using a displacement sensor after the impact (Figure III-2.b).

The indentation left on the clay after impact must be between 16 and 22mm according to the NIJ standard to validate the consistency of the clay. The maximum displacement measured is 21mm, which is acceptable.

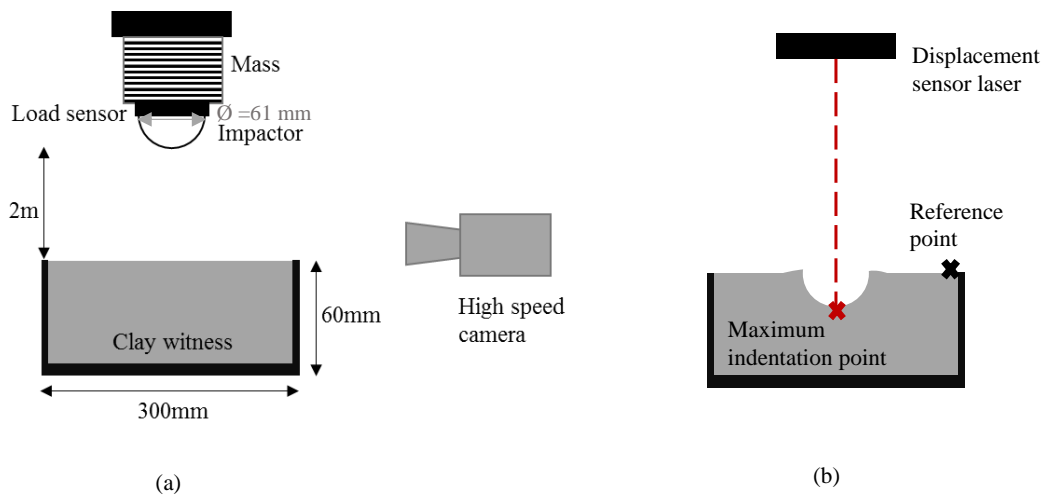


Figure III-2: (a) Drop-weight test validation, (b) post-impact Back Face Signature measurements of the clay witness.

#### **III.2.4 High-velocity impact test**

The performance of the hybrid structures is studied through high-velocity impact tests. A gas gun of 60 mm diameter is used in the present study. The projectile is a steel sphere having a diameter of 14 mm and a weight of 11 g. The gas gun impact pressure is set to 7.2 bars to reach an impact velocity of 180 m/s leading to impact energy of 227 kJ.

Figure III-3.a describes the test device. Elastic bands are used to place the specimen against the backing material (Figure III-3.b). The backing material is confined in a wooden box and heated to a temperature between 38 and 40°C.

## *Experimental study of high-velocity impact behavior of hybrid structures*

These high-velocity impact test outputs are the BFS, the permanent indentation in the specimen, and the damage morphology left on the structures. The BFS is measured using the methodology shown in Figure III-2.b. The permanent indentation is measured using a displacement sensor; by taking a reference point at the corner of the structure, and the second point is taken on the impact area underneath the projectile. The morphology of damage and statement of the crack under the impactor is assessed through visual inspection. Those parameters are used to evaluate and compare the impact behavior of the hybrid structures.

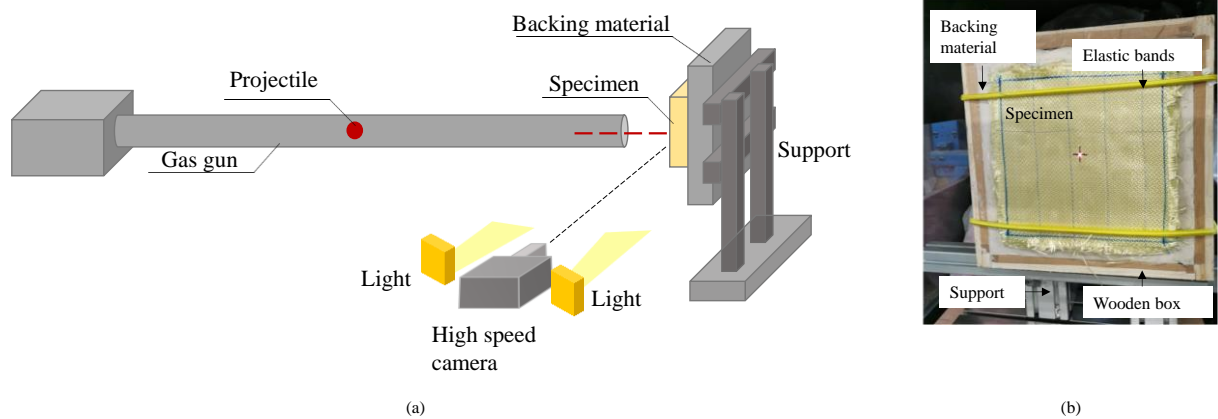


Figure III-3: (a) Graphical representation of the high-velocity impact setup, (b) structure fixation to the support system.

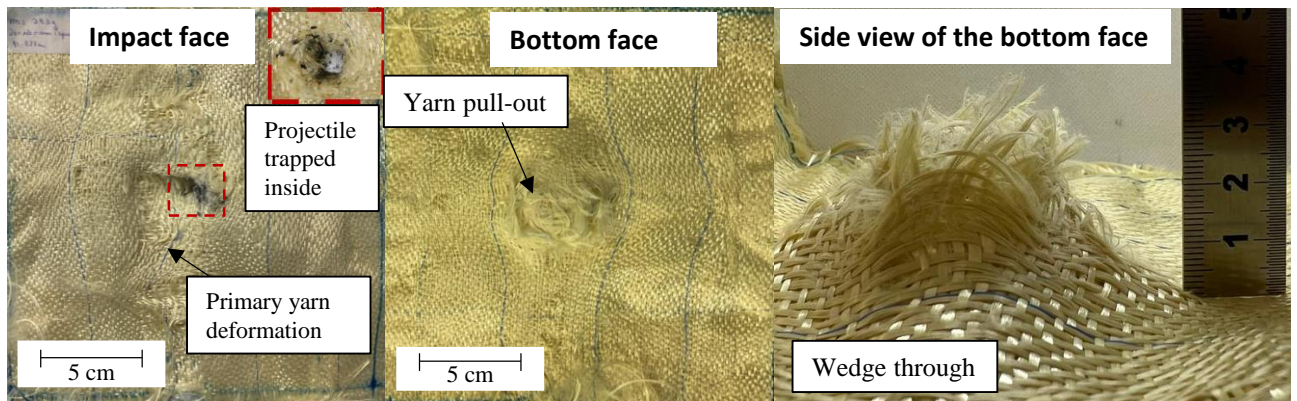
## **III.3 Results and discussion**

### **III.3.1 Morphology of damage**

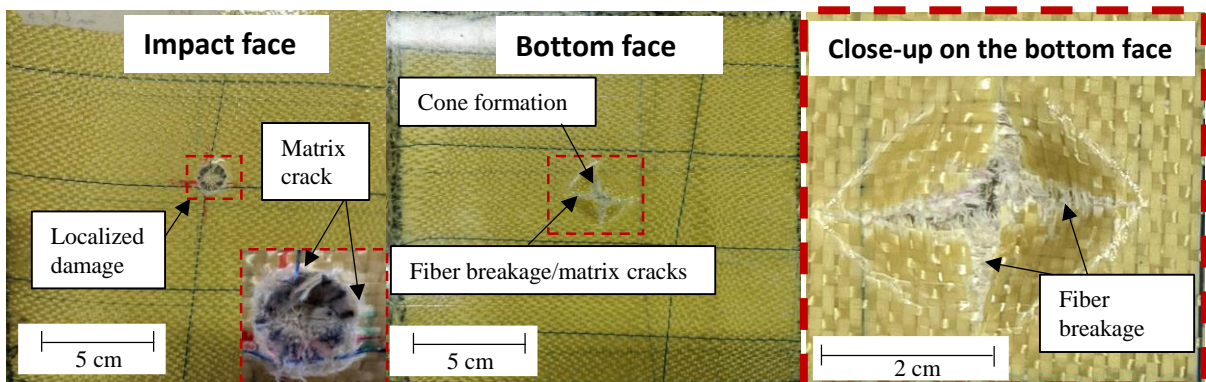
The morphology of damage to the structures is evaluated through visual inspection. Figure III-4 shows the damage mode of neat aramid plies (structure A) and impregnated aramid plies (structure B). Figure III-4.a shows that the whole structure responds against the impact. The deformation is extended from the impact region towards the edges of the structure. The damage is mainly represented by the deformation of the primary yarns underneath the projectile. Khodadadi et al. [5] cite this mode failure for neat aramid plies when subjected to high-velocity impact. The back face of the neat aramid structure shows yarn pull-outs, and the projectile creates a wedge-through behavior. The projectile is trapped inside the aramid plies. As for the impregnated structure (structure B), the damage is highly localized (Figure III-4. b). The epoxy

*Experimental study of high-velocity impact behavior of hybrid structures*

resin fails around the impactor edges due to its high brittleness. Matrix crack is the first mode of failure that appears in composites when subjected to impact. It is a classic result (Abrate [17]). The damage on the back face of structure B is represented by cone formation and failure of the fibers. The close-up on the bottom face impact region shows a cross-shape resulting from fiber breakage.



(a)



(b)

Figure III-4: Post impact inspection of (a) neat aramid plies and (b) impregnated aramid plies

Figure III-5, Figure III-6, and Figure III-7 show the morphology of damage to the hybrid structures. All the hybrid structures stop the impactor.

The location of the aramid plies significantly influences the response of the structures. In all the structures having the epoxy foam as impact face, whether it is PB250 (structures I and J) or PB400 (structures E and F), the projectile perforates the foam layer (~ 44mm) fully. The damage inside the epoxy foam is highly localized (Figure III-5. c, d, and Figure III-6. c, d). The foam underneath the impactor could not resist the impact, and it failed due to high tensile and shear

stresses. The impactor creates a clear path while crushing the foam from the impact face until reaching the aramid plies at the bottom of the structures. The diameter of this path is around 16 mm for most structures with foam as the impact face, similar to the diameter of the projectile.

Structures with 25 aramid plies (neat and impregnated) as impact face, whether backed with PB250 (structure G and H) or PB400 (structure C and D), do not show complete perforation of the aramid plies. The behavior of impregnated aramid and neat aramid as impact face is similar to structures B and A, respectively. The mode of failure of epoxy foam when located at the back (structure C, Figure III-5. a) is different than when located at the impact face (structure E, Figure III-5. c). To analyze the damage in the foam, the aramid plies of structures C and G are removed, and the damage is evaluated (Figure III-8). The epoxy foam (PB400) of structure C (Figure III-8. a) fails due to tensile and shear fracture, yet the damage is not as localized as in structure E. The damage diameter in the foam is increased by 51% since the aramid plies increase the contact area between the impactor and the foam resulting in an extended response of foam crushing. The same analysis applies when comparing structures G and I (Figure III-6. a, c).

Results illustrated in Figure III-5 and Figure III-6 show that the aramid plies placed as impact face are not perforated; they protect the epoxy foam from complete perforation.

Figure III-7 shows structures with 20+5 impregnated aramid plies distribution, five plies as impact face and 20 plies as the back face, and vice versa. The projectile perforates the aramid plies located as impact face, whether it is 5 or 20 plies. Structure N (Figure III-7.d), having 20 plies as impact face and PB250 as epoxy foam, shows slight damage on the back face and a crack length of 10.8 mm. However, structure M (Figure III-7. c) with PB250 and five plies as impact face shows a cross-shaped fiber breakage on the back face. The damage diameter is 23 mm. This means that the 20 plies as impact face reduces the velocity of the projectile and decreases the damage on the back face by 53%, compared to structures with five plies as impact face. Moreover, structure J, where 25 plies are placed as the back face, shows a cross-shaped fiber breakage of 29 mm. Placing the same number of aramid plies but with different distributions can improve the back face damage by up to 63%.

### *Experimental study of high-velocity impact behavior of hybrid structures*

Structure K (Figure III-7. a), with PB400 and five plies as impact face, shows no damage on the back face, similarly to structure L. On the top face of structure L, the foam arrests the projectile after perforating the 20 aramid plies (Figure III-7. b).

The influence of aramid plies impregnation is shown when comparing structure G (Figure III-6.a) and H (Figure III-6.b). The neat aramid as the impact face of structure G shows an extended deformation from the impact area towards the extremities of the structures. The impregnated aramid plies in structure H show localized response, and matrix cracks are shown on the edges around the impact area. The same analysis applies to structures with PB400 (Structure C (Figure III-5.a) and structure D (Figure III-5.b)).

Structures F (Figure III-5.d) and E (Figure III-5.c), having PB400 as impact face with impregnated and neat aramid, respectively, are compared. The damage left on the bottom face is compared for both structures. Neat aramid plies show deformation and pull-outs in the yarn underneath the impact area and global deformation on the back face of the structure. Impregnated aramid plies show minor matrix cracks on the top and minor deformation on the back face. This is due to the presence of epoxy resin that controls and prevents the deformation of the fibers. The same analysis applies to structures with PB250 (Structure J (Figure III-6.d) and structure I (Figure III-6.c)).

The influence of the epoxy foam density can be seen when structures F (Figure III-5.d) and J (Figure III-6.d) are compared. For Structure J with PB250 as the impact face, the projectile fully perforates the epoxy foam layer and induces damage to the impregnated aramid plies on the bottom (matrix crack, fiber failure, and a slight cone formation). On the contrary, structure F, having PB400 as the impact face, does not show significant damage on the bottom face of the aramid plies. PB400 having a higher density limits the damage induced on the back face of the aramid plies.

This is also observed when comparing structures C (Figure III-8. a) and G (Figure III-8. a). The damage left on PB250 (structures G) is around 51 mm with a depth of 24 mm, whereas the damage left on PB400 (structures G) is around 31mm with a depth of 13 mm. The impact damage depth left on PB250 is 46% more significant than that left on PB400. This means that PB400 can reduce the velocity of the impactor and resist the impact more effectively than



*Experimental study of high-velocity impact behavior of hybrid structures*

PB250. As for the mechanisms of damage, it is shown that PB250 leads to more material crushing than PB400. To further compare the foam density influence under the impact, structures K (Figure III-7.a) and M (Figure III-7.c) are studied. Both have the same configuration, structure K with PB400 shows no damage on the back face, yet structure M shows fiber breakage and cone formation (damage length 23 mm). The comparison between structures L and N leads to the same results. PB400 shows a higher ability to stop the projectile, leading to minor damage on the aramid plies at the back. This density influence is extensively studied in the literature. The impact behavior and the mechanical properties increase as the foam density increases [8,18].

The morphology of damage is affected by the location of the aramid plies, the foam density, and the aramid plies impregnation.

Further assessment of the performance of the hybrid structures is investigated in the next section.

*Experimental study of high-velocity impact behavior of hybrid structures*

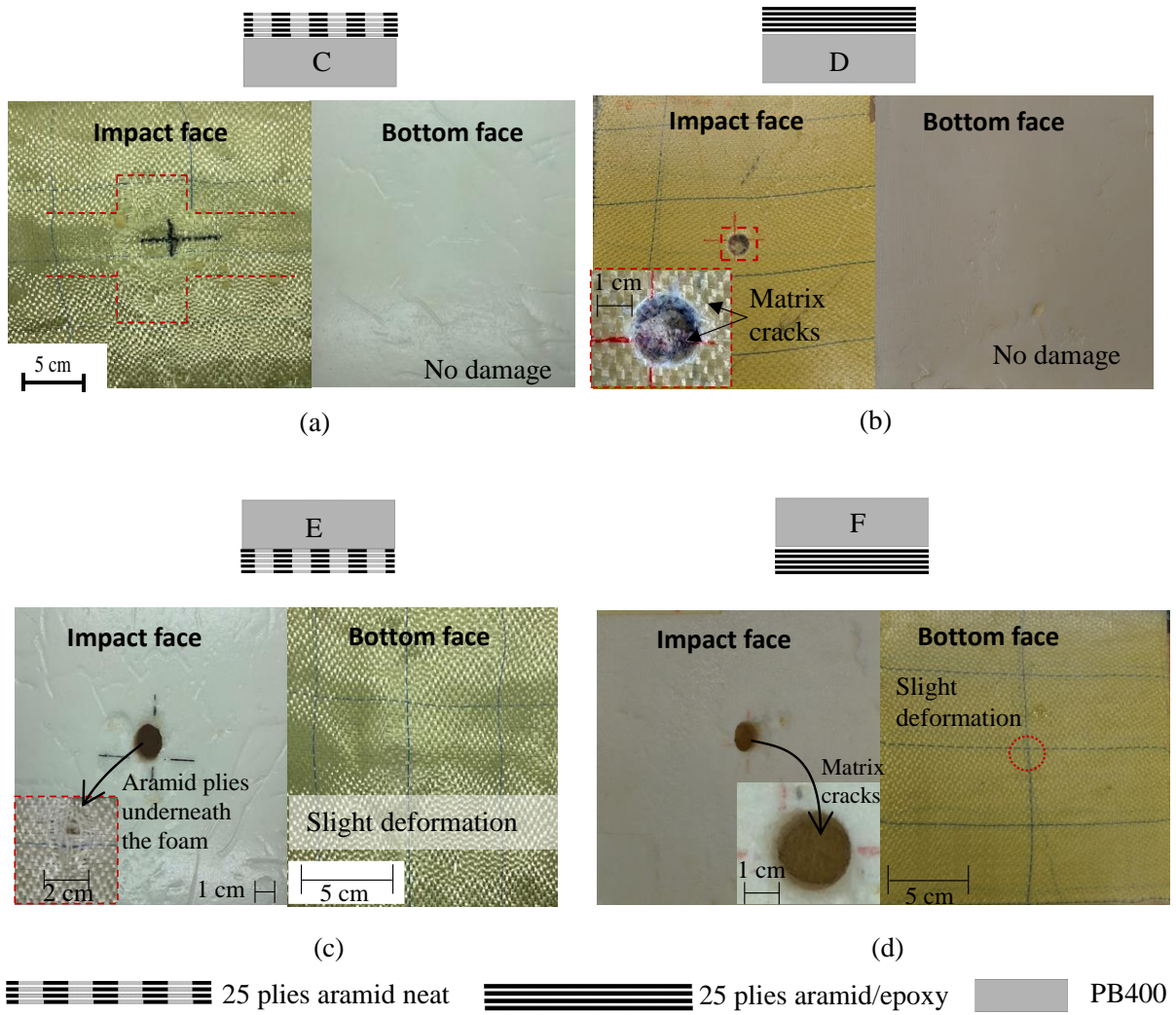


Figure III-5: Post-impact inspection of the hybrid structures with 25 plies (impregnated and neat) and PB400

*Experimental study of high-velocity impact behavior of hybrid structures*

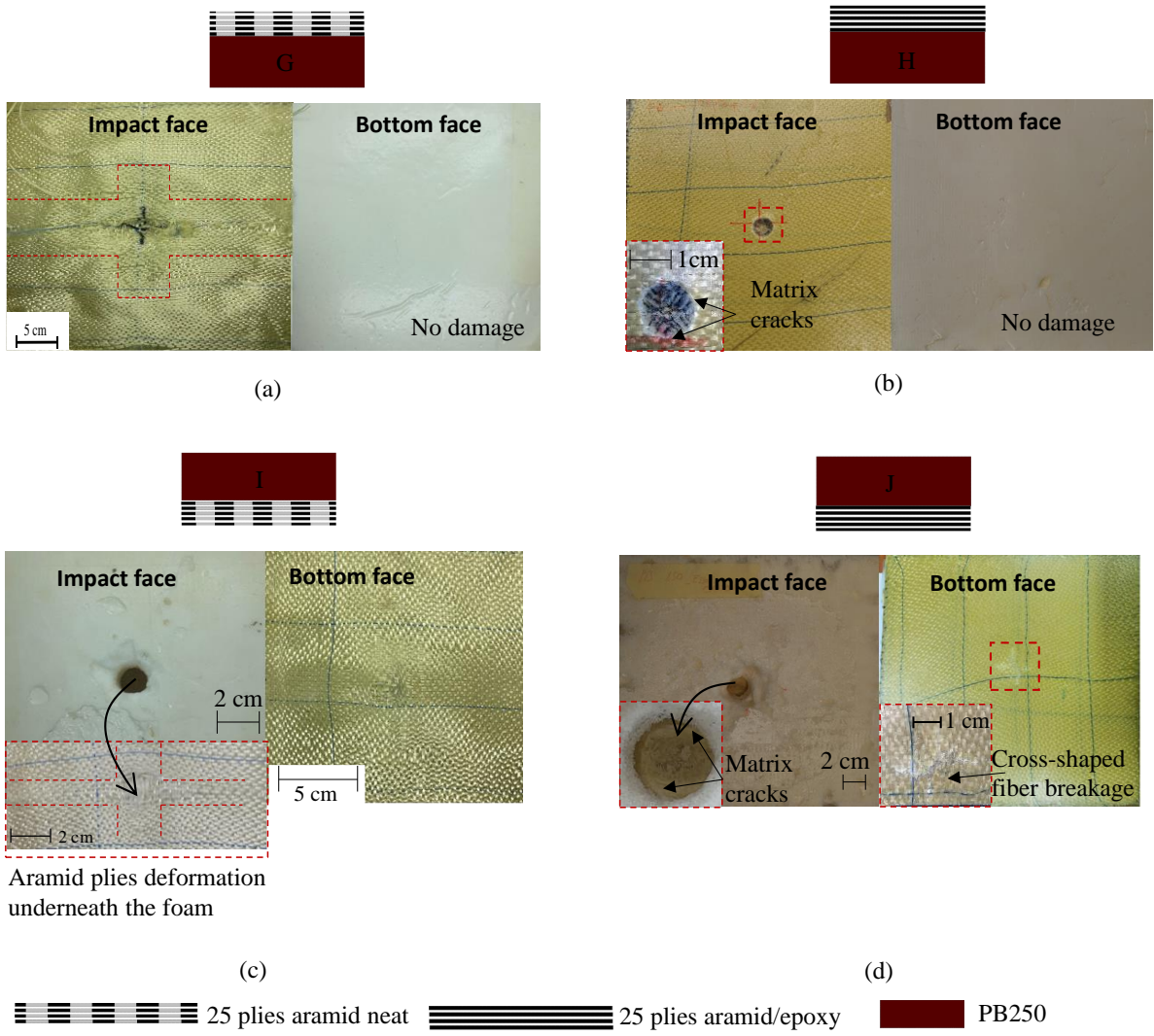


Figure III-6: Post-impact inspection of the hybrid structures with 25 plies (impregnated and neat) and PB250

*Experimental study of high-velocity impact behavior of hybrid structures*

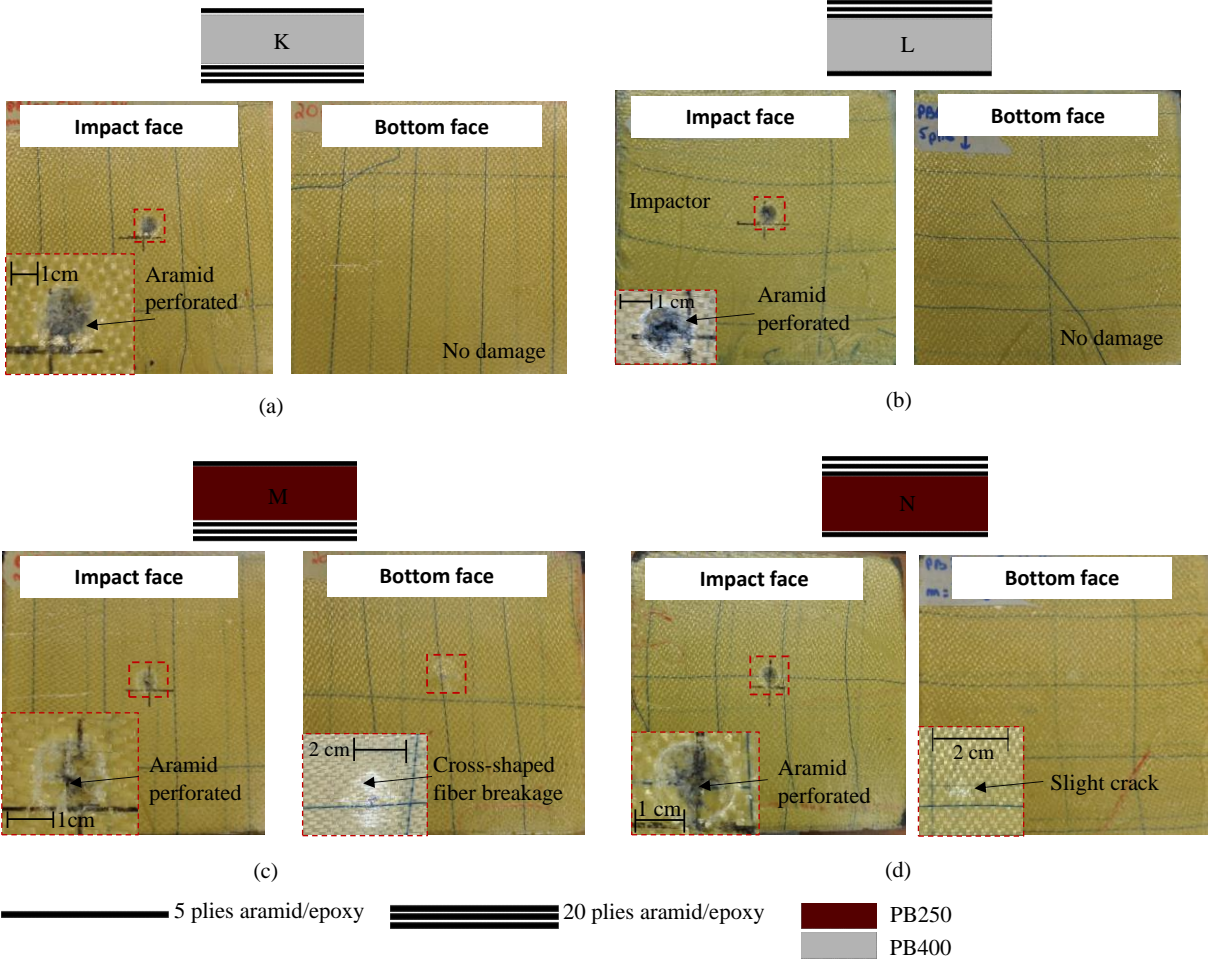


Figure III-7: Post impact inspection of the hybrid structures with 25 impregnated plies distributed with PB250, and PB400

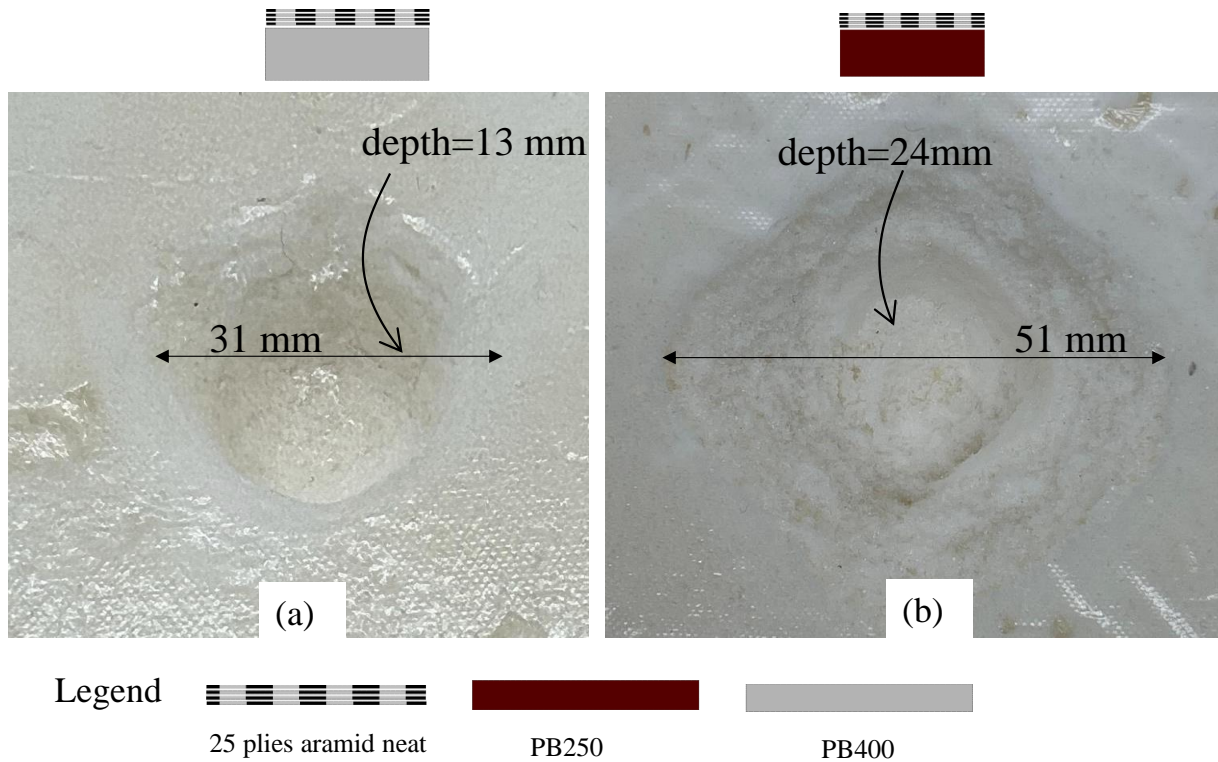


Figure III-8: Damage mechanisms of structures with neat aramid as impact face, (a) for PB400, and (b) for PB250

### **III.3.2 Back Face Signature and indentation.**

After each impact test, the BFS left on the backing material and the permanent indentation is measured. These parameters describe the capacity of protection that the structures have when subjected to impact. The results of the impact test are summarized in Table III-3.

Table III-3: Indentation and Back Face Signature of the hybrid structures



*Experimental study of high-velocity impact behavior of hybrid structures*

	Structures	Impact velocity (m/s)	Sample thickness (mm)	Sample mass (g)	Permanent indentation (mm)	Back Face Signature (mm)
Aramid	A	178	11.5	200	34	34
	B	183	8.3	451	4.35	8.7
PB400+aramid	C	182	57	821	13.43	0
	D	175	49	888	8.9	0
	E	170	57	800	46	13
	F	180	52	900	37.8	1.1
	K	179	48	902	35.73	0.4
	L	176	48	885	22.47	0
PB250+aramid	G	185	57	669	24.36	0
	H	175	50	789	8.7	0
	I	177	58	700	57	14
	J	186	50	801	40.62	5.37
	M	169	49	762	39.92	7.8
	N	172	49	770	41.8	1.8

For the non-hybrid structures, the 25-impregnated aramid plies show less BFS and permanent indentation than neat ones by 74% and 87%, respectively.

The permanent indentation and BFS of the hybrid structures are presented in Figure III-9, Figure III-10, Figure III-11, and Figure III-12.

Results show that hybrid structures with aramid plies as impact face (structures C, D, G, and H) have 100% less BFS than conventional composite laminates (impregnated, structure B and neat, structure A), which means a BFS equal to zero. However, the hybrid structures have a 50% higher mass than the samples without foam.

Figure III-9 shows the permanent indentation and the BFS of the structures with PB250. The influence of aramid plies position is discussed at first for structure with PB250. Structure H with 25 impregnated plies as impact face shows zero BFS since the aramid plies stop the impactor. However, when the aramid plies are placed at the back face (structure J), the BFS is increased to 5.37 mm. The permanent indentation reveals the complete perforation of the epoxy foam, showing a 366% increase compared to structure H. Structure G and I with neat aramid plies show similar results, where placing the aramid plies as impact face prevents the BFS and decreases the permanent indentation by 57%. The comparison between structures J, M, and N reflects the influence of aramid plies position. The permanent indentation of the three structures shows that the projectile perforates the PB250 foam layer. Adding 5 or 20 impregnated aramid plies as impact face is not enough to prevent the projectile penetration inside the foam. Structure M with five aramid plies as impact face and 20 as back face shows a 38% increase in BFS

*Experimental study of high-velocity impact behavior of hybrid structures*

compared to structure J. Structure N with 20 plies as impact face decreases the BFS by 76% compared to structure M. This means that structure N can reduce the damage induced on the back face more effectively than structures J and M. The 20 aramid plies as the impact face reduce the velocity of the projectile. The latter is then stopped by the five bottom plies preventing the full perforation of the structure.

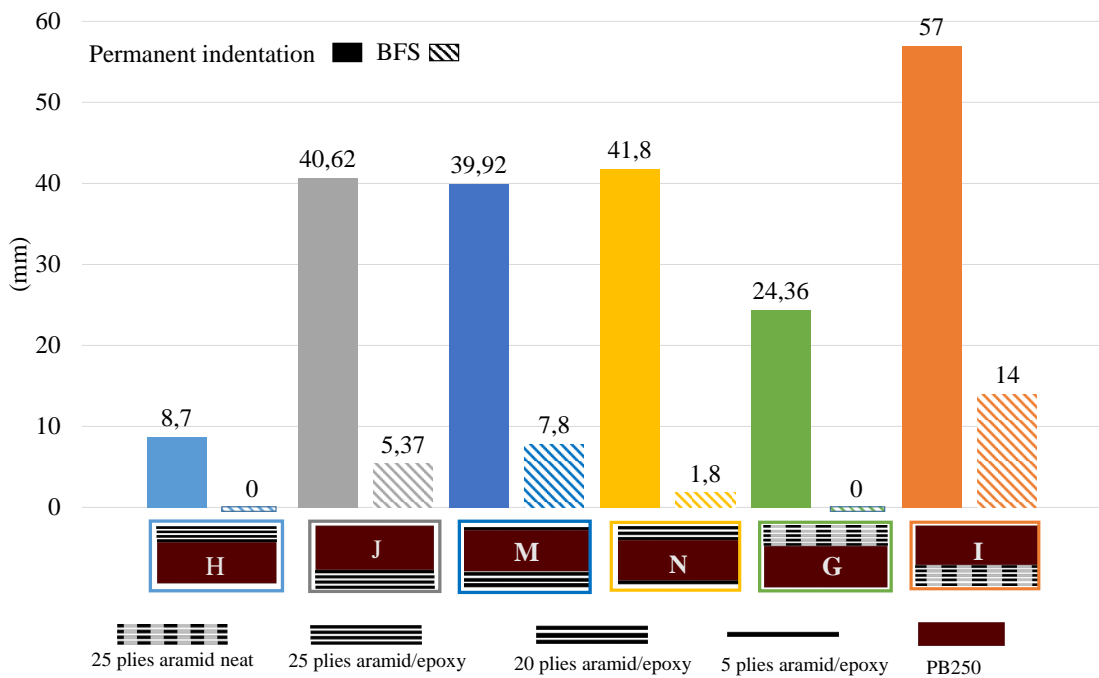


Figure III-9: Permanent indentation and Back Face Signature of structures with PB250

The influence of aramid plies location is also seen when comparing structures with PB400 (Figure III-10). Structures C and E with 25 neat aramid plies and structures D and F with 25 impregnated plies show similar results regarding the aramid position. The projectile did not perforate the 25 aramid plies (neat or impregnated), leading to zero damage on the back face (BFS=0 mm). However, when the aramid plies are located at the back (structure E and F), the projectile perforates the whole foam layer, increasing the permanent indentation of 324% for structure F and 242% for structure E. This induces a BFS of 1.1 mm and 13 mm for structures F and E, respectively. For structures L and K, where the 25 impregnated plies are distributed, the structure with 20 plies as impact face (structure L) reduced the permanent indentation by 37% and the BFS from 0.4 to zero compared to the structure with five plies as impact face. In both cases, the permanent indentation shows that the projectile did not perforate the whole thickness of the PB400. Comparing structures F and K, adding five plies as impact face and 20

*Experimental study of high-velocity impact behavior of hybrid structures*

as back face instead of a stack of 25 plies on the back improved the BFS by 63%. This means that in the case of PB400, both configurations with 20/5 plies distribution show enhanced impact behavior compared to 25 plies at the back.

The behavior of the structure, when subjected to impact, is significantly dependent on the aramid plies position. Twenty-five aramid plies can stop the projectile, and the cone formed on the back face or the wedge-through is contained inside the thickness of the epoxy foam leading to zero BFS.

The impregnation of the aramid plies directly influences the amount of deformation seen on the back face and the dent depth left by the impactor. Figure III-9 shows structures H and G, both having aramid plies as impact faces. The impregnated aramid plies (structure H) show 64% less permanent indentation than the neat ones (structure G). The neat aramid plies of structure I, placed at the bottom, increased the BFS by 160% compared to impregnated aramid (structure J). Likewise, Figure III-10 shows that 25 impregnated plies of structure F reduced the BFS by 91% compared to neat aramid (structure E). This means that the impregnated aramid plies can reduce the BFS by limiting the deformation of the aramid plies on the back. An additional mass results from the impregnation, a maximum weight increase of 17 % is shown between structures G and H.

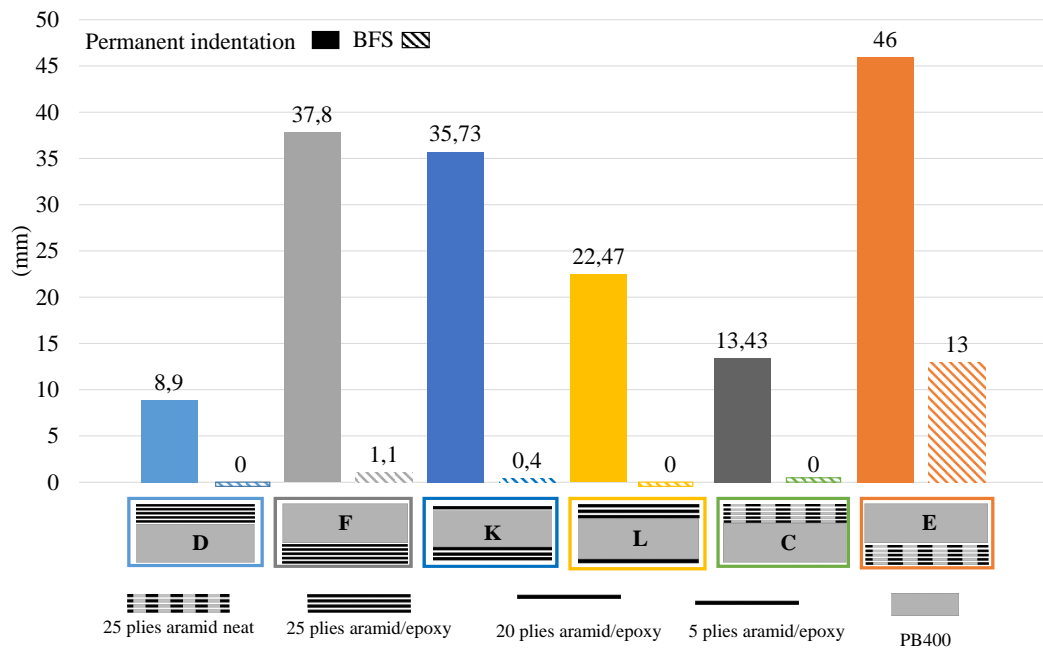


Figure III-10: Permanent indentation and Back Face Signature of structures with PB400



### *Experimental study of high-velocity impact behavior of hybrid structures*

The influence of the epoxy foam density is observed in Figure III-11 and Figure III-12.

Structures C and G (Figure III-11) have the same configurations, neat aramid plies as impact faces but with PB400 and PB250, respectively. Structure C show 45% less permanent indentation than structure G. Structures F and J have the same configuration; 25 impregnated aramid plies are located at the back face, with PB400 and PB250 as impact faces, respectively. PB400 as impact face shows 80% less BFS and 7% less permanent indentation than the structure with PB250 as impact face.

Figure III-12 shows the density influence of the structure with 20/5 impregnated aramid plies distribution. Structure M and K have the same configurations, yet structure M with PB400 show 94% less BFS and 11% less permanent indentation compared to structure K with PB250. Structures with 20 plies as impact face show that structures with PB400 (structure L) reduced the BFS from 1.8 mm to zero and reduced the permanent indentation by 46%. The projectile in the case of structure L is stopped after perforating the aramid plies, and its penetration in the epoxy foam is minimized; this is also seen in Figure III-7.b. It shows that the behavior of PB400 is more efficient than PB250 in terms of BFS and permanent indentation. However, this amelioration results in a maximum increase of 23 % in weight (comparing structures C and G).

These results are compatible with the ones seen in section 3.1 and with the literature regarding the density influence of the mechanical properties of foams.

Experimental study of high-velocity impact behavior of hybrid structures

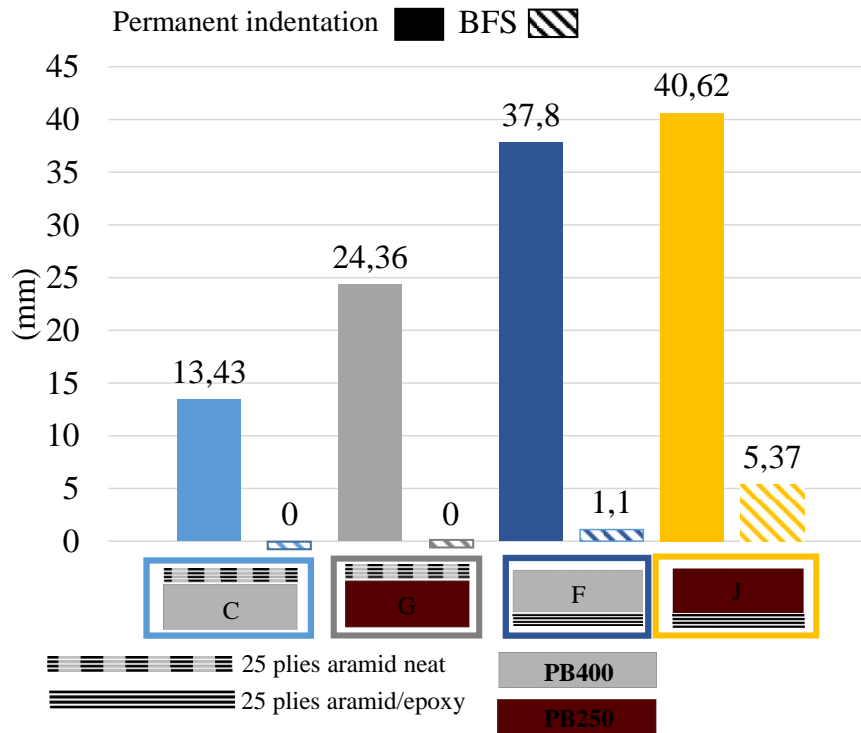


Figure III-11: Indentation and BFS of same configuration structures with 25 aramid plies with different foam densities

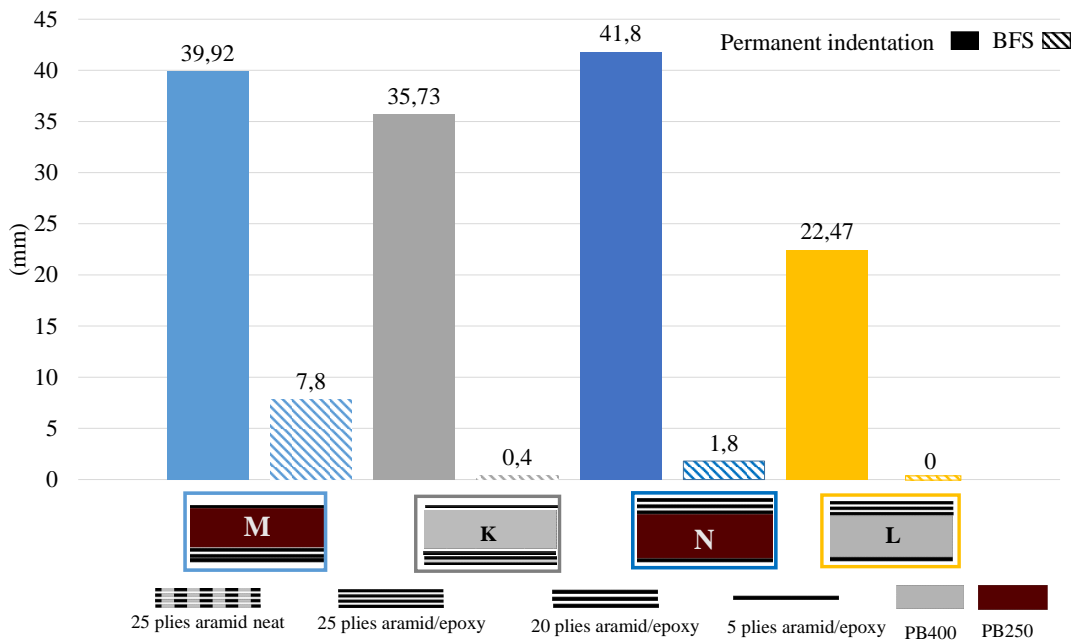


Figure III-12: Indentation and BFS of same configuration structures with 20/5 aramid plies with different foam densities

*Experimental study of high-velocity impact behavior of hybrid structures*

The studied hybrid materials have different masses since the configurations include different foam densities and different impregnation levels for aramid plies. To compare the protection efficiency of the hybrid structures per unit mass, a ratio *margin/mass* is calculated, Figure III-13. The margin is the thickness left undamaged in the structure after impact; it is calculated according to Eq. 1. As the ratio increases, the specific protection capacity of the structure and ability to stop the impactor per unit mass increases. The results are presented in Figure III-14.

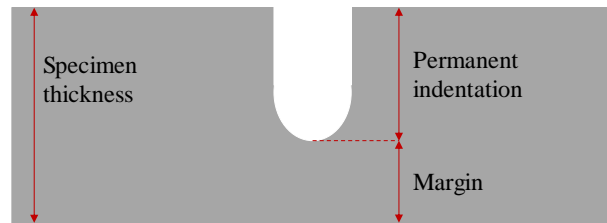


Figure III-13: Schematic of the margin

$$ratio = \frac{(permanent\ indentation - specimen\ thickness)}{mass} = \frac{margin}{mass} \text{ (mm/g)} \quad (1)$$

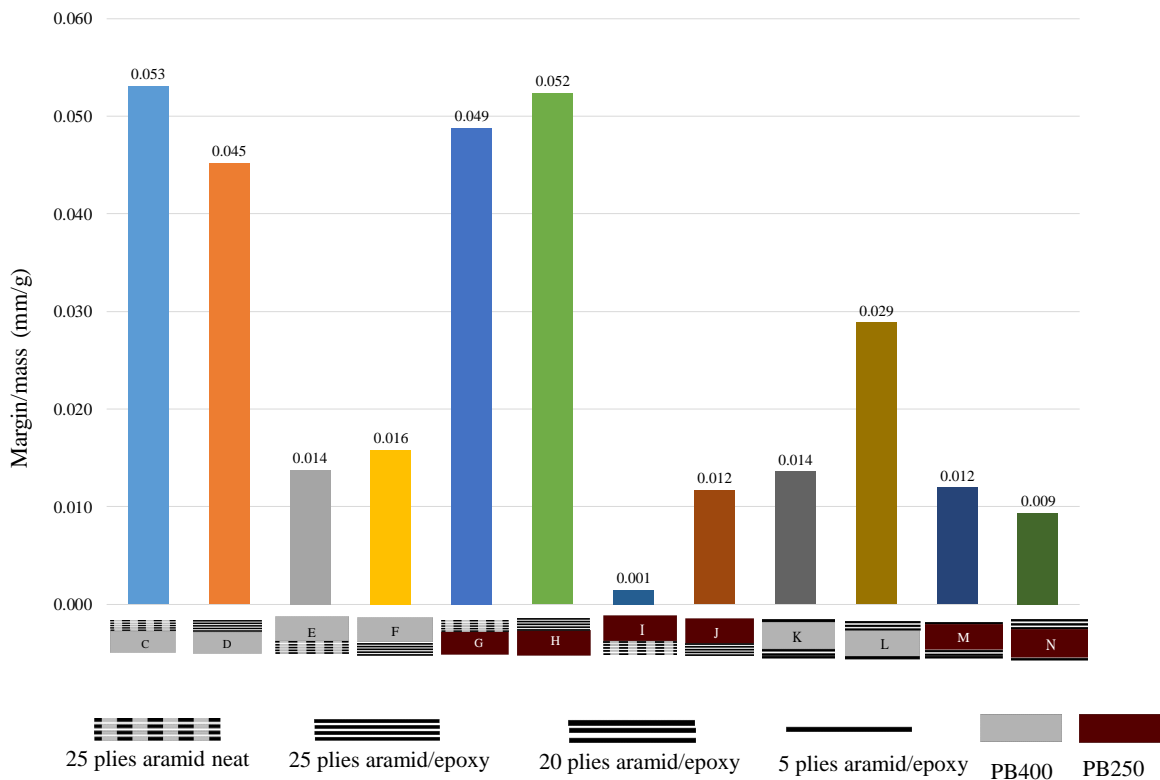


Figure III-14: Margin/mass ratio for hybrid structures

### *Experimental study of high-velocity impact behavior of hybrid structures*

The highest ratios are achieved with structures having aramid plies as impact faces. Structures C with neat aramid as impact face backed with PB400 show an increased ratio of 17 % compared to structures D, which has impregnated aramid as impact face. However, structures with PB250, having aramid plies as impact face, the impregnated plies (structure H) show a higher ratio of 6% compared to neat aramid (structure G). Structure C and structure H have a similar ratio, meaning they can achieve the same level of protection.

Among the structures with epoxy foam as impact face, structure F with PB400 and 25 impregnated aramid plies show a higher ratio. Neat aramid plies as the bottom face, compared to impregnated ones, show a 13% decrease in the ratio in the case of PB400 and 91% in the case of PB250. This is due to higher permanent indentation seen in neat aramid plies.

The 20/5 plies distribution of impregnated aramid did not significantly improve the ratio *margin/mass* compared to structures with 25 aramid plies as impact face. Structures with the lowest density (structures M and N) show poor specific protection capacity, and no improvement is shown compared to structure J. This is due to the lack of resistance of the foam against the impactor after perforating the aramid plies. Whereas structure L with PB400 and 20 plies as impact face improves the ratio by 81% compared to a structure with 25 plies as the back face (structure F and E). The capacity of protection of structure L is still 44% and 35 % lower compared to structures H and D, respectively. The above analysis indicates that 25 aramid plies located as the impact face are necessary to reach the highest level of protection. A structure with 25 neat aramid plies backed with PB400 has the same level of protection as 25 impregnated aramid plies backed with PB250.

Those structures can eliminate the BFS seen in structures without epoxy foam. This BFS improvement comes with a 50 % weight increase. Since the impactor does not perforate the 25 plies, there is a potential to reduce the thickness of the foam placed on the back, resulting in a weight decrease while conserving zero BFS. The parameters studied in this work offer a solid ground for weight and design optimization of the hybrid structures.

### **III.4 Conclusion**

The impact behavior of the hybrid epoxy foam/aramid fibers structures is studied when subjected to high-velocity impact. This work investigates the ability of this hybrid material to

### *Experimental study of high-velocity impact behavior of hybrid structures*

preserve the integrity of the protected structure. The protection capacity is studied for several configurations by comparing the dent left on the backing material (BFS), permanent indentation, and the post-impact visual inspection of the structures. This work evaluation gave the following outcomes:

- Compared to neat aramid, impregnated plies reduce BFS by 74% when impacted at a velocity of 180m/s.
- The location of aramid plies plays an essential role in the performance of hybrid structures. When it is located on the impact face, it eliminates the BFS (reduce it to zero) compared to structures without epoxy foam, yet with a 50% increase in mass.
- The layer of epoxy foam as impact face, whether PB250 or PB400, fails to withstand the impact of the projectile, and it is only at the aramid level that the projectile is stopped.
- The closed-cell epoxy foam PB400 proved to have a higher protection capacity. It shows an 80% improvement over PB250 concerning the BFS. PB400 as impact face decreases the velocity of the impactor more efficiently than PB250, leaving minor damage on the aramid plies.
- Since weight is essential in evaluating protection materials, the ability to stop the projectile per unit mass for hybrid material is compared. It is shown that a structure with 25 impregnated plies as the top face backed with 44 mm of PB250 epoxy foam has the optimal ratio compared to the other hybrid structures.

Based on the investigations done in this study, the hybrid structures with impregnated aramid plies as impact faces prove to be a potential protective material. The proposed material can be used in protection applications where thickness is not a constraint. Several amelioration factors can be outlined, such as decreasing the thickness of the epoxy layer, distributing the aramid plies in the core of the structures, and using multiple foam densities inside a single structure to improve the effectiveness-to-weight ratio.

## **References**

- [1] Abtew MA, Boussu F, Bruniaux P, et al. Ballistic impact mechanisms – A review on textiles and fibre-reinforced composites impact responses. *Compos Struct.* 2019;223:110966.
- [2] Lightweight Ballistic Composites | ScienceDirect [Internet]. [cited 2022 Jun 9]. Available from: <https://www.sciencedirect.com/book/9780081004067/lightweight-ballistic-composites>.
- [3] Lee YS, Wetzel ED, Wagner NJ. The ballistic impact characteristics of Kevlar® woven fabrics impregnated with a colloidal shear thickening fluid. *J Mater Sci.* 2003;38:2825–2833.
- [4] Bandaru AK, Chavan VV, Ahmad S, et al. Ballistic impact response of Kevlar® reinforced thermoplastic composite armors. *Int J Impact Eng.* 2016;89:1–13.
- [5] Khodadadi A, Liaghat G, Bahramian AR, et al. High velocity impact behavior of Kevlar/rubber and Kevlar/epoxy composites: A comparative study. *Compos Struct.* 2019;216:159–167.
- [6] Haro EE, Szpunar JA, Odeshi AG. Ballistic impact response of laminated hybrid materials made of 5086-H32 aluminum alloy, epoxy and Kevlar® fabrics impregnated with shear thickening fluid. *Compos Part Appl Sci Manuf.* 2016;87:54–65.
- [7] Mishra VD, Mishra A, Singh A, et al. Ballistic impact performance of UHMWP fabric impregnated with shear thickening fluid nanocomposite. *Compos Struct.* 2022;281:114991.
- [8] Mills NJ. *Polymer foams handbook: engineering and biomechanics applications and design guide.* 1. ed. Amsterdam Heidelberg: Elsevier; 2007.
- [9] Hazell PJ, Appleby-Thomas G. A study on the energy dissipation of several different CFRP-based targets completely penetrated by a high velocity projectile. *Compos Struct.* 2009;91:103–109.
- [10] Grujicic M, Pandurangan B, Koudela KL, et al. A computational analysis of the ballistic performance of light-weight hybrid composite armors. *Appl Surf Sci.* 2006;253:730–745.

- [11] Bandaru AK, Ahmad S, Bhatnagar N. Ballistic performance of hybrid thermoplastic composite armors reinforced with Kevlar and basalt fabrics. *Compos Part Appl Sci Manuf*. 2017;97:151–165.
- [12] Tirillò J, Ferrante L, Sarasini F, et al. High velocity impact behaviour of hybrid basalt-carbon/epoxy composites. *Compos Struct*. 2017;168:305–312.
- [13] Okhawilai M, Hiziroglu S, Rimdusit S. Measurement of ballistic impact performance of fiber reinforced polybenzoxazine/polyurethane composites. *Measurement*. 2018;130:198–210.
- [14] product-pdf\_fr19.pdf [Internet]. [cited 2022 Jun 22]. Available from: [http://sicomin.com/datasheets/product-pdf\\_fr19.pdf](http://sicomin.com/datasheets/product-pdf_fr19.pdf).
- [15] NIJ Standard 0101.06 Ballistic Resistance of Body Armor - [PDF Document] [Internet]. [fdocuments.nl](https://fdocuments.nl). [cited 2022 Jun 9]. Available from: <https://fdocuments.nl/document/nij-standard-010106-ballistic-resistance-of-body-armor.html>.
- [16] Tubes 1kg et 5kg [Internet]. Plastiline. [cited 2022 Jun 14]. Available from: <https://www.plastiline.fr/tubes-1kg-et-5kg/>.
- [17] Abrate S. *Impact Engineering of Composite Structures*. Springer Science & Business Media; 2011.
- [18] On the effect of relative density on the crushing and energy absorption of open-cell foams under impact | Elsevier Enhanced Reader [Internet]. [cited 2022 Jun 23]. Available from: <https://reader.elsevier.com/reader/sd/pii/S0734743X15000536?token=8DF830B109368D28B57591ABE98E82CBDB8F71541EAC8406EBB6B19C7660B2AFA5AF94937BFAA8663AB548D6AA430EF7&originRegion=eu-west-1&originCreation=20220623135831>.







---

# **Chapter IV. Numerical Modeling of Epoxy Foam/Aramid Fabric Hybrid Structures**

---

## **Résumé en français**

### **MODÉLISATION DES STRUCTURES HYBRIDES MOUSSES ÉPOXY/TOISSUS ARAMIDES**

#### Introduction :

Ce chapitre présente la modélisation des structures hybrides mousses époxy/tissus aramides soumises à un impact à faible et moyenne vitesse. La modélisation des plis d'aramides est basée sur l'approche semi-continue. La mousse époxy est modélisée avec une loi de matériau élastique-plastique dite 'crushable foam' en compression et par un paramètre d'endommagement utilisateur pour représenter la rupture fragile observée expérimentalement en traction. La stratégie de modélisation des structures hybrides est validée par des essais expérimentaux d'impact à faible et moyenne vitesse.

#### Principaux travaux et résultats :

L'objectif du modèle numérique est de représenter le scénario d'endommagement observé expérimentalement lorsque la structure hybride est soumise à un impact. Le modèle numérique sera un outil d'optimisation pour de futurs travaux. Les plis d'aramide sont modélisés avec une approche semi-continue basée sur des études précédentes réalisées au sein de l'équipe. Le modèle semi-continu est introduit par Navarro et al. et développé par Pascal et al. Ce modèle, basé sur des observations expérimentales de la structure soumise à un impact, est capable de représenter les comportements suivants : les plis non endommagés, l'endommagement matriciel qui laisse les torons de fibres non stabilisés et l'endommagement de tous les composants des plis. Dans ce modèle, la résine est représentée par des éléments plaques et les torons de fibres par des éléments barres. Pour respecter le motif de tissage, les éléments barres, placés sur des nœuds virtuels, sont reliés aux éléments plaque par des liens rigides. Lorsque l'élément plaque casse, le contact peut difficilement être représenté entre les fibres. Par conséquent, dans la

présente étude, un élément volume 3D est développé pour représenter la résine et des éléments barres sont placés sur ses nœuds réels, ce qui permet de représenter le contact entre les fibres. Une loi de contact est introduite entre les fibres. Les paramètres du modèle numérique sont choisis par identification inverse basée sur des essais de traction ainsi que des essais d'impact poids tombant sur des échantillons de fibres imprégnées disposées à  $90^\circ$  et  $\pm 45^\circ$ . Le modèle numérique représentant la mousse époxy est une loi matériau élastoplastique. Le domaine élastique est définie par la loi de Hook et le domaine plastique, par des courbes définies par l'utilisateur. Des paramètres d'endommagement sont introduits dans la loi du matériau afin de représenter la rupture observée expérimentalement sur la mousse époxy. Les paramètres du modèle numérique sont choisis par identification inverse basée sur des essais de traction, de cisaillement et de compression dynamique.

Le matériau du support est modélisé avec la loi matériau de Cowper Symonds et dont les paramètres sont basés sur la littérature.

L'essai à basse vitesse est modélisé pour trois configurations comportant trois plis d'aramide répartis différemment dans l'épaisseur de la structure. Le modèle numérique décrit bien le comportement observé expérimentalement et les courbes effort/déplacement montrent un bon accord entre les résultats numériques et expérimentaux. Le scénario d'endommagement est identifié. On constate que la mousse époxy se densifie sous l'impacteur et forme un bouchon. Le bouchon appuie sur les plis d'aramide et conduit à leur rupture. Une rupture par traction est observée sur la face opposée à l'impact sur la mousse époxy.

Les impacts à vitesse moyenne sont modélisés. Cinq configurations différentes sont testées numériquement et la morphologie des dommages et la BFS (empreinte laissée après impact dans le matériau de support) sont comparés. Le modèle numérique montre une bonne corrélation en termes de propagation des dommages et de BFS par rapport aux résultats expérimentaux. Le mode de rupture des plis d'aramide est représenté par des fissures de la matrice et par la rupture des fibres. Une rupture en forme de croix est observée sur la face opposée à l'impact dans les plis d'aramide. La mousse s'endommage par écrasement.

#### Conclusion :

Le modèle numérique est capable de capturer plusieurs modes de dommages observés expérimentalement. Le modèle semi-continu développé représente bien les modes

*Numerical modeling of epoxy foam/aramid fabric hybrid structures*

d'endommagement observés dans les stratifiés composites imprégnés, caractérisés par la fissuration de la matrice et la rupture des fibres. La mousse époxy s'écrase sous l'impacteur et rompt en traction sur la face opposée à l'impact. Ce modèle numérique aidera à trouver une configuration optimale de structure hybride pour une application de protection.

**On the low and high-velocity impact modeling of hybrid epoxy foam/aramid fabrics structures**

L. Boutros, P. Navarro, S. Marguet, I. Tawk, J.F.Ferrero

**Abstract**

*This paper models epoxy foam /aramid woven plies hybrid structures subjected to low and medium-velocity impact. The modeling of the aramid woven plies is based on the semi-continuous approach. Epoxy foam is modeled with an elastic-plastic material law known as crushable foam and a user failure model to represent the experimentally observed brittle failure. The modeling strategy of the hybrid structures is validated by experimental low-velocity impact tests and medium-velocity impact tests. The numerical model represents damage sequences and correlates well with the experimental results.*

**IV.1 Introduction**

Lightweight, protective materials are widely used in transportation, sports accessories, packaging, satellites, and many more. Their protection capacity strongly depends on the material, design, and application environment. This article deals with modeling hybrid protective structures subjected to low and high-velocity impact. The hybrid structures combine aramid woven plies with different densities of epoxy foams.

In the pursuit of lightweight and protective materials, cellular materials are widely studied for impact resistance. Honeycomb, open-cell, and closed-cell foams show high-energy absorption due to their ability to deform over a long stroke at an almost constant load in compression [1]. Polymeric foam can absorb a high amount of specific energy when the cells bend, buckle or crush [2]. Three main phases can describe the typical behavior of polymeric foams under the impact, localized deformation, buckling of the cells and crushing, and finally, the densification where the cell walls are in contact, theoretically leaving zero voids. The behavior of polymeric foams is highly dependent on their complex microstructure, cell type, size, and density [3,4]. Despite the complex microstructure of polymeric foams on a small scale, they can be considered homogenous on a larger scale. Several studies drew necessary attention to modeling their mechanical behavior, particularly under impact. Two primary modeling levels

exist, the microscopic scale and the macroscopic scale. The micro modeling of open and closed cell foams is done through a particular unit cell geometry suitable to be a repeated unit. Hence, the mechanical behavior of this unit cell can be deduced by considering that the cell edges are made of structural elements [5]. However, this simplified modeling does not provide accountability for the onset damage [6]. Aubry et al. [7] proposed a modeling strategy for polymeric foam. The foam is modeled on the scale of the microstructure using a representative unit cell, then a change in scale strategy is applied. This strategy succeeded in analyzing the fine degradation of the foam, even for large structures, since significant computational time gains can be achieved due to the change in scale strategy. As for the modeling on the macroscopic level, the foam is considered homogenous and treated as a continuum material.

Foam material models can be differentiated into non-linear elastic and elastic-plastic. For the non-linear elastic, the response is usually calculated from a strain energy function [8]. The non-linear elastic foam behavior, usually presented by high compressible low-density foams, is modeled based on hyper-elastic and viscoelastic theories. Ogden [9] proposed a strain energy function to derive the stress-strain relationship for isotropic foams. Then, Jemiolo et al. extended this model to cover the anisotropy under finite deformation [9,10].

On the other hand, elastic-plastic constitutive models include the most common one developed by Deshpande and Fleck [11], which is also known in commercial FE software under "crushable foam" [12]. Deshpande and Fleck's model is based on defining a yield surface, and the evolution of this surface is studied for uniaxial and hydrostatic stress paths. The developed model is applied to the metallic foams and shows good agreement between experimental and theoretical results. While the definition of this model consists of defining the hydrostatic strength, it was found to be challenging to get this type of data experimentally. Carranza et al. propose a characterizing procedure for polymeric foam by defining the yield surface with more straightforward uniaxial tests. The authors used a subroutine to account for the failure in tension and shear. The study showed good agreement between numerical and experimental results [13].

Nevertheless, the classical material law crushable foam shows some limitations in representing some failure modes observed experimentally, especially for brittle foams.

Another material widely used against impact is composite materials. Their effectiveness-to-weight ratio makes composite materials interesting for protection applications. One of the most

used fibers in protection applications is aramid fibers. Aramid fibers marked under Kevlar® and Twaron® show superior impact properties since they have high strength, high modulus, and good tenacity [14]. Usually, the impact on woven composite plies generates different modes of damage, such as matrix cracking, delamination, and fiber breakage [15,16]. Modeling those woven plies can be challenging, especially when there is an interest in representing the exact damage mechanisms. Several modeling scales exist for composite plies: the macroscopic scale, the microscopic scale, and the mesoscale. The macroscopic scale modeling is based on the level of the laminate or sub-laminate. It is usually used for modeling significant scale structures. This model aims to predict the global response of the laminate, the global stiffness, load-carrying capacity, stability, and post-peak behavior of the laminates rather than predicting the detailed damage events [17]. The damage criteria in such models can be homogenous criteria like Tsai-Wu or Tsai-Hill [18]. The microscopic scale is built at the fiber level. The primary purpose of this modeling scale is to understand the physical behavior of the composite. The modeling is based on a representative unit cell with a detailed geometry.

Several studies focused on microscale modeling to investigate progressive failure, fiber-matrix debonding, and friction [19–21]. This modeling scale is not usually used for design engineering problems since it is computationally costly. The mesoscale, ply-based model is intermediate between macro and micro-level modeling. Homogenous layers represent the laminates or sub-laminates throughout the thickness [22], and cohesive interfaces are added between the layers to model the delamination [17]. This modeling scale can predict the essential mode of failure in composite laminates: delamination, fiber failure, and matrix crack. The discussed scales can be combined in multiscale modeling. The material/structure is represented at different scales [17]. Two types of multiscale exist, the hierarchical and the concurrent multiscale models. Hierarchical is one of the popular approaches, where the property of the material is transferred from microscale modeling to macroscale modeling, using homogenization theories [17], [23]. As for the concurrent multiscale modeling, both scales can exist simultaneously in the model. The macroscopic scale represents the undamaged areas, whereas the microscopic scale models the damaged area. Despite the advantages of multiscale modeling, it suffers from some limitations regarding crack initiation and evolution on the ply level [24].

As for damage modeling, two main strategies exist the continuum and the discrete. The continuum damage model is typically used to model intralaminar damage. The continuum damage mechanics (CDM) aims to predict the influence of microscale damage on the macroscale level. This prediction is made through mathematical relations linking the damage to the macroscale properties of the material [17,25]; those relations are based on stress, strain, or energy equivalence [25]. Several damage variables are introduced into the stiffness matrix. This model cannot provide an accurate representation of delamination or crack propagation. Another damage modeling approach is the cohesive zone models (CZM) approach which aims to model the intralaminar and the interlaminar damage using cohesive elements [26]. Bouvet et al. [27] proposed a modeling approach called Discrete Ply Modeling Method; the model introduces cohesive elements representing the matrix crack in the plies and between them. The proposed model could represent the impact response on UD carbon/epoxy laminates taking into account the relationship between intralaminar matrix cracking and delamination. The CZM requires a predefined crack path and additional crack propagation criterion leading to limitations in the case of more complex crack propagation [28].

Another approach is the semi-continuous approach found by Navarro et al. and further developed by Pascal et al. [29,30], which is used to model the impact on woven laminates. The main principle of this strategy is to differentiate between matrix and fiber failure. It can represent the continuous behavior of the undamaged composite plies and the discrete behavior where the bundles of fibers are left non-stabilized when the matrix is fully damaged. In this approach, the resin is modeled with damageable shell elements, and the fibers are modeled with rod elements. The positioning of the rod elements represents the weaving pattern. In these semi-continuous models, once the shell element is damaged, the model can hardly represent the slippage and the friction between the yarns since rigid links remain and avoid contact between the rods.

This study presents a modeling strategy for the hybrid epoxy foam/ aramid fabric layer structures. The epoxy foam is modeled with an elastic-plastic material law (crushable foam). A user failure law is implemented to represent the modes of failure observed experimentally. Aramid/epoxy composite is modeled with a strategy based on the semi-continuous approach. The epoxy resin is modeled with a damageable eight nodes volume element, and the bundles of



fibers are modeled with 1D rod elements. To represent slippage and friction, a contact law between rods is introduced.

## IV.2 Aramid plies modeling strategy

This study presents an extended version of the semi-continuous approach to model a 4-harness satin weave aramid/epoxy composite. A contact is added between the bundles of fibers.

### IV.2.1 Developed semi-continuous model

The developed semi-continuous model in the present study includes volume elements representing the epoxy matrix of the composite and rod elements representing the fibers, Figure IV-1. The placement of the rod elements respects the weaving pattern. A penalty-based contact is added between the rods. This modeling strategy is developed in the software RADIOSS.

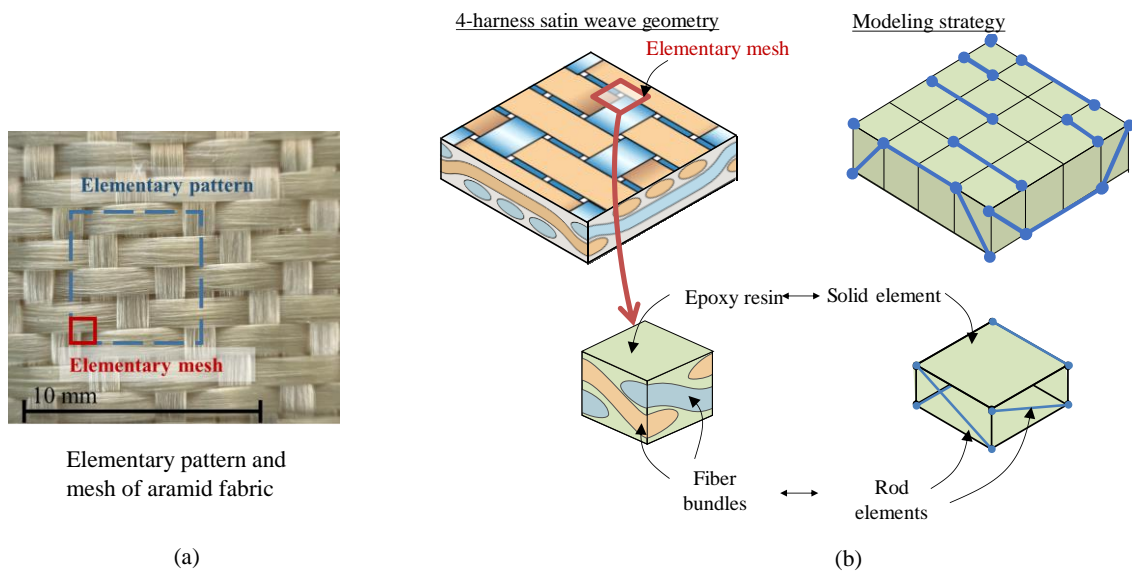


Figure IV-1: (a) aramid ply elementary pattern and mesh, (b) semi-continuous modeling strategy

#### IV.2.1.1 Solid elements

##### Formulation:

The eight nodes hexahedral brick element is widely used in 3D finite element analysis. However, many numerical challenges might be encountered when using this element. A full integration scheme may lead to volumetric locking, whereas reduced integration leads to zero energy modes, also known as hourglass energy modes. In the presented model, a volume element with a single integration point in addition to the hourglass control treatment defined in [31] is implemented. The formulations used for the volume element and the hourglass control are described [32]. For more details refer to Appendix C.

##### Constitutive law and damage variables:

The volume element representing the resin has an elastic orthotropic behavior, with three damage variables representing the cracks in each direction.

The damageable stiffness matrix  $[C]$  defines the stress and elastic strain relationship. It comprises the normal stresses stiffness matrix  $[C_n]$ , and shear stresses stiffness matrix  $[C_s]$ . The stiffness matrix  $[C_n]$  is described by the elastic modulus  $E_{ii}$  for each direction ( $i=x,y,z$ ). The  $[C_s]$  stiffness matrix is described by the in-plane shear modulus  $G_{xy}$ , and the out-of-plane shear modulus  $G_{iz}$ , ( $i=x,y$ ).

$$[C] = \begin{bmatrix} C_n & 0 \\ 0 & C_s \end{bmatrix} \quad (1)$$

$$[C_n] = \begin{bmatrix} \frac{(1 - \nu_{yz} \nu_{zy} \cdot d_{zy})E_{xx}^*}{1 - \nu_{deg}} & \frac{(\nu_{yx}(1 - d_y) + \nu_{zx} \nu_{yz} \cdot d_{zy})E_{xx}^*}{1 - \nu_{deg}} & \frac{(\nu_{zx}(1 - d_z) + \nu_{yx} \nu_{zy} \cdot d_{zy})E_{xx}^*}{1 - \nu_{deg}} \\ \frac{(\nu_{xy}(1 - d_x) + \nu_{zy} \nu_{xz} \cdot d_{xz})E_{yy}^*}{1 - \nu_{deg}} & \frac{(1 - \nu_{xz} \nu_{zx} \cdot d_{xz})E_{yy}^*}{1 - \nu_{deg}} & \frac{(\nu_{zy}(1 - d_z) + \nu_{xy} \nu_{zx} \cdot d_{xz})E_{yy}^*}{1 - \nu_{deg}} \\ \frac{(\nu_{xz}(1 - d_x) + \nu_{xy} \nu_{yz} \cdot d_{xy})E_{zz}^*}{1 - \nu_{deg}} & \frac{(\nu_{yz}(1 - d_y) + \nu_{yx} \nu_{xz} \cdot d_{xy})E_{zz}^*}{1 - \nu_{deg}} & \frac{(1 - \nu_{xy} \nu_{yx} \cdot d_{xy})E_{zz}^*}{1 - \nu_{deg}} \end{bmatrix} \quad (2)$$

$$[C_S] = \begin{bmatrix} 2G_{xy}^* & 0 & 0 \\ 0 & 2G_{xz}^* & 0 \\ 0 & 0 & 2G_{zy}^* \end{bmatrix} \quad (3)$$

where,  $v_{deg} = v_{xy} v_{yx} d_{xy} \times v_{xz} v_{zx} d_{xz} \times v_{yz} v_{zy} d_{zy} - 2(v_{yx} v_{yz} v_{xz} d_{xy}(1 - d_z))$

$$E_{xx}^* = E_{xx}(1 - d_x), E_{yy}^* = E_{yy}(1 - d_y), E_{zz}^* = E_{zz}(1 - d_z), G_{xy}^* = G_{xy} \cdot d_{shear},$$

$$G_{xz}^* = G_{xz} \cdot d_{xz}, G_{yz}^* = G_{yz} \cdot d_{zy},$$

$$d_{xy} = (1 - d_y)(1 - d_x), d_{xz} = (1 - d_z)(1 - d_x), d_{zy} = (1 - d_y)(1 - d_z)$$

$E_{xx}$ ,  $E_{yy}$  and  $E_{zz}$  are Young's moduli in directions x, y, and z.  $G_{xy}$ ,  $G_{xz}$ , and  $G_{zy}$  are the shear modulus of the x-y, x-z, and y-z planes.  $v_{ij}$  is the material Poisson's ratio ( $i, j = x, y, z$ ).  $d_i$  is the damage variable in directions x, y, and z.  $d_{shear}$  is the damage variable of the shear modulus in the x-y plane.

The evolution of the damage variables is based on the thermodynamic forces, also known as energy release rates:

$$d_i = \sup_{t \geq \tau} \begin{cases} 0 & \text{if } Y_i < Y_0 \\ \frac{\sqrt{Y_i} - \sqrt{Y_0}}{\sqrt{Y_C}} & \text{if } Y_i \geq Y_0 \\ 1 & \text{if } \sqrt{Y_i} - \sqrt{Y_0} > \sqrt{Y_C} \end{cases} \quad (4)$$

The parameter  $Y_0$  controls the damage initiation inside the resin matrix, and  $Y_C$  controls its evolution.  $Y_i$ , which is the thermodynamic force in the local direction  $i$ , can be calculated through:

$$Y_i = \frac{\partial W_e}{\partial d_i} \quad (5)$$

Where  $W_e$  is the elastic energy.

The pseudo-elastic behavior of the woven plies under in-plane shear loads is represented classically by an elastic behavior with a plastic correction based on the Newton-Raphson iteration scheme. An elastic field is defined by:

$$f = |\tau_{xy}| - K_{plas}p^\beta - \tau_0 \quad (6)$$

where  $\tau_{xy}$  is the in-plane shear stress,  $\tau_0$  is the yield stress,  $K_{plas}$  and  $\beta$  are material parameters defining the plastic hardening law, and  $p$  is the cumulative plastic strain. The plastic correction occurs if the elastic field  $f$  is greater than 0. It is based on the Newton-Raphson iteration scheme to update the plastic shear strain,  $\gamma_{xy}^p$ , and  $p$ :

$$\gamma_{xy} = \gamma_{xy}^e + \gamma_{xy}^p \quad (7)$$

where  $\gamma_{xy}$  is the total shear strain and  $\gamma_{xy}^e$  is the elastic shear strain.

Based on the experimental observation of Pascal et al. [30], another damage variable is added concerning the in-plane shear modulus  $G_{xy}$ . The damage variable  $d_{xy}$  is introduced:

$$d_{shear} = \begin{cases} 0 & \text{if } \gamma_{xy}^p < \gamma_{max}^p \\ 1 & \text{if } \gamma_{xy}^p > \gamma_{max}^p \end{cases} \quad (8)$$

where  $\gamma_{max}^p$  is the in-plane shear plastic strain to rupture. The shear behavior is fully damaged when this value is reached.

#### IV.2.1.2 Rod elements

Rod elements of RADIOSS (truss elements) represent the bundles of fibers. The cross-sectional area ( $S$ ) of the rod elements is calculated based on the fiber volume fraction, the thickness of the woven aramid ply and the mesh size. The rod elements are placed in a way to represent the weaving pattern of the aramid fabric (Figure IV-1). These elements have an elastic behavior with a brittle failure in tension. A maximum strain criterion ( $\epsilon_{max}$ ) monitors the failure

in the rod elements. A penalty-based edge-to-edge contact is introduced between the rod elements.

### IV.2.2 Parameter identification

The material parameters of the aramid/epoxy composite are identified with experimental tests, and it is based on reverse identification. The values are presented in Table IV-1. First, the fiber modulus  $E_f$  and strain at rupture  $\varepsilon_{max}$  are deduced by conducting a tensile test on neat aramid specimens having  $(0/90)^\circ$  orientation. The matrix elastic modulus ( $E_{mat} = E_{ii}$ ), shear modulus ( $G_{mat} = G_{ij}$ ) and the plasticity parameters ( $\tau_0, K_{plas}, \beta$ ) are established through tensile tests on  $(0/90)^\circ$  and  $\pm 45^\circ$  oriented impregnated specimens. Impregnated aramid/epoxy specimens have a fiber volume fraction of 37%. As for the failure parameters of the matrix, drop-weight impact tests are achieved to determine the damage evolution variables. The coefficient of friction between the rods is set to 0.3 based on literature [33].

Table IV-1: Identified parameters of impregnated aramid ply

Volume elasticity	In-plane shear plasticity	Volume damage	Rod elasticity and failure
$E_{mat}$ (MPa) 4500	$G_{mat}$ (MPa) 3500	$Y_0$ (MPa) 0.5	$E_f$ (MPa) 45000
$\nu$ 0.3	$\tau_0$ (MPa) 50	$Y_c$ (MPa) 5.2	$\varepsilon_{max}$ (%) 1.7
	$K_{plas}$ (MPa) 25	$\gamma_{max}^p$ (%) 26	$S$ ( $mm^2$ ) 0.078
	$\beta$ 0.2		

## IV.3 Epoxy foam modeling strategy

### IV.3.1 Formulation

The material law used to model the epoxy foam is usually used for honeycomb and crushable foams found in RADIOSS under MAT/LAW28 [32]. A Hookian law governs the elastic region. The plastic and the densification region are governed by user-defined functions describing their behavior. The user-defined functions are input curves for true stress and true strain. The curves are identified by conducting experimental tensile, shear, and compression tests. Volume elements are used to model the foam.

### IV.3.2 Damage

A time-dependent dynamic failure law is introduced to handle the damage inside the epoxy foam. The objective is to represent the behavior observed when the foam is crushed. To do so, only the deviatoric part of the stress tensor is deleted when reaching the failure criteria. The spherical part of the stress tensor will remain to represent the change in volume in the elements. This damage law is based on Tuler-Butcher [34] cumulative damage integral  $D$ . This failure law is not considered instantaneous but it needs a specific amount of time to initiate the failure, where it takes place when  $\sigma$  (the maximum principal stress) exceeds  $\sigma_r$  (the fracture stress) and lasts for a certain period until the cumulative damage integral reaches the critical value  $K$ . The cumulative damage parameter  $D$  is presented in (Eq.9), and when it reaches 1, the failure occurs:

$$D = \int_0^t \frac{\max(0, (\sigma - \sigma_r)^\lambda) dt}{K} \quad (9)$$

Where  $t$  is the time,  $\lambda$  is a material constant (typically set to 2 [34]).  $\sigma_r$  can be identified as the dynamic tensile yield point or the true static tensile stress for failure.

Experimental observation showed that the epoxy foam specimen encounters tensile failure when subjected to impact with a hemispherical shape indenter. Consequently, a failure model in tension is introduced. This law is based on calculating the principal strains ( $\varepsilon_I, \varepsilon_{II}, \varepsilon_{III}$ ) at each time step and comparing them to  $\varepsilon_{rup}$ , the maximum strain to failure criterion defined by the tensile test. The element is deleted if one of the principal strains exceeds the failure criteria. For more details refer to Appendix D.

$$\text{if } \max(\varepsilon_I, \varepsilon_{II}, \varepsilon_{III}) > \varepsilon_{rup} \quad \text{then rupture} \quad (10)$$

### IV.3.3 Parameters identification

The calibration process of the material is based on mechanical tests using the fitting technique. Dynamic compression is conducted to extract the compressive modulus. Tensile tests are performed to extract the tensile modulus, the fracture stress  $\sigma_r$ , and the maximum strain to

failure parameters. As for the shear tests, they are achieved to identify the shear modulus. In addition, these tests are used to define the input curves for the material law describing the epoxy foam. A dynamic indentation test is also performed to identify the parameter K. The identification is performed for an epoxy foam PB250 (density of 250 kg/m<sup>3</sup>). The results are presented in Table IV-2.

Table IV-2: Material properties for each foam used in the RADIOSS model

Compressive modulus (MPa)	72	
Tensile elastic modulus (MPa)	180	
Shear modulus (MPa)	18	
	K (MPa <sup>λ</sup> .ms)	7.15
Damage variables	$\sigma_r$ (MPa)	2.9
	$\varepsilon_{rup}$	0.048

## **IV.4 Numerical results and discussion**

The following section presents the ability of the numerical model to predict impact damage inside the hybrid structures. The assessment is done through drop weight mechanical tests and gas gun tests.

### **IV.4.1 Drop weight impact test**

This section describes the drop-weight experimental test, the modeling of the test, and a comparison between numerical and experimental results.

#### **IV.4.1.1 Experimental apparatus and numerical modeling**

Three configurations of hybrid structures combining epoxy foam and aramid fibers have been tested. The configurations are presented in Table IV-3. The solid black lines represent the aramid plies. The structure combines PB250 epoxy foam with three aramid plies. The first configuration [PB250-3plies-PB250] contains three aramid plies embedded in the middle of the structure. In the structure [1ply-PB250-2plies-PB250], one aramid ply is placed on top, and two in the middle. Structure [PB250-2plies-PB250-1ply] has two aramid plies in the middle and one on the bottom. The hybrid structures have a dimension of 100x100x30mm<sup>3</sup>.

*Numerical modeling of epoxy foam/aramid fabric hybrid structures*

The low-velocity impact test is done through a drop-weight machine (Figure IV-2). A hemispherical impactor of 16 mm diameters, weighing 2 kg, is dropped to reach an impact velocity of 6 m/s.

A technique used to assess body armor materials is used in this work. A backing material called clay witness is put behind the structures during the impact to measure the indentation left on the back. The dent depth left on the clay is known as the back face signature (BFS); it helps assess the protection capacity of the hybrid structures. The clay is confined inside a wooden box having a dimension of 130x130x25mm.

Table IV-3: Hybrid structures configuration having one or more foam densities, where aramid plies are distributed in different locations

Configuration	[PB250-3plies-PB250]	[1ply-PB250-2plies-PB250]	[PB250-2plies-PB250-1ply]
Representation			

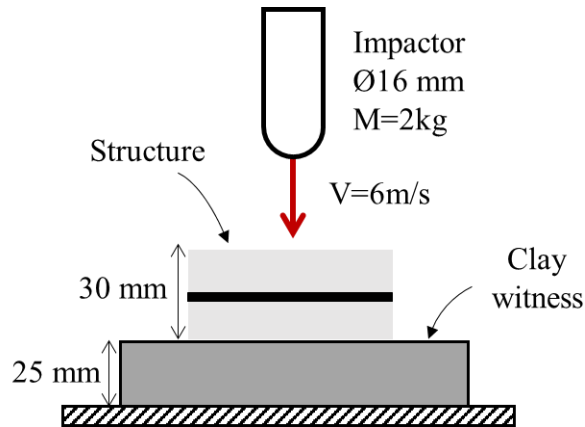


Figure IV-2: Experimental setup of drop weight impact test

The impact is modeled with a rigid sphere with an imposed initial velocity and the same mass as the experimental test. A solid-to-solid contact is defined between the hybrid structures and the clay. The clay bottom face and the four edges are fixed. An elastoplastic material law implemented in RADIOSS (/MAT/LAW44-COWPER [32] ) is used to model the clay material, and its mechanical properties are identified following the National Institute of Justice standards [35]. The mesh size used for all the components is 1 mm, which corresponds to the weaving size of the aramid fabric (Figure IV-3). The calculation time is around 6 hours over 72 processors, and the number of elements in the model is  $7 \times 10^5$ .



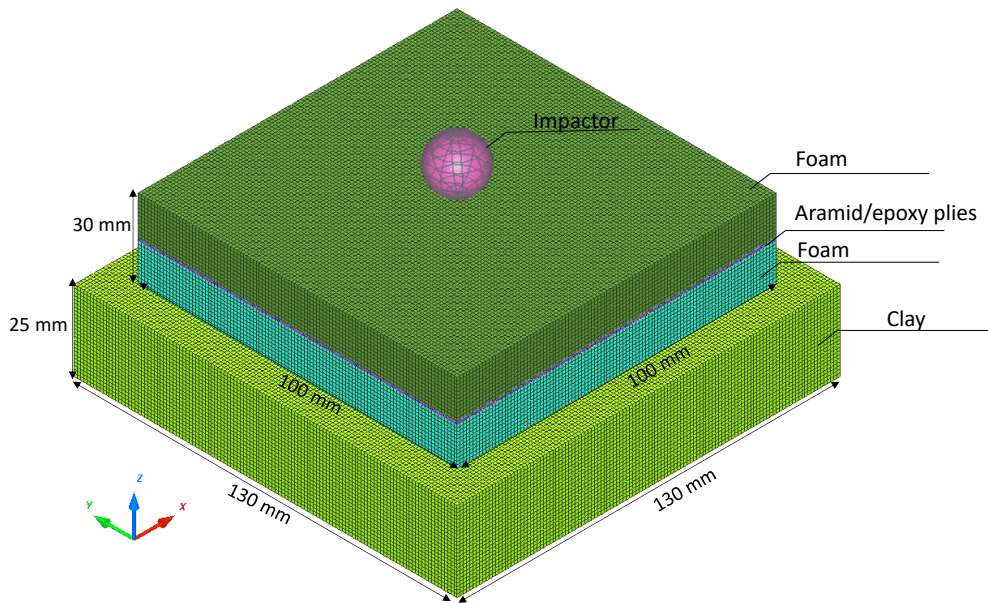


Figure IV-3: Numerical modeling of the low-velocity impact

#### **IV.4.1.2 Results and discussion of drop weigh test**

This section compares the experimental and numerical results regarding load versus displacement curves, permanent indentation, and back face signature of the low-velocity test. Finally, the scenario of damage to the hybrid structures is analyzed.

The experimental and numerical load versus displacement curves for structure [PB250-3plies-PB250] and the scenario of damage are shown in Figure IV-4. The presented curves show a satisfactory correlation between the experimental and numerical results. From 0 mm to 10 mm in displacement, the behavior begins with a linear response. Then, the slope increases at 10 mm in displacement (point A); at this stage, the elements underneath the impactor are subjected to crushing and densification, leading to a plug creation. This plug is also seen experimentally. The plug pushes against the aramid plies, increasing the load to 2.5 kN. Afterward, at point B, aramid plies begin to fail. A drop in load is measured. Matrix cracks and fiber breakage characterize the failure. The damage sizes for matrix crack, fiber breakage on the top layer of aramid plies, and bottom face are 14 mm, and 15 mm, respectively. A cross shape failure occurs after the tensile fracture strain is reached. The damage propagation inside the matrix starts on the lower ply and moves upwards. During the aramid failure, cracks appear on the bottom face of the epoxy foam placed on the bottom. The damage is characterized by

*Numerical modeling of epoxy foam/aramid fabric hybrid structures*

element deletion underneath the impact area due to tensile failure. Later, a slight gain in load occurs due to the penetration of the impactor in the bottom layer of epoxy foam. At point C, the cracks on the bottom face of the foam propagate from the center towards the extremities. In the end, the impactor rebounds after a displacement of around 23mm.

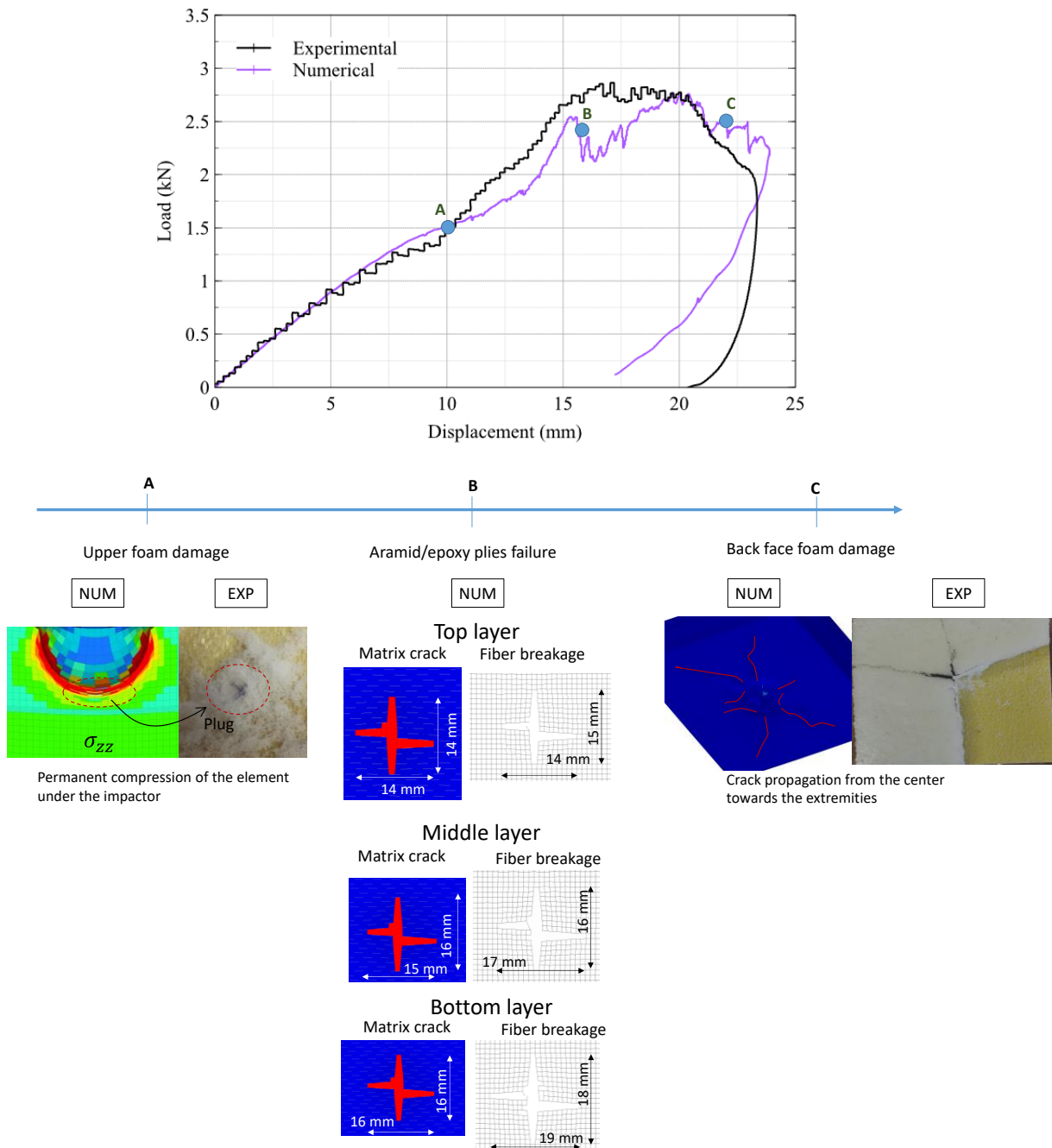


Figure IV-4: Experimental/numerical results of [PB250-3 plies-PB250]

### Numerical modeling of epoxy foam/aramid fabric hybrid structures

The permanent indentation and BFS for structure [PB250-3plies-PB250] are compared in Figure IV-5. It is shown that the numerical model provides a comparable permanent indentation with the experimental results. However, the numerical model underestimates the BFS inside the clay by 26% compared to the experimental BFS. This is due to the failure mode of the bottom face in those structures, where epoxy foam fails due to high tensile stress, leading to crack propagation. Some pieces of the epoxy foam sink inside the clay, which results in higher BFS.

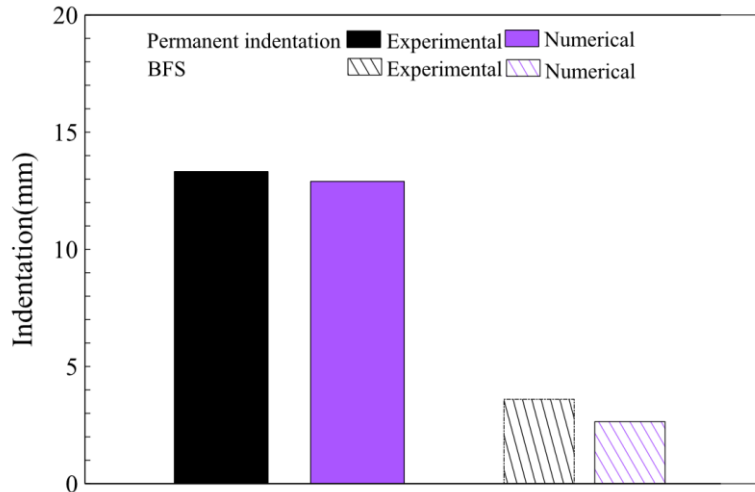


Figure IV-5: Back Face Signature and permanent indentation of structure [PB250-3plies-PB250]

The experimental and numerical load versus displacement curves and section view of structure [1ply-PB250-2plies-PB250] and [PB250-2plies-PB250-1ply] are shown in Figure IV-6. In both cases, the numerical model agrees well with the experimental results. The load-displacement curves in Figure IV-6.a show an increased initial stiffness due to the aramid ply at the impact face. The ply is fully perforated, and the indenter reaches the two plies in the middle, causing their failure. Element deletion due to tensile failure occurs on the bottom face of the lower epoxy foam. The actual structure also suffers from cracks propagation on the bottom face. The impactor rebounds at the displacement of 23 mm. Figure IV-6.b shows similar behavior compared to structure [PB250-3plies-PB250] (Figure IV-4). However, no crack propagation is captured on the bottom face. This is due to the presence of the aramid/epoxy ply located at the bottom. This is also seen experimentally. The two aramid plies in the middle fail due to fiber breakage and matrix crack. The impactor rebound after 20 mm in displacement.

Figure IV-7 shows the permanent indentation and BFS of structures [PB250-2plies-PB250-1ply] and [1ply-PB250-2plies-PB250]. The numerical model predicted a comparable

*Numerical modeling of epoxy foam/aramid fabric hybrid structures*

permanent indentation with a maximum error of 4% for both structures. Both structures do not show any significant BFS, neither experimentally nor numerically. (For more comparative results refer to Appendix E).

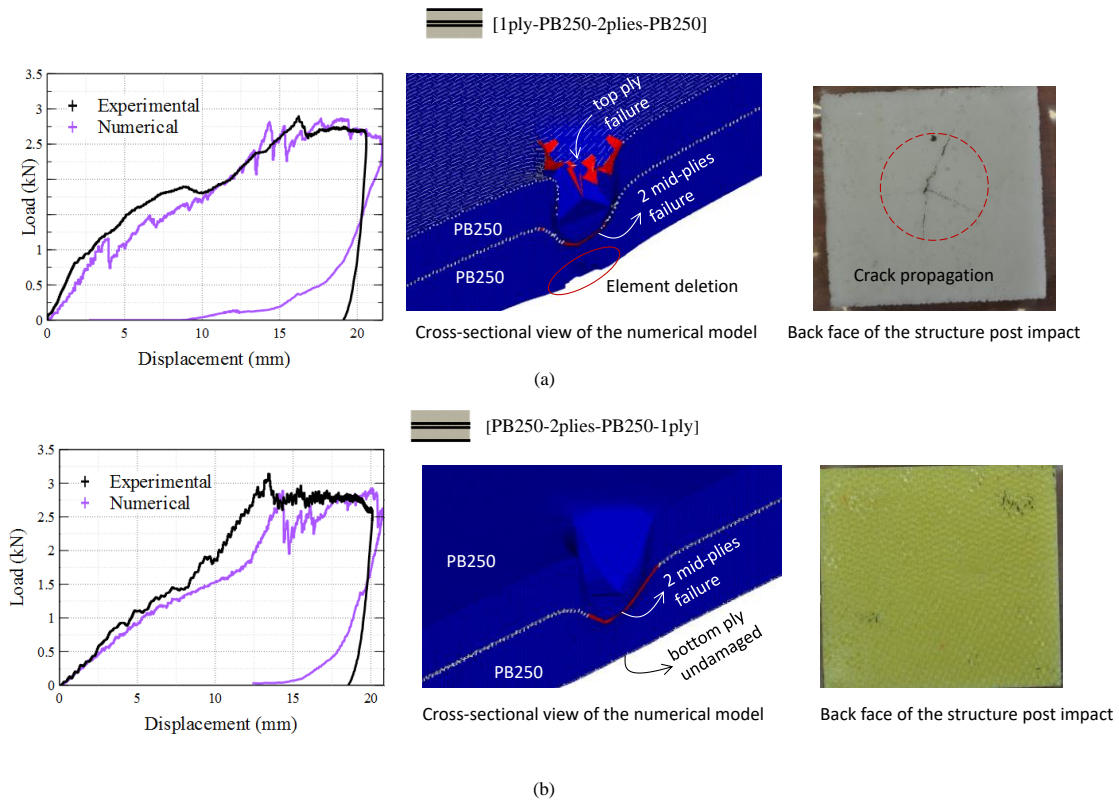


Figure IV-6: Experimental/numerical results of structures [PB250-2plies-PB250-1ply] and [1ply-PB250-2plies-PB250]

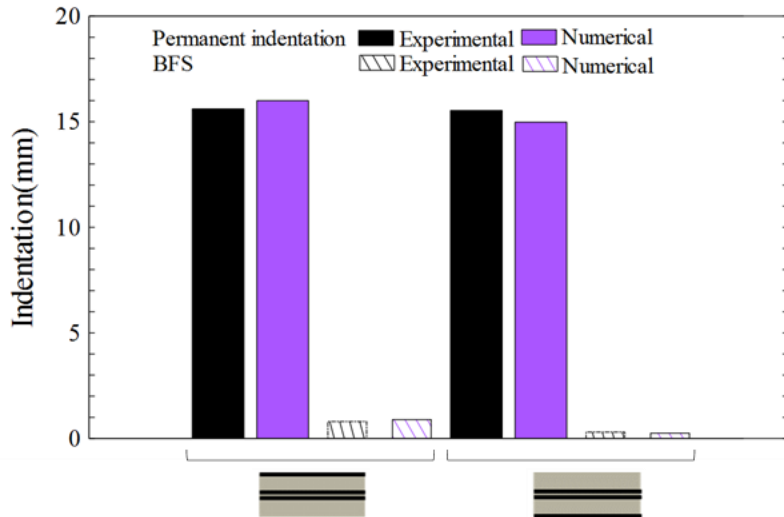


Figure IV-7: Permanent indentation and BFS results of structures [PB250-2plies-PB250-1ply] and [1ply-PB250-2plies-PB250]

#### IV.4.2 Gas gun impact test

This section describes the gas gun experimental test, the modeling of the test, and a comparison between numerical and experimental results.

##### IV.4.2.1 Experimental apparatus and numerical modeling

The gas gun test specimens contain 25 aramid/epoxy plies combined with PB250 epoxy foam. The different configurations are presented in Table IV-4. A structure made of only aramid/epoxy plies is tested as a reference (dimension 200x200x11 mm). Two configurations are fabricated with 25 plies of aramid/epoxy stacked together and placed on the epoxy foam top or bottom. The other two configurations are fabricated with a 20/5 plies distribution. The first has five plies as the impact face and 20 plies on the bottom, and the second is the reverse. The dimensions of the hybrid specimens are 200x200x50 mm

The structures are tested with the gas gun device, where a steel sphere having a weight of 11 g and a diameter of 14 mm impacts the structures. The velocity of the impact is 180 m/s. Figure IV-8 shows the experimental test apparatus. A high-speed camera is used to measure the speed of the impactor just before striking the structures. The structures are fixed with elastic bands on

*Numerical modeling of epoxy foam/aramid fabric hybrid structures*

the clay witness. The clay is confined in a wooden box, having a dimension of 300x300x60 mm.

Table IV-4: Hybrid structures configuration tested with a gas gun device

Configuration	[25 plies*]	[PB250-25 plies*]	[25 plies*-PB250]	[5 plies*-PB250-20 plies*]	[20 plies*-PB250-5 plies*]
Representation					

\* aramid/epoxy plies

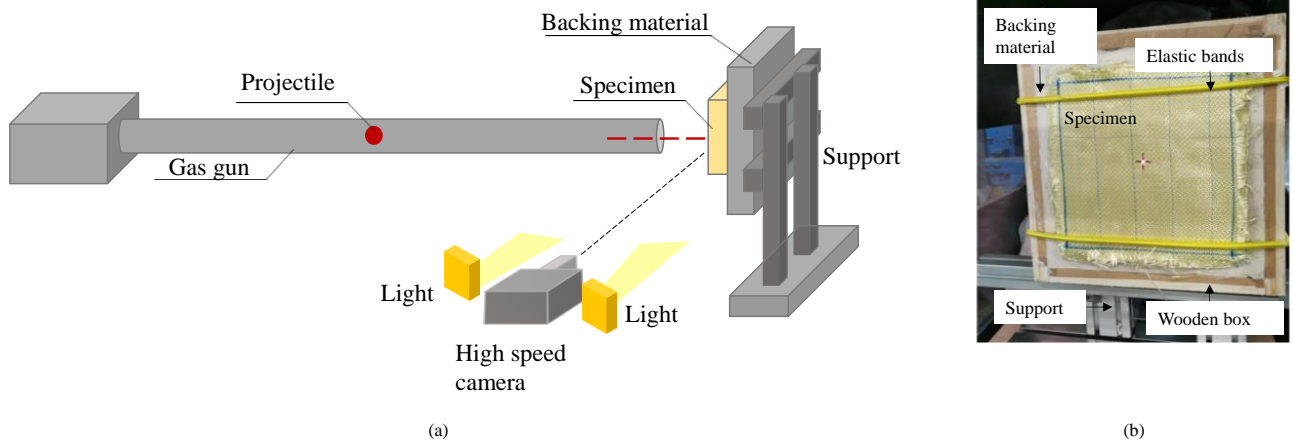


Figure IV-8: (a) Graphical representation of the medium-velocity impact setup, (b) structure fixation to the support system.

The impact is modeled with a rigid spherical wall with a mass and velocity corresponding to the experimental test (Figure IV-9). Contact between the structure and the clay witness is defined. The clay boundary conditions are replicated by blocking the three translations of the nodes of the bottom and the four edges.

The mesh size used for all the components is 1 mm. To limit the time calculation, and since the damage of the hybrid structures is localized, only an area of 100x100mm of the structure neighboring the impact is modeled. The calculation time is around 50 minutes over 72 processors, and the number of elements in the model is  $1.33 \times 10^6$ .

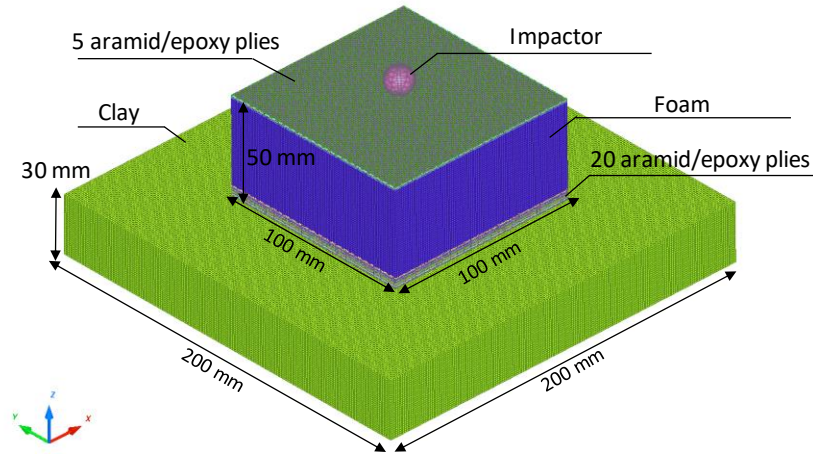


Figure IV-9: Numerical modeling of the high-velocity impact

#### **IV.4.2.2 Results and discussion of the gas gun test**

The experimental and numerical results are compared based on the damage morphology and the back face signature. Unlike the drop weight test, the load versus displacement curves is not recorded for these tests.

Figure IV-10 shows the simulated impact and back face damage in matrix cracking, fiber failure, and the back face signature for the structure with 25 aramid/epoxy plies. The predicted damage is consistent with the experimental results for both damage modes. In both cases, the impactor rebounded after the impact. The impact face damage is localized experimentally around the impactor edges and beneath it having a damage diameter of 18 mm. This is manifested numerically in cross-shaped matrix and fiber damage of 21mm diameter. However, cross-shaped damage (matrix and fibers) appears numerically on the bottom face, increasing the damage diameter by 76% compared to the impact face. The predicted bottom face damage is coherent with the experimental results. The clay is also shown numerically, where the 25 aramid/epoxy plies leave a BFS of 9.5 mm on the backing material.



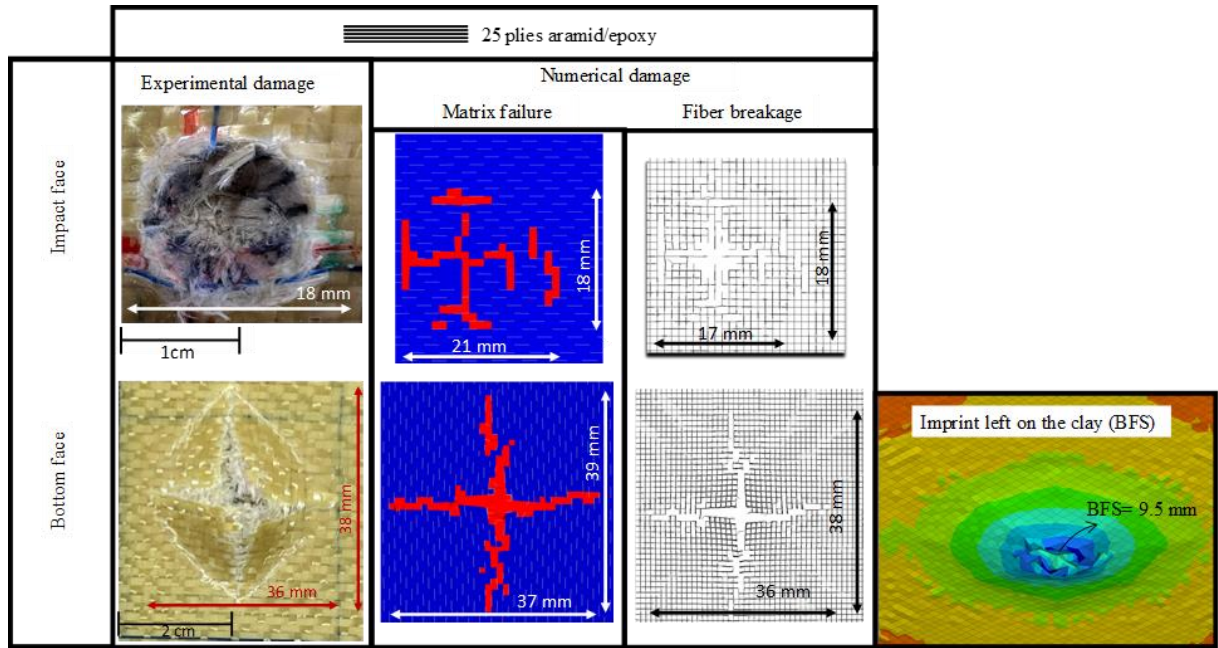


Figure IV-10: Comparison of numerical damage of the back face of the 25 impregnated plies with experimental damage.

Figure IV-11 shows the morphology of damage of the structures having PB250 with 25 impregnated plies located on the top or the bottom.



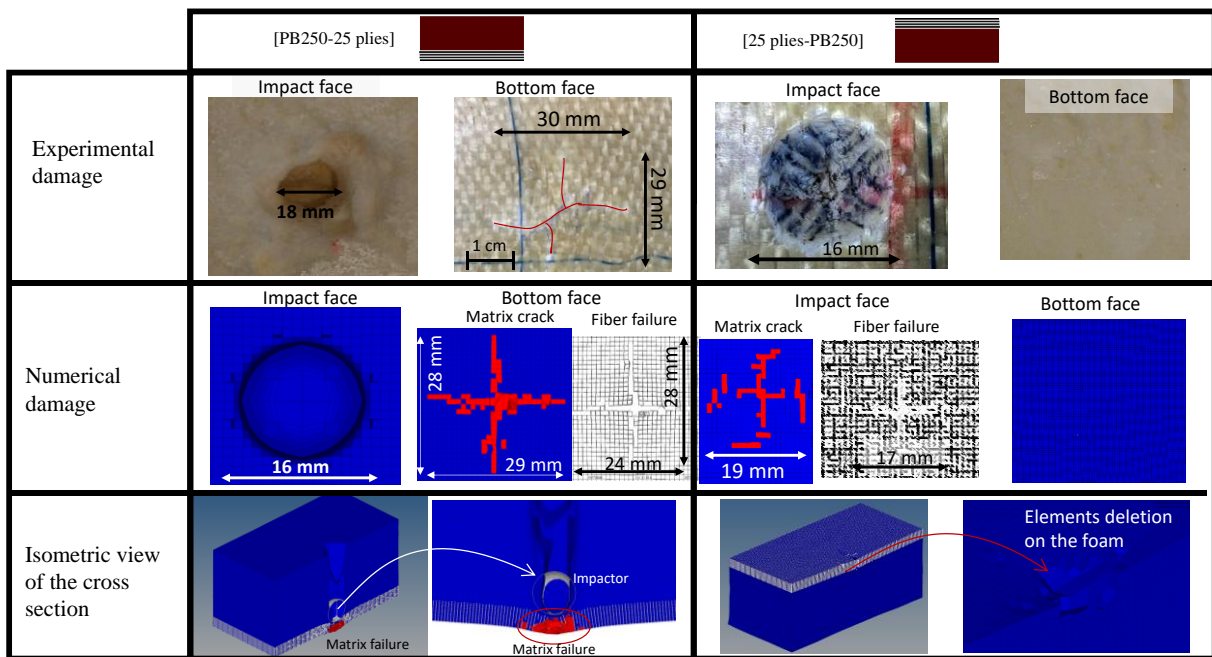


Figure IV-11: Comparison of numerical damage of hybrid structure, with PB250 and 25 plies, with experimental damage

The hybrid structure [PB250 + 25 plies] shows a complete perforation of the epoxy foam as the impact face. A clear hole is observed on the top face for both numerical and experimental structures. Regardless of the foam perforation, the 25 plies of aramid/epoxy stop the impactor after leaving damage on the back face. Matrix cracks and fiber failure characterize the damage. The numerical model succeeds in predicting this cross-shaped damage. An isometric view of the cross-section for the numerical model is also presented in Figure IV-11, where it is observed that the aramid plies stop the impactor and the matrix damage is visible underneath the impact area.

For the hybrid structure [25 plies + PB250], the impactor rebounds without perforation of the aramid. The damage presented on the top face is localized, having a dimension similar to the diameter of the steel impactor. The simulation predicts the same damage on the top face as the experimental results. In addition, on the bottom face, no damage is detected on the foam. However, the isometric view of a cut made in the middle of the structure shows element deletion in the foam layer underneath the impact. The foam elements fail due to attaining the critical tensile stress. The damage depth left on the foam numerically is 5 mm.

*Numerical modeling of epoxy foam/aramid fabric hybrid structures*

The numerical model captures the influence of aramid plies location and gives similar results as the experimental tests. The simulations prove that PB250 does not stop the impactor when located as an impact face. Complete foam perforation is seen numerically.

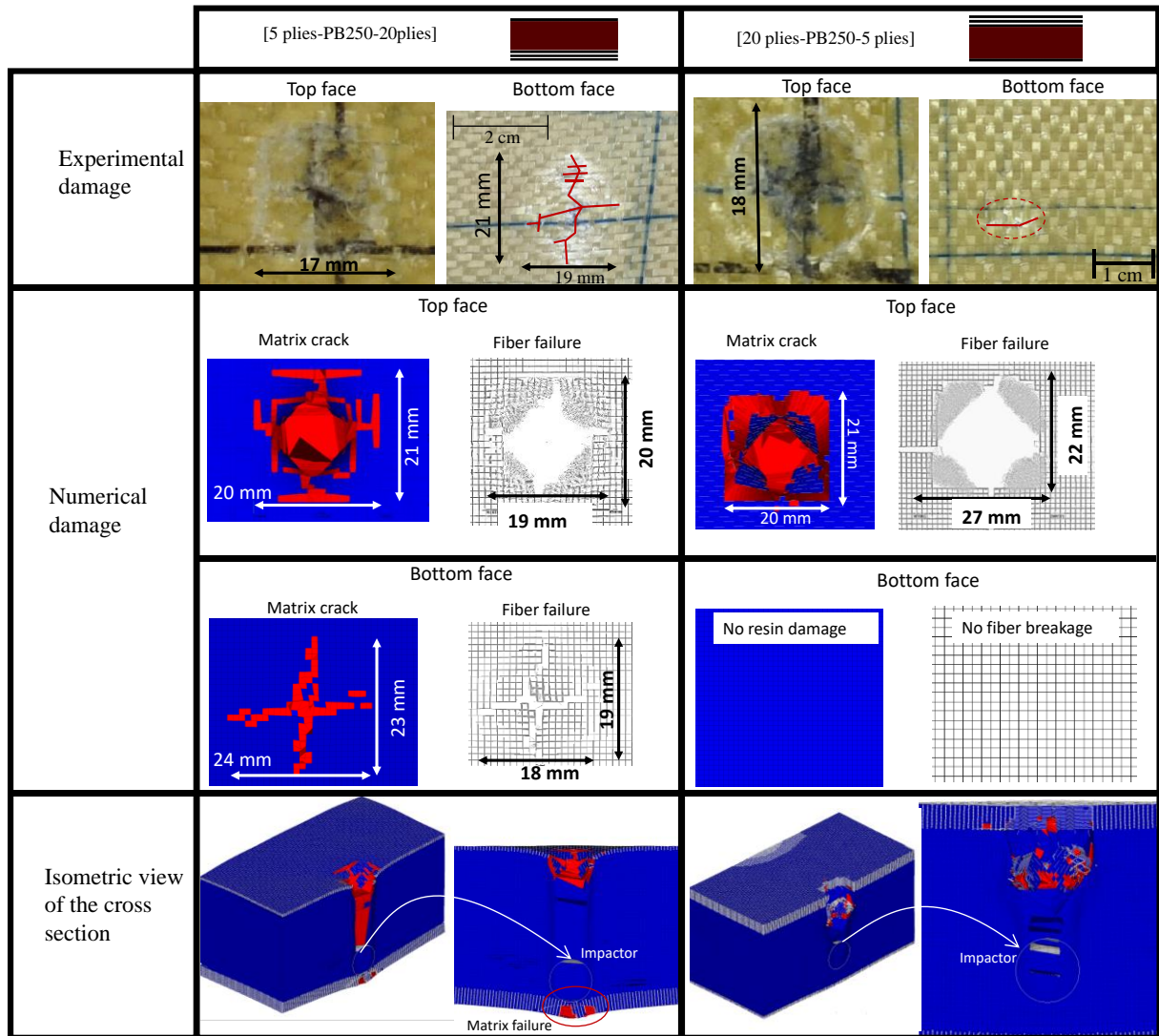


Figure IV-12: Comparison of numerical damage of hybrid structure, with PB250 with 20/5 plies distribution, with experimental damage

Figure IV-12 compares the experimental and predicted impact damage of the structure with a 20/5 plies distribution. Structure [5 plies-PB250-20 plies] shows the complete perforation of the five plies as impact face. The experimental results show matrix crack and fiber failure around the impactor edge; the damage diameter is 17 mm. The numerical model also predicted concentrated damage around the edges of the penetration hole. The matrix damage is 20 mm in

diameter. The cross-shaped failure characterizes the back face failure of the 20 aramid plies. The numerical model overpredicted the bottom face damage by 13%. The isometric view of the cross-section shows the material densification underneath the impactor after perforation of the upper plies. Similar to [PB250-25 plies], the impactor only stops at the aramid level.

As for the structure [20 plies-PB250-5 plies], similarly to the experimental results, the upper plies are fully perforated. The numerical model shows that the upper plies suffer from matrix crack and fiber breakage. The model overpredicted the damage diameter by 17%. Unlike the experimental results showing a very slight matrix crack of 6 mm of the bottom face, the numerical model does not show any damage. This is justified by the isometric view where the PB250 stops the impactor before attaining the aramid plies.

The damage modes greatly influence the back face signature left on the clay. Figure IV-13 compares the predicted BFS and the one measured experimentally. The structure with 25 aramid/epoxy plies shows a 9 % difference between experimental and numerical results. This structure attains a higher BFS compared to the other structures. Hybrid structures with 25 aramid plies as impact faces showed no significant BFS. The one illustrated in Figure IV-13 is only the depth of the edges of the structures when they sink into the clay. Structure with 25 and 20 aramid plies on the bottom face shows coherent results between the predicted BFS and the experimental one with a maximum difference of 14%. However, for structure [20 plies-PB250-5 plies], the predictive model underestimated the BFS by 44%. This is because the impactor is stopped before reaching the aramid plies, leaving a none significant dent in the clay. The numerical model succeeded in representing the impact performance of most hybrid structures in terms of damage morphology and back face signature. It is found that the numerical results are coherent with the experimental ones. The same conclusions can be drawn based on the numerical BFS, where the structure with aramid plies as the top face did not induce any significant BFS. The numerical model captures the aramid plies position influence.

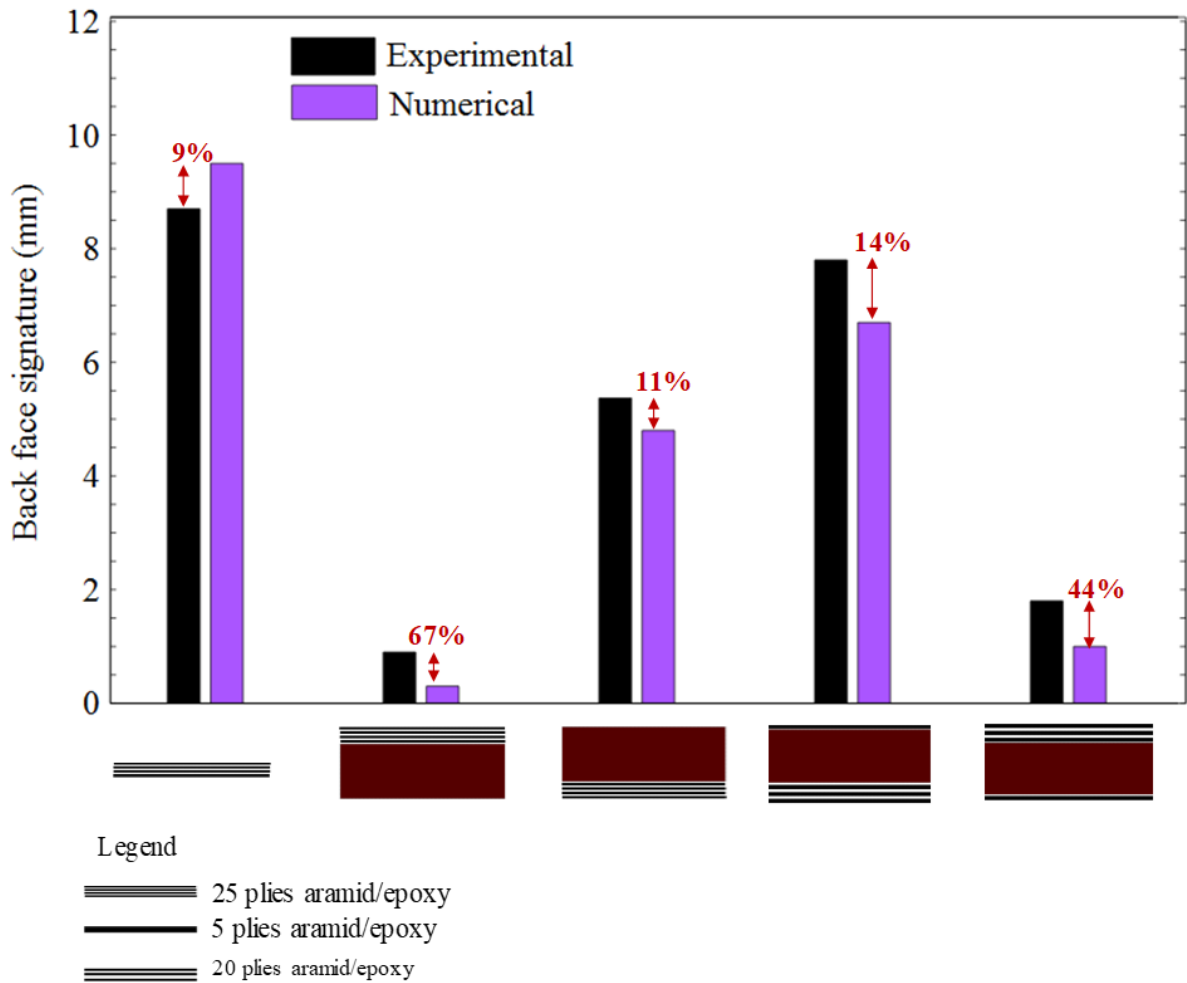


Figure IV-13: Comparison of BFS of simulations and experimental impact test

## IV.5 Conclusion

The behavior of epoxy foam/aramid plies hybrid structures is investigated numerically. The aramid/epoxy plies are modeled with a semi-continuous modeling approach, representing the resin with a damageable solid element and the fibers with 1D rod elements. A series of low and high-velocity impact modeling is achieved and compared to experimental results.

For the low-velocity impact, the comparison is based on force versus displacement curves, back face signature, and permanent indentation. The low-velocity impact modeling helps deduce the damage events of the hybrid structures. The aramid/epoxy plies in those structures fail due to matrix cracks and fiber breakage. In most configurations, the densified plug formed in epoxy foam causes the failure of the aramid plies. Epoxy foam suffers from tensile failure,

especially on the bottom face. The numerical model replicates similar permanent indentation and BFS compared to experimental results.

High-velocity impacts are modeled, and the comparison with the actual tests is based on damage morphology and the BFS. The numerical model showed comparable damage length with the physical test.

The main contribution of this work is the development of a volume element that is integrated into a semi-continuous modeling approach. A parameter identification methodology of a classical elastoplastic material law to model crushable foams is proposed. The suggested numerical modeling strategy of the hybrid structures will be used for optimization purposes.

### **Acknowledgment**

This work was granted access to the HPC resources of CALMIP supercomputing center under the allocation 2019-P09105.

## **Reference**

- [1] Karagiozova D, Langdon GS, Nurick GN. Blast attenuation in Cymat foam core sacrificial claddings. *Int J Mech Sci.* 2010;52:758–776.
- [2] Avalor M, Belingardi G, Montanini R. Characterization of polymeric structural foams under compressive impact loading by means of energy-absorption diagram. *Int J Impact Eng.* 2001;25:455–472.
- [3] Gibson LJ, Ashby MF, Schajer GS, et al. The mechanics of two-dimensional cellular materials. *Proc R Soc Lond Math Phys Sci.* 1982;382:25–42.
- [4] Gibson IJ, Ashby MF. The mechanics of three-dimensional cellular materials. *Proc R Soc Lond Math Phys Sci.* 1982;382:43–59.
- [5] Aubry J, Navarro P, Marguet S, et al. change of scale strategy for the microstructural modelling of polymeric rohacell foams. *CMC-Comput Mater Contin.* 2014;21–47.
- [6] Sullivan RM, Ghosn LJ, Lerch BA. A general tetrakaidecahedron model for open-celled foams. *Int J Solids Struct.* 2008;45:1754–1765.
- [7] Marvi-Mashhadi M, Lopes CS, LLorca J. Effect of anisotropy on the mechanical properties of polyurethane foams: An experimental and numerical study. *Mech Mater.* 2018;124:143–154.
- [8] Eaves D, editor. *Handbook of polymer foams.* Shawbury, Shrewsbury, Shropshire: Rapra Technology Limited; 2004.
- [9] Ogden RW. *Non-linear Elastic Deformations.* Courier Corporation; 1997.
- [10] Jemioło S, Telega JJ. Transversely isotropic materials undergoing large deformations and application to modelling of soft tissues. *Mech Res Commun.* 2001;28:397–404.
- [11] Deshpande VS, Fleck NA. Isotropic constitutive models for metallic foams. *J Mech Phys Solids.* 2000;48:1253–1283.
- [12] *Abaqus Theory Manual.* :1172.

- [13] Carranza I, Crocombe AD, Mohagheghian I, et al. Characterising and modelling the mechanical behaviour of polymeric foams under complex loading. *J Mater Sci.* 2019;54:11328–11344.
- [14] Lightweight Ballistic Composites | ScienceDirect [Internet]. [cited 2022 Jun 9]. Available from: <https://www.sciencedirect.com/book/9780081004067/lightweight-ballistic-composites>.
- [15] Abrate S. *Impact Engineering of Composite Structures*. Springer Science & Business Media; 2011.
- [16] Impact on Composite Structures [Internet]. [cited 2022 Jun 9]. Available from: <https://www.cambridge.org/core/books/impact-on-composite-structures/F77D6F3382519F7CC0E32492602DDA81>.
- [17] Camanho P, Hallett S. *Numerical Modelling of Failure in Advanced Composite Materials*. Woodhead Publishing; 2015.
- [18] Tsai SW, Wu EM. A General Theory of Strength for Anisotropic Materials. *J Compos Mater.* 1971;5:58–80.
- [19] Table A, Ivanov I. Materially and geometrically non-linear woven composite micromechanical model with failure for finite element simulations. *Int J Non-Linear Mech.* 2004;39:175–188.
- [20] Caporale A, Luciano R, Sacco E. Micromechanical analysis of interfacial debonding in unidirectional fiber-reinforced composites. *Comput Struct.* 2006;84:2200–2211.
- [21] Rao GVG, Mahajan P, Bhatnagar N. Micro-mechanical modeling of machining of FRP composites – Cutting force analysis. *Compos Sci Technol.* 2007;67:579–593.
- [22] Boubaker BB, Haussy B, Ganghoffer J-F. Consideration of the yarn–yarn interactions in meso/macro discrete model of fabric: Part II: Woven fabric under uniaxial and biaxial extension. *Mech Res Commun.* 2007;34:371–378.
- [23] Wu L, Noels L, Adam L, et al. A multiscale mean-field homogenization method for fiber-reinforced composites with gradient-enhanced damage models. *Comput Methods Appl Mech Eng.* 2012;233–236:164–179.

- [24] Paepegem WV. Multi-Scale Continuum Mechanics Modelling of Fibre-Reinforced Polymer Composites. Woodhead Publishing; 2020.
- [25] Williams KV, Vaziri R, Poursartip A. A physically-based continuum damage mechanics model for thin laminated composite structures. *Int J Solids Struct.* 2003;40:2267–2300.
- [26] Abrate S. Cohesive zone models and impact damage predictions for composite structures. *Meccanica.* 2015;
- [27] Bouvet C, Castanié B, Bizeul M, et al. Low velocity impact modelling in laminate composite panels with discrete interface elements. *Int J Solids Struct.* 2009;46:2809–2821.
- [28] Oterkus E, Oterkus S, Madenci E. *Peridynamic Modeling, Numerical Techniques, and Applications.* Elsevier; 2021.
- [29] Navarro P, Aubry J, Marguet S, et al. Semi-continuous approach for the modeling of thin woven composite panels applied to oblique impacts on helicopter blades. *Compos Part Appl Sci Manuf.* 2012;43:871–879.
- [30] Pascal F, Navarro P, Marguet S, et al. On the modelling of low to medium velocity impact onto woven composite materials with a 2D semi-continuous approach. *Compos Struct.* 2015;134:302–310.
- [31] Flanagan DP, Belytschko T. A uniform strain hexahedron and quadrilateral with orthogonal hourglass control. *Int J Numer Methods Eng.* 1981;17:679–706.
- [32] theory\_mat\_laws.pdf [Internet]. [cited 2022 Jun 19]. Available from: [https://altairhyperworks.com/hwhelp/Altair/hw14.0/help/hwsolvers/theory\\_mat\\_laws.pdf](https://altairhyperworks.com/hwhelp/Altair/hw14.0/help/hwsolvers/theory_mat_laws.pdf).
- [33] Martinez MA, Navarro C, Cortes R, et al. friction and wear behaviour of Kevlar fabrics. *J Mater Sci.* 1993;28:1305–1311.
- [34] Tuler FR, Butcher BM. A criterion for the time dependence of dynamic fracture. :7.
- [35] NIJ Standard 0101.06 Ballistic Resistance of Body Armor - [PDF Document] [Internet]. fdocuments.nl. [cited 2022 Jun 9].





---

# **Chapter V. General Conclusion and Perspectives**

---

## **Résumé en français**

### CONCLUSION GENERALE ET PERSPECTIVES

#### Conclusion :

Les matériaux de protection sont soumis à différents types d'impacts en fonction de la forme, de la masse et de la vitesse de l'impacteur. Un matériau de protection doit idéalement combiner légèreté et efficacité.

Différents matériaux sont largement utilisés dans les systèmes de protection, tels que les métaux, les céramiques, les matériaux composites et les matériaux cellulaires. Les matériaux composites sont intéressants car ils présentent un excellent rapport masse/résistance. Cependant, le matériau composite peut présenter de mauvaises performances lorsqu'il est soumis à un impact. Quant aux matériaux cellulaires, en raison de leur microstructure, ils sont capables d'absorber une grande quantité d'énergie sous sollicitation de compression. La présente thèse combine des tissus d'aramide et de la mousse époxy à cellules fermées. Les composants des structures hybrides sont caractérisés par un test mécanique classique afin d'identifier plusieurs paramètres nécessaires au développement d'un modèle numérique.

Afin d'étudier l'influence de différentes densités de mousse ainsi que du nombre de plis d'aramide et de leurs positions au sein de la structure, plusieurs architectures sont mises en place et soumises à un essai d'impact poids tombant. Le test d'impact à basse vitesse a permis la validation du modèle numérique.

Les capacités de protection respectives de ces structures sont ensuite étudiées avec un impact à haute vitesse, et sont comparées sur la base de la BFS (l'indentation laissée par la structure sur le matériau de support).

### *General conclusion and perspectives*

Une stratégie de modélisation numérique est développée pour prédire les dommages à l'intérieur de ces structures hybrides. Un modèle numérique prédictif pour les couches d'aramide est développé sur la base de l'approche semi-continue. Cette approche se situe à l'échelle de la maille. Elle peut représenter le tissu non endommagé, l'endommagement de la résine qui laisse les torons de fibres non stabilisés, et enfin, les stratifiés composites endommagés. Le modèle développé représente la résine avec un élément de volume endommageable et les fibres avec des éléments barres. La mousse époxy est modélisée avec une loi de matériau élastoplastique ainsi qu'une loi de rupture qui représente les modes d'endommagement observés expérimentalement.

Basé sur la théorie de Cowper Symonds, le matériau du support est également modélisé avec une loi matériau utilisateur. Les paramètres sont identifiés à partir de la littérature. Le développement de cette stratégie de modélisation est intégré dans le code de calcul explicite RADIOSS.

Le modèle numérique s'accorde bien avec les résultats expérimentaux en ce qui concerne les courbes effort-déplacement ainsi que les phénomènes observés physiquement et la BFS.

Ce travail expérimental et numérique a montré d'une part que les structures hybrides ont un fort potentiel d'utilisation dans une application de protection et d'autre part, le modèle développé peut aider à trouver la configuration optimale d'une structure hybride.

#### Perspectives :

Les perspectives concernant l'architecture, les structures présentées au Chapitre 3 peuvent être améliorées par différentes modifications structurelle. En particulier, trois paramètres peuvent être modifiés : l'épaisseur de la mousse (qui peut être réduite), la répartition des plis d'aramide et les densités des différentes épaisseurs de mousses au sein d'une même structure. Le modèle numérique développé Chapitre 4 permettra l'étude de l'impact de ces différents paramètres sur les performances du matériau, et permettra le choix d'une structure optimale.

Concernant le modèle semi-continu, il peut être amélioré par la prise en compte des phénomènes de frottements entre les fils observés lors de l'endommagement de la résine. Ceci peut se faire par l'intégration d'un terme de frottement dans la formulation de l'élément développé Chapitre 4.

### *General conclusion and perspectives*

Quant au modèle représentant la mousse époxy, la prise en compte des contraintes de cisaillement permettrait une représentation plus fidèle de son comportement.

## **V.1 Conclusion**

Over recent years, the engineering industries have raised the bar for the criteria needed in protective material. Protective materials must be lightweight, highly effective, low-cost, and environmentally friendly. As a practical solution, hybrid structures seek to twin the advantage of different materials to improve their protection characteristic, resulting in a hybrid material having superior features to the original ones.

This thesis provides a newly developed hybrid material with aramid plies embedded inside a closed-cell epoxy foam (PB170, PB250, PB400 kg/m<sup>3</sup>). The hybrid structures are presented in different configurations, and their impact performance is studied when subjected to low to high-velocity impact. The energy absorption capacity in the proposed material is studied by its ability to minimize the trauma left on the protected material. This work also proposes a numerical model that simulates the damage of the aramid plies and the crushing of the epoxy foam when subjected to impact.

This work aims to understand the scenario of damage inside the hybrid materials when subjected to low to high-velocity impacts when varying several parameters, such as the number and location of aramid plies embedded inside the epoxy foam and the density of the foam. On the other hand, a semi-continuous model, previously developed for thin woven laminates [1,2], is implemented to model the aramid plies while adding several modifications. A built-in material law in the FE package RADIOSS is used to model the epoxy foam. This numerical model aims to predict the damage propagation inside the hybrid structures and be used for future optimization work.

In the first part, an experimental campaign was carried out to observe the behavior of the hybrid structures under low-velocity impact and to study the influence of the number and location of aramid plies in the hybrid structures as well as the density of epoxy foam since three different ones are used in this study. This experimental study allowed us to observe the vital influence of the aramid plies in increasing the stiffness when being on the impact face and hindering the crack propagation in the epoxy foam when being bottom face. The density of the epoxy foam also monitored the impact behavior of the hybrid structures. When the highest density is placed as the impact face, the peak load increases, and the permanent indentation inside the structures decreases, leading to improved impact behavior. The aramid plies in the

### *General conclusion and perspectives*

middle of the structures also enhanced the performance when increased from 1 to three plies. The low-velocity series of tests enabled us to get maximum information on the behavior and the mode of failure in these hybrid structures. During the impact tests, it was identified that the aramid plies failed due to matrix cracking and fiber failure. With its high cross-linked density, the epoxy foam's failure is described by brittleness and crack propagation on the bottom side when not protected with aramid ply.

The capacity of these hybrid structures to protect the back face or the protected material is studied through a parameter called back face signature. The BFS is the trauma left on the protected material after impact. This parameter is obtained by placing a backing material, usually a soft clay, behind the structure during impact. Post-impact, the indentation left on the clay, or the BFS, is measured. This parameter is studied for each configuration, showing that structures with aramid plies on the bottom decrease the BFS. The higher density of epoxy foam proved to stop the projectile earlier and decrease its kinetic energy faster than structures with lower epoxy foam density, leading to lower BFS.

In the second part, high-velocity impact tests are conducted on hybrid structures with a fixed number of aramid plies. The parameters studied in this campaign were the density of the epoxy foam, the location of the 25 aramid plies, and their degree of impregnation. Those structures were assessed based on the BFS and permanent indentation left by the projectile inside the structures. This campaign showed that aramid plies as impact face, backed with 44mm of epoxy foam, can improve the BFS, eliminated to zero, compared to conventional structures while increasing the weight by 75% when subjected to a velocity of around 180m/s.

Permanent indentation per weight ratio is studied, and it is shown that a structure with 25 impregnated plies as the top face backed with 44 mm of PB250 epoxy foam has the optimal ratio compared to the other hybrid structures. The lower the ratio, the better the structure can decrease the projectile's kinetic energy per unit mass.

The density of the epoxy foam also plays an important role, showing that the high density, PB400, absorbs more energy than PB250 when subjected to 180m/s impact. It was also proven that neat aramid plies deform more than impregnated ones since the fibers are not stabilized and controlled by a resin matrix. The deformation of the neat aramid on the face parallel to the

### *General conclusion and perspectives*

impact leads to higher deformation, therefore a lower ability to minimize the trauma on the protected material.

In the third part, a model has been proposed to reproduce the response of hybrid structures numerically when subjected to impact.

The impregnated aramid fabric was represented with rod elements with different configurations stabilized inside a damageable matrix. The matrix is represented by volume elements with 1 point of integration in the middle with hourglass control. This volume element considers the pseudo-plasticity in-plane shear. The damage of the volume element is managed by damage variables that degrade the stiffness matrix. The rod elements fail in traction. A contact with friction between the rod elements is added to simulate the friction between the yarns, one of the energy dissipation modes in woven plies. This modeling strategy is a user subroutine implemented in the FE software RADIOSS.

The behavior of epoxy foams was investigated via dynamic indentation, dynamic compression, shear tests, and tensile tests. The classical behavior of foams was found in compression; three regions were identified, elastic, plastic, and densification. The tensile and indentation tests showed that the epoxy foam was brittle. Based on these grounds, the material law to simulate the behavior of the epoxy foam is chosen. A user-failure subroutine is added to represent the brittle failure of the epoxy foams.

The parameters of the aramid plies have been identified from static tensile tests on specimens with  $(0/90)^\circ$  and  $(45)^\circ$  orientations, in addition to a dynamic indentation test to identify the damage variables for the numerical model.

The backing material is modeled with an elastic-plastic law, similar to Johnson Cook but with a different strain rate formulation.

The numerical model was validated with the low-velocity impacts and agreed with the experimental results in load versus displacement curves, the permanent indentation, and the back face signature. The numerical model predicted the damage scenario on these hybrid structures when subjected to low-velocity impacts.

As for modeling the high-velocity impacts, the numerical model simulated the physical damage to the structures when subjected to a 180m/s impact with a spherical projectile. The

numerical model also predicted the BFS left on the backing material and agreed well with the experimental results.

A predictive numerical model is a tool for finding the optimal configuration of these hybrid structures and for optimization purposes for future works.

## **V.2 Perspectives**

After the outcomes maintained during this thesis, the possibilities for improvement are numerous and involve many different aspects.

### **V.2.1 Structures design**

The design of the structure can be improved by varying several parameters. The optimization might include the foam thickness of the hybrid structures. The thickness can be reduced by half since the aramid plies are not perforated, Figure V-1. A sufficient foam thickness is needed to contain the cone formed on the back face of the aramid plies. Hence, a weight reduction will occur without affecting the performance of the structures.

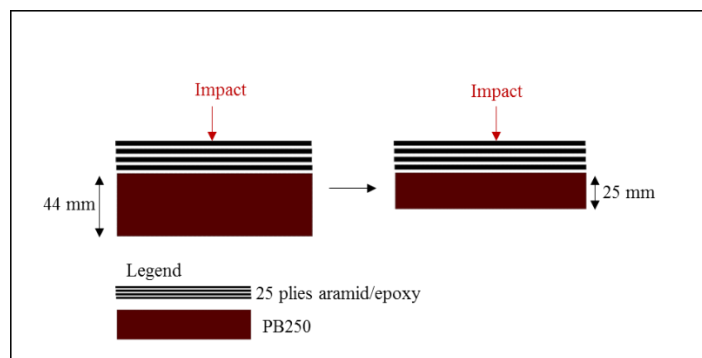


Figure V-1: Thickness reduction of the high-velocity tests structures

Another aspect concerning the architecture of the hybrid structures will be distributing the aramid plies throughout the thickness, Figure V-2. This architecture might improve energy absorption by increasing the number of interfaces aramid/foam and, therefore, help decrease the projectile's kinetic energy. This strategy was adopted in the literature on hybrid composite materials and found effective [3].



### General conclusion and perspectives

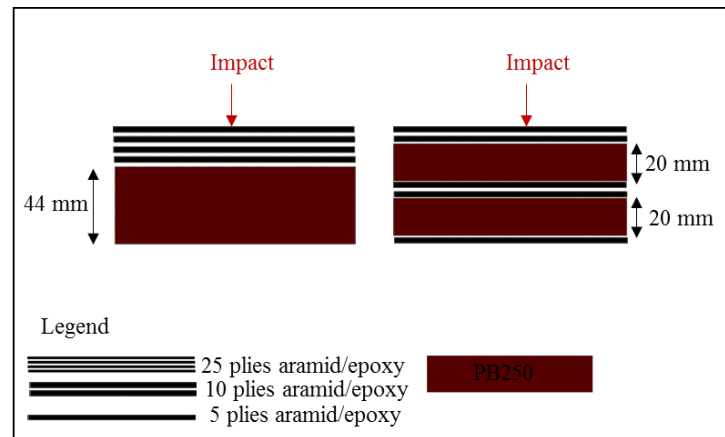


Figure V-2: Aramid plies distribution inside PB250 to increase the number of interfaces aramid/foam

Different foam densities might be present inside a single structure; PB400 can be the first layer of epoxy foam since it proved to have higher impact resistance due to its higher mechanical properties, backed with PB250 to reduce the weight, Figure V-3.

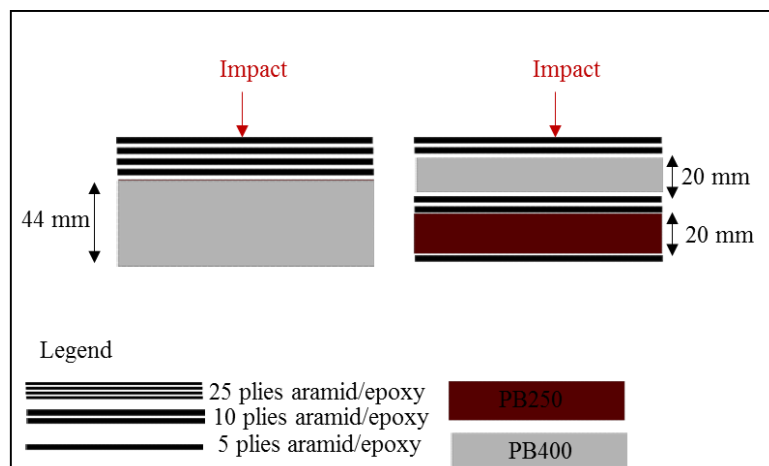


Figure V-3: Bi-foam structures with 25 aramid plies for effective weight improvements

These architectures aim to create a plug underneath the impactor that makes the whole structure respond against impact instead of a localized response. Another purpose is to decrease the weight since it is a crucial feature when designing a protective material.

The impact resistance of these hybrid structures can be optimized by varying multiple factors. Therefore, the numerical model will play an essential role in finding the optimal configuration while saving the time and cost of fabrication and testing.

### *General conclusion and perspectives*

The optimization aspects might include layering the aramid plies with different orientation angles between the plies. The present work uses only a  $(0/90)^\circ$  orientation. Recent studies discuss the effectiveness of the helicoidal fiber architecture compared to conventional stacking orientation. It appeared to show through-thickness damage and an increase in the residual strength [4].

The various optimization strategies can be explored using the numerical model developed during this work. The numerical model can represent the general tendency of the impact behavior of the hybrid structures when subjected to low and high velocity impacts.

The numerical model will serve as a tool to study the influence of several parameters: the aramid plies distribution, the aramid plies number, and the epoxy foam density. After analyzing the influence of each parameter, an optimization study can be achieved to find the optimal structure.

#### **V.2.2 Semi-continuous numerical model**

The proposed numerical model can represent the global behavior of the hybrid structures when subjected to impact. However, several improvements can be implemented in this model.

During impact on impregnated fabric, friction between the fibers occurs, and the residue and fragments of the failed resin can lead to friction. It is shown that using the edge-to-edge interface already built-in RADIOSS with friction did not show any influence compared to the one without friction. The influence of friction can be included in the formulation of the 3D volume element, representing the friction between the failed resin and the fibers.

Another aspect of future work is a 3D woven fabric. The first chapter of this manuscript shows that 3D fabric is taking significant interest based on its superior impact resistance. The developed solid element offers the potential to replicate 3D fabric weaving patterns. This behavior and potential of this 3D fabric can be studied numerically using the developed model in this thesis.

#### **V.2.3 Epoxy foam model**

The numerical modeling of polymer foams is very challenging. Their behavior highly depends on their cell geometry, size, and density. The brittleness of the epoxy foam used in this work presented several challenges. The numerical model proposed to simulate the behavior of

### *General conclusion and perspectives*

the epoxy foam, the /MAT/LAW28 coupled with two failure models, can represent well the behavior of the foam under compression and tensile loadings. However, it is less representative of the shear stresses. The numerical model seems limited in modeling complex solicitations (combined compression-shear loading). Since modeling is a process that normally starts with the realization of experimental tests, it would be interesting to conduct experimental tests to study the influence of compression loading on the shear resistance of the foam.

Based on the literature, the behavior of polymer foam can be viscoelastic and hyperplastic. A more adaptable numerical model can be used to represent this behavior. Ogden model is a constitutive law available in RADIOSS, normally used to model hyperplastic behavior. This model offers a perspective that deserves to be to be explored.

## **References**

- [1] Navarro P, Aubry J, Marguet S, et al. Semi-continuous approach for the modeling of thin woven composite panels applied to oblique impacts on helicopter blades. *Compos Part Appl Sci Manuf*. 2012;43:871–879.
- [2] Pascal F, Navarro P, Marguet S, et al. On the modelling of low to medium velocity impact onto woven composite materials with a 2D semi-continuous approach. *Compos Struct*. 2015;134:302–310.
- [3] Tirillò J, Ferrante L, Sarasini F, et al. High velocity impact behaviour of hybrid basalt-carbon/epoxy composites. *Compos Struct*. 2017;168:305–312.
- [4] Grunenfelder LK, Suksangpanya N, Salinas C, et al. Bio-inspired impact-resistant composites. *Acta Biomater*. 2014;10:3997–4008.



---

Appendix A.      **Hybrid Structures fabrication**

---

## **1. Introduction**

This section presents the fabrication process of the hybrid structures tested in the low and high velocity impact experimental campaign. The fabrication process of each test campaign specimen differs by the number of aramid plies, foam density, and location of aramid plies. The hybrid structure fabrication tackled challenges concerning integrating the aramid plies inside the expansible epoxy foam. This section is divided into two sub-section, one for the targets for the low-velocity campaign and the second for targets tested in the high-velocity campaign.

## **2. Base materials**

The base materials used for all the structures are the following:

- Expansible epoxy foam including three different densities PB170, PB250, and PB400 with respectively a density of  $170 \text{ kg/m}^3$ ,  $250 \text{ kg/m}^3$ , and  $400 \text{ kg/m}^3$  [1].
- Aramid fabrics with a satin four architecture and  $(0/90)^\circ$  orientation in all configurations [2].
- Epoxy resin, Araldite<sup>®</sup> LY 5052 / Aradur<sup>®</sup> 5052, is used to impregnate the aramid woven plies [3].

## **3. Low-velocity campaign structures fabrication**

In this experimental campaign, the density, the location, and the number of aramid plies are varied. The main components of the specimens are the epoxy foam and the impregnated aramid plies. The structures are fabricated in a two-part rectangular mold having a dimension of  $150 \times 190 \times 30 \text{ mm}$ . A picture and a schematic of the mold are presented in Figure A- 1. The top and bottom sides have the same dimension with a depth of 15 mm each.

## Hybrid Structures fabrication

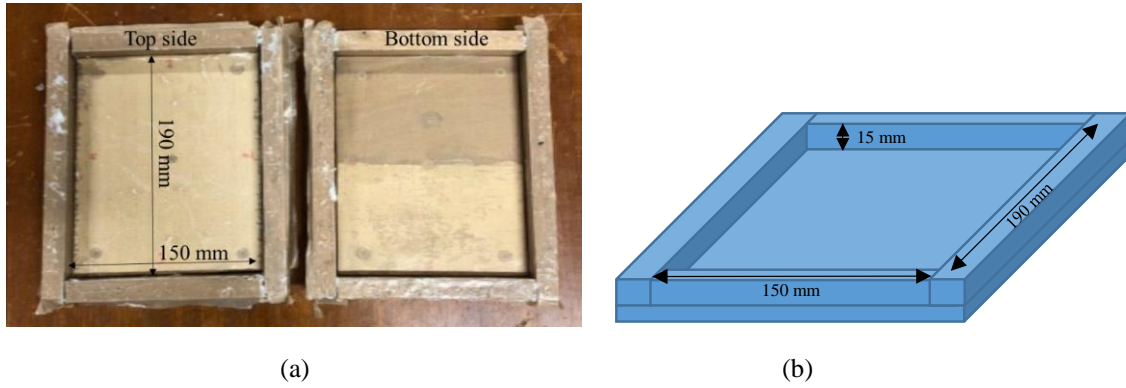


Figure A- 1: (a) Picture of the molds of the low-velocity campaign, and (b) schematic and dimensions of one of the sides of the mold

### *Epoxy foam preparation:*

The epoxy foams used are closed-cell foams with different expansion rates. Sicomin (France) supplies epoxy foam [1]. The PB epoxy foam has two components: epoxy resin (PB) and a hardener (DM03). When the two components are mixed, they expand due to chemical foaming. The epoxy foam dosing is dependent on the volume that must be filled. The volume of the mold is around 0.855 L. Table A- 1 presents the amount of epoxy resin and hardener needed to fill the mold.

Table A- 1: Dosages of PB epoxy resin and DM03 hardener

	PB 170	PB 250	PB 400
PB resin (g)	116	179	285
DM03 (g)	36	56	91

Following the weighing procedure, the two-component are mixed inside a container and mechanically frothed for 4 minutes.

### *Aramid plies preparation:*

The aramid fibers used in this study are a four harness satin woven fabric with an areal density of  $175 \text{ g/m}^2$  and thickness of 0.26 mm. Gaches Chimie (France) supplies the aramid fabric [2]. The matrix is an Araldite® LY 5052 (resin)/Aradur® 5052 (hardener) epoxy with a fiber volume fraction of 37%. The impregnation of the aramid is done through a hand layup technique.



## Hybrid Structures fabrication

### Structures fabrication:

Table A- 2 and Table A- 3 represent some of the configurations fabricated. Table A- 2 shows the specimens with only epoxy foam, [PB-neat], fabricated for comparison purposes. Table A- 2 also presents [PB-1ply] and [1ply-PB], the specimens with one aramid ply placed on the top or the bottom of the specimen. These configurations are fabricated with the three different epoxy foam densities, PB170, PB250, and PB400.

Table A- 3 shows configurations with aramid plies in the middle, whether with mono-foam or bi-foam. Specimens [PB-1ply-PB] and [PB-3plies-PB] are mono-foam specimens with one and three aramid plies in the middle. Specimens [PB-2plies-PB-1ply-PB], [1ply-PB-2plies-PB], and [1ply-PB-1ply-PB-1ply] are mono-foam specimens with three aramid plies distributed differently in the middle, bottom and upper sides of the specimens. Specimens [PB-1ply-PB\*] and [PB-3plies-PB\*] are bi-foam specimens where the upper foam density is different than the bottom one, separated by one or three aramid plies in the middle.

Table A- 2: Configurations with neat epoxy foam and hybrid structures with one aramid ply











configuration	[PB-neat]	[PB-1ply]	[1ply-PB]
representation			

Table A- 3: Hybrid structures configurations that contain aramid plies in the middle

configuration	[PB-1ply-PB]	[PB-3plies-PB]	[1ply-PB-2plies-PB]	[PB-2plies-PB-1ply]
representation				
configuration	[1ply-PB-1ply-PB-1ply]	[PB-1ply-PB*]	[PB-3plies-PB*]	
representation				

PB\* different density than PB

The fabrication of those specimens described above is detailed in the following paragraphs.

[PB-neat] is fabricated by pouring the frothed epoxy foam liquid inside the bottom side of the mold. Then the top side is placed on top to close the mold. In the case of [PB-1ply] and [1ply-PB], where only one aramid ply is added to the epoxy foam, the impregnated aramid ply

### Hybrid Structures fabrication

is placed on the bottom side of the mold before pouring the epoxy foam. Then the foam is poured on top of it, and the top part is used for closing. Mechanical clamps are used to secure the top and bottom sides. Then the mold is placed in a hot air oven at 40°C for 12 hours.

Fabricating the structures with aramid plies in the middle is more challenging. The foam mixture is divided into two containers, one for the top side and the other one for the bottom side. In the case of having structures with bi-foam, the foam mixture poured on the top side has a different density than the one poured on the bottom side. Figure A- 2 explains the fabrication steps of the hybrid structures with one or three aramid plies in the middle. In step 1, half of the foam mixture is poured into the bottom side of the mold. In step 2, the aramid ply that is already impregnated is fixed on the four edges of the bottom side of the mold using a stapler. The stapling of the aramid fabric effectively keeps the aramid ply straight and prevents waviness. In step 3, the other half of the foam mixture is poured into the top side of the mold. In step 4, the top side of the mold is rapidly put on top of the bottom side. Both mold sides are joined together with clamps and tied to secure the closing in step 5. Finally, the mold is put in a hot air oven at 40°C for 12 hours.

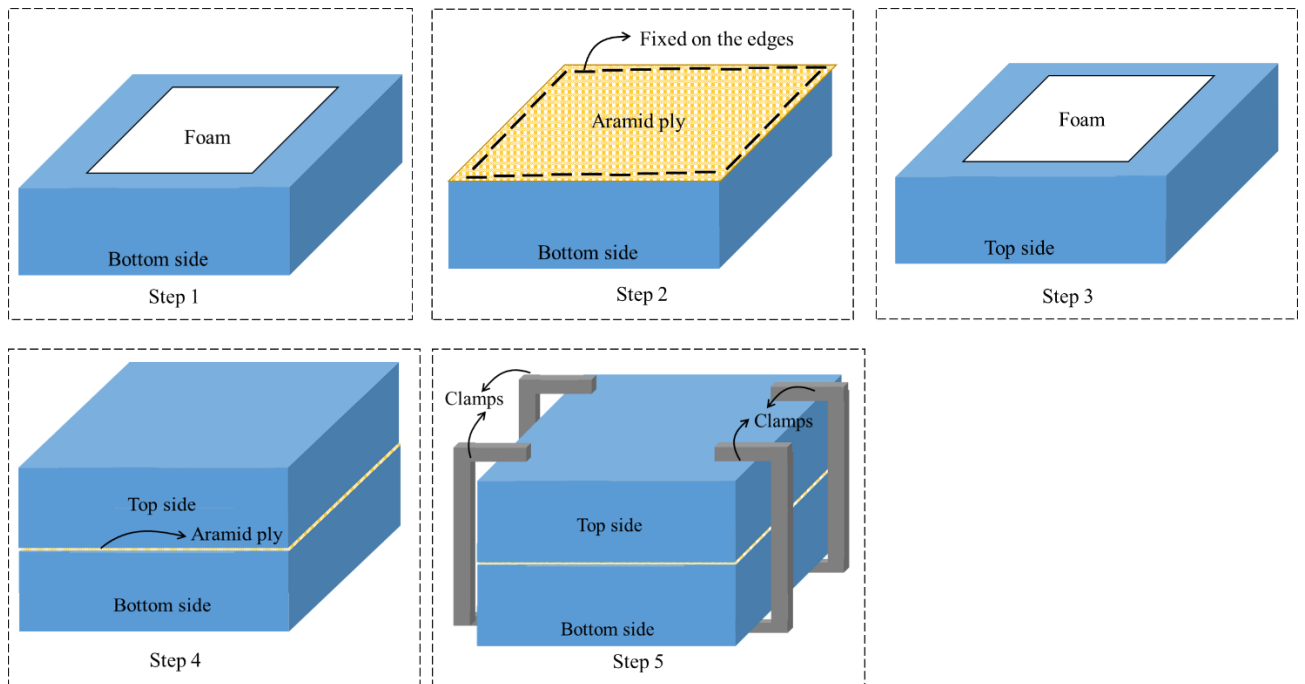


Figure A- 2: Fabrication steps of hybrid structures with aramid ply in the middle

## Hybrid Structures fabrication

### Structures cutting:

After demolding the structures, the 190x150x30mm hybrid structures are cut into squares of 100x100x30mm. The cutting procedure is done using a water jet machine since the aramid is a critical material to cut. Figure A- 3 shows the water jet machine during the cutting procedure of the hybrid structures.



Figure A- 3: Hybrid structure cutting process with a water jet machine

Figure A- 4 shows that the aramid plies are stabilized inside the epoxy foam without any significant waviness.



Figure A- 4: Structure with three aramid plies in the middle after being cut

#### **4. High-velocity campaign structures fabrication**

The hybrid structures for the high-velocity campaign consist of epoxy foam PB250 and PB400 and aramid fibers impregnated and neat. As a reference, non-hybrid structures are also fabricated with 25 plies of aramid, impregnated, and neat.

##### *Non-hybrid structures:*

The dimension of the structure is around 200x200mm. The 25 plies are stacked together and attached with a double tape adhesive on the four edges for the neat aramid specimen. The procedure presented in Figure A- 5 shows how the plies are bonded on their edges.

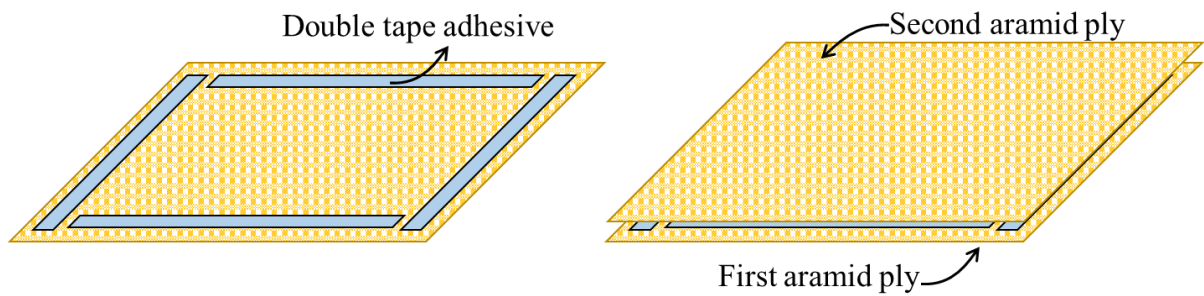


Figure A- 5: Stacking procedure of the neat aramid plies

For the impregnated aramid specimen, the manufacturing procedure is presented in Figure A- 6. The epoxy resin needed for impregnation is calculated to provide a fiber volume fraction of 37%. The 25 plies are impregnated with a hand layup technique using a roller to distribute the poured resin evenly on each ply; the exact process is repeated for the 25 plies. The laminate is left to polymerize for 48 hours at room temperature.

### *Hybrid Structures fabrication*

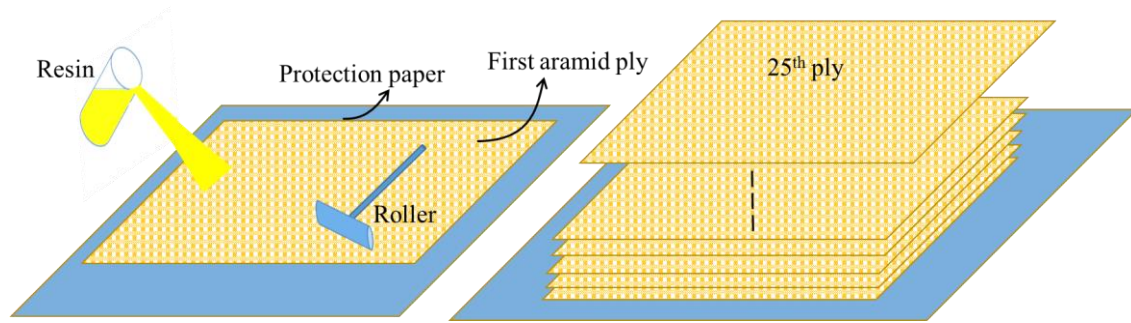


Figure A- 6: Hand layup technique for impregnated aramid structure

### *Hybrid structures:*

The hybrid structures are fabricated inside a closed wooden mold with 200x200x50mm. The hybrid structures are represented in Figure A- 7.

The hybrid structures with neat aramid plies are fabricated in two steps. The foam is fabricated inside the wooden mold, as described previously. After 12 hours, the foam block is ready, and the neat aramid plies are attached to the foam block with double-sided adhesive.

As for the hybrid structures with impregnated aramid plies, inside the wooden mold, the 25 plies of impregnated aramid plies are put on the bottom side, then the mixture of foam is poured on top. The mold is closed with clamps and put inside the hot air oven for 12 hours at 40°C.

*Hybrid Structures fabrication*

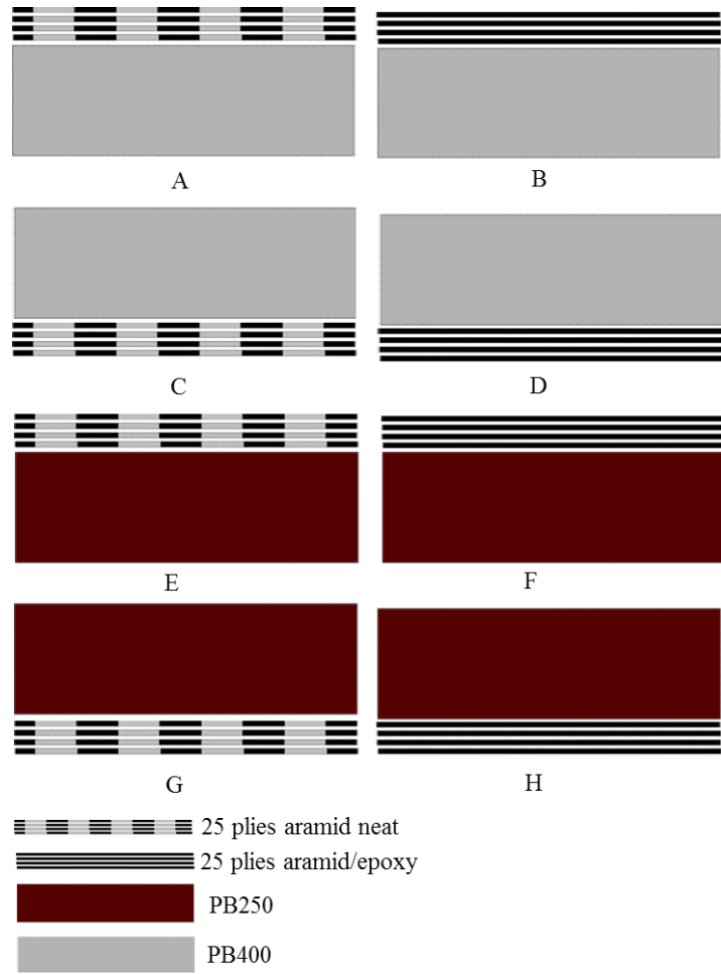


Figure A- 7: Hybrid structure with PB250 and PB400 combined with 25 plies of aramid

**Reference**

- [1] Sicomin. (2014). Systèmes époxydes pour production de mousses alvéolaires. <http://sicomin.com/produits/systemes-epoxy/moussage-structurel>
- [2] Gaches chimie. (2014). HexForce ® 20914 7 1200 ARAMID FABRIC. [https://kevra.fi/wp-content/uploads/20914\\_TDS.pdf](https://kevra.fi/wp-content/uploads/20914_TDS.pdf)
- [3] 909hoja-tecnica-Araldite LY 5052\_Aradur 5052.pdf [Internet]. [cited 2022 Jun 14]. Available from: [https://www.generaladhesivos.com/proveedor-pegamento/909hoja-tecnica-Araldite%20LY%205052\\_Aradur%205052.pdf](https://www.generaladhesivos.com/proveedor-pegamento/909hoja-tecnica-Araldite%20LY%205052_Aradur%205052.pdf).

Appendix B.            **Clay witness validation and  
modeling**

---



## **1. Introduction**

Clay witness material is typically used to measure the back face deformation left after impacting a specific structure. This section concerns the testing and modeling the clay witness used as backing material for the hybrid structures. A numerical model is proposed to model the backing material based on literature. The parameters identification methodology is achieved through a drop-weight test. The purpose of the drop weight is also to validate the consistency of the backing material based on the NIJ standard.

## **2. Material law formulation**

Clay material is widely used as backing material for impact tests; therefore, modeling such material is of extensive interest. Hernandez et al. [1] propose a methodology to simulate the behavior of soft clay using an inverse analysis technique. The clay is modeled with a Power Law plasticity material model. The extraction of the numerical model parameters is based on a drop-weight test. Li et al. [2] propose two constitutive models for the soft clay, Johnson Cook and Johnson Cook modified. The numerical model parameters are identified using an inverse identification technique.

It is challenging to find a numerical model that can describe the behavior of such material, which is highly dependent on strain, strain rate, and temperature.

The present study uses a constitutive material law already implemented in the FE software RADIOSS under the name /MAT/LAW44 (COWPER). Cowper-Symonds material law is used to model the clay. It is similar to the Johnson-Cook material law but with a different strain rate dependency formulation. Unlike Cowper-Symonds law, Johnson-Cook can consider the temperature's influence on the behavior of the material.

Cowper-Symonds material law is an elastic-plastic material law. The flow stress can be defined as follows:

$$\sigma = (a + b\varepsilon_p^n) \left( 1 + \left( \frac{\dot{\varepsilon}}{c} \right)^{\frac{1}{p}} \right) \quad (1)$$

where  $a$  is the initial plasticity yield stress,  $b$  is the plasticity hardening parameter,  $n$  is the plasticity hardening exponent,  $p$  is the strain rate exponent,  $c$  is the strain rate coefficient,  $\dot{\epsilon}$  is the strain rate, and  $\epsilon_p$  is the plastic strain.

### **3. Drop weight test**

The drop weight test aims first to validate the consistency of the backing material based on the NIJ standard's proposed method and then to identify the parameters needed for the numerical model.

The material used, “plastiline” is purchased from a commercial clay provider [3]. The firmness level of the clay is soft, and the density is around 1525 kg/m<sup>3</sup>. The clay material is confined inside a wooden box having a dimension of 300x300x60mm. The clay is heated at 40°C for three hours to reach a temperature between 38 and 40°C in different locations. The test conditions are based on the NIJ Standard 0101.06 [4].

A drop weight test is performed. A spherical shape impactor of 61 mm diameter with a weight of 1 kg is dropped from 2 m (Figure B- 1.a). A high-speed camera is placed to measure the velocity of the impactor just before the impact occurs. The maximum indentation inside the clay is measured using a displacement sensor after the impact (Figure B- 1.b).

The indentation left on the clay after impact must be between 16 and 22mm according to the NIJ standard to validate the consistency of the clay.

The maximum displacement measured is 21mm, which is in the acceptable range.

The drop weight test aims to first validate the consistency of the backing material at the proposed conditions in this section based on the NIJ standard and second to identify the parameters needed for the numerical model.

## Clay witness validation and modeling

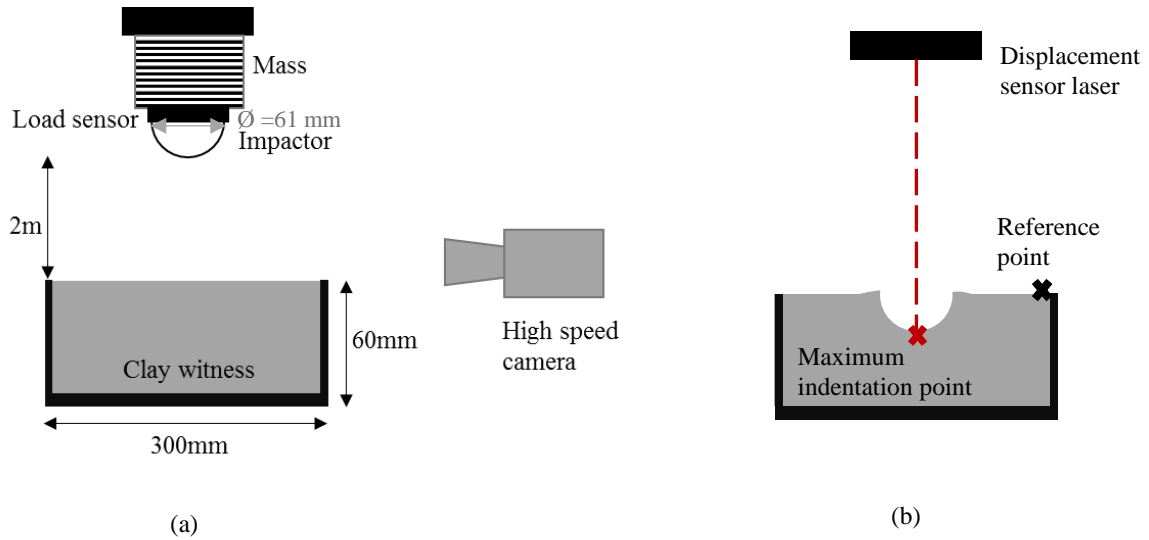


Figure B- 1: (a) Drop weigh test validation, (b) post-impact back face signature measurements of the clay witness.

### 4. Numerical modeling

The parameter identification of the material law proposed is adopted from the study [1]. The authors of the study use a Power law to model the clay. The parameter  $a$  in the Cowper Symonds is set to zero to eliminate this part of the yield stress calculation. By doing this, the flow stress calculation is similar to the one computed in [1].

Parameters  $b$ ,  $c$ , and  $n$  are adopted from [1]. The elastic modulus  $E$  is also defined based on literature. The parameter  $p$  is defined using an inverse identification technique, so the experimental and numerical curves fit. The parameters are listed in Table B- 1.

Table B- 1: Cowper-Symonds material law parameters determined based on literature and inverse identification technique [3]

$E$ (MPa)	$b$ (MPa)	$c$	$n$	$p$
5	0.175	1	0.101	5

The numerical model represents the drop weight test by a rigid wall representing the spherical indenter. The rigid wall has the same conditions as the experimental one. The fixed boundary conditions representing the wooden box are applied on the four edges of the clay and the bottom face by blocking the translation in the three directions. The indenter displacement history over time and the back face signature are extracted from the numerical model and compared to the

### Clay witness validation and modeling

experimental results. Figure B- 2 compares the experimental and numerical results of the indenter displacement throughout the time. The numerical model shows good agreement with the experimental results.

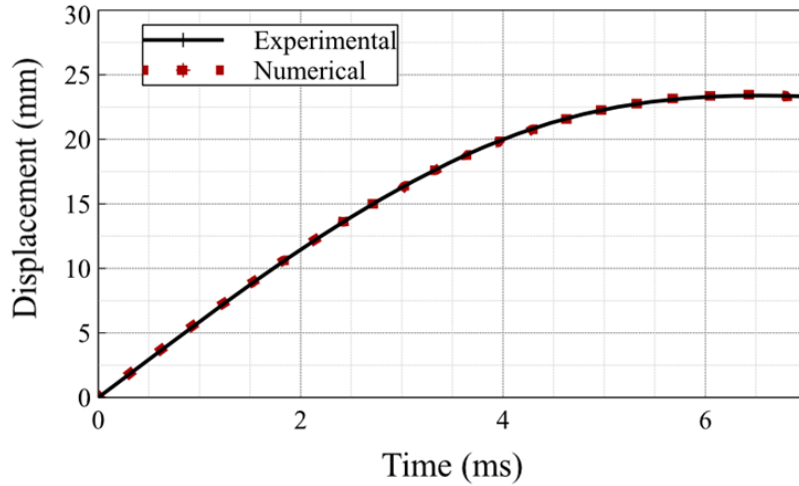


Figure B- 2: Comparison of numerical and experimental displacement versus time

In addition, Figure B- 3 shows the maximum BFS found numerically, consistent with the one found experimentally with around a 3% difference. Noting that the experimental BFS is within the proposed limits by the NIJ standards, the heating conditions and the clay consistency are validated.

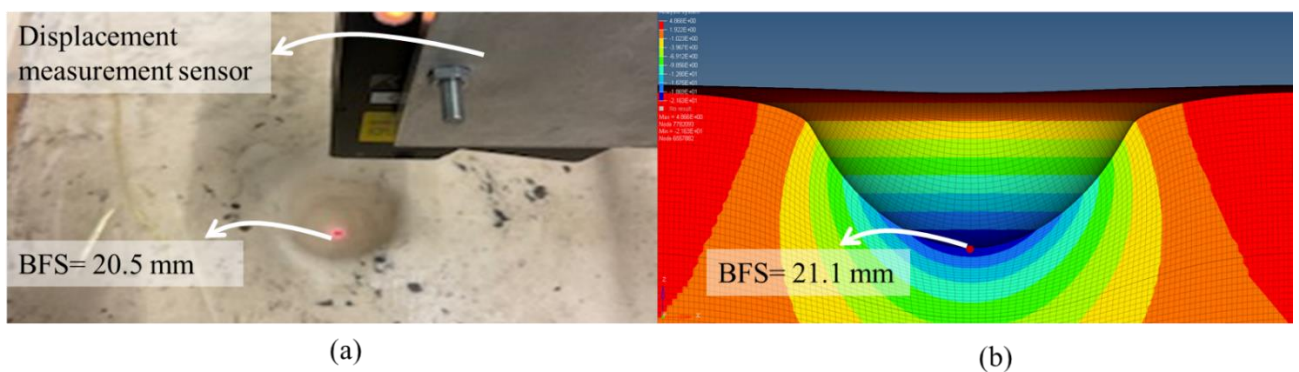


Figure B- 3: (a) Impact BFS measurement after experimental test, (b) Numerical cut showing the maximum displacement on the clay after impactor rebound

**References**

- [1] Hernandez C, Buchely MF, Maranon A. Dynamic characterization of Roma Plastilina No. 1 from Drop Test and inverse analysis. *Int J Mech Sci.* 2015;100:158–168.
- [2] Li YQ, Gao X-L, Fournier AJ, et al. Two new penetration models for ballistic clay incorporating strain-hardening, strain-rate and temperature effects. *Int J Mech Sci.* 2019;151:582–594.
- [3] Tubes 1kg et 5kg [Internet]. Plastiline. [cited 2022 Jun 14]. Available from: <https://www.plastiline.fr/tubes-1kg-et-5kg/>.
- [4] NIJ Standard 0101.06 Ballistic Resistance of Body Armor - [PDF Document] [Internet]. fdocuments.nl. [cited 2022 Jun 9]. Available from: <https://fdocuments.nl/document/nij-standard-010106-ballistic-resistance-of-body-armor.html>.





Appendix C.      **Aramid epoxy semi-continuous  
model development and parameters identification**

---



## **Model Development**

### **1. Objective**

The modeling of the aramid plies is chosen to be at the mesh level. Navarro et al. [1] first introduced this modeling strategy, which is based on the experimental observation of the behavior of woven plies subjected to impact. Pascal et al. [2] further developed this strategy to account for the weaving pattern of composite. Both authors worked on modeling carbon and glass woven plies by representing the resin by shell elements and the fibers by rod elements. This approach is called the semi-continuous approach since it can model the continuous behavior of the undamaged resin and fibers and the damaged resin with undamaged bundles of fibers that behave like a net. Despite all the advantages of this strategy, where it can capture the real damage observed during experimental impact, the purpose of the developed model is to represent the behavior of the fabric even when the resin is damaged. Therefore, in the present work, a new element has been developed to introduce a contact between the bundles of fibers which was not possible in the previous models. The following section describes the modeling strategies of the existing semi-continuous approaches and then the formulation of the developed element, which is integrated into an explicit scheme in the FE software RADIOSS through a USER subroutine.

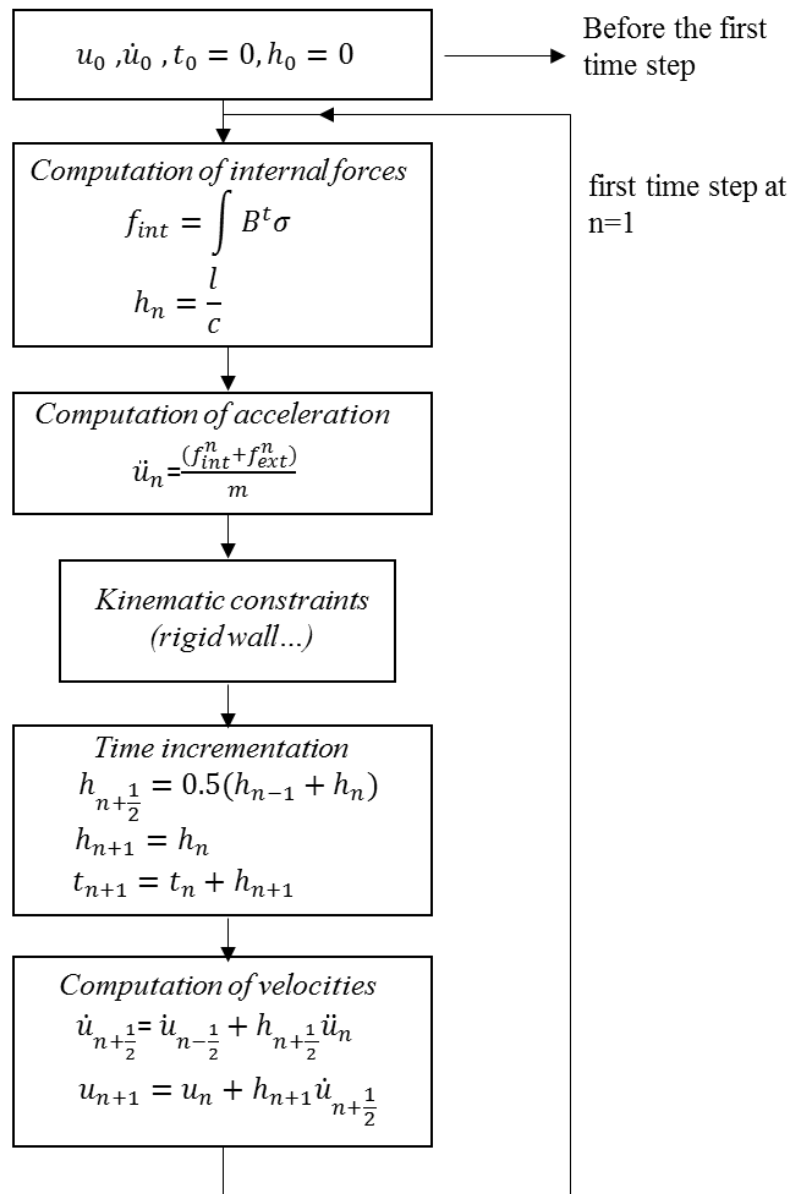
### **2. The explicit scheme in RADIOSS**

The explicit calculation is preferable when dealing with impact or crash problems with significant nonlinearity. Most of the time, implicit calculation with this type of problem fails to converge. The calculation code used in this study is RADIOSS explicit finite element code, which is a part of the commercial finite element package Hyperworks. It is based on solving the equation of motion, Equation 1, at each time step after discretizing the calculation domain into elementary meshes.

$$[M]\ddot{\mathbf{u}} = \mathbf{f}_{ext} - \mathbf{f}_{int} \quad (1)$$

Where  $[M]$  is the mass matrix,  $\ddot{\mathbf{u}}$  is the nodal acceleration vector, and  $\mathbf{f}_{ext}$  and  $\mathbf{f}_{int}$  are the external and internal nodal forces, respectively.

The central difference algorithm is used to solve the above equation of motion. Using the past value at time  $n$ , the displacement and velocity are obtained at  $n + \frac{1}{2}$ . The below flow chart describes the central difference algorithm, Algorithm C- 1. Where  $u$  is the displacement,  $\dot{u}$  is the velocity,  $\ddot{u}$  is the acceleration,  $t$  is the time,  $h$  is the time step,  $l$  is the characteristic element length,  $B$  is the shape functions gradient, and  $n$  is the number of integration points.

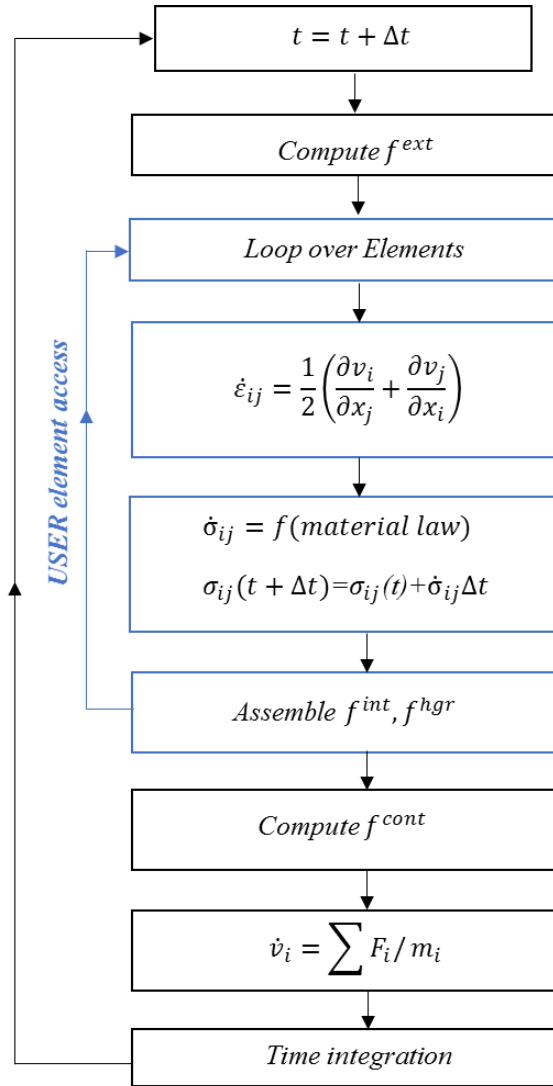


Algorithm C- 1 : Central difference algorithm [3]

The routine described in the below flow chart Algorithm C- 2 is used to calculate the internal force and the next time step. A USER element feature can be used, where a modification can be integrated. The user can code the element formulation and its behavior law. The user inputs

*Aramid epoxy semi-continuous model development and parameters identification*

in this algorithm are translational and rotational coordinates of each node, velocity, and acceleration, and the outputs are the internal nodal forces. The user defines the steps in between.



Algorithm C- 2 : RADIOSS numerical solver algorithm [3]

Where  $t$  is the time,  $\Delta t$  is the time step,  $\dot{\epsilon}_{ij}$  is the strain rate,  $\dot{\sigma}_{ij}$  is the stress rate,  $f^{int}$  is the internal force,  $f^{hgr}$  is the hourglass force,  $f^{ext}$  is the external force,  $\dot{v}_i$  is the acceleration,  $F_i$  is the inertial force, and  $m_i$  is the mass matrix.

### 3. Existing semi-continuous strategies

Navarro et al. [1] first introduced this strategy based on the experimental observation of low and medium velocity impact tests on woven carbon/epoxy and woven glass/ epoxy plies. The strategy was further improved by Pascal et al. [2]. The authors distinguish between three main scenarios of damage, Figure C- 1. First, damage appears in the resin. As a result, another behavior appears where the bundles of fibers are no longer stabilized. Finally, the total damage to fiber occurs when the maximum tensile limit of the fiber material is attained [1].

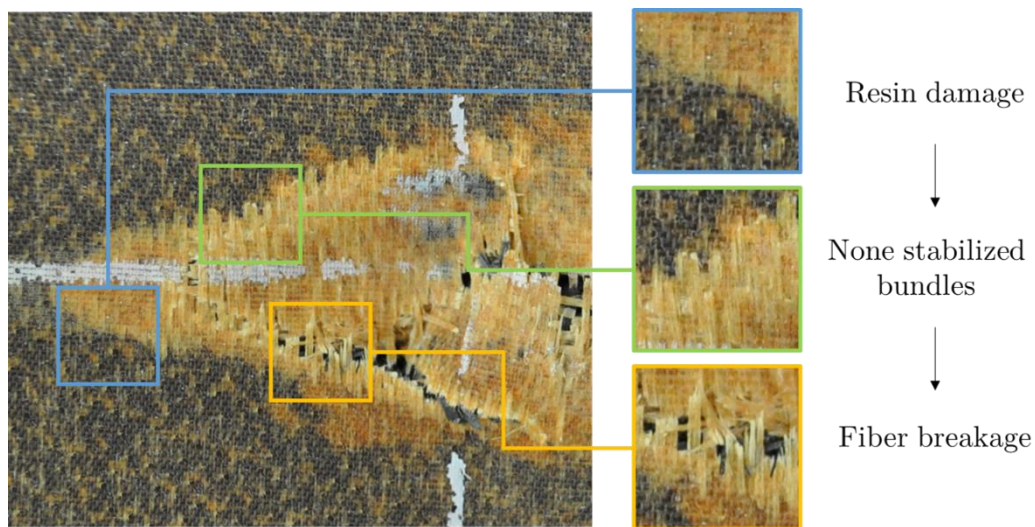


Figure C- 1: Damage mechanisms of the woven skin [1]

#### 3.1. Modeling strategies

A damageable shell element is developed to represent the resin and the physical phenomena that occur during the impact on woven plies. 1D rod elements represent the fibers. The modeling is at the woven fabric mesh scale, and both components are integrated into a USER element subroutine.

Figure C- 2 shows the modeling strategy. The rod elements are placed between two virtual nodes and connected using rigid links. The virtual nodes are placed at the height of  $h/4$  from the shell plane ( $h$  is the thickness of the ply). Five elementary bricks are assembled to replicate the fabric architecture (satin 5 in the presented case). The representation of the fiber architecture results in an improved predictive model that can capture the exact scenario of damage observed experimentally in woven laminates.

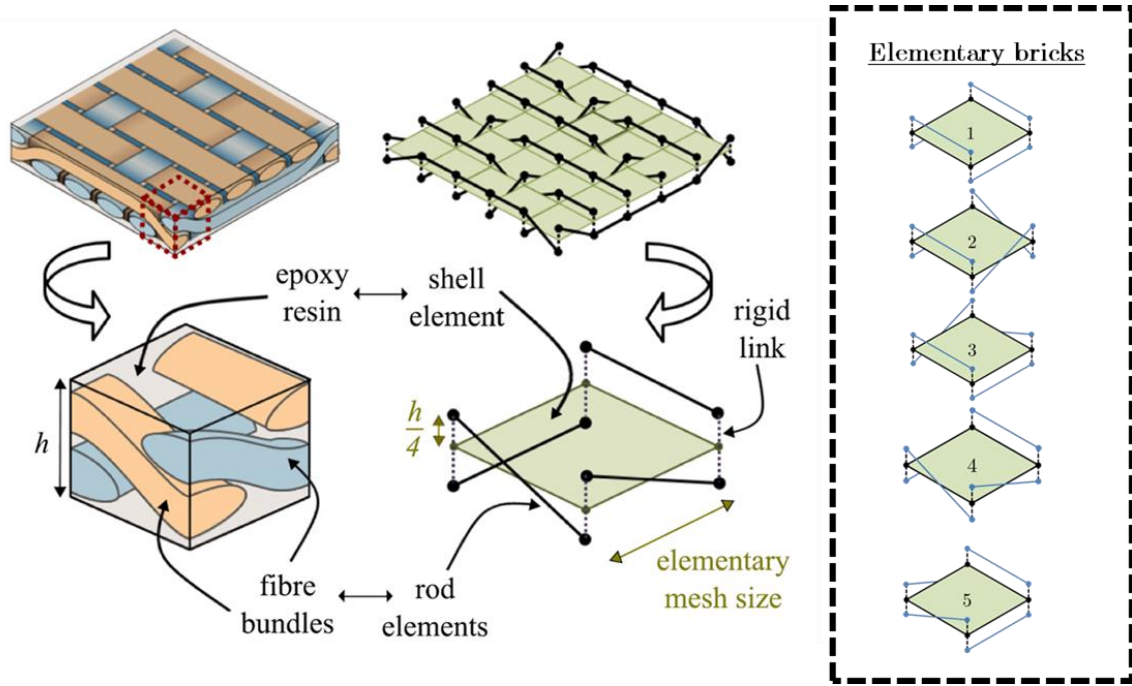


Figure C- 2: Modeling strategy of 5-harness satin woven ply [4]

### 3.2.Shell element

The formulation of the element representing the resin is a damageable shell element, based on Belytschko's formulation with four points of integration [5]. The developed model has an isotropic behavior with anisotropic damage, where two damage variables exist,  $d_1$  and  $d_2$ . The compliance matrices are differentiated between membrane/flexion  $[C]$  and out-of-plane shear  $[C_S]$  :

$$[C] = \begin{bmatrix} \frac{(1-d_1)E}{1-(1-d_1)(1-d_2)v^2} & \frac{(1-d_1)(1-d_2)vE}{1-(1-d_1)(1-d_2)v^2} & 0 \\ \frac{(1-d_1)(1-d_2)vE}{1-(1-d_1)(1-d_2)v^2} & \frac{(1-d_2)E}{1-(1-d_1)(1-d_2)v^2} & 0 \\ 0 & 0 & G_{12}d_{12} \end{bmatrix} \quad (2)$$

$$[C_S] = \begin{bmatrix} (1-d_1)G_{13} & 0 \\ 0 & (1-d_2)G_{23} \end{bmatrix} \quad (3)$$

Where  $E$  is the young modulus,  $\nu$  is the Poisson ratio, and  $G_{ij}$  is the in-plane and out-of-plane shear modulus of the resin. The damage variable  $d_{12}$  is defined by a plastic law that will be presented further in this section. The damage variables  $d_1$  and  $d_2$  are calculated through the thermodynamic forces,  $Y_1$  and  $Y_2$ , calculated from the elastic properties of the resin:

$$Y_i = \sup_{t \leq \tau} \left( \frac{E}{2(1-\nu^2)} \langle \varepsilon_{ii}^m + \varepsilon_{ii,max}^f \rangle_{\geq 0}^2 \right) (i = 1,2) \quad (4)$$

where  $\langle \varepsilon_{ii}^m + \varepsilon_{ii,max}^f \rangle_{\geq 0}$  is the positive part of the sum of the membrane strain and the maximum flexion strain in the corresponding direction.

Then, the damage variables are calculated through:

$$d = \begin{cases} \frac{\langle \sqrt{Y_i} - \sqrt{Y_0} \rangle}{\sqrt{Y_c}} & \text{if } d_i < 1 \quad (i = 1,2), \\ 1 & \text{otherwise} \end{cases} \quad (5)$$

The parameter  $Y_0$  controls the damage initiation inside the resin matrix, and  $Y_c$  controls its evolution.

It was shown experimentally that pseudo-plastic behavior governs the in-plane shear. The behavior is represented by an elastic behavior with a plastic correction based on the Newton-Raphson iteration scheme. The elastic field is defined by:

$$f = |\tau_{xy}| - K_{plas} p^\beta - \tau_0 \quad (6)$$

where  $\tau_{xy}$  is the in-plane shear stress,  $\tau_0$  is the plastic strength,  $K_{plas}$  and  $\beta$  are material parameters defining the plastic hardening law, and  $p$  is the cumulative plastic strain. The total shear strain is decomposed into elastic shear strain ( $\gamma_{xy}^e$ ) and plastic shear strain ( $\gamma_{xy}^p$ ). The plastic correction occurs when  $f > 0$ , leading to plastic shear strain update.

Then, the damage variable  $d_{12}$  can be introduced, and a plastic law defines its evolution:

$$d_{12} = \begin{cases} 0 & \text{if } \gamma_{xy}^p < \gamma_{max}^p \\ 1 & \text{if } \gamma_{xy}^p > \gamma_{max}^p \end{cases} \quad (7)$$

where  $\gamma_{max}^p$  is the in-plane shear plastic strain to rupture

### **3.3.Rod element:**

The rod elements are linked to the shell element in five different configurations to represent the weaving pattern of the woven fabric. The behavior of the rod elements is elastic, with a brittle failure in tension. The normal force of the rod  $F_{rod}$ , is calculated as follows:

$$F_{rod} = \sigma_{rod} \cdot S = E_{rod} \cdot S \cdot \varepsilon_{rod,t} \quad \text{with} \quad \varepsilon_{rod,t} = \frac{\Delta u}{L} \quad (8)$$

where  $E_{rod}$  is Young's modulus of the fibers,  $S$  is the cross-sectional area of the fibers,  $L$  is the length of the fiber, and  $\Delta u$  is the elongation.

The rupture of the fibers occurs when:

$$\varepsilon_{rod,t} > \varepsilon_{rod,t}^{max} \quad (9)$$

where  $\varepsilon_{rod,t}$  is the strain at each time step, and  $\varepsilon_{rod,t}^{max}$  is the maximum strain to failure of the fibers.

## **4. Studied material: Aramid 49**

The woven plies used in the current study are Aramid 49 with satin 4 architecture [6]. Figure C- 3.a shows a close-up of a neat aramid fabric. The elementary weaving pattern is marked with a blue dotted line box, and the mesh size is indicated with the red box. The elementary mesh size was found to be around 1mm. Identifying those elementary mesh sizes is crucial when modeling with the semi-continuous approach. Figure C- 3.b, shows the geometrical representation of the elementary pattern for the four-harness satin aramid ply with a cross-sectional view showing the warp and weft fibers.

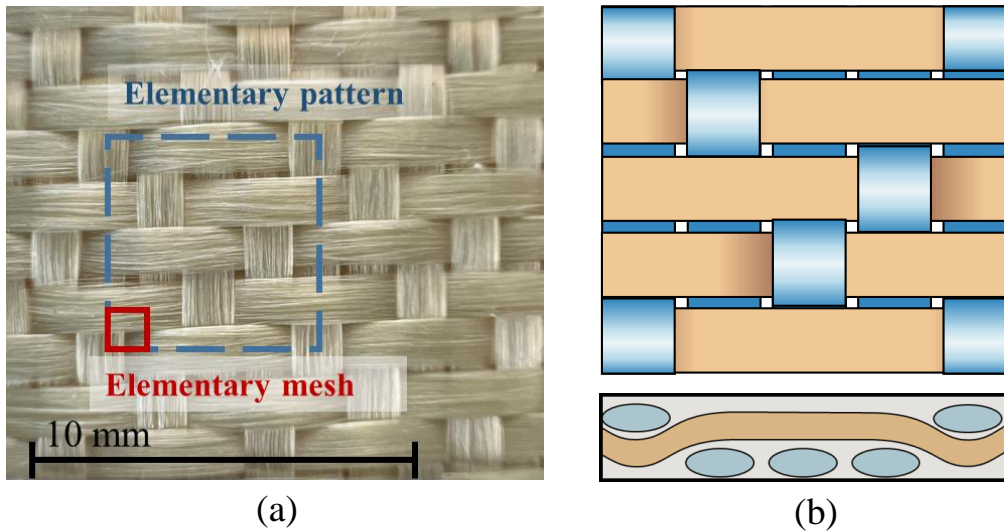


Figure C- 3: Aramid ply (a) elementary motif and mesh size and (b) geometrical representation of the elementary motif

In the present study, the aramid plies are impregnated with epoxy resin, Araldite®LY 5052 / Aradur®5052 [7], using a hand layup technique and leading to the following properties, Table C- 1:

Table C- 1: Parameters of aramid 49 / epoxy resin

Parameter	Value
Fiber volume fraction (%)	37
Areal density (g/m <sup>2</sup> )	175
Ply thickness (mm)	0.26

## 5. Development of the new element

This section describes the newly developed modeling strategy. Previously, the rod elements were placed on virtual nodes and connected by rigid links in the pre-existing models. Once the shell elements are deleted, those rigid links will always separate the rod. Consequently, the rod elements will hardly have contact with each other or any friction. The modeling strategy of the new model is represented in Figure C- 4.

The addition in the currently developed model is the establishment of an eight-node solid element, representing the resin, with rod elements representing the fibers placed on the eight real nodes. Thus, the contact between the fibers can be represented when the solid elements are



deleted. The eight nodes solid element is integrated via the USER element subroutine, while the rod elements used are the built-in truss elements of the FE software RADIOSS. A classic contact law existing in the software introduces the contact between the rod elements. In their turn, rod elements are placed to replicate the architecture of the 4 harness satin aramid plies.

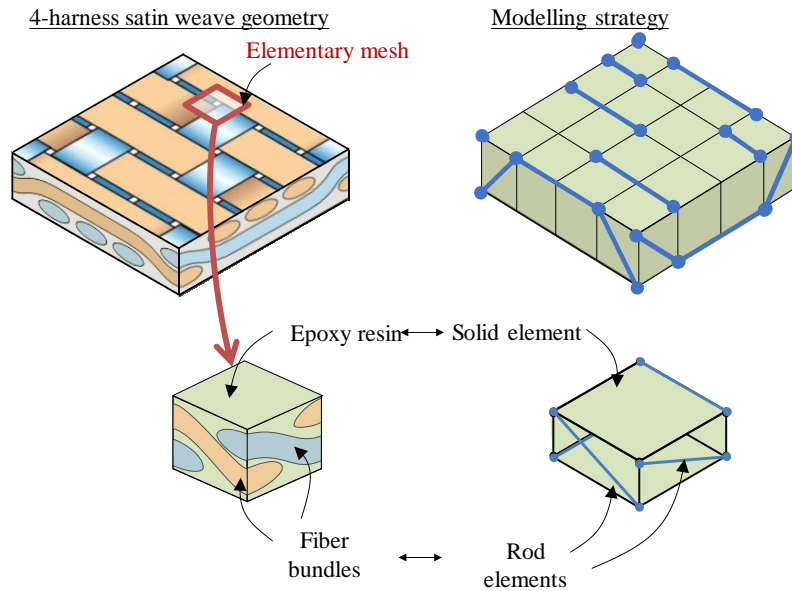


Figure C- 4: Modeling strategy of the developed model

### **5.1.Solid element**

Integrating a USER solid element gives the advantage of introducing user damage variables that can represent the damage observed experimentally.

The eight nodes hexahedral brick element is the most used in 3D finite element analysis. However, many numerical challenges might be encountered when using this type of element. A full integration scheme may lead to volumetric locking, whereas the reduced integration leads to zero energy modes, also known as hourglass modes. In the presented model, a user subroutine is used to develop a volume element with a single integration point in addition to the hourglass control treatment defined in [8].

#### **Definition of the referential and local coordinate system**

The developed solid element is isoparametric. Each element is associated with a referential parent element with simpler geometry. Hence, the referential coordinate system  $(\xi, \eta, \zeta)$  is to express the local coordinates in simpler coordinates, which will be more efficient in numerical integration [3] (Figure C- 5).

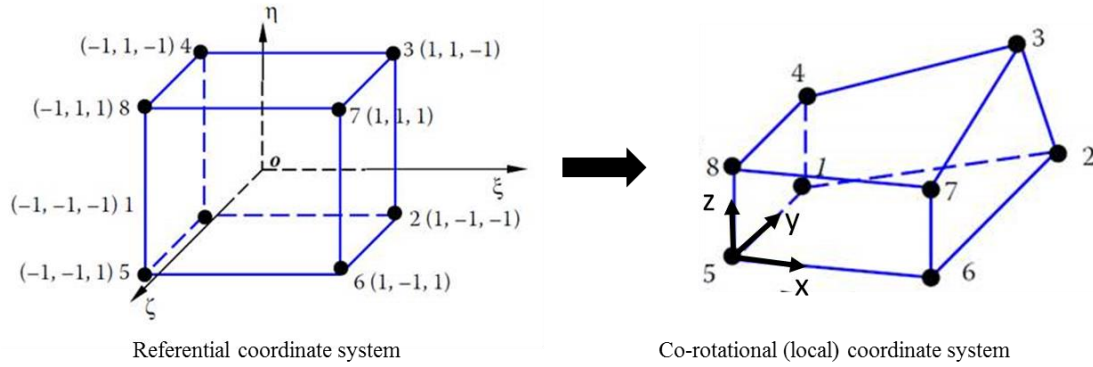


Figure C- 5: Coordinate systems of the three-dimensional isoparametric element

The geometry of the element in the system is defined by shape functions expressed in terms of  $\xi, \eta, \zeta$  [3]. The shape functions are defined in the referential coordinate system as follows:

$$\begin{aligned}
 N_1(\xi, \eta, \zeta) &= \frac{1}{8} (1 - \xi) (1 - \eta) (1 - \zeta); & N_5(\xi, \eta, \zeta) &= \frac{1}{8} (1 - \xi) (1 + \eta) (1 - \zeta) \\
 N_2(\xi, \eta, \zeta) &= \frac{1}{8} (1 - \xi) (1 - \eta) (1 + \zeta); & N_6(\xi, \eta, \zeta) &= \frac{1}{8} (1 - \xi) (1 + \eta) (1 + \zeta) \\
 N_3(\xi, \eta, \zeta) &= \frac{1}{8} (1 + \xi) (1 - \eta) (1 + \zeta); & N_7(\xi, \eta, \zeta) &= \frac{1}{8} (1 + \xi) (1 + \eta) (1 + \zeta) \\
 N_4(\xi, \eta, \zeta) &= \frac{1}{8} (1 + \xi) (1 - \eta) (1 - \zeta); & N_8(\xi, \eta, \zeta) &= \frac{1}{8} (1 + \xi) (1 + \eta) (1 - \zeta)
 \end{aligned} \tag{10}$$

Thus, the position,  $x$ , displacement,  $u$ , and velocity,  $\dot{u}$ , of any point,  $M(\xi, \eta, \zeta)$  in the referential coordinate system can be expressed as follows:

$$x(M) = \sum_{k=1}^8 N_k(\xi, \eta, \zeta) x_k; \quad u(M) = \sum_{k=1}^8 N_k(\xi, \eta, \zeta) u_k; \quad \dot{u} = \sum_{k=1}^8 N_k(\xi, \eta, \zeta) \dot{u}_k \tag{11}$$

Where  $k$  represents the number of nodes, and  $N_k$  represents the shape functions.

The transition from the referential coordinate system to the co-rotational one happens using the Jacobian matrix  $[J]$ :

$$[J](\xi, \eta, \zeta) = \begin{bmatrix} \sum_{k=1}^8 N_{k,\xi}(\xi, \eta, \zeta) \mathbf{x}_k & \sum_{k=1}^8 N_{k,\eta}(\xi, \eta, \zeta) \mathbf{x}_k & \sum_{k=1}^8 N_{k,\zeta}(\xi, \eta, \zeta) \mathbf{x}_k \\ \sum_{k=1}^8 N_{k,\xi}(\xi, \eta, \zeta) \mathbf{y}_k & \sum_{k=1}^8 N_{k,\eta}(\xi, \eta, \zeta) \mathbf{y}_k & \sum_{k=1}^8 N_{k,\zeta}(\xi, \eta, \zeta) \mathbf{y}_k \\ \sum_{k=1}^8 N_{k,\xi}(\xi, \eta, \zeta) \mathbf{z}_k & \sum_{k=1}^8 N_{k,\eta}(\xi, \eta, \zeta) \mathbf{z}_k & \sum_{k=1}^8 N_{k,\zeta}(\xi, \eta, \zeta) \mathbf{z}_k \end{bmatrix} \quad (12)$$

To express the derivatives of the shape functions in terms of the co-rotational coordinate, the inverse of the Jacobian,  $[J]^{-1}$ , matrix is needed:

$$\begin{bmatrix} N_{k,x} \\ N_{k,y} \\ N_{k,z} \end{bmatrix} = [J]^{-1} \cdot \begin{bmatrix} N_{k,\xi} \\ N_{k,\eta} \\ N_{k,\zeta} \end{bmatrix} \quad (13)$$

### **Internal force computation**

The steps for internal forces calculation will follow the same order presented in Algorithm C-2.

#### a) Strain rate:

The element strain rate is calculated at the integration points  $P_i(\xi_i, \eta_i, \zeta_i)$  using the velocities  $\dot{\mathbf{u}}_k = (\dot{u}_{xk}, \dot{u}_{yk}, \dot{u}_{zk})$ . Noting that k denotes the nodes of the element.

$$\begin{bmatrix} \dot{\epsilon}_{xx} \\ \dot{\epsilon}_{yy} \\ \dot{\epsilon}_{zz} \\ 2\dot{\epsilon}_{xy} \\ 2\dot{\epsilon}_{xz} \\ 2\dot{\epsilon}_{zy} \end{bmatrix} = \sum_{k=1}^8 [B] \cdot \begin{bmatrix} \dot{u}_{xk} \\ \dot{u}_{yk} \\ \dot{u}_{zk} \end{bmatrix} \quad (14)$$

where [B] is the strain-displacement matrix at node k, its components are the derivative of the shape functions at the points of integration  $P_i$ :

$$[B] = \begin{bmatrix} N_{k,x}^i & 0 & 0 \\ 0 & N_{k,y}^i & 0 \\ 0 & 0 & N_{k,z}^i \\ N_{k,x}^i & N_{k,y}^i & 0 \\ N_{k,x}^i & 0 & N_{k,z}^i \\ 0 & N_{k,y}^i & N_{k,z}^i \end{bmatrix} \quad (15)$$

b) Stresses and compliance matrix

The material law used in the model is orthotropic, with three damage variables in order to represent the cracks in each direction. The damage variable calculation will be discussed later in this section. The damageable stiffness matrix [C] is presented below:

$$[C] = \begin{bmatrix} \frac{(1-v_{yz} v_{zy} \cdot d_{zy})E_{xx}^*}{1-v_{deg}} & \frac{(v_{yx}(1-d_y)+v_{zx} v_{yz} \cdot d_{zy})E_{xx}^*}{1-v_{deg}} & \frac{(v_{zx}(1-d_z)+v_{yx} v_{zy} \cdot d_{zy})E_{xx}^*}{1-v_{deg}} & 0 & 0 & 0 \\ \frac{(v_{xy}(1-d_x)+v_{zy} v_{xz} \cdot d_{xz})E_{yy}^*}{1-v_{deg}} & \frac{(1-v_{xz} v_{zx} \cdot d_{xz})E_{yy}^*}{1-v_{deg}} & \frac{(v_{zy}(1-d_z)+v_{xy} v_{zx} \cdot d_{xz})E_{yy}^*}{1-v_{deg}} & 0 & 0 & 0 \\ \frac{(v_{xz}(1-d_x)+v_{xy} v_{yz} \cdot d_{xy})E_{zz}^*}{1-v_{deg}} & \frac{(v_{yz}(1-d_y)+v_{yx} v_{xz} \cdot d_{xy})E_{zz}^*}{1-v_{deg}} & \frac{(1-v_{xy} v_{yx} \cdot d_{xy})E_{zz}^*}{1-v_{deg}} & 0 & 0 & 0 \\ 0 & 0 & 0 & 2G_{xy}^* & 0 & 0 \\ 0 & 0 & 0 & 0 & 2G_{xz}^* & 0 \\ 0 & 0 & 0 & 0 & 0 & 2G_{zy}^* \end{bmatrix} \quad (16)$$

Where,  $v_{deg} = v_{xy} v_{yx} d_{xy} \times v_{xz} v_{zx} d_{xz} \times v_{yz} v_{zy} d_{zy} - 2(v_{yx} v_{yz} v_{xz} d_{xy}(1 - d_z))$

$E_{xx}^* = E_{xx}(1 - d_x)$ ,  $E_{yy}^* = E_{yy}(1 - d_y)$ ,  $E_{zz}^* = E_{zz}(1 - d_z)$ ,  $G_{xy}^* = G_{xy} \cdot d_{shear}$ ,

$G_{xz}^* = G_{xz} \cdot d_{xz}$ ,  $G_{yz}^* = G_{yz} \cdot d_{zy}$ ,  $d_{xy} = (1 - d_y)(1 - d_x)$ ,  $d_{xz} = (1 - d_z)(1 - d_x)$ ,  $d_{yz} = (1 - d_y)(1 - d_z)$ .

Hence, stresses can be calculated at time  $t + \Delta t$ , at the integration points  $P_i(\xi_i, \eta_i, \zeta_i)$ , using the strain rate and the compliance matrix:

$$\sigma(\xi_i, \eta_i, \zeta_i)|_{t+\Delta t} = \begin{bmatrix} \sigma_{xx} \\ \sigma_{xy} \\ \sigma_{xz} \\ \sigma_{xy} \\ \sigma_{xz} \\ \sigma_{zy} \end{bmatrix} = \sigma(\xi_i, \eta_i, \zeta_i)|_t + [C] \dot{\epsilon}(\xi_i, \eta_i, \zeta_i)|_t \Delta t \quad (17)$$

c) Damage variables:

The developed brick element distinguishes between three damage variables for the linear and out-of-plane shear stresses  $d_i$  ( $i = x, y, \text{ and } z$ ). For the in-plane shear stresses, there is a single damage variable  $d_{shear}$ .

The evolution of the damage variables,  $d_i$ , is based on the thermodynamic forces, also known as energy release rates:

$$d_i = \sup_{t \geq \tau} \begin{cases} 0 & \text{if } Y_i < Y_0 \\ \frac{\sqrt{Y_i} - \sqrt{Y_0}}{\sqrt{Y_c}} & \text{if } Y_i \geq Y_0 \\ 1 & \text{if } \sqrt{Y_i} - \sqrt{Y_0} > \sqrt{Y_c} \end{cases} \quad (18)$$

The parameter  $Y_0$  controls the damage initiation inside the resin matrix, and  $Y_c$  controls its evolution.  $Y_i$ , which is the thermodynamic force in the local direction  $i$ , can be calculated through:

$$Y_i = \frac{\partial W_e}{\partial d_i} \quad (19)$$

Where  $W_e$  is the elastic energy.

The elastic energy can be calculated as follows:

$$W_e = \int_V \frac{1}{2} \cdot \sigma_{ij} \cdot \varepsilon_{ij} \cdot dV \quad (20)$$

where  $\sigma_{ij}$ , and  $\varepsilon_{ij}$  ( $i=x,y,z$ ) are the stresses and strains, respectively.

The in-plane shear damage is based on the pseudo-plastic behavior on the aramid plies when loaded at  $\pm 45^\circ$ . The same behavior was observed in Navarro et al. and Pascal et al. work [1,2] with carbon/epoxy and glass/Epoxy. Therefore, the exact formulation is applied to compute the damage variable  $d_{shear}$ . The behavior is represented by an elastic behavior with a plastic correction. The elastic field  $f$  is defined by:

$$f = |\tau_{xy}| - K_{plas} p^\beta - \tau_0 \quad (21)$$

where  $\tau_{xy}$  is the in-plane shear stress,  $\tau_0$  is the yield stress,  $K_{plas}$  and  $\beta$  are material parameters defining the plastic hardening law, and  $p$  is the cumulative plastic strain. If the elastic field  $f$  is greater than 0, the plastic correction occurs based on the Newton-Raphson iteration scheme to update the plastic shear strain,  $\gamma_{xy}^p$ , and  $p$ :

$$\gamma_{xy} = \gamma_{xy}^e + \gamma_{xy}^p \quad (22)$$

where  $\gamma_{xy}$  is the total shear strain and  $\gamma_{xy}^e$  is the elastic shear strain.

Hence, the damage variable  $d_{shear}$  presented:

$$d_{shear} = \begin{cases} 0 & \text{if } \gamma_{xy}^p < \gamma_{max}^p \\ 1 & \text{if } \gamma_{xy}^p > \gamma_{max}^p \end{cases} \quad (23)$$

where  $\gamma_{max}^p$  is the in-plane shear plastic strain to rupture.

d) Internal force computation:

The final step is to compute the internal forces. For the numerical integration of a three-dimensional problem, the domain  $\Omega_e$  is converted to another one by a change of variable, where  $\xi$ ,  $\eta$ , and  $\zeta$  are between -1 and 1. To compute the integral numerically, Gaussian quadrature is used to convert the integrals into summation, using a single gauss point.

$$\int_{\Omega_e} f(x, y, z) dx dy dz = \iiint_{-1}^1 f(\xi, \eta, \zeta) J(\xi, \eta, \zeta) d\xi d\eta d\zeta = \sum_{i=1}^{nIP} w(\xi_i, \eta_i, \zeta_i) f(\xi_i, \eta_i, \zeta_i) \quad (24)$$

As discussed previously, the present model is formulated with a reduced integration scheme, where one point of integration is considered at the center of the element ( $nIP = 1$ ), having the following coordinates and weight:

Table C- 2: Gauss single point of integration position and corresponding weight

$i$	$\xi$	$\zeta$	$\eta$	$w$
1	0	0	0	8

At this level, the constant part of the internal force can be calculated using the above mechanical variables at a single gauss point of integration for the eight nodes of the brick:

$$\begin{aligned} f_{XI} &= \int_{\Omega} \left( \sigma_{xx} \cdot \frac{\partial N_k}{\delta_x} + \sigma_{xy} \cdot \frac{\partial N_k}{\delta_y} + \sigma_{xz} \cdot \frac{\partial N_k}{\delta_z} \right) \cdot d\Omega = w \cdot J \cdot \left( \sigma_{xx} \cdot \frac{\partial N_k}{\delta_x} + \sigma_{xy} \cdot \frac{\partial N_k}{\delta_y} + \sigma_{xz} \cdot \frac{\partial N_k}{\delta_z} \right) \\ f_{YI} &= \int_{\Omega} \left( \sigma_{yy} \cdot \frac{\partial N_k}{\delta_y} + \sigma_{yx} \cdot \frac{\partial N_k}{\delta_x} + \sigma_{yz} \cdot \frac{\partial N_k}{\delta_z} \right) \cdot d\Omega = w \cdot J \cdot \left( \sigma_{yy} \cdot \frac{\partial N_k}{\delta_y} + \sigma_{yx} \cdot \frac{\partial N_k}{\delta_x} + \sigma_{yz} \cdot \frac{\partial N_k}{\delta_z} \right) \quad (25) \\ f_{ZI} &= \int_{\Omega} \left( \sigma_{zz} \cdot \frac{\partial N_k}{\delta_z} + \sigma_{zx} \cdot \frac{\partial N_k}{\delta_x} + \sigma_{zy} \cdot \frac{\partial N_k}{\delta_y} \right) \cdot d\Omega = w \cdot J \cdot \left( \sigma_{zz} \cdot \frac{\partial N_k}{\delta_z} + \sigma_{zx} \cdot \frac{\partial N_k}{\delta_x} + \sigma_{zy} \cdot \frac{\partial N_k}{\delta_y} \right) \end{aligned}$$

e) Hourglass force

The one point of integration generated hourglass energy modes. There are 12 hourglass modes, four modes of each of the three coordinate directions (Figure C- 6),  $\Gamma$  is the hourglass mode vector defined in Flanagan & Belytschko [8].

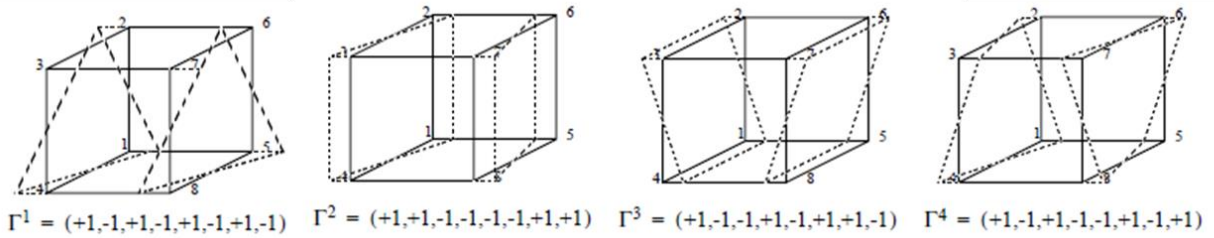


Figure C- 6: Hourglass modes [3]

To prevent those zero-energy modes, the treatment proposed by Flanagan & Belytschko [8] is integrated into the solid element formulation.

The hourglass internal forces are computed as follows:

$$(f_{ii}^{int})^H = \sum_{\alpha=1}^4 Q_{i\alpha} \gamma_i^\alpha \quad (26)$$

Where:

- $i$  is the direction index, running from 1 to 3,
- $I$  is the node index, from 1 to 8,
- $\alpha$  is the hourglass mode index, from 1 to 4,
- $Q_{i\alpha}$  is the 12 generalized hourglass stresses,
- $\gamma_i^\alpha$  is the hourglass shape vector.

Several variables must be defined to compute the hourglass internal force computation. Four base vectors define the 12 hourglass modes,  $\Gamma_I^\alpha$ :



Table C- 3: Hourglass base vector

	$\alpha = 1$	$\alpha = 2$	$\alpha = 3$	$\alpha = 4$
$\Gamma_1$	1	1	1	1
$\Gamma_2$	1	-1	-1	-1
$\Gamma_3$	-1	-1	1	1
$\Gamma_4$	-1	1	-1	-1
$\Gamma_5$	-1	-1	1	-1
$\Gamma_6$	-1	1	-1	1
$\Gamma_7$	1	1	1	-1
$\Gamma_8$	1	-1	-1	1

Accordingly,  $\gamma_I^\alpha$  can be computed as follows:

$$\gamma_I^\alpha = \Gamma_I^\alpha - \frac{1}{V} (N_{I,i} \cdot \sum_{j=1}^8 x_i^j \Gamma_j^\alpha) \quad (27)$$

where  $V$  is the element volume, computed by integrating the determinant of the Jacobian matrix over the unit cube.

Consequently, after getting  $\gamma_I^\alpha$ , the *hourglass nodal velocities*  $\frac{\delta q_i^\alpha}{\delta t}$  is computed as follows, where  $v_{il}$  is the nodal velocity:

$$\frac{\delta q_i^\alpha}{\delta t} = \gamma_I^\alpha \cdot v_{il} \quad (28)$$

The hourglass nodal velocities  $\frac{\delta q_i^\alpha}{\delta t}$  will be used to get the 12-*hourglass rates*,  $\dot{Q}_{i\alpha}$ , noting that the indices  $i, j$ , and  $k$  are permuted according to the below table:

Table C- 4: Permutations of i, j, k

<i>i</i>	<i>j</i>	<i>k</i>
1	2	3
1	3	2
2	3	1
2	1	3
3	1	2
3	2	1

Then,

$$\begin{aligned}
 \dot{Q}_{ii} &= \mu [(H_{jj} + H_{kk})\dot{q}_{ii} + H_{ij}\dot{q}_{jj} + H_{ik}\dot{q}_{kk}], \\
 \dot{Q}_{ij} &= 2\mu \left[ \frac{1}{1-\nu} H_{ii}\dot{q}_{ij} + \nu H_{kk}\dot{q}_{ii} \right], \\
 \dot{Q}_{i4} &= 2\mu \left( \frac{1+\nu}{3} \right) H_{ii}\dot{q}_{i4},
 \end{aligned} \tag{29}$$

where,

$$\begin{aligned}
 H_{ii} &= \frac{1}{3} \frac{(\Lambda_j^T x_j)(\Lambda_i^T x_i)}{(\Lambda_k^T x_k)} \quad i \neq j \neq k, \\
 H_{ij} &= \frac{1}{3} (\Lambda_k^T x_k) \quad i \neq j \neq k
 \end{aligned} \tag{30}$$

and  $\mu$  is the shear modulus, and  $\nu$  is the Poisson ratio of the material.

In the above equation,  $x_k$  is the nodal coordinates in the co-rotational system, and  $\Lambda_j$  represents an  $8 \times 1$  matrices of the referential coordinates  $(\xi, \eta, \zeta)$ :

Table C- 5: The linear base vectors  $\Lambda_j$

<i>Node</i>	$\Lambda_1$	$\Lambda_2$	$\Lambda_3$
<i>1</i>	-1	-1	-1
<i>2</i>	1	-1	-1
<i>3</i>	1	1	-1
<i>4</i>	-1	1	-1
<i>5</i>	-1	-1	1
<i>6</i>	1	-1	1
<i>7</i>	1	1	1
<i>8</i>	-1	1	1

Finally, the hourglass stress can be computed from the hourglass stress rate by applying the below relationship:

$$Q_{i\alpha}^{n+1} = Q_{i\alpha}^n + \Delta t \dot{Q}_{i\alpha}^{n-\frac{1}{2}} \quad (31)$$

Therefore, the hourglass internal forces can be calculated using Equation 26, and the total internal force can be deduced by adding the constant internal force to the hourglass internal force:

$$\{f_I^{int}\} = \{(f_I^{int})^0\} + \{(f_I^{int})^H\} \quad (32)$$

## 5.2.Rod Element

### Formulation and cross-sectional area calculation

To represent the bundles of fibers, rod elements already exist in RADIOSS as truss elements are used.

Rod elements have an elastic behavior with a brittle failure in tension. A maximum strain criterion represents the failure in the rod elements. As for the cross-sectional area,  $S$  of the rod elements is defined similarly to the existing semi-continuous approach [1]. Figure C- 7 shows the elementary mesh of the woven fabric, representing the volume that the resin and the fibers occupy. Where  $h$  is the ply thickness,  $V_f$  is the fiber volume fraction, and  $L$  is the mesh size.

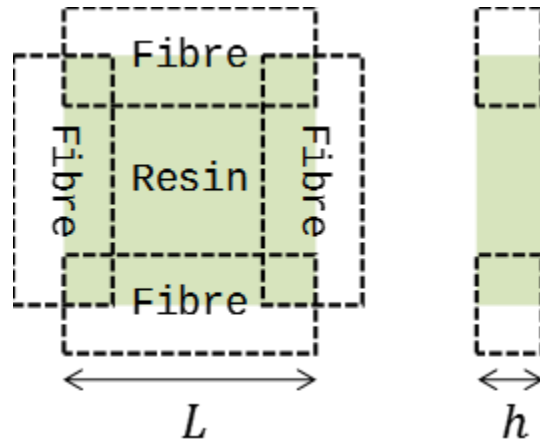


Figure C- 7: Elementary mesh representation [1]

Based on the schematic of the elementary mesh, the cross-section can be deduced from:

$$V_f = \frac{\Omega_f}{\Omega_f + \Omega_r} = \frac{2LS}{2LS + hL^2} \rightarrow S = \frac{hLV_f}{2(1-V_f)} \quad (33)$$

where,  $\Omega_f$  and  $\Omega_r$  are the volumes occupied by the fibers, and the resin, respectively.

The fiber volume fraction for the aramid/epoxy plies is defined by taking the weight of the ply before and after impregnation. Knowing the weight of resin ( $W_{resin}$ ) and fibers ( $W_{fiber}$ ) in addition to the density ( $\rho_{fiber}, \rho_{resin}$ ), the volumes ( $V_{fiber}, V_{resin}$ ) can be calculated according to

$$V_{fiber} = \frac{W_{fiber}}{\rho_{fiber}}, V_{resin} = \frac{W_{resin}}{\rho_{resin}} \quad (34)$$

Therefore,  $V_f$  can be determined:

$$V_f = \frac{V_{fiber}}{V_{fiber} + V_{resin}} \quad (35)$$

All the values concerning the cross-section calculations are summarized in the below table.

Table C- 6: Cross-sectional area calculation parameters

Parameter	L (mm)	h (mm)	$V_f$	S (mm <sup>2</sup> )
Value	1	0.26	0.37	0.078

### 5.3.Rod to-rod contact

A penalty-based edge-to-edge contact is implemented to introduce the contact between the rod elements and integrate the friction. The contact law “Interface type 11” built-in RADIOSS simulates the impact between truss elements by defining a minimum gap to activate the contact. The contact is detected when the distance between the two edges is smaller than the sum of the gaps between the two edges,  $N_i$ , Figure C- 8. A cylindrical volume defines the gap around each edge.

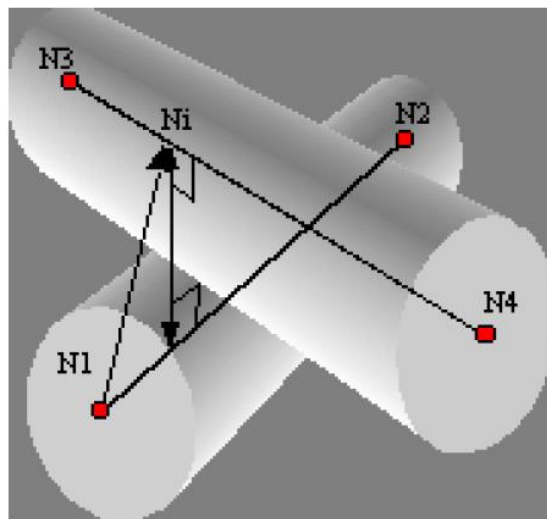


Figure C- 8: Schematic of the gap between two truss elements [3]

The contact input parameters include a minimum stiffness, Coulomb friction coefficient, and a minimum gap  $Gap_{min}$ . The recommended value for the stiffness is  $St_{min} = 1000$  N/mm to avoid too soft contact.  $Gap_{min}$  is calculated according to the cross-sectional area of the rod element.

## **Parameters Identification**

### **1. Introduction**

This section deals with the parameters identification for the numerical model of the aramid/epoxy woven composite. The main two components used to model the aramid plies are the volume elements, representing the epoxy resin, and the 1D rod elements, representing the bundles of fibers. The strategy involves using numerous parameters that represent the physics observed experimentally. The parameters identification method will be presented in the following section.

### **2. Parameters identification**

#### **2.1. Identification strategy**

Aramid fibers with a four-harness satin weave architecture impregnated with hand layup techniques are used in this work. This section aims to identify the material parameters needed for the numerical model. As discussed in the previous section, the model is composed of resin modeled as a solid element and bundles of fibers represented as 1D rod elements.

Experimental tests are conducted to identify the behavior of the aramid/epoxy composite correctly. Three main tests took place:

- Quasi-static tensile tests on specimens with  $(0/90)^\circ$  orientation impregnated with epoxy resin and neat.
- Quasi-static tensile tests on specimens with  $(\pm 45)^\circ$  orientation for impregnated plies
- Drop weight indentation tests on impregnated aramid plies

First, the purpose is to define the parameters of the aramid plies before impregnation, then define the parameters of the resin matrix. In addition, indentation tests are performed to adjust the damage parameters by comparing the numerical and experimental results. The parameters and the experimental tests associated with them are summarized in Table C- 7.

Table C- 7: Experimental test and parameters for aramid/epoxy modeling

Parameter	Symbole	Identification test
Fibers Young's Modulus	$E_f$	Tensile test for neat aramid at (0/90) <sup>o</sup> orientation
Maximum strain to failure	$\varepsilon_{max}$	
Resin Young's Modulus	$E_m$	Tensile test for aramid/epoxy at (0/90) <sup>o</sup> orientation
Shear modulus (MPa)	$G_{xy} = G_{iz}$	Tensile test for aramid/epoxy at $\pm 45^\circ$ orientation
Elastic limit (MPa)	$\tau_0$	
Plasticity parametere 1	$K_{plas}$	
Plasticity parametere 2	$\beta$	
Rupture plastic strain	$\gamma_{max}^p$	
Energy release rate-initiation	$Y_0$	Drop weight impact on 3plies of aramid/epoxy
Energy release rate-evolution	$Y_c$	

## 2.2.Quasi-static tensile tests

### a) Experimental conditions:

The quasi-static tensile tests at (0/90) ° and  $\pm 45^\circ$  orientation are realized through an INSTRON universal tensile machine. The dimensions of the specimens and configurations are shown in Figure C- 9. They are made of one ply of woven fabric with a thickness of around 0.26 mm, and five samples of each configuration are tested.

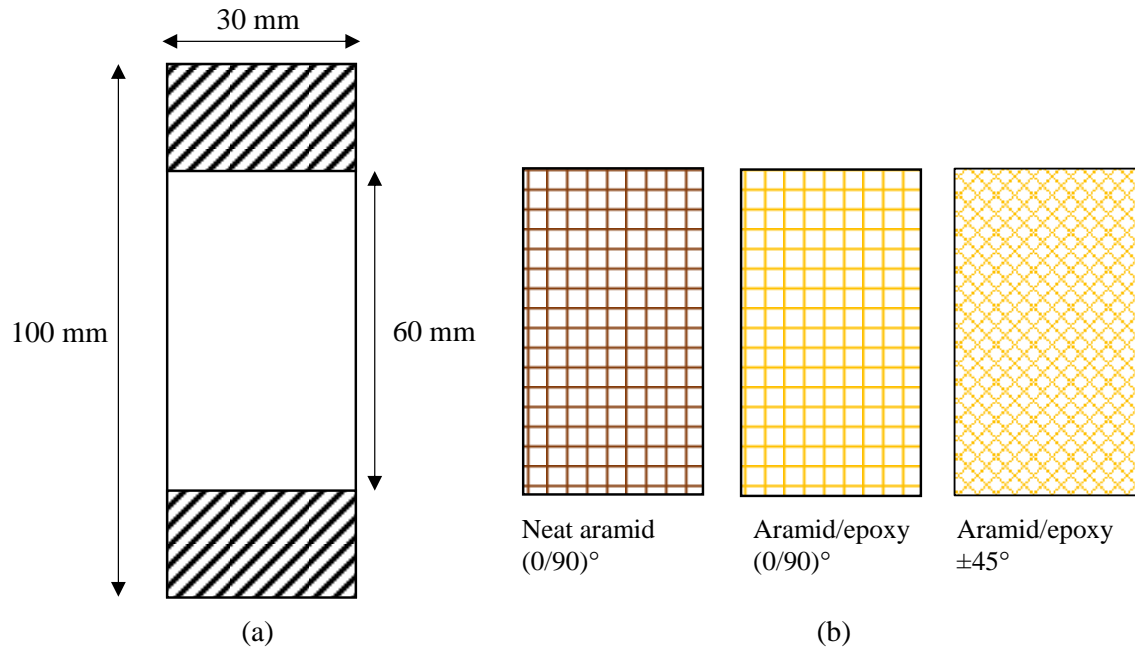


Figure C- 9: Tensile tests specimens (a) dimensions and (b) configurations

### 2.3. Tensile test for (0/90)° orientation

-Neat aramid:

The tensile tests conducted on *neat aramid* lead to the definition of Young's modulus of the fibers and the maximum strain to failure. The numerical modeling of this test is done using a rigid body on the extremities of the modeled sample to represent the boundary condition and to impose a velocity of  $1\text{m}\cdot\text{s}^{-1}$ . Recalling that the mesh size defined experimentally is  $1\text{mm}$ . Since the aramid plies are neat in this test, the cross-sectional area  $S$  is calculated as follows:

$$S_{fiber} = \frac{m}{\rho_{fiber} L} \quad (36)$$

where  $m$  is the weight of the fibers,  $\rho_{fiber}$  is the density of the fibers, and  $L$  is the length of the fibers.

The load-displacement curves of the tensile test on neat aramid plies are presented in Figure C-10. The modulus of the fibers,  $E_f$ , monitors the slope of the curves, and the maximum strain to failure,  $\varepsilon_{max}$ , is responsible for the final rupture of the sample. Both parameters are defined numerically by reverse identification, comparing the experimental and numerical curves, and minimizing the difference between the two.



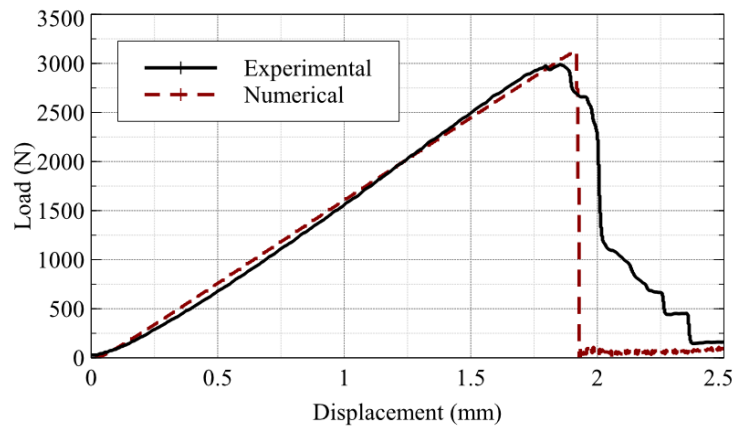


Figure C- 10 : Comparison of experimental/numerical tensile test on neat aramid ply

-Aramid/epoxy composite:

The aramid/epoxy composite is fabricated with a hand layup method; therefore, the fiber volume fraction is calculated with Equation 35 ( $V_f = 0.37$ ). The numerical load case and boundary conditions are similar to the previous neat aramid test. This test aims to define Young's modulus of the resin  $E_m$ . The supplier gives the Poisson's ratio of the resin, which is equal to 0.3. As defined previously, the fibers represented by 1D rod elements have  $E_f$  as fiber modulus and  $\varepsilon_{max}$  as the maximum strain to failure. When integrated with the resin, the cross-sectional area of the fibers is calculated based on Equation 33. A reverse identification technique is used to define the modulus of the resin. Results are shown in Figure C- 11.

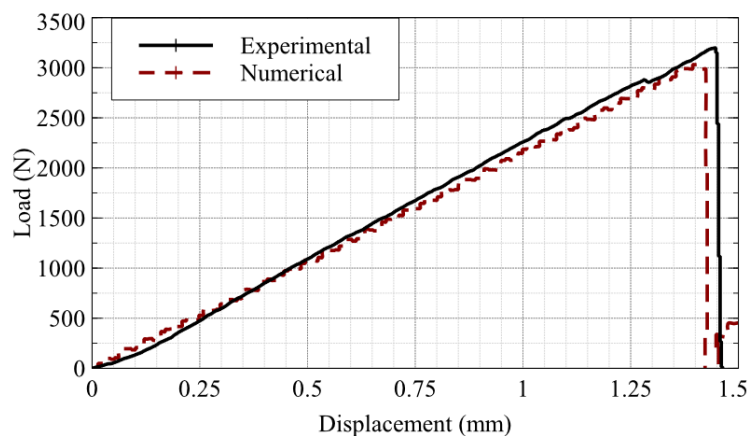


Figure C- 11: Comparison of experimental/numerical tensile test on impregnated aramid

Table C- 8 summarizes the parameters identified with the tests above.

Table C- 8: Parameters identified with the tensile test for plies at (0/90) ° orientation

Parameter	Symbole	Value
Fiber modulus(Gpa)	$E_f$	45
Fiber tensile strain failure(%)	$\varepsilon_{max}$	1.7
Epoxy resin modulus(Gpa)	$E_m$	4.5

#### 2.4.Tensile test for $\pm 45^\circ$ orientation

Pseudo-plastic behavior was observed during a quasi-static tensile test with  $\pm 45^\circ$  orientation for impregnated aramid. The shear modulus monitors the linear part of the load-displacement curve  $G_{xy}$ . The shear modulus  $G_{xy}$  is supposed to be equal to  $G_{xz} = G_{zy}$  since finding it experimentally is complicated, and its influence is negligible on the behavior of the composite ply. Three main parameters monitor the elastoplastic material law,  $K_{plas}$ ,  $\tau_0$ , and  $\beta$ . A maximum plastic deformation  $\gamma_{max}^p$  achieves the final rupture. Results are shown in Figure C-12. Figure C- 13 shows the experimental and numerical damage to the specimens.

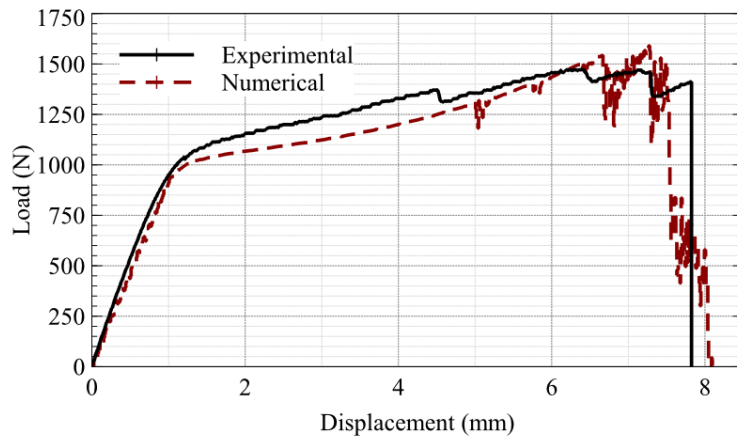


Figure C- 12: Comparison of experimental/numerical tensile test on aramid/epoxy at  $\pm 45^\circ$  orientation



Figure C- 13: Comparison of experimental/numerical damage of the aramid/epoxy at  $\pm 45^\circ$  orientation

The parameters identified are listed in Table C- 9.

Table C- 9: Parameters identified for the elastoplastic behavior of the ( $45^\circ$ ) oriented woven aramid

Parameter	Symbole	Value
Shear modulus (MPa)	$G_{12}$	3500
Elastic limit (MPa)	$\tau_0$	50
Plasticity parametere 1 (MPa)	$K_{plas}$	25
Plasticity parametere 2	$\beta$	0.2
Rupture plastic strain (%)	$\gamma_{max}^p$	26

## 2.5.Drop weight impact test

### Experimental test conditions

To identify the damage parameters of the impregnated woven ply, a drop weight test was performed on three impregnated plies. The indenter has a hemispherical shape, made of steel, having a weight of 2 kg and a diameter of 16 mm. The impact velocity reached 6m/s. A 100x100x0.26mm aramid/epoxy plies are simply posed on a clay witness having a thickness of 25 mm, Figure C- 14. The clay witness serves as a boundary condition. A load sensor is used to record the effort throughout the time.

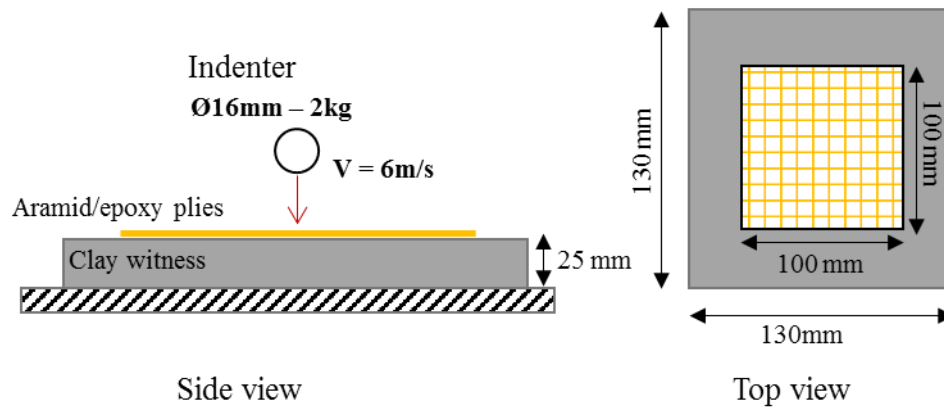


Figure C- 14: Drop weight apparatus on three aramid/ epoxy plies

The energy release rates control the damage parameters of the matrix,  $Y_0$  and  $Y_c$ . However, the estimation of their values is complicated to measure directly experimentally. The identification of those parameters is based on the data found in the literature for similar materials and by comparing the crack length between experimental and numerical results. This comparison shows that  $Y_0$  and  $Y_c$  are 5.2 MPa and 0.5 MPa, respectively. Noting that  $Y_0$  is the damage initiation parameter and  $Y_c$  its evolution. Figure C- 15 compares numerical and experimental matrix damage after the impact on three aramid/epoxy plies. The numerical model overestimated the crack length by a maximum error of 8%.

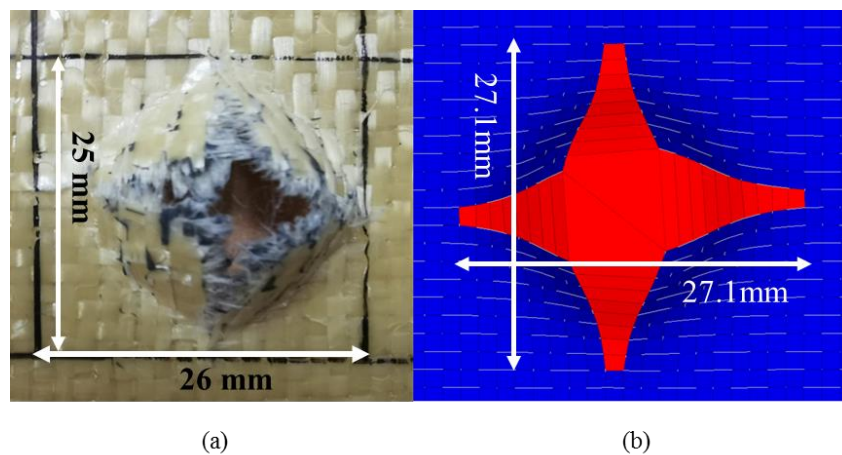


Figure C- 15: Back face damage length a) experimental results, and b) numerical simulation.

## 2.6.Friction influence

A comparative numerical study is held to understand better the influence of friction on the behavior of the aramid plies. The same drop weight test presented in Figure C- 14 is modeled.

### *Aramid epoxy semi-continuous model development and parameters identification*

All the conditions for the numerical model are the same. However, concerning the contact parameters, one model did not include contact (edge to edge), the second one included contact, and the third one included contact with a coefficient of friction  $\mu$  equal to 0.3 based on literature. Figure C- 16 shows the load-displacement curves of the numerical models and the drop weight test experimental curve.

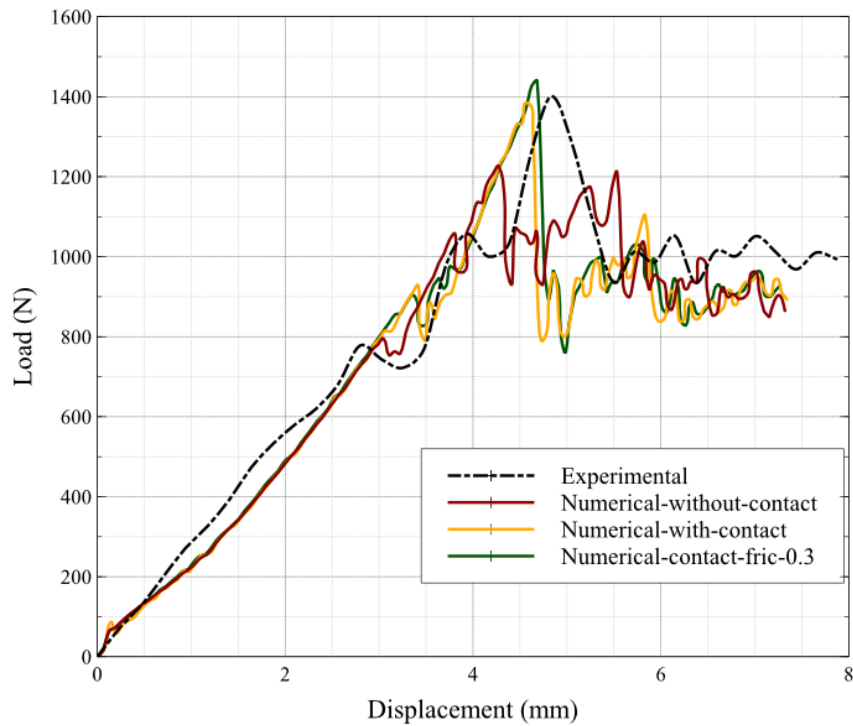


Figure C- 16: A comparison of the load-displacement curves for experimental indentation results and the two numerical cases results

The load-displacement curves show that the numerical model that does not have contact between the rod elements fails at a displacement of around 4.3 mm after attaining a maximum effort of 1200 N.

The model having contact with or without a coefficient of friction of 0.3 attains the same load level as the experimental model, which is 17% higher than the model without contact. The addition of the friction coefficient only increased the load by 4% compared to the model with just contact, meaning that it did not influence the behavior of the fibers.

*Aramid epoxy semi-continuous model development and parameters identification*

This might be because the energy dissipation mechanisms in impregnated fibers result from resin fragments and precipitation contact. This means that simple edge-to-edge contact with friction cannot simulate this type of energy dissipation.

- [1] Navarro P, Aubry J, Marguet S, et al. Semi-continuous approach for the modeling of thin woven composite panels applied to oblique impacts on helicopter blades. *Compos Part Appl Sci Manuf*. 2012;43:871–879.
- [2] Pascal F, Navarro P, Marguet S, et al. On the modelling of low to medium velocity impact onto woven composite materials with a 2D semi-continuous approach. *Compos Struct*. 2015;134:302–310.
- [3] theory\_mat\_laws.pdf [Internet]. [cited 2022 Jun 14]. Available from: [https://altairhyperworks.com/hwhelp/Altair/hw14.0/help/hwsolvers/theory\\_mat\\_laws.pdf](https://altairhyperworks.com/hwhelp/Altair/hw14.0/help/hwsolvers/theory_mat_laws.pdf)
- [4] Rogani A, Navarro P, Marguet S, et al. Study of post-impact behaviour of thin hybrid carbon/epoxy and glass/epoxy woven composite laminates under fatigue tensile loading – Part II: Numerical study. *Compos Struct*. 2021;260:113451.
- [5] Belytschko T, Lin JJ, Chen-Shyh T. Explicit algorithms for the nonlinear dynamics of shells. *Comput Methods Appl Mech Eng*. 1984;42:225.
- [6] 20914\_TDS.pdf [Internet]. [cited 2022 Jun 14]. Available from: [https://kevra.fi/wp-content/uploads/20914\\_TDS.pdf](https://kevra.fi/wp-content/uploads/20914_TDS.pdf).
- [7] 909hoja-tecnica-Araldite LY 5052\_Aradur 5052.pdf [Internet]. [cited 2022 Jun 14]. Available from: [https://www.generaladhesivos.com/proveedor-pegamento/909hoja-tecnica-Araldite%20LY%205052\\_Aradur%205052.pdf](https://www.generaladhesivos.com/proveedor-pegamento/909hoja-tecnica-Araldite%20LY%205052_Aradur%205052.pdf).
- [8] Flanagan DP, Belytschko T. A uniform strain hexahedron and quadrilateral with orthogonal hourglass control. *Int J Numer Methods Eng*. 1981;17:679–706.







Appendix D.      **Epoxy foam characterization and  
parameters identification**

---

## 1. Introduction

This section deals with the parameters identification strategy for a material law that simulates the behavior of closed-cell epoxy foams PB170, PB250, and PB400. The proposed numerical model is MAT/LAW28, a built-in material law in the FE software RADIOSS. A USER failure model is integrated into the material law to represent failure modes seen experimentally. Experimental tests are performed to identify the parameters needed.

## 2. Modeling Strategy of epoxy foams

### 2.1. Material law formulation (MAT/LAW28)

The material law used to model the epoxy foam is typically used to simulate honeycombs and crushable foams [1]. Hookian law describes the elastic region with a Poisson's ratio equal to zero. The stress-strain relationship is described as follows:

$$\begin{bmatrix} \sigma_{11} \\ \sigma_{22} \\ \sigma_{33} \\ \sigma_{12} \\ \sigma_{23} \\ \sigma_{13} \end{bmatrix} = \begin{bmatrix} E_{11} & 0 & 0 & 0 & 0 & 0 \\ 0 & E_{22} & 0 & 0 & 0 & 0 \\ 0 & 0 & E_{33} & 0 & 0 & 0 \\ 0 & 0 & 0 & G_{12} & 0 & 0 \\ 0 & 0 & 0 & 0 & G_{23} & 0 \\ 0 & 0 & 0 & 0 & 0 & G_{13} \end{bmatrix} \cdot \begin{bmatrix} \varepsilon_{11} \\ \varepsilon_{22} \\ \varepsilon_{33} \\ \varepsilon_{12} \\ \varepsilon_{23} \\ \varepsilon_{13} \end{bmatrix} \quad (1)$$

where  $\sigma$  is the material stress,  $\varepsilon$  is the material strain in each direction.  $E_{ii}$  and  $G_{ii}$  are Young's modulus and shear modulus in the three directions.

The user defines the plastic region and densification with the input of the true stress versus true strain curves for each direction. The input curves are deduced from experimental tests (compression, tensile, shear).

The compression and tensile modulus for the epoxy foam used in the present work are different.

## **2.2.Damage parameters**

A time-dependent dynamic failure law is introduced to handle the damage inside the epoxy foam. The objective is to represent the behavior observed when the foam is crushed. To do so, only the deviatoric part of the stress tensor is deleted when reaching the failure criteria. The spherical part of the stress tensor will remain to represent the change in volume in the elements. This damage law is based on Tuler-Butcher [34] cumulative damage integral  $D$ . This failure law is not considered instantaneous but it needs a specific amount of time to initiate the failure, where it takes place when  $\sigma$  (the maximum principal stress) exceeds  $\sigma_r$  (the fracture stress) and lasts for a certain period until the cumulative damage integral reaches the critical value  $K$ . The cumulative damage parameter  $D$  is presented in (Equation 2), and when it reaches 1, the failure occurs:

$$D = \int_0^t \frac{\max(0, (\sigma - \sigma_r)^\lambda) dt}{K} \quad (2)$$

Where  $t$  is the time,  $\lambda$  is a material constant (typically set to 2 [34]).  $\sigma_r$  can be identified as the dynamic tensile yield point or the true static tensile stress for failure.

Experimental observation showed that the epoxy foam specimen encounters tensile failure when subjected to impact with a hemispherical shape indenter. Consequently, a failure model in tension is introduced. This law is based on calculating the principal strains ( $\varepsilon_I, \varepsilon_{II}, \varepsilon_{III}$ ) at each time step and comparing them to  $\varepsilon_{rup}$ , the maximum strain to failure criterion defined by the tensile test. The element is deleted if one of the principal strains exceeds the failure criteria.

$$\text{if } \max(\varepsilon_I, \varepsilon_{II}, \varepsilon_{III}) > \varepsilon_{rup} \quad \text{then rupture} \quad (3)$$

To identify the parameters needed for the numerical models, a series of experimental tests is conducted, compression, tensile, shear, and indentation. Dynamic tests took place when possible regarding machine availability (compression and indentation on the drop weight machine). However, quasi-static tests were conducted in the case of inaccessibility to dynamic machines. The parameters that are identified with experimental tests are summarized in Table D- 1

Table D- 1: Parameters of the material and the experimental tests associated with them

Parameter	Symbole	Identification test
Compressive modulus	$E_{comp}$	Dynamic compression test
Tensile modulus	$E_{tensile}$	
Rupture strain	$\epsilon_{rup}$	Quasi-static tensile test
Fracture stress	$\sigma_r$ (MPa)	
Shear modulus	$G_{shear}$	Quasi-static shear test
Critical value of the damage integral	$K$ (MPa $^\lambda$ .ms)	Dynamic indentation test

### 3. Parameter identification

#### *Dynamic compression*

Dynamic compression tests are performed on 40 mm diameter and 20 mm diameter cylindrical specimens for PB170, PB250, and PB400 through a drop weight machine. A high-speed camera is used to capture the velocity of the impactor just before impact, Figure D- 1. The weight of the impactor is 8 kg. PB170 epoxy foam samples are tested at a velocity of  $V= 4$  m/s. PB250 and PB400 samples are tested at  $V= 6$  m/s to capture the three regions of the foam behavior under compressive loading (linear, plateau, densification). A load sensor is used to record the impact behavior of the samples throughout the time.

*Epoxy foam characterization and parameters identification*

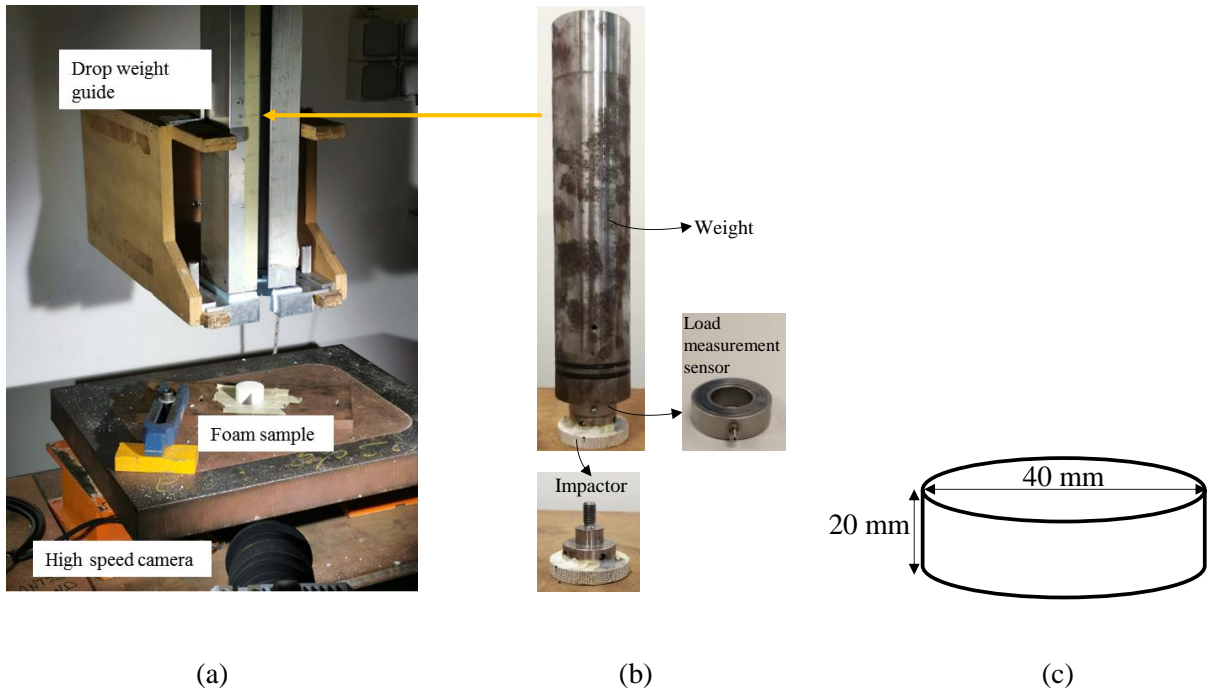


Figure D- 1 : Dynamic compression (a) test set-up, (b) impactor configuration and (c) sample dimensions

The compression test is modeled using two rigid walls. The rigid wall on the bottom constrains the translation of the nodes on the bottom face. The second rigid wall is moving, representing the weight and initial velocity of the impactor. The mesh size of the elements is 1 mm. Figure D- 2.a shows the numerical model, and Figure D- 2.b shows the numerical and experimental load versus displacement curves.

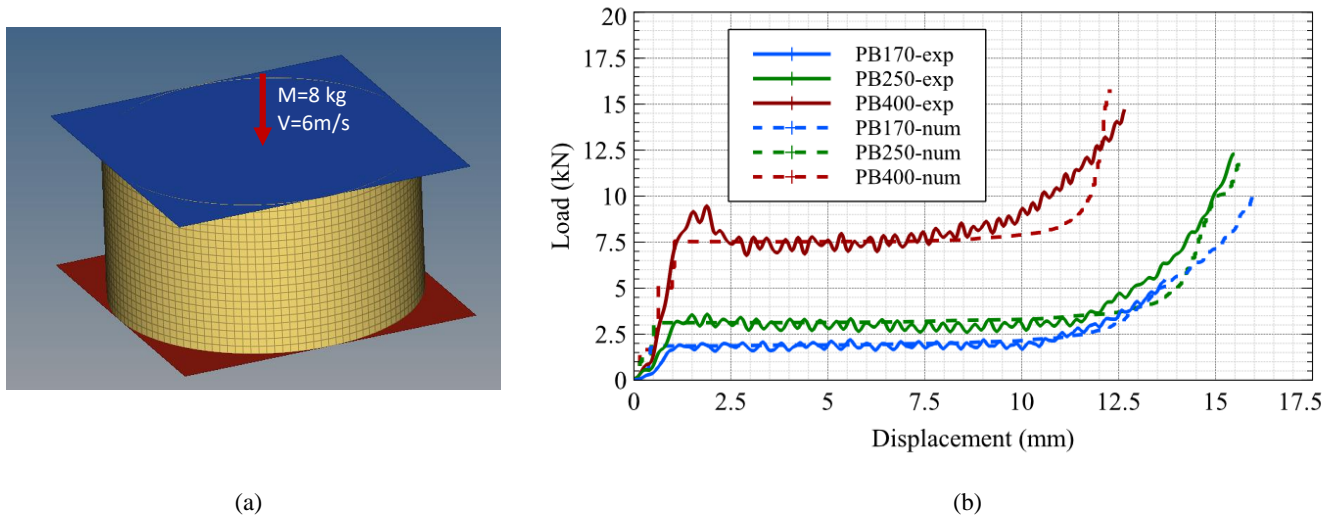


Figure D- 2: (a) compression test numerical model, and (b) load-displacement curves for the dynamic compression test on samples PB170, PB250, and PB400

### *Epoxy foam characterization and parameters identification*

The compression test results helped define the user input curves for the plastic and densification region. The values of those curves are implemented in the material law. The compression modulus is determined for the three epoxy foams by adjusting the slope of the elastic region by comparing experimental and numerical curves. The curves of Figure D- 2.b show that the chosen law can represent the classic behavior of the epoxy foams (linear-elastic, plateau, and densification). The density of the foam influences the foam stiffness, plateau, and densification.

#### ***Quasi-static tensile test***

The tensile behavior of the epoxy foams is studied through a quasi-static tensile test. The tensile test is established using an ultimate tensile machine (INSTRON) with a 10 kN load cell, with a velocity of 1mm/min (Figure D- 3.a). The sample tested has a geometry presented in Figure D- 3.b, a cylindrical shape sample with a diameter of 40 mm and a narrower one in the middle of 22 mm. The geometry of the sample makes it complicated to get the stress-strain curves. Therefore, only the load versus displacement curves are presented.

The tensile behavior of the epoxy foams is studied through a quasi-static tensile test. The tensile test is established using a tensile machine (INSTRON) with a 10 kN load cell, with a velocity of 1 mm/min (Figure D- 3.a). The sample tested has the geometry presented in Figure D- 3. b, a dog-bone cylindrical shape sample with a diameter of 40 mm and a narrower one in the middle of 22 mm. Two metallic substrates attached to two screws adhere on each side of the specimen. This system is used to mount the specimen unto the tensile machine.

*Epoxy foam characterization and parameters identification*

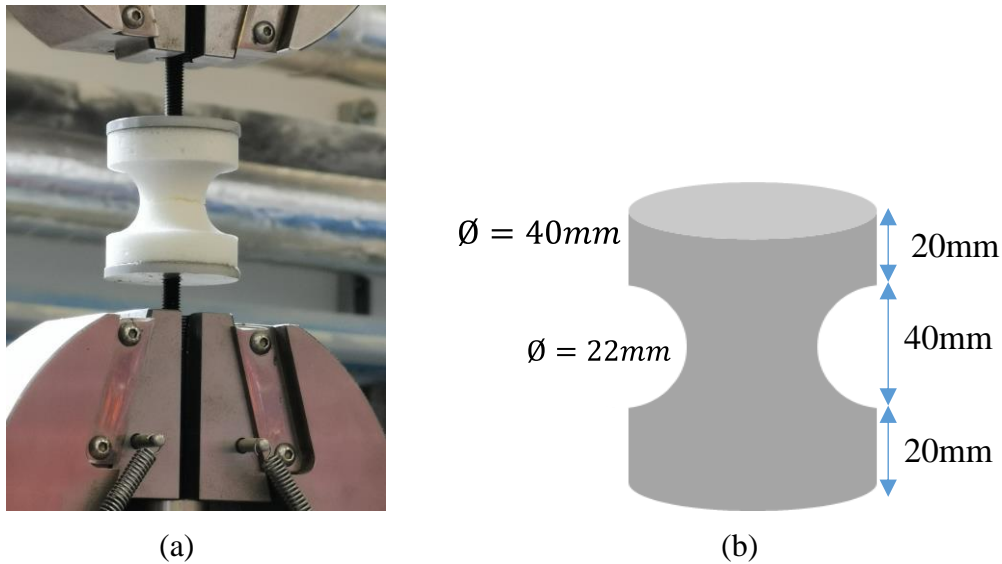


Figure D- 3: Tensile test (a) apparatus and (b) sample dimensions

Based on this test, the tensile modulus of the three foams, the fracture stress, and the strain to failure are defined. The numerical model and load-displacement curves are presented in Figure D- 4. The experimental test is modeled with two rigid bodies, one to fully constrain the bottom nodes of the specimen and the other one to impose the velocity. The mesh size ranged from 1 mm to 1.7 mm. The numerical model is shown in Figure D- 4.a, and Figure D- 4.b shows that the behavior of the samples is linear with a brittle failure.

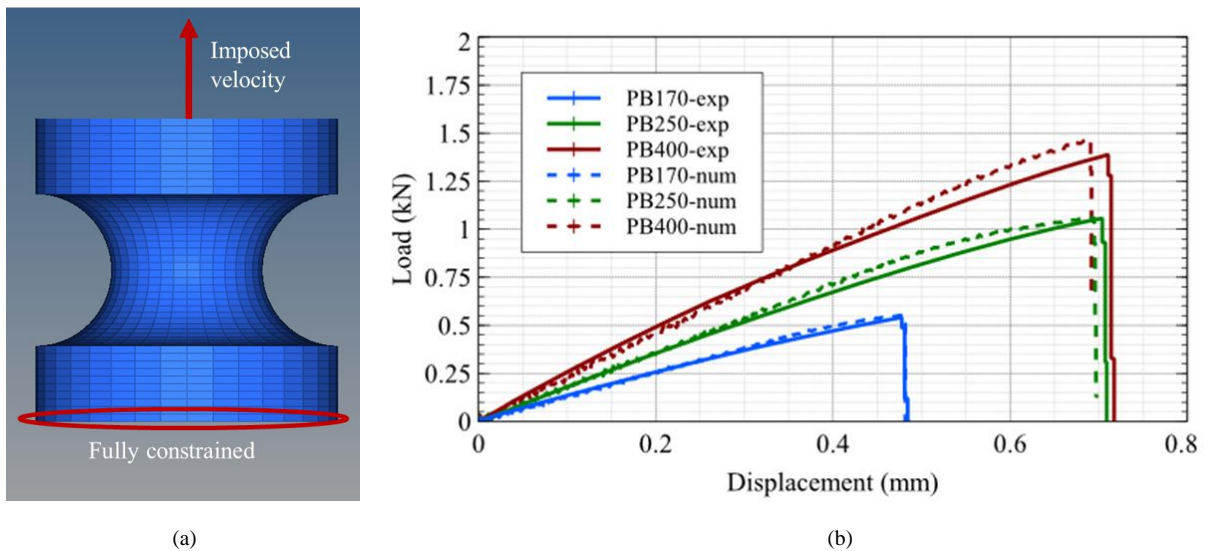


Figure D- 4: (a) Tensile test numerical model, and (b) Load-displacement curves of tensile test on epoxy foam samples PB170, PB250, and PB400.



***Quasi-static shear test:***

Quad-bloc shear tests are performed to test the shear behavior of the epoxy foams. The geometry of the test sample is illustrated in Figure D- 5. The sample consists of four rectangular blocks of foam with 25x20 mm dimensions and 5 mm thickness. The foam blocks are bonded on metallic substrates using an adhesive.

The samples are tested with a tensile machine (INSTRON) with a 10 kN load cell with a 1 mm/min velocity.

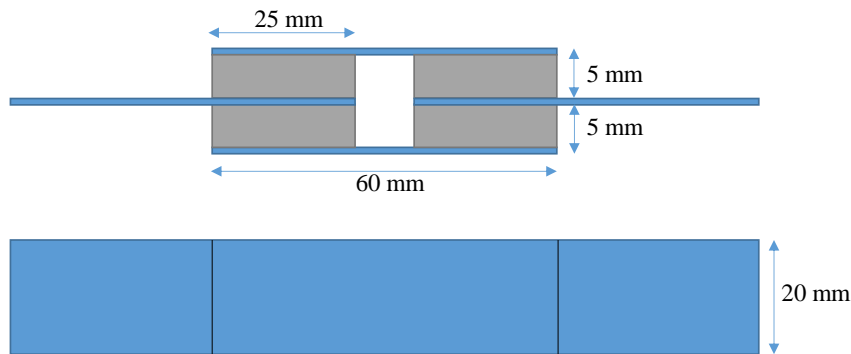


Figure D- 5: Schematic of the sample geometry

The modeling of the shear test is done using two rigid bodies to impose the velocity and boundary conditions Figure D- 6.a. The mesh size of the foam is 1 mm. This test helped define the shear modulus of the epoxy foams. However, the failure strain definition is challenging since the model failed prematurely, as Figure D- 6.b shows. Figure D- 7.a shows the stress XZ contour, where homogenous shear stress distribution is seen. Figure D- 7.b shows the stress ZZ contour. Stress concentration is seen on the substrates/foam level. The premature failure is due to reaching the tensile failure criteria in those elements located at the substrate/foam level (Figure D- 7.b).

## Epoxy foam characterization and parameters identification

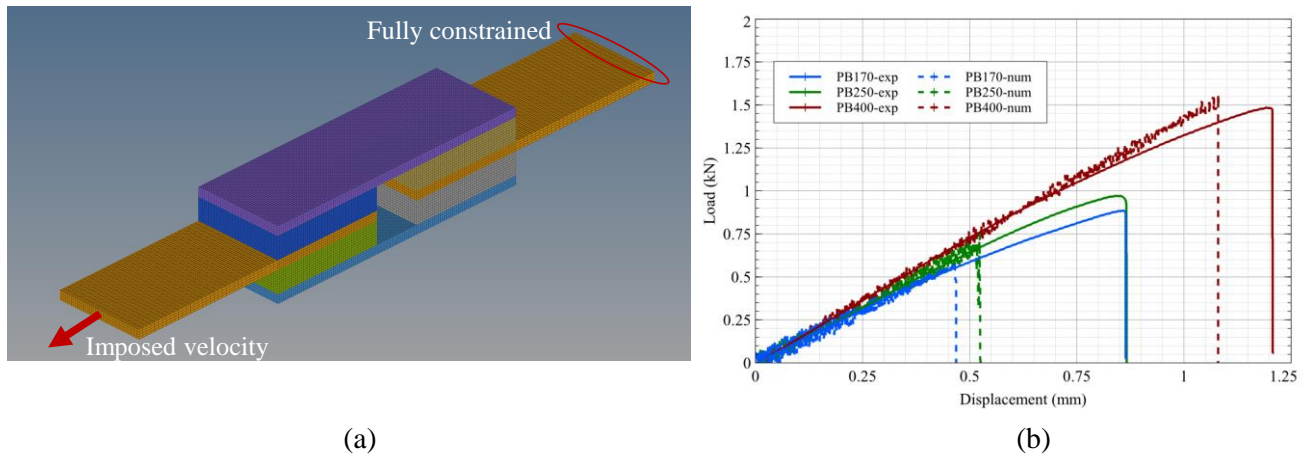


Figure D- 6: (a) Shear test numerical model, and (b) Experimental/numerical comparison of load-displacement curves for the quasi-static quad-bloc shear test samples PB170, PB250, and PB400.

## Epoxy foam characterization and parameters identification

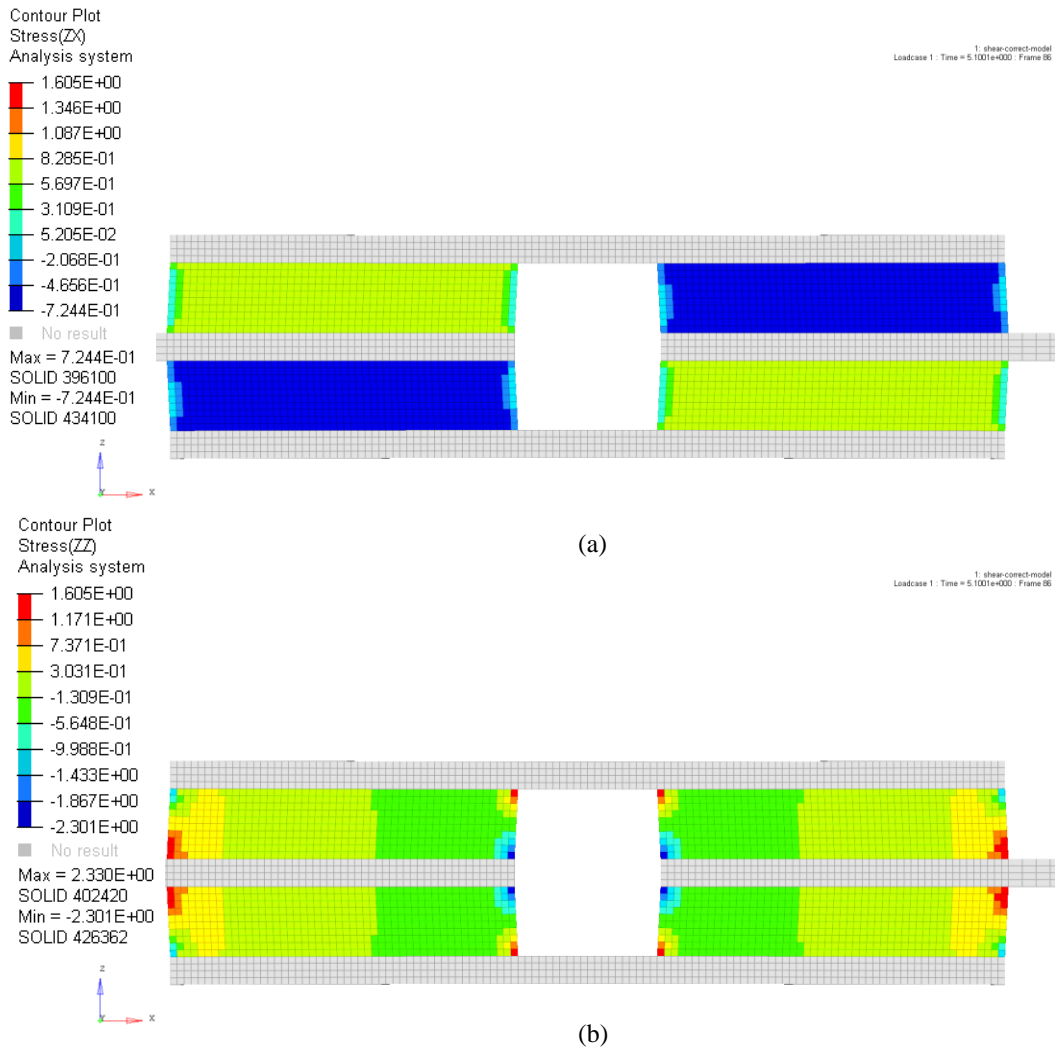


Figure D- 7: (a) Stress ZX and (b) stress ZZ contour of the quad bloc shear test numerical model of PB170 foam

### ***Dynamic indentation test:***

A series of dynamic indentation tests is achieved to validate the material law and define the damage parameter K. The setup and the sample dimensions are presented Figure D- 8. Foam densities PB170 and PB250 are tested with an impact velocity of 3.6 m/s and impact energy of 12.96 J. Sample with PB400 is tested with an impact velocity of 6.3 m/s and impact energy of 39.6 J. The dynamic indentation test is performed with an indenter having a hemispherical shape with a diameter of 16 mm and a mass of 2 kg.

### Epoxy foam characterization and parameters identification

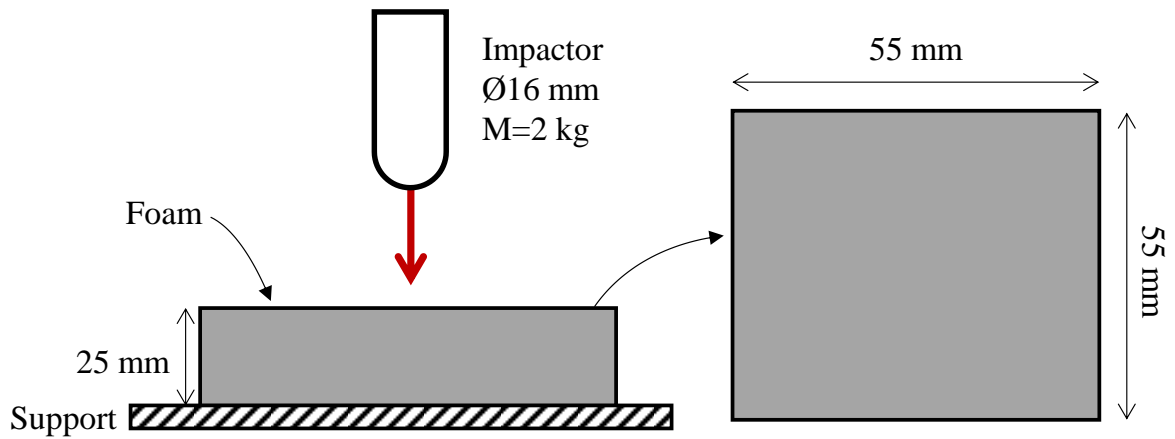


Figure D- 8: Schematic of the test apparatus and sample geometry of the dynamic indentation test

The dynamic indentation test is modeled by representing the indenter by a spherical rigid body, respecting the condition of the experimental test. The foam boundary conditions are imposed by introducing a fixed rigid wall on the bottom face of the foam, Figure D- 9. The mesh size under the impact area is 1 mm.

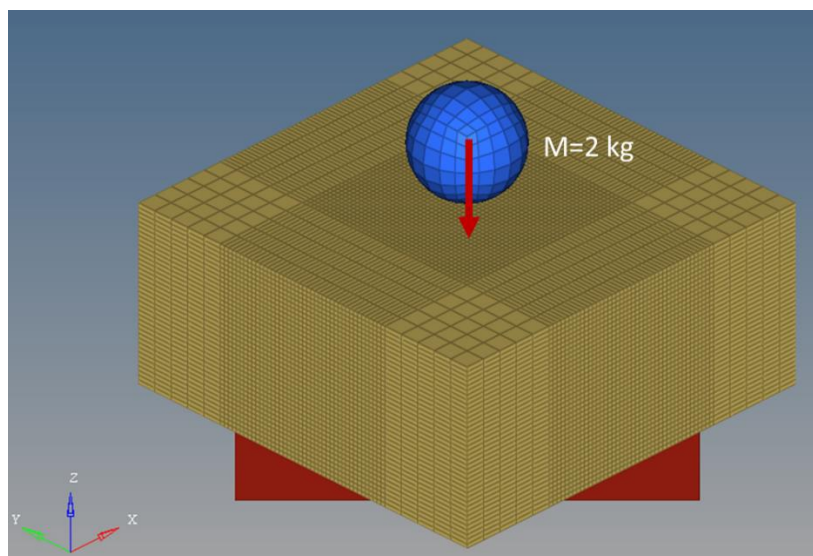


Figure D- 9: Numerical model for dynamic indentation test

The parameter  $K$  is defined for the three foams by comparing the experimental and numerical curves for the dynamic indentation test. The load-displacement results are presented in Figure D- 10 and Figure D- 11. The numerical models show a good correlation with the experimental curves, where the linear and densification regions are well represented.

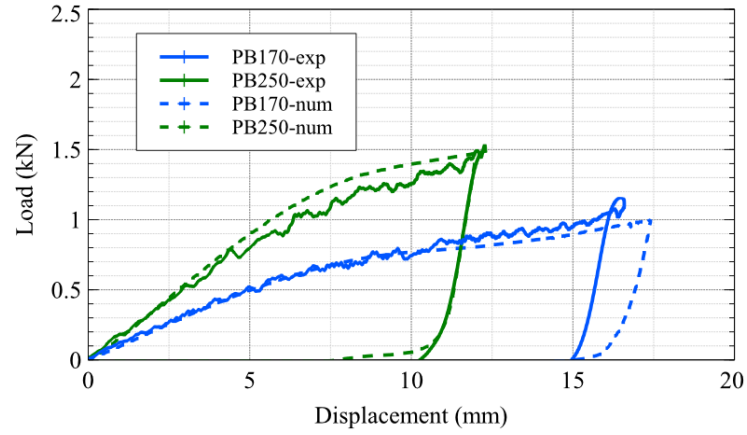


Figure D- 10: Load-displacement curve for dynamic indentation load, of 13 J, on PB170 and 250, experimental (solid line) and numerical (dotted line)

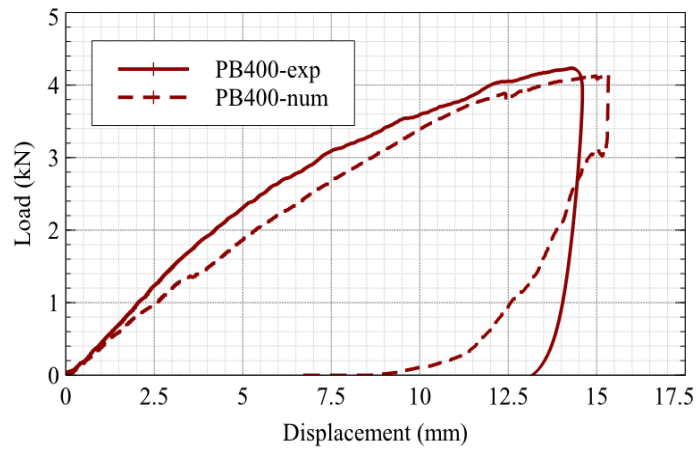


Figure D- 11: Load-displacement curve for dynamic indentation load, of 40 J, on PB400, experimental (solid line) and numerical (dotted line)

#### 4. Summary of the identified parameters

All the parameters identified throughout this section are summarized in Table D- 2.

## *Epoxy foam characterization and parameters identification*

Table D- 2: Parameters identified from the foam material law

Material properties	PB170	PB250	PB400	
Compressive modulus (MPa)	60	72	150	
Tensile elastic modulus (MPa)	130	180	200	
Shear modulus (MPa)	15	18	21	
	$K(\text{MPa}^\lambda \cdot \text{ms})$	2.2	7.15	15.23
Damage variables	$\sigma_r$ (MPa)	1.65	2.9	5.32
	$\varepsilon_{rup}$	0.037	0.048	0.068

### **5. Conclusion**

This appendix presents the formulation of the material law used to simulate the behavior of the epoxy foams. A numerical modeling strategy is developed to represent the physical behavior of the epoxy foam by adopting an existing material law (MAT/LAW28) in the FE software RADIOSS. Failure models are integrated into the material law based on physical observation.

Experimental tests are conducted to identify the parameters needed for the numerical model. The experimental tests also reveal a direct relationship between the density of the foams and their mechanical properties. The results of the numerical modeling are coherent with the experimental ones.



Appendix E.            **Experimental and Numerical  
Results for Low-Velocity Impact**

---



## **1. Introduction**

This appendix presents additional numerical versus experimental results of the drop weight tests in chapter II. The constitutive laws used in the numerical model are detailed in Appendix B, C, and D.

## **2. Numerical versus experimental results**

### *Influence of the number of aramid plies in the middle*

Figure E- 1 shows the experimental and numerical results of the drop weight test performed on mono-foam structures with one or three aramid plies in the middle. The numerical model shows a good correlation with the experimental results. However, the location of the peak load, indicating that the impactor reaches the aramid ply or plies, might vary due to fabrication difficulties (up to 12% error).

## Experimental and Numerical Results for Low-Velocity Impact

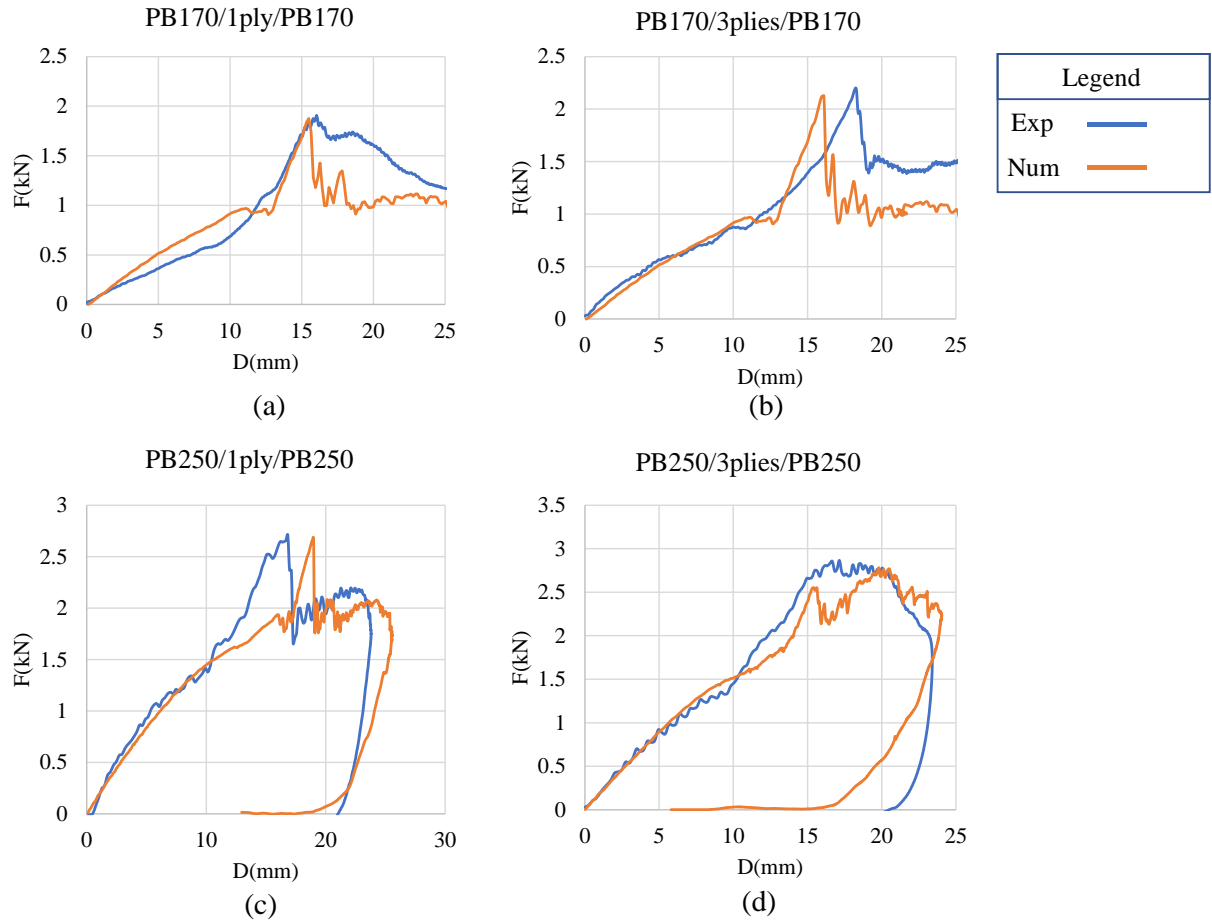


Figure E- 1: Numerical/experimental force versus displacement curves of mono-foam density structures with one or three aramid plies in the middle

### *Influence of the location of aramid plies*

Figure E- 2 and Figure E- 3 present the numerical and experimental results of the drop weight test on mono-foam structures with aramid distributed differently in thickness. The numerical curves correlate well with the experimental ones for PB170, PB250, and PB400. Nevertheless, the numerical curve in Figure E- 3.c shows a higher load (from 5 to 15 mm in displacement) with an error of about 47%. Figure E- 4 shows some PB400 numerical results with different fibers distribution; since the impactor is stopped before reaching the aramid plies in the middle, only two results are presented.

*Experimental and Numerical Results for Low-Velocity Impact*

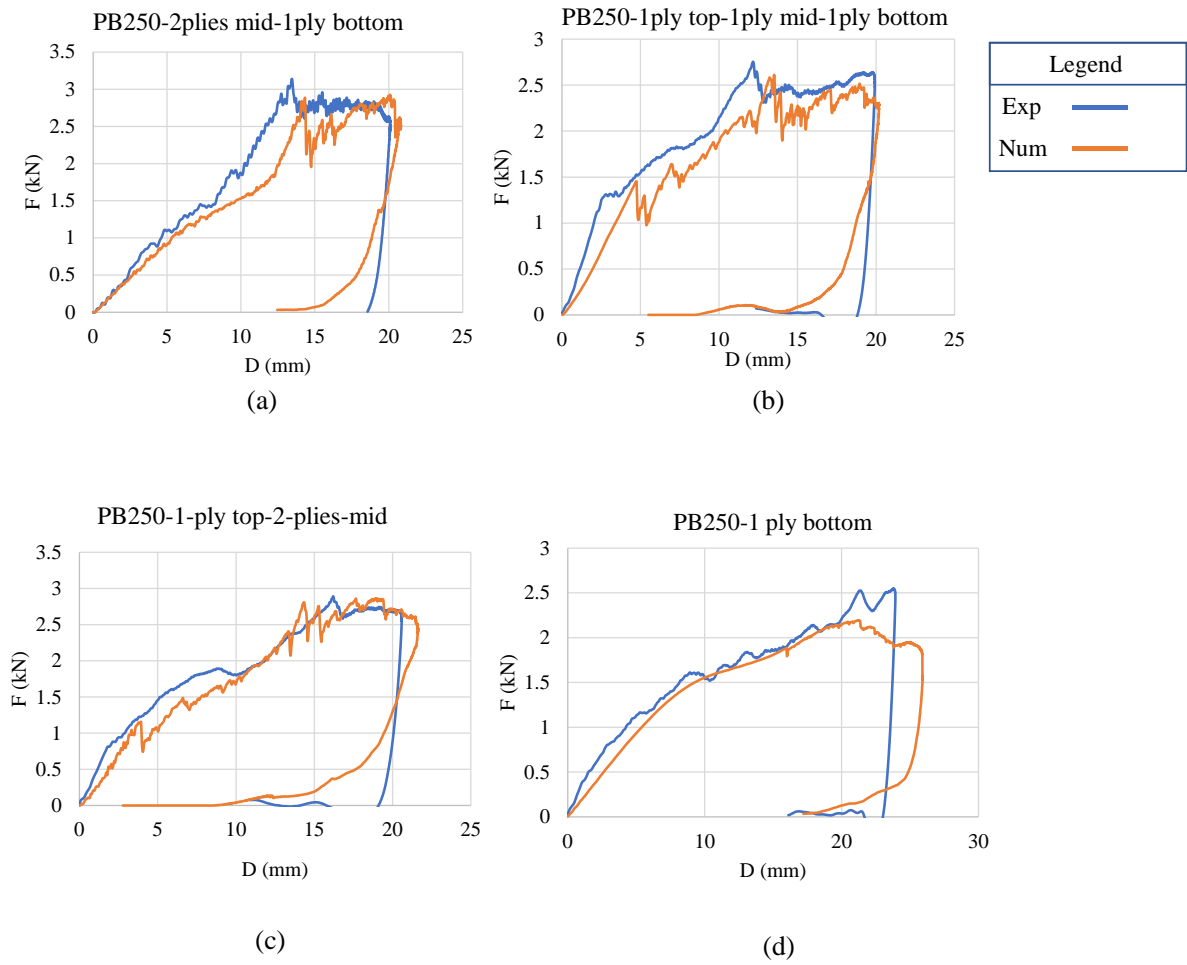


Figure E- 2: Numerical/experimental force versus displacement curves of mono-foam density (PB250) structures with aramid plies distributed differently in the foam thickness

*Experimental and Numerical Results for Low-Velocity Impact*

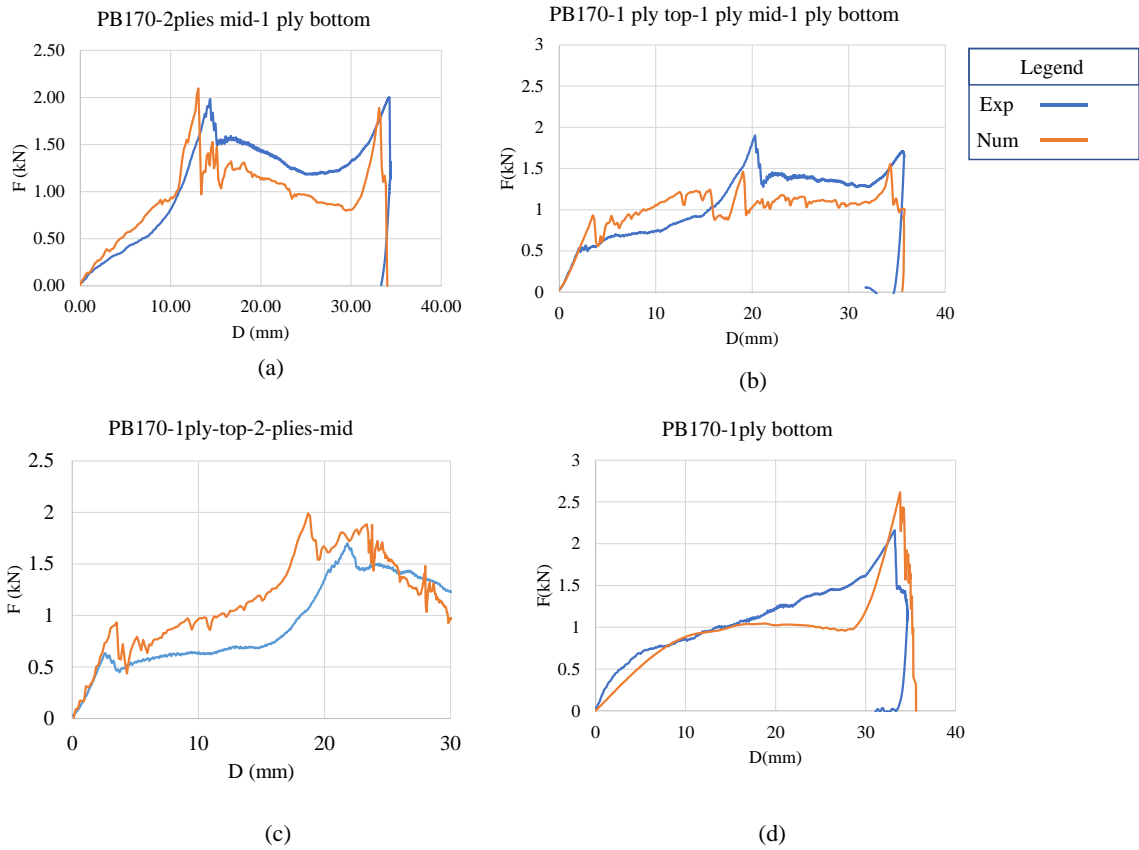


Figure E- 3: Numerical/experimental force versus displacement curves of mono-foam density (PB170) structures with aramid plies distributed differently in the foam thickness

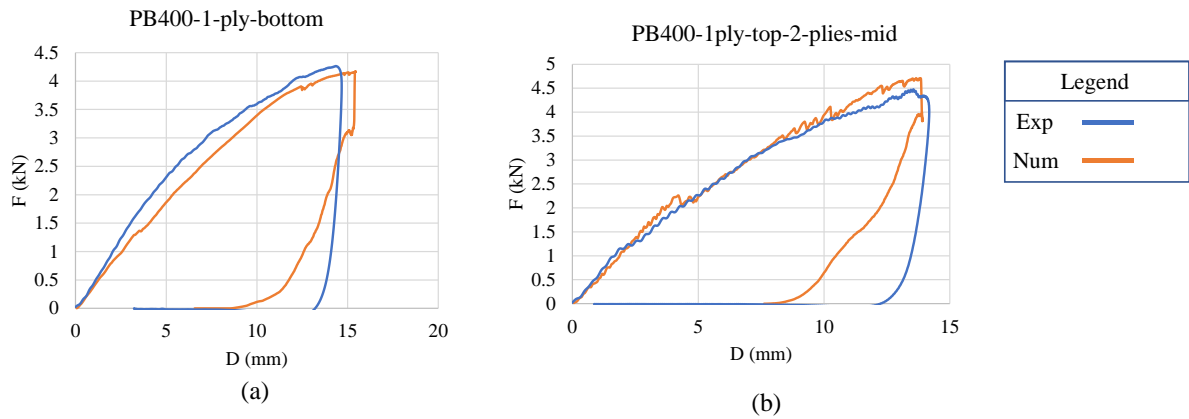


Figure E- 4: Numerical/experimental force versus displacement curves of mono-foam density structures with aramid plies distributed differently in the foam (PB400) thickness

Influence of foam density

The comparison between numerical and experimental results of structures with bi-foam densities with one and three aramid plies is presented in Figure E- 5 and Figure E- 6. It can be shown that the numerical model agrees with the experimental results.

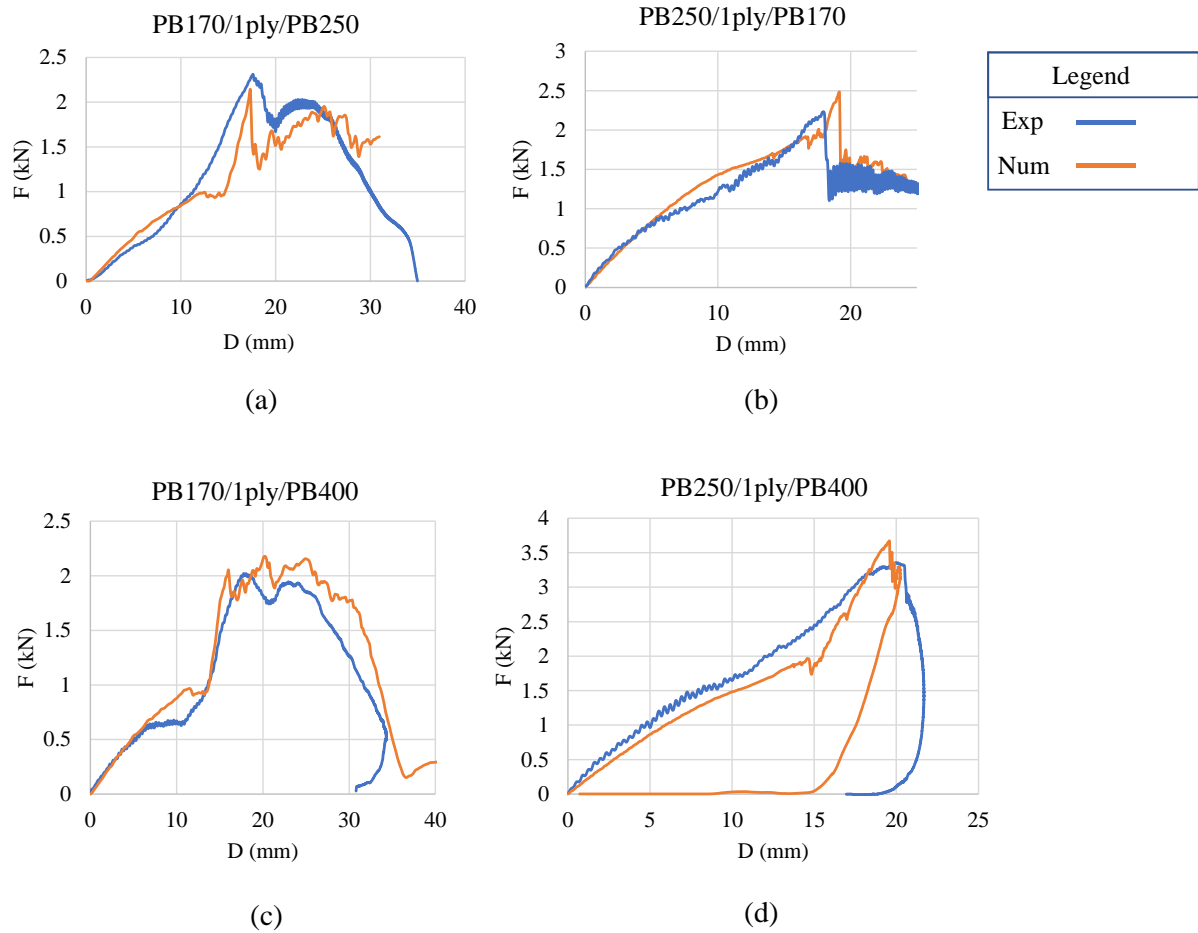


Figure E- 5: Numerical/experimental force versus displacement curves of bi-foam densities structures with one aramid ply in the middle

*Experimental and Numerical Results for Low-Velocity Impact*

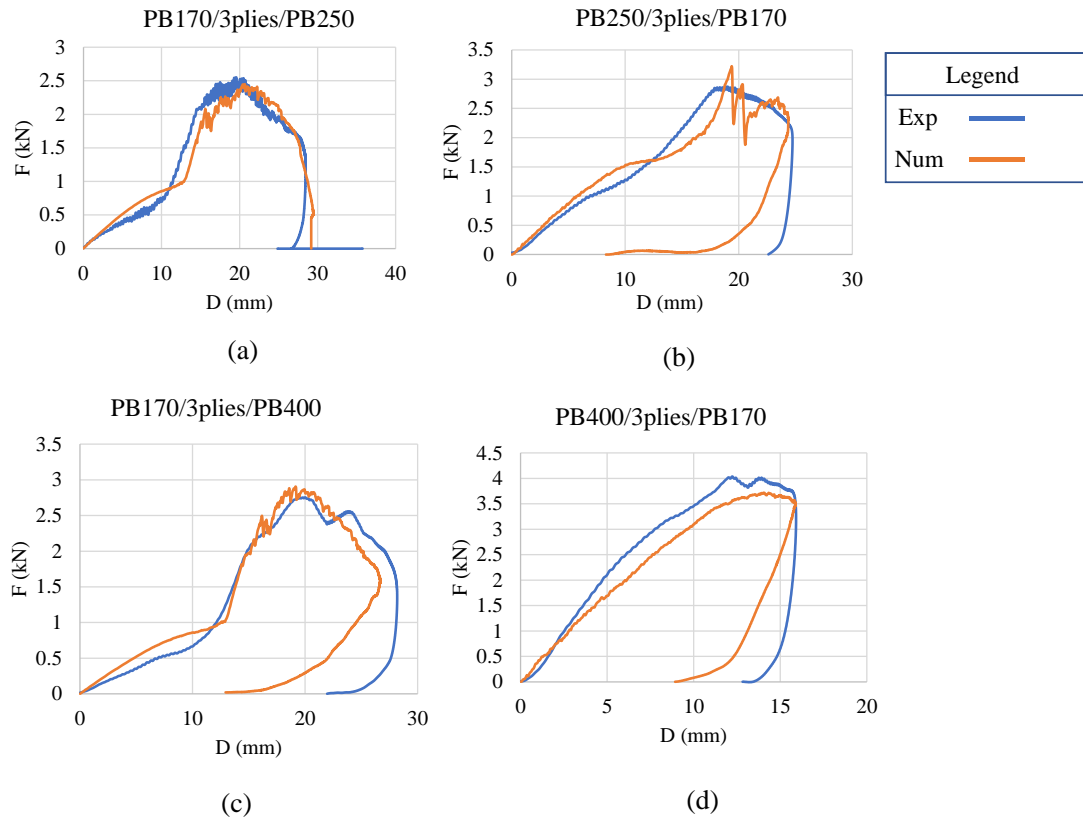


Figure E- 6: Numerical/experimental force versus displacement curves of bi-foam densities structures with three aramid plies in the